

COMPOSITE BORON DOPED HYDROXYAPATITE-TRICALCIUM
PHOSPHATE/ALGINATE/GELATIN HYDROGEL COATING ON
TITANIUM IMPLANTS: OSSEointegration AND
IMMUNOMODULATION STUDY

A THESIS SUBMITTED TO
THE GRADUATE SCHOOL OF NATURAL AND APPLIED SCIENCES
OF
MIDDLE EAST TECHNICAL UNIVERSITY

BY

AHMET ENGİN PAZARÇEVİREN

IN PARTIAL FULFILLMENT OF THE REQUIREMENTS
FOR
THE DEGREE OF DOCTOR OF PHILOSOPHY
IN
ENGINEERING SCIENCES

JULY 2022

Approval of the thesis:

**COMPOSITE BORON DOPED HYDROXYAPATITE-TRICALCIUM
PHOSPHATE/ALGINATE/GELATIN HYDROGEL COATING ON
TITANIUM IMPLANTS: OSSEOINTEGRATION AND
IMMUNOMODULATION STUDY**

submitted by **AHMET ENGİN PAZARÇEVİREN** in partial fulfillment of the requirements for the degree of **Doctor of Philosophy in Engineering Sciences, Middle East Technical University** by,

Prof. Dr. Halil Kalıpçılar
Dean, Graduate School of Natural and Applied Sciences

Prof. Dr. Murat Dicleli
Head of the Department, **Engineering Sciences**

Prof. Dr. Ayşen Tezcaner
Supervisor, **Engineering Sciences, METU**

Prof. Dr. Zafer Evis
Co-Supervisor, **Engineering Sciences, METU**

Examining Committee Members:

Prof. Dr. Dilek Keskin
Engineering Sciences, METU

Prof. Dr. Ayşen Tezcaner
Engineering Sciences, METU

Asst. Prof. Dr. Özge Erdemli
Molecular Biology and Genetics, Başkent University

Asst. Prof. Dr. Arda Büyüksungur
Basic Medical Sciences, Faculty of Dentistry, Ankara University

Asst. Prof. Dr. Bengi Yılmaz
Biomaterials, University of Health Sciences Turkey

Date: 25.07.2022

I hereby declare that all information in this document has been obtained and presented in accordance with academic rules and ethical conduct. I also declare that, as required by these rules and conduct, I have fully cited and referenced all material and results that are not original to this work.

Last name, Name : Pazarçeviren, Ahmet Engin

Signature :

ABSTRACT

COMPOSITE BORON DOPED HYDROXYAPATITE-TRICALCIUM PHOSPHATE/ALGINATE/GELATIN HYDROGEL COATING ON TITANIUM IMPLANTS: OSSEOINTEGRATION AND IMMUNOMODULATION STUDY

Pazarçeviren, Ahmet Engin
Doctor of Philosophy, Engineering Sciences
Supervisor: Prof. Dr. Ayşen Tezcaner
Co-Supervisor: Prof. Dr. Zafer Evis

July 2022, 213 pages

A successful bridging and osseointegration of Ti-6Al-4V implant (Ti) at the defect site are strongly dependent on the effectiveness of the interphase. Achieving such a robust interface could diminish micromovements, shearing on the defected bone and loosening over time. Here, a boron doped hydroxyapatite (A/G/BHT) loaded alginate/gelatin-based (A/G) hydrogel coating on Ti was produced to support bone integration through prompting osteoinduction, vascularization and immunomodulation. Initially, highly reproducible, cheap and time-effective BHT was produced and it significantly promoted higher osteogenic and angiogenic maturation while a mild innate immune response was obtained. Proving the bone tissue engineering (BTE) potential of BHT, a gap-filling A/G/BHT layer was fabricated on Ti to mimic bone extracellular matrix to establish biofunctional bridge. Ti surface was aminosilanized the implant surface by 3-Aminopropyl ethoxysilane (APTES), then coated implant surface with 0.25% w/v alginate with 20 mM 1-Ethyl-3-(3-dimethylaminopropyl) carbodiimide (EDC) and N-hydroxysuccinimide (NHS) to allow A/G/BHT pre-gel to disperse homogeneously and covalently attach on the

surface. The pre-gel was added 0.2 M sodium chloride (NaCl) to blend BHT in the structure without inducing ionic crosslinking. Then, coated implants were freeze-dried. The interphase layer demonstrated high cohesive and adhesive strength (A/G/BHT as 2.66 N compared to A/G 1.72 N), 8 month-long shelf-life at room temperature and normal humidity. Osteoblasts and endothelial cells thrived on A/G/BHT, which allowed improved osteogenic and angiogenic activity. Moreover, A/G/BHT generated an acute increase in immune response that could be resolved rapidly. Finally, A/G/BHT was shown to induce robust integration of the implant in rabbit femur osteochondral model within 2 months.

Keywords: Boron; Hydroxyapatite; Alginate/gelatin; Implant Coating; Titanium

ÖZ

KOMPOZİT BOR İLE KATKILANDIRILMIŞ HİDROKSİAPATİT- TRİKALSİYUM FOSFAT/ALJİNAT/JELATİN HİDROJEL İLE TİTANYUM İMPLANTLARIN KAPLAMASI: OSSEOENTTEGRASYON VE İMMÜNOMODULASYON ÇALIŞMASI

Pazarçeviren, Ahmet Engin
Doktora, Mühendislik Bilimleri
Tez Yöneticisi: Prof. Dr. Ayşen Tezcaner
Ortak Tez Yöneticisi: Prof. Dr. Zafer Evis

Temmuz 2022, 213 sayfa

Başarılı bir kemik dokusu-implant ara fazı kalıcı olarak yerleştirilecek Ti-6Al-4V implantın (Ti) etkin bir şekilde fonksiyon göstermesi için çok büyük bir önem taşımaktadır. Bu şekilde, güçlü bir ara faz mikrohareketlenmeleri, doku sürtünmesini ve gevşemeyi azaltabilir. Bu çalışmada Ti üzerine bor ile katkılandırılmış hidroksiapatit yüklü aljinat/jelatin hidrojel kaplaması osteoindüksiyonu, damarlaşmayı ve immünomodülasyonu tetikleyerek kemik entegrasyonunu sağlaması amacıyla üretilmiştir. İlk olarak, tekrarlanabilir bir şekilde, ucuz ve zamandan tasarruf sağlayarak bor katkılı hidroksiapatit/trikalsiyum fosfat (BHT) üretimi gerçekleştirilmiş ve belirgin ölçüde daha yüksek osteojenik ve anjiyojenik olgunlaşmayı sağladığı ve hafif immün reaksiyon verdiği görülmüştür. BHT'nin kemik doku mühendisliği alanındaki potansiyeli ispatlandıktan sonra biyofonksiyonel köprü oluşturma amacıyla Ti üzerine ekstraselüler matrisi taklit eden boşluk doldurucu A/G/BHT katmanı kaplanmıştır. Ti yüzeyi 3-Aminopropil etoksisilan ile aminosilanize edilmiş ve ardından %0.25 aljinatın 20 mM 1-Ethyl-3-(3-dimethylaminopropyl) carbodiimide (EDC) ve N-hydroxysuccinimide (NHS) ile

kaplanarak A/G/BHT pre-jelinin yüzeyde homojen dağılması ve kovalent baş ile yüzeye bağlanması sağlanmıştır. Pre-jel içerisine 0.2 M sodyum klorür eklenerek BHT'in iyonik çapraz bağlama yapmadan yapı içerisinde karışması sağlanmıştır. Sonrasında kaplanan implantlar dondurularak kurutulmuştur. Ara faz kaplaması oda sıcaklığı ve normal nem altında yüksek kohezif ve adesif güç ile yüzeye bağlandığını ve 8 aylık raf ömrü olduğunu göstermiştir. Osteoblast ve endotel hücrelerinin A/G/BHT üzerinde büyüdüğü ve hem osteojenik hem de anjiyojenik potansiyelin artırıldığı görülmüştür. Ek olarak, A/G/BHT'nin akut immün tepkiye yol açtıktan sonra iyileşme gösterdiği tespit edilmiştir. A/G/BHT'nin 2 ay içerisinde güçlü bir osseoentegrasyon sağladığı tavşan femur osteokondral modeli ile tespit edilmiştir.

Anahtar Kelimeler: Bor; Hidroksiapatit; Aljinat/jelatin; İmplant Kaplaması; Titanyum

ACKNOWLEDGEMENTS

The author would like to express his gratitude to his supervisor Prof. Dr. Ayşen Tezcaner and co-supervisor Prof. Dr. Zafer Evis.

The author acknowledges the infrastructural support provided by METU Center of Excellence in Biomaterials and Tissue Engineering (BIOMATEN). The author also acknowledges the support provided by Prof. Dr. Korhan Altunbaş, Asst. Prof. Dr. Mustafa Volkan Yaprakçı and Dr. Tayfun Dikmen for *in vivo* studies.

This work is funded by TENMAK BOREN (Grant number: 2018-31-07-25-001).

The author is sincerely thankful for the support, love, criticism, encouragement, appreciation and assistance of his family and friends.

TABLE OF CONTENTS

ABSTRACT	v
ÖZ.....	vii
ACKNOWLEDGEMENTS	ix
TABLE OF CONTENTS	x
LIST OF TABLES	xvi
LIST OF FIGURES.....	xviii
LIST OF ABBREVIATIONS	xxiv
CHAPTERS	
1 INTRODUCTION.....	1
1.1 Metallic Implants.....	2
1.1.1 Types of Metallic Implants.....	2
1.1.2 Properties of Titanium-based Implants	9
1.1.3 Challenges of Using Titanium Implants.....	9
1.2 Surface Modifications of Titanium Implants	12
1.2.1 Surface Treatments	12
1.2.1.1 Anodization.....	14
1.2.1.2 Electrochemical Etching and Hydrothermal Treatment.....	15
1.2.1.3 Microarc Oxidation	15
1.2.2 Bioceramic-based Coatings	18
1.2.2.1 Pure HA Coatings on Ti-based Implants	19
1.2.2.2 Ion Doped HA Coatings on Ti-based Implants.....	21

1.2.2.3	Composite Bioceramic-based Coatings with Biological Factors and Antimicrobial Agents	22
1.2.3	Polymer-based Coatings	28
1.2.3.1	Synthetic Polymer-based Coatings	28
1.2.3.2	Natural Polymer-based Coatings	32
1.2.3.2.1	Gelatin	33
1.2.3.2.2	Collagen	35
1.2.3.2.3	Silk Fibroin.....	36
1.2.3.2.4	Alginate	38
1.2.3.2.5	Chitosan.....	40
1.2.3.2.6	Glycosaminoglycans	41
1.3	Aim of the Study	44
2	MATERIALS AND METHODS.....	49
2.1	Materials	49
2.2	Methods.....	50
2.2.1	Preparation and Characterization of BHT.....	50
2.2.1.1	Preparation of BHT	50
2.2.1.2	XRD Analysis.....	51
2.2.1.3	FTIR Analysis.....	51
2.2.1.4	Particle Size, Elemental Composition, Total Surface Area and Mesoporous Volume Analyses	52
2.2.1.5	SEM-EDX Analysis	52
2.2.1.6	CaP Deposition Analysis	52
2.2.1.7	<i>In vitro</i> Biocompatibility Analysis with HT and all BHTs	53

2.2.1.8	<i>In vitro</i> Cell Culture Studies with HT and Selected BHT.....	54
2.2.1.8.1	Cell Proliferation Analysis.....	54
2.2.1.8.2	Osteogenic Properties	54
2.2.1.8.2.1	ALP Activity and OCN Release	54
2.2.1.8.2.2	Osteogenic Gene Expression Analysis	56
2.2.1.8.3	Angiogenic Properties.....	58
2.2.1.8.3.1	Tube Formation Analysis.....	58
2.2.1.8.3.2	Vascular Endothelial Growth Factor A Release Study...	58
2.2.1.8.4	Immunomodulatory Properties	59
2.2.1.8.4.1	Inflammasome Response	59
2.2.1.8.4.2	Inflammatory Response	61
2.2.2	Grafting and Optimization of Aminosilane on Ti-6Al-4V	61
2.2.2.1	XPS Analysis	63
2.2.2.2	TNBS Analysis.....	63
2.2.3	Fabrication of Alginate/Gelatin Coating on APTES Grafted Ti-6Al-4V and Optimization Studies	65
2.2.3.1	Rheological Analysis	67
2.2.3.2	Morphology Analysis.....	68
2.2.3.3	Water Uptake and Hydrolytic Degradation.....	68
2.2.3.4	Qualitative Adhesion Test.....	69
2.2.3.5	Microscratch Analysis.....	69
2.2.3.5.1	Scratch Test for As-is Coatings	69
2.2.3.5.2	Scratch Test to Determine Shelf-Life	70
2.2.3.6	Cell Viability Assay	70

2.2.4	Fabrication of A/G/BHT Coating on Ti-APTES and Optimization Studies	71
2.2.4.1	Rheological and Thermogravimetric Analyses	72
2.2.4.2	Morphological Analysis	72
2.2.4.3	Water Uptake and Hydrolytic Degradation Analysis	72
2.2.4.4	Microscratch Analysis	73
2.2.4.5	Shelf-Life Analysis.....	73
2.2.4.6	<i>In vitro</i> Cell Culture Studies	73
2.2.4.6.1	hFOB Proliferation and Morphology Analysis	73
2.2.4.6.2	Osteogenic Response.....	74
2.2.4.6.2.1	ALP Activity Assay	74
2.2.4.6.2.2	Osteocalcin Release Assay	74
2.2.4.6.2.3	Osteogenic Gene Expression Analysis.....	75
2.2.4.6.3	Angiogenic Response	76
2.2.4.6.3.1	HUVEC Proliferation and Morphology Analysis	76
2.2.4.6.3.2	VEGF-A Release Assay	77
2.2.4.6.4	Immunomodulatory Response.....	77
2.2.4.7	<i>In vivo</i> Study	78
2.2.4.7.1	Preparation of Sections with Intact Implant-Bone Interface .	78
2.2.4.7.2	Masson-Goldner Trichrome Staining.....	79
2.2.4.7.3	Decalcification prior to immunohistochemical staining	80
2.2.5	Statistical analysis.....	80
3	RESULTS and DISCUSSION	83
3.1	Characterization and Optimization of BHTs	83

3.2	<i>In Vitro</i> Biological Characterization of BHT	93
3.2.1	Bioactive Ion Release	93
3.2.2	Effect of BHT on Cellular Proliferation	94
3.2.3	Osteogenic Properties	95
3.2.4	Angiogenic Properties	97
3.2.5	Immunomodulatory Properties	99
3.3	Characterization And Optimization of Ti-Aptes And A/G Coatings	105
3.3.1	APTES grafting on Ti-APA surfaces	105
3.3.2	A/G Coating on Ti-APTES	115
3.3.3	Biological Characterization of A/G Coatings.....	125
3.4	Design Considerations and <i>In Vitro</i> Properties of A/G/BHT	128
3.4.1	Rheological and Thermogravimetric Properties.....	128
3.4.2	Morphological Properties	129
3.4.3	Water Uptake and Hydrolytic Degradation Properties.....	130
3.4.4	Mechanical, Shelf-Life and Ion Release Properties	132
3.4.5	Osteogenic Properties	138
3.4.6	Angiogenic Properties	143
3.4.7	Immunomodulatory Properties.....	145
3.5	Osseointegration of A/G/BHT In Rabbit Femur Osteochondral Defect Model 152	
4	CONCLUSION	159
	REFERENCES	161
	APPENDICES	
A.	Wavelength scan of TNBS for finding λ_{\max}	203

B.	ALP Calibration Curve Using 4-nitrophenol	204
C.	Calibration curve of DNA using Picogreen Dye Calibration	205
D.	Calibration Curve of OCN	206
E.	Calibration Curve of VEGF-A	207
F.	Calibration Curve of CAS-1	208
G.	Calibration Curve of IL-10	209
H.	Calibration Curve of iNOS	210
	CURRICULUM VITAE	211

LIST OF TABLES

TABLES

Table 1.1 Metallic BTE implants, their manufacturing method and the outcome of their analyses <i>in vitro</i> and/or <i>in vivo</i> conditions.	3
Table 1.2 Surface treatments for Ti-based implants to improve osseointegration and/or antibacterial properties.	16
Table 1.3 Various bioceramic coatings with or without additional biological factors or antimicrobial agents on Ti-based implants.	26
Table 1.4 Synthetic polymer-based coatings on Ti-based implants.	30
Table 1.5 Natural polymer-based coatings on Ti-based implants.	42
Table 2.1 Molar percent of each component in HT and BHT species.....	51
Table 2.2 Composition of SBF (Kokubo & Takadama, 2006).	53
Table 2.3 Media used in biocompatibility, cell proliferation and osteogenic differentiation analyses with hFOBs.	56
Table 2.4 Primers used in osteogenic gene expression analyses. Primers were designed and tested using BLAST (NIH, USA) and Primer3 software.	57
Table 2.5 Media used in immunomodulatory studies (Tweedell, et al., 2020).	60
Table 2.6 Parameters tested and optimized for APTES coating.	64
Table 2.7 Concentration of A/G coating components.	66
Table 2.8 Concentration of the components employed in the composite coatings.	72
Table 2.9 Primers used in osteogenic, angiogenic and immunomodulatory gene expression analyses.	75
Table 3.1 SSA and mesopore volume, and grain sizes of BHT samples detected with BET analysis (n=3) and SEM analysis (n=50).	84
Table 3.2 Structural properties of BHT samples (n=3).	89
Table 3.3 ICP results of HT and BHTs (n=3).	90
Table 3.4 Release of Ca and B from HT and BHT (n=3).	94
Table 3.5 Atomic ratios of N1s and Si2p against Ti2p3 on APTES grafted samples in various media (n=3).	107

Table 3.6 Active amine content on Ti-APTES samples prepared with different conditions (n=6).....	110
Table 3.7 Roughness (R_q) and contact angle measurements of surface modified implants (n=3).....	113
Table 3.8 Microscratch analysis results conducted on A/G coatings (n=3).....	123
Table 3.9 Microscratch results of A/G 1:3 after incubation at room temperature for different periods (n=3).....	125
Table 3.10 Results of microscratch analysis conducted on A/G coatings (n=3)..	132
Table 3.11 Microscratch testing of A/G and A/G/BHT for determination of coating strength and shelf-life (n=3).....	134
Table 3.12 Cumulative release of Ca and B from A/G and A/G/BHT (n=3).	136
Table 3.13 Osseointegration scores of samples 1 st month and 2 nd month of post-implantation (n=4). Scoring was done in accordance with Masson Trichrome staining.....	157

LIST OF FIGURES

FIGURES

Figure 1.1 Failure modes of Ti implants.	11
Figure 1.2 Proposed composite coating layer on Ti-6Al-4V as gap-filling interphase to support osseointegration of implant.	46
Figure 2.1 APTES activation of Ti-OH on Ti-6Al-4V implants.	62
Figure 2.2 The reactions occurring during crosslinking in between the components of A/G coatings on Ti-APTES.	67
Figure 2.3 Image of A/G/20BHT after adhesion strength test.	71
Figure 3.1 SEM electrographs of BHT samples in disc form. Scale bar is 5 μ m...	85
Figure 3.2 XRD (A) and FTIR (B) spectra of HT and BHTs.	87
Figure 3.3 Mineral deposition on samples after 1 and 7 days of incubation in SBF (Scale bar: 100 μ m, inset scale bar: 2 μ m).	91
Figure 3.4 Ca/P ratio obtained after SBF analysis at the end of 1 st day and 7 th day of incubation. All groups showed statistically higher Ca/P ratio at the end of the analysis compared to HT.	92
Figure 3.5 Indirect elution test results using MTT conducted with the extracts of HT and BHTs (n=8).	93
Figure 3.6 Proliferation analysis of HT and BHT (n=12). Proliferation rate of samples were given as relative viability having hFOB seeded on tissue culture plates as positive control (100%). Statistical differences were given as $*p<0.05$, $**p<0.01$ and $***p<0.001$	94
Figure 3.7 Osteogenic protein production analysis in terms of ALP activity (A, n=18) and OCN release (B, n=6). Statistical differences are denoted by $*p<0.05$, $**p<0.01$ and $***p<0.001$ as not significant.	95
Figure 3.8 Osteogenic gene expression analysis results HT and BHT (n=6). Statistical differences were given as $*p<0.05$, $**p<0.01$ and $***p<0.001$	96

Figure 3.9 HUVEC viability after incubation in HT and BHT conditioned media for 4 h (A) and total amount VEGF-A released from these cells (B) (n=3). Statistical differences were shown as $*p<0.05$, $**p<0.01$ and $***p<0.001$	98
Figure 3.10 Phase contrast micrographs of HUVECs after incubation for 4 h with media only, HT and BHT extracts (A), number of nodes formed (B), tube length (C) and tube area (D) obtained at the end of tube formation study (n=5). Statistical differences are shown as $*p<0.05$, $**p<0.01$ and $***p<0.001$	99
Figure 3.11 Pyroptotic immune response and cell viability of THP-1s with HT and BHT extracts (n=6). Cells were primed with 50 ng/mL PMA, and activated with 1 μ M Nig prior to CAS-1 ELISA analysis (A) and cell viability analysis during inflammasome assembly (B). Statistical differences are shown as $*p<0.05$, $**p<0.01$ and $***p<0.001$	101
Figure 3.12 Fluorescence microscopy images of GFP conjugated ASC specks. White arrows indicate ASC specks in inflammasome assembly. General morphologies of the cells are round, characteristic “M0” state of monocyte-derived macrophage-like (MDM-like) morphology was achieved. Lesser green fluorescent reflection was acquired from PMA ⁺ Nig ⁺ with extensive ASC-GFPs, hence, a high pyroptosis can be inferred.	102
Figure 3.13 Inflammatory immune response and cell viability of THP-1s in HT and BHT extracts (n=6). PMA conditioned cells were also activated with 150 ng/mL LPS (without Nig) to allow either release IL-10 (A) or produce iNOS (B) to direct inflammatory response. During IL-10 and iNOS ELISA analyses, cell viability was also determined (C). Statistical differences are shown at $*p<0.05$	104
Figure 3.14 XPS spectra of Ti-SB and Ti-APA (A), and 4% (v/v) APTES grafted surfaces in different silanization media (B).	106
Figure 3.15 FTIR spectra of Ti-APA and Ti-APTES.	109
Figure 3.16 SEM electrographs of various sample surfaces. Ti-SB denotes initial Ti surface obtained after sandblasting, Ti-APA after acid:peroxide:alkali treatment and Ti-APTES after APTES grafting. Scale bar is 100 μ m, inset scale bar is 10 μ m.	111

Figure 3.17 Images obtained for AFM surface topography analysis for various samples. APTES grafting slightly decreased the surface roughness.	112
Figure 3.18 Water contact angle (A) and macroscopic images of Ti-SB, Ti-APA, Ti-APA and Ti-APTES stained with TNBS, and as prepared Ti-APA and Ti-APTES (B). APTES grafting drastically increased the hydrophobicity. APTES presence was shown by TNBS staining, and could be detected by naked eye due to high reflectance of APTES grafted samples.	114
Figure 3.19 Schematic display of A/G coating steps (A), and photos and microscopic images of dip-coated A/G hydrogel on Ti-APTES as coated and after freeze-dried (B).....	115
Figure 3.20 Apparent viscosity of A/G pre-gel samples (n=1).	116
Figure 3.21 Water uptake (A) and hydrolytic degradation (B) test results of A/G coatings.....	118
Figure 3.22 SEM electrographs of freeze-dried coatings (A) and macroscopic images of swollen coatings on Ti-APA (B) and Ti-APTES (C). SEM scale bar is 500 μm	120
Figure 3.23 SEM images of scratched A/G coatings on Ti-APTES (A, scale bar is 1 mm), and average FT (B) and PD (C) obtained during the scratch test of different A/G coatings. White arrows indicate the start of scratching, red arrows demonstrate the locations of L_c for each coating, yellow arrows show end of the scratch test, and green arrows show the thickness of coating.	122
Figure 3.24 Representative SEM image of A/G 1:3 coatings demonstrating fine wrapping around a cylindrical implant with a small kink at the top (A) to determine coating thickness, and SEM images of scratched A/G 1:3 samples after shelf-life analysis (B). Scale bar for SEM images is 1 mm. White arrows indicate the start of scratching, red arrows demonstrate the locations of L_c for each coating, yellow arrows show end of the scratch test, and green arrows show the thickness of coating.	124

Figure 3.25 Proliferation of hFOB on Ti-APA and A/G coatings on Ti-APTES (n=8). Statistical differences among samples at given incubation period are denoted by * ($p<0.05$).	126
Figure 3.26 CLSM and SEM images of hFOB seeded on Ti-APA and A/G coatings after 1 and 7 days of incubation. hFOB on A/G coatings showed cell proliferation and migration into the coating layer as much as 50 μm . Highest cell density was observed on A/G coatings after 7 days. CLSM scale bars: White bar is 250 μm and yellow bar is 50 μm . SEM scale bars: Long red bar is 1 mm, short red bar is 200 μm	127
Figure 3.27 Apparent viscosity measurement of pre-gels (A) and TGA analysis of the coatings (B). Statistical differences were given as * $p<0.05$, ** $p<0.01$ and *** $p<0.001$	129
Figure 3.28 Macroscopic (A) and SEM images (B) of samples. Scale bar is 100 μm and inset scale bar is 20 μm	130
Figure 3.29 Water uptake (A) and hydrolytic degradation (B) results of the coatings (n=4).	131
Figure 3.30 SEM images of scratched A/G coatings on Ti-APTES. White arrows indicate the start of scratching, red arrows demonstrate the locations of L_c for each coating, and yellow arrows show the end of the scratch test. Scale bar is 1 mm.	133
Figure 3.31 SEM images taken during microscratch testing. As-is images (A), accompanying F_T and PD data measurements to determine L_c and thickness (B), and images of resultant surfaces at the end of each period of shelf-life analysis (C). Black arrows indicate the starting point of scratching and red arrows show the point where tip reached the bottom surface. Scale bars are 1 mm.	135
Figure 3.32 Results of Alamar Blue study (n=12, A), CLSM (B) and SEM (C) analyses for characterization of hFOB attachment and proliferation on various surfaces. Scale bar in part B is 450 μm , scale bar in part C is 200 μm and inset bar is 20 μm . Statistical differences are given as * $p<0.05$, ** $p<0.01$ and *** $p<0.001$	137

Figure 3.33 Osteogenic differentiation of hFOB seeded on Ti-APA, A/G and A/G/BHT analyzed in terms of ALP activity (n=12, A) and OCN release (n=6, B). Statistical differences are denoted by $*p<0.05$, $**p<0.01$ and $***p<0.001$	139
Figure 3.34 Osteogenic ALP (A), RUNX2 (B), Smad4 (C), BMP-2 (D), OSX (E) and OCN (F) gene expression analysis of Ti-APA, A/G and A/G/BHT using qPCR (n=6). Statistical differences are denoted by $*p<0.05$, $**p<0.01$ and $***p<0.001$	142
Figure 3.35 HUVEC proliferation over time on Ti-APA, A/G and A/G/BHT surfaces (n=4, A) and total VEGF-A at 4 th day of incubation (n=5, B).	143
Figure 3.36 SEM and CLSM images obtained during angiogenesis study. Images were obtained at the 4 th day of incubation. CLSM scale bar is 450 μ m, SEM scale bar is 200 μ m and inset bar is 20 μ m.	144
Figure 3.37 Relative viability of THP-1s incubated on samples under various conditions (n=6). Statistical differences are denoted by $*p<0.05$, $**p<0.01$ and $***p<0.001$	146
Figure 3.38 SEM electrographs of THP-1s incubated on samples under two different conditions. Cells on Ti-APA showed colonization in a larger area than other samples and cells appeared separate. A/G and A/G/BHT led to clustered appearance of THP-1s which colonized their surface. Ruffled appearance of THP-1s on Ti-APA after PMA+LPS+ shows extensive inflammatory action. Scale bars in large electrographs are 200 μ m, and scale bar in insets are 50 μ m.	147
Figure 3.39 Immunomodulatory properties of Ti-APA, A/G and A/G/BHT samples. CAS-1 and IL-10 releases were determined via ELISA (n=4). Statistical differences are denoted by $*p<0.05$, $**p<0.01$ and $***p<0.001$	148
Figure 3.40 Immunomodulatory properties of Ti-APA, A/G and /A/G/BHT in terms of gene expression. Changes in gene expression of THP-1s on different surfaces and under inflammatory condition were detected by qPCR study (n=4). Statistical differences are denoted by $*p<0.05$, $**p<0.01$ and $***p<0.001$	151

Figure 3.41 Photo taken during implantation at the osteochondral defect of rabbit femur osteochondral zone (A) and implant sectioning scheme for Ti-APA, A/G and A/BHT groups after harvest at the end of 4 and 8 weeks (B).....	153
Figure 3.42 Microscopic images of Ti-APA, A/G and A/G/BHT groups after histochemical staining for qualitatively and quantitatively scoring bone-implant integration. The abbreviations used in B and C are as follows: Ti shows implant, FT fibrous tissue, COAT coating, NB new bone, NBF new bone formation, HB host bone, BM bone marrow and NBM new bone marrow formation.	155
Figure 3.43 Microscopic images of Ti-APA, A/G and A/G/BHT groups after immunohistochemical staining for qualitatively and quantitatively scoring bone-implant integration. The abbreviations used in B and C are as follows: Ti shows implant, FT fibrotic tissue, COAT coating, NB new bone, NBF new bone formation, HB host bone, BM bone marrow, NBM new bone marrow formation, OB osteoblast and OCN osteocalcin.	156

LIST OF ABBREVIATIONS

ABBREVIATIONS

3D	3 dimensional
A/G/BHT:	Alginate/gelatin/BHT coating
A/G:	Alginate/gelatin coating
AFM:	Atomic Force Microscopy
ALG:	Alginate
ALP	Alkaline phosphatase
APA:	Acidic:Peroxide:Alkaline treated Ti surface
APTES:	3-Aminopropyl ethoxysilane
ATP:	Adenosine-3-phosphate
B:	Boron
BET:	Brunauer-Emmett-Teller
BHT:	Boron doped hydroxyapatite/tricalcium phosphate
BJH:	Barrett-Joyner-Halenda
BMP-2:	Bone morphogenic protein-2
BO ²⁻ :	Metaborate
BO ₃ ³⁻ :	Borate
Ca:	Calcium
CAS-1:	Caspase-1
CLSM:	Confocal Laser Scanning Microscopy
EDC:	1-Ethyl-3-(3-dimethylaminopropyl) carbodiimide
EDX:	Energy Dispersive X-Ray Analysis
GEL:	Gelatin
HA:	Hydroxyapatite
HT:	Hydroxyapatite/tricalcium phosphate
ICP-OES:	Inductively Coupled Plasma Optical Emission Spectroscopy
IL-10:	Interleukin 10
IL-1 β :	Interleukin 1 β

iNOS:	Inducible nitric oxide synthase
L:	Crystallite size
LPS:	Lipopolysaccharide
NaCl:	Sodium chloride
NfκB:	Nuclear factor kappa-light-chain-enhancer of activated B cells
OCN:	Osteocalcin
OH ⁻ :	Hydroxyl
OSX:	OSX: Osterix
P:	Phosphorus
PMA:	Phorbol 12-myristate 13-acetate (PMA)
PMA ⁺ LPS ⁻ :	PMA treated, LPS untreated THP-1s
PMA ⁺ LPS ⁺ :	PMA treated, LPS treated THP-1s
PMA ⁺ Nig ⁻ :	PMA treated, Nigericin untreated THP-1s
PMA ⁺ Nig ⁺ :	PMA treated, Nigericin treated THP-1s
PO ₄ ³⁻ :	Phosphate
SEM:	Scanning Electron Microscopy
Smad4:	Mothers against decapentaplegic homolog 4
Ti:	Titanium
TNBS:	2,4,6-Trinitrobenzenesulfonic acid
TSA:	Total surface area
X _c :	Crystallinity percentage
XRD:	X-Ray Diffraction
β-TCP:	β-Tricalcium phosphate

CHAPTER 1

INTRODUCTION

This PhD thesis study focuses on the production of a multifunctional and highly versatile 3-dimensional (3D) coating layer that helps to improve the osseointegration capacity of metallic implants. The coating was made of alginate (ALG), gelatin (GEL) and boron doped hydroxyapatite (HA)/tricalcium phosphate (BHT) in various compositions (A/G/BHTs). The coated gap filling 3D structure was designed to accommodate stem cells and allow both bone deposition and vascularization to boost the rate of osseointegration of Ti-based implant. Furthermore, this layer was aimed to serve as a reproducible and long shelf-life reservoir which further improves the clinical abilities of metallic implants by allowing local release of bioactive ions to prompt biological responses. To disclose, the following research articles were published in international refereed SCI-A journals by the author and allowed to be reused in the dissertation as whole or in part:

1. Material from: AHMET ENGİN PAZARÇEVİREN et al., Boron Doped Biphasic Hydroxyapatite/ β -Tricalcium Phosphate for Bone Tissue Engineering, Biological Trace Element Research, published in 2020, issue date as 2021, Springer Nature (Pazarçeviren et al., 2021).
2. Material from: AHMET ENGİN PAZARÇEVİREN et al., Multifunctional natural polymer-based metallic implant surface modifications, Biointerphases, Published in 2021, issue date 2021, American Vacuum Society (Pazarçeviren et al., 2021).
3. Material from: AHMET ENGİN PAZARÇEVİREN et al., Seamless and robust alginate/gelatin coating on Ti-6Al-4V as a gap filling interphase, Applied Surface Science, published in 2022, issue date 2022, Elsevier (Engin Pazarçeviren et al., 2022).

1.1 Metallic Implants

High energy trauma due to traffic accidents, tumor resection, avascular necrosis or congenital diseases could cause large bone deformations and/or bone loss (Matsuno et al., 2001). Although bone has regeneration and self-renewal capacity, critically large defects cannot be healed (Poser et al., 2014; Yamada & Egusa, 2018). Therefore, these defects are generally treated with a permanent metallic implant in order to recover the loss of function and provide a continuous implant structure for the bone to adhere and grow (Saini et al., 2015). Demand for high quality of life in aging population and the need of minimizing the loss of workforce have dramatically increased the usage of metallic implants (Prasad et al., 2017). Global market of orthopedic implants was valued at \$45.9 billion while dental implant market size was approximated to \$4.6 billion worldwide (Allied Market Research, 2019; Grand View Research, 2019). In addition, the annual growth of orthopedic implant market was determined to be ca. 4.7% and thus it was accounted for \$64 billion by 2026 (Intrado GlobeNewsWire, 2019). With an estimated 5.6% of annual growth rate, dental implant market is expected to reach a value of approximately \$6.1 billion by the end of 2026 (Acumen Research and Consulting, 2019). Moreover, studies on orthopedic and dental implants both in private sector and academia resulted in 2743 international (World Intellectual Property Organization (WO)) patents in the orthopedic endosseous implant area (metal+orthopedic+implant+A61L27/04 classification) and 7022 patents in dental endosseous implant area (metal+dental+implant+A61L27/04 classification).

1.1.1 Types of Metallic Implants

Metallic implants are mostly employed in load bearing locations where primary stability plays vital role in both the early and late success of implants. Especially metallic implants, which possess high yield strength and toughness, are employed in such critical defects (Duraccio et al., 2015). In addition, these metallic implants are

expected to achieve biomechanical stability at the defect zone to prevent further damage and replace loss function at the same time. Irrespective to the procedures of combination and production of metallic 3D structures, metallic implants are generally made up of iron (Fe), titanium (Ti), zirconium (Zr), nickel (Ni), cobalt (Co), tantalum (Ta) and chromium (Cr) (Lv et al., 2021). The types of implants manufactured from these elements are summarized in Table 1.1. It is important to note that among these metals, Ti has been widely used and it has been the main focus of a plethora of studies.

Table 1.1 Metallic BTE implants, their manufacturing method and the outcome of their analyses *in vitro* and/or *in vivo* conditions.

Implant	Method	Outcome	Reference
NiTi	3D printed via SLM ^a , annealed at 500°C under an oxide-free environment and laser cut into a cylindrical shape	<ul style="list-style-type: none"> • Significant improvement in peri-implant bone growth at the end of 16 weeks compared to Ti. • Significantly lower bone-implant contact at the end of 16 weeks compared to Ti. • Similar foreign body reaction (low reaction) with Ti. 	(Naujokat et al., 2022)
NiTi	NiTi rod processed into discs and anodized by 10 V for 5-80 min. Some treated with zinc acetate	<ul style="list-style-type: none"> • Zn addition drastically increased the corrosion resistance. • Osteogenic capacity as well as antibacterial effect were improved with Zn. • Zn addition allowed a greater rate of ECM mineralization. 	(Sun et al., 2022)
NiTi	NiTi rod was processed in to discs, acid etched and coated with HA/zinc oxide layer via PED ^b	<ul style="list-style-type: none"> • The tremendous increase in corrosion resistance and roughness. • Slight improvement in bioactivity in terms of CaP deposition. 	(Mehrvarz et al., 2021)

Table 1.1 (cont'd) Metallic BTE implants, their manufacturing method and the outcome of their analyses *in vitro* and/or *in vivo* conditions.

CoCrMo	Casted CoCrMo alloys were thermally shaped into discs (14 mm x 1 mm)	<ul style="list-style-type: none"> CoCrMo tested against Ti demonstrated significantly lower osteogenic response although similar surface properties were achieved. 	(Lohberger et al., 2020)
CoCrMo	Co, Cr and Mo powders were mixed with porogens. Then, the mixture was cold pressed under 250 MPa into a cylindrical shape and sintered at 1250°C. Samples dipped in sol of 58S bioglass and calcined at 600°C	<ul style="list-style-type: none"> CoCrMo surface coated with 58S bioglass significantly improved surface properties such as roughness and porosity. 58S allowed rapid and more extensive CaP deposition in SBF c. 	(Haftbaradaran-Esfahani et al., 2020)
CoCrMo	3D dome shaped CoCrMo implant was casted, sandblasted and surface treated with UV irradiation (15 W, 2.5 mW/cm ²)	<ul style="list-style-type: none"> Bone volume increased compared to non-UV treated CoCrMo after implanted in rabbit tibia. Histological data demonstrated formation of osteoid tissue on UV treated CoCrMo. 	(Zuchuat et al., 2021)
316L ^d	As obtained 316L was polished and surface textured with laser to form microgrooves	<ul style="list-style-type: none"> Higher corrosion resistance and an increase in surface wettability were obtained. U2OS pre-osteoblasts demonstrated contact guidance and significantly higher proliferation compared to untreated 316L. 	(Kedia et al., 2021)
316L	Polished 316L cylinders were dipped in HA/Titanium oxide (TiO ₂)/aluminum oxide (Al ₂ O ₃) sol and air dried	<ul style="list-style-type: none"> Higher corrosion resistance was achieved. Rapid stoichiometric HA deposition and good MG63 pre-osteoblast proliferation were achieved on ceramic coated samples. 	(Ahmadi & Afshar, 2021)

Table 1.1 (cont'd) Metallic BTE implants, their manufacturing method and the outcome of their analyses *in vitro* and/or *in vivo* conditions.

316L	Discs of 316L were alkaline treated and coated with collagen/chitosan alternating layers containing silver and strontium doped HA	<ul style="list-style-type: none"> • Composite polymer/bioceramic coating resulted in an extensive increase in CaP deposition rate, bone marrow stem cells (BMSC) growth, angiogenic differentiation, osteogenic differentiation and antibacterial activity against <i>Escherichia coli</i> (<i>E. coli</i>). • Samples also demonstrated a better bone deposition rate and thinner fibrous tissue formation. 	(Kuo et al., 2022)
TiTa	Ti and Ta powders were mixed, sintered at 800-1400°C under 40 MPa, cold rolled to a cylindrical shape and quenched in water	<ul style="list-style-type: none"> • Slight improvement in tensile strength. • Good corrosive and chemical stability. • Significantly improved bone mineral density and trabecular density compared to pure Ti in rat femur after 10 weeks. 	(Huang et al., 2021)
TiTa	Ti and Ta powders were formed into gyroid scaffolds via SLM	<ul style="list-style-type: none"> • The drastic increase in bioactivity was obtained when compared to Ti after incubated in SBF. • Significant improvement in BMSC adhesion, proliferation and osteogenic differentiation as well as ECM mineralization. 	(Zhao et al., 2021)
Cp-Ti ^e	Ti discs cleaned, acid etched and anodized in alkali solution in low or high current to create surface topography	<ul style="list-style-type: none"> • Highly hydrophilic and rough surfaces formed, and shown to increase albumin and fibronectin adsorption rate. • Higher BMSC adhesion and increment in osteogenesis-related markers were achieved on Cp-Ti treated with high current anodization. 	(Yang & Huang, 2021)
Cp-Ti	Ti discs cleaned, acid etched and anodized in alkali solution in low or high current to create surface topography	<ul style="list-style-type: none"> • Highly hydrophilic and rough surfaces formed, and shown to increase albumin and fibronectin adsorption rate. • Higher BMSC adhesion and increment in osteogenesis-related markers were achieved on Cp-Ti treated with high current anodization. 	(Yang & Huang, 2021)

Table 1.1 (cont'd) Metallic BTE implants, their manufacturing method and the outcome of their analyses *in vitro* and/or *in vivo* conditions.

Cp-Ti	Ultrafine grained (UFG-Ti) surface texture was formed on Cp-Ti by equal mechanical pressing, and samples were polished without further treatment	<ul style="list-style-type: none"> • Higher tensile strength and formation of nanoscale texture on UFG-Ti. • Similar bone formation rate and pull-out strength were achieved with Cp-Ti. 	(Wu et al., 2019)
Cp-Ti	Copper (10% w/w) and Cp-Ti were additively manufactured into a new implant (Ti-Cu) and polished	<ul style="list-style-type: none"> • Post-implantation 14 days in rabbit muscle demonstrated significant decrease in inflammation with Ti-Cu. • Ti-Cu implanted with <i>Staphylococcus aureus</i> (<i>S. aureus</i>) completely stopped invasion and showed very good bactericidal effect. 	(Wang et al., 2019)
Cp-Ti	Cp-Ti soaked in alkali solution, and then incubated in either calcium chloride/strontium chloride (CaSr-Ti) or both solution added silver nitrate (Ag(NO ₃)) to form CaSrAg-Ti	<ul style="list-style-type: none"> • Highly porous and rough implant surface was achieved. • Ag incorporation demonstrated complete bactericidal effect against <i>E. coli</i> and methicillin susceptible <i>S. aureus</i>. • Ca and Sr incorporation significantly improved both <i>in vitro</i> and <i>in vivo</i> osteogenesis. 	(Masamoto et al., 2021)
Cp-Ti	Cp-Ti was etched by alkali medium, grafted with pDA, then interacted with ZnO, and finally chitosan (CHI)/HA suspension was casted on implants to form CHI/HA/ZnO-Ti	<ul style="list-style-type: none"> • Coated CHI/HA/ZnO layer statistically increased hydrophilicity and plasma protein adhesion. • Cell adhesion and proliferation were not enhanced compared to pure Ti but osteogenic differentiation marker, ALP, significantly enhanced with coated layer. 	(Wang et al., 2021)
Cp-Ti	Cp-Ti was alkali treated, pDA grafted, and finally layer-by-layer coated with gelatin (GEL)/Bone morphogenic protein type 2 (BMP-2) and CHI/Vancomycin solutions	<ul style="list-style-type: none"> • Coatings tremendously improved early antibacterial effect up to 7 days. But, regrowth of bacteria was observed from 7th day to 14th day. • Coated layer significantly enhanced osteogenic activity. • This layer also demonstrated increased rate of vascularization and no acute inflammatory response was observed in a rat subcutaneous pocket model. 	(Yavari et al., 2020)

Table 1.1 (cont'd) Metallic BTE implants, their manufacturing method and the outcome of their analyses *in vitro* and/or *in vivo* conditions.

Ti-6Al-4V	Ti alloy scaffolds either machined or produced via SLM in the form of densely printed structure or lattice printed structure with a defined pattern	<ul style="list-style-type: none"> • An increased roughness and porosity were achieved with SLM samples. • Lattice printed samples demonstrated significantly lower density but also lower hardness and elastic modulus. • Lattice printed samples showed a drastic increase in MC3T3-E1 adhesion and proliferation over time. 	(Suresh et al., 2021)
Ti-6Al-4V	Discs were dipped in suspension of fluor/strontium doped HA (FSrHA) dispersed in polyvinyl alcohol (PVA)	<ul style="list-style-type: none"> • FSrHA coated Ti alloy exhibited highly rough and hydrophilic surface characteristics • Coated alloys induced good antibacterial activity and very good osteogenic activity 	(Ganjali et al., 2021)
Ti-6Al-4V	Computer assisted designed Ti alloy in various shapes and porosities were produced by SLM without further treatment	<ul style="list-style-type: none"> • Scaffolds with 60% porosity and 500 µm pore size tremendously increased osteogenic properties when tested with BMSCs • Scaffolds in rat subcutaneous pocket model demonstrated low immunogenicity and high vascularization while rat distal femoral condyle implanted samples demonstrated very rapid bone formation 	(Chen et al., 2020)

^a Selective Laser Melting (SLM) is the most commonly applied method to produce 3D metallic implants from a powder mixture.

^b Pulse electrochemical deposition (PED) is one of the widely employed method to coat ceramic layers on the metallic surfaces using electric voltage.

^c SBF is the abbreviation of Simulated Body Fluid.

^d 316L is a form of stainless steel, known to have high molybdenum content (molar 16.6%) and lowest carbon content (molar 0.03%) (Muley et al., 2016).

^e Cp-Ti is the abbreviation of commercially pure Ti. It is also abbreviated as pure Ti or grade II Ti or commercial grade Ti.

Metallic implants could be produced through various methods, surface treated and they could be biologically “improved” with different kinds of reinforcements including bioceramics and synthetic/natural polymers as given in Table 1.1. Osseointegration of the metallic implants with bone is the ultimate goal. In this respect, biodegradable or bioresorbable coatings, grafts and proteins or bioceramics and additional metal ions could be employed to induce osseointegration and *de novo* bone formation (Dehghanghadikolaei & Fotovvati, 2019). In time, loss of such a significant and transient effect, however, should be accommodated with the new bone formed at the periphery of the metallic implant. As much as it is key to obtain good primary stability, achieving secondary stability over time is also significant and it may drastically affect the service time of the metallic implant.

As reported by Priyadarshini et al. (2019), the major concerns for metallic implant stability at the defect site are their mechanical and chemical stability (Priyadarshini et al., 2019). In the sense of mechanical stability, these permanent bone replacement or functional support implants are expected to show high fatigue resistance and yield stress to reach primary stability (He & Hagiwara, 2006). Whereas, in a more practical comparison, the mechanical behavior of the implants can be improved through manufacturing methods, but it is a tremendous challenge to alter the bulk chemistry of the metals. In this regard, manufacturing with highly suitable metal elements to obtain a composite structure has become an alternative procedure in metal implant designing for BTE.

Gautam et al. (2022) reviewed metallic implants in regards with biofunctionality and success rate in the human body (Gautam et al., 2022). They reported that Ti-based implants demonstrated outstanding properties in comparison to other metals in terms of non-toxicity, corrosion resistance, low elastic modulus (similar to that of bone), wear resistance and biocompatibility. In detail, they illustrated that metallic implants either show high elastic modulus with very low rate of corrosion (Ta implants), or low elastic modulus with high corrosion (stainless steel implants). Ti-based implants, on the other hand, were determined to have an optimal performance by showing low

elastic modulus, high biocompatibility, low corrosion rate as well as cost-effectiveness when compared to other metals such as Ta.

1.1.2 Properties of Titanium-based Implants

One of the highly used implant materials is medical grade Ti-6Al-4V (Grade 5, Extra Low Interstitial Elements (ELI)). It contains 6% aluminum (Al) as α -phase stabilizer and 4% vanadium (V) as β -phase stabilizer (Yadroitsev et al., 2014). As stabilizer added, yield strength and fatigue resistance were shown to increase in pure Ti. Moreover, the surface of Ti can be spontaneously covered with the chemically and biologically inert titanium oxide (TiO₂) layer and become pacified to prevent the movement of corroded layer inwards (Diebold, 2003).

Although mechanically and structurally stable Ti-6Al-4V can be applied as bone implants, the inert surface on implants creates osseointegration problem at the interface leading to implant loosening, debris accumulation and implant fibrosis rendering whole structure practically dysfunctional as implant (Keselowsky et al., 2007). In addition, there have been various reports showing high corrosion and particle formation on Ti-based implants if not surface modified in addition to physical/electrochemical treatment aforementioned (Davis et al., 2022). The following section gives a detailed outlook on the use solely surface treated Ti-based implants.

1.1.3 Challenges of Using Titanium Implants

In order to maintain implant retention, Ti implants should integrate functionally with the host bone. However, bioinertness of Ti surface impedes the formation of an organic-metal interaction. Hence, it functionally fails to integrate with the host bone. For these reasons, Ti-based structures require surface treatments and modifications to integrate effectively with the surrounding bone tissue. Combination of sand-

blasting and acid-etching techniques (Lin et al., 2017; Marenzi et al., 2019), alkali etching (Jemat et al., 2015; Komasa et al., 2019), anodization (Lee et al., 2015; Yeo, 2020), plasma electrolytic oxidation (Hartjen et al., 2018; Rameshbabu et al., 2019), micro-arc oxidation (Bai et al., 2017; Wu et al., 2019), plasma surface treatment (Chou et al., 2018; Lee et al., 2017) have been utilized. There are also diverse studies involving surface modifications such as bioceramic/bioglass coatings, bioactive molecule grafting on metallic substrates, employing metallurgical methods for obtaining new alloys or polymer coating of metals to achieve a functional permanent bone implant.

Up to date, surface modified Ti implants used in major orthopedic operations were observed to fail mainly due to aseptic loosening (Bahraminasab et al., 2013). Unsuccessful osseointegration of Ti brings about a probable loss of mechanical fixation. Consequently, micromotion and wear debris accumulation at the interface could occur (Javed et al., 2013). Khan et al. (2016) compiled and presented metallic implant failure modes and rate in total knee arthroplasty in Great Britain, Sweden, Australia, New Zealand and USA (Khan et al., 2016). The major reason in revision surgery was found to be aseptic loosening (29.8%) and peri-implant infection (14.8%). In another study, Sadoghi et al. (2013) revealed that aseptic loosening has been observed more frequently in total hip arthroplasty at around 55.2% of all revision operations (out of 15% implant failures) and the most common failure mode in total ankle arthroplasty implants was found to be aseptic loosening, observed in 38% of all revision operations (out of 17% implant failures) (Sadoghi et al., 2013). Regarding Ti implants employed in dental applications, the major mode of failure was also determined to be inadequate osseointegration (Chrcanovic et al., 2016). Bacterial infection caused around the implant, peri-implantitis, has been established as the etiology of the long-term failure of the dental implants (Esposito et al., 2000). The survival rate of dental implants, therefore, indirectly depends on the potential of peri-implantitis incidence. Changi et al. (2019) assessed peri-implantitis prevalence and incidence rate of 2127 patients with 6129 implants (Kordbacheh Changi et al.,

2019). An average 2-year follow-up of patients revealed that 21% of peri-implantitis incidents were a result of Ti implant-related failure such as osseointegration. Therefore, it can be stressed that implant success strictly depends on accomplishment of healthy bone-implant integration to decrease aseptic loosening and peri-implantitis (Figure 1.1).

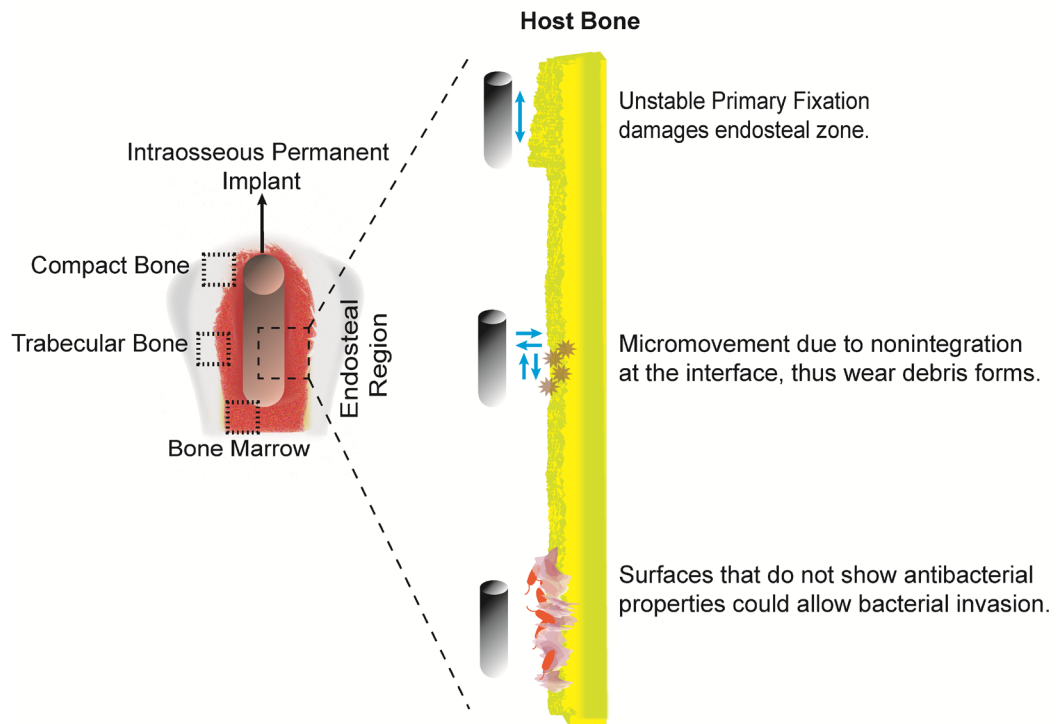


Figure 1.1 Failure modes of Ti implants.

As of last 5 years, there have been over five thousand studies involving in metallic implants, with a majority of Ti-6Al-4V alloy implant as the main structure. To ameliorate the bioinertness of Ti, surface treatments are the main approach applied to ensure improved osteoblast adhesion and growth due to altered topography, roughness and energy at the implant surface. However, it has been observed that surface treatments alone would not create a significant improvement in Ti

bioactivity. Hence, different methodologies involving surface coating have been developed. Since 2018, 760 studies were published based on surface coating to induce rapid and robust osseointegration of Ti implants. These studies included bioceramic-based coatings, polymer-based coatings, and their composited forms as multifunctional coatings.

1.2 Surface Modifications of Titanium Implants

1.2.1 Surface Treatments

Previously, osseointegration of metallic implants was found to be a result of surface topography (Wennerberg & Albrektsson, 2009). Then, the surface texture of these implants was tried to be improved through various chemical, physical and thermal treatments (Wennerberg & Albrektsson, 2009). Physical surface properties such as roughness, patterns and topography have been tailored to increase implant anchor and stability. Mesenchymal stem cells and pre-osteoblasts taking part in osteogenesis were shown to express $\alpha2\beta1$ integrin complex to adhere roughened surfaces and proliferate more than on smooth counterparts (Olivares-Navarrete et al., 2015). Moreover, an interesting study by Li et al. (2019) confirmed that nanorough Ti plate implant surfaces tend to increase osteogenesis as observed by significantly higher *in vitro* ALP and OSX expression of MC3T3-E1 (murine osteoblasts), and good bone-implant contact *in vivo* (Li et al., 2019). Furthermore, increase in autophagy of Yes-associated protein (YAP) protein (inhibitor of Wnt/ β -catenin pathway responsible for processing of ECM-related and mechanical signals) in MC3T3-E1 cells incubated on nanorough surfaces proved that environmental cues could improve osteoblastogenesis and osteoblast adhesion (Raines et al., 2010). Recently, acid:alkali etched Ti surfaces were hydrothermally treated to form microscale pyramids and nanopits by Manivasagam et al. (2021), and tested for attachment, growth and osteogenic differentiation of adipose derived stem cells (ADSCs)

(Manivasagam & Popat, 2021). Higher cell area, proliferation rate and higher osteogenic marker expression such as ALP activity and osteocalcin (OCN) production were observed in accord with increasing roughness. Surface properties of a Ti alloy was shown to improve with titanium oxide-copper oxide (TiO₂-CuO) coating by (Zhang et al., 2022). Coated layer showed extensive roughness increment which allowed higher pre-osteoblast MC3T3-E1 attachment and higher rate of osteogenic differentiation as evident by rapid calcium phosphate (CaP) deposition and increase in ALP and OCN.

Apart from roughness, surface pattern on an implant is an important determinant of cellular fate. In a study by Zwahr et al. (2019), direct laser interference patterning was applied on Ti for establishing microgrooves with different spatial periodic patterns (Zwahr et al., 2019). They observed better human osteoblast attachment and uniaxial alignment on samples showing largest patterns with 17 µm spatial period, thus higher osteoconductivity. Furthermore, Karazisis (2016) coated nanobeads on Ti implants with sputtering to form nanopatterns on machined dental implants, and analyzed for immunomodulatory and osteogenic responses in rats (Karazisis et al., 2016). After 28 days of implantation, nanopatterned surfaces decreased inflammatory TNF- α , osteoclastic Cathepsin K (CatK) and calcitonin receptor (CTR) expression of cells adherent to implant while increasing osteoblastic ALP, OC and RUNX2, and woven bone formation *in vivo*. Recently, an important study by Sun et al. (2021) reported a significant increase in osteogenic capacity of the surfaces after forming microgroove patterns (Sun et al., 2021). These surfaces demonstrated not only *in vitro* osteogenic differentiation but also a thinner fibrous tissue formation and rapid integration *in vivo*. In an interesting study by Silva et al. (2021), different commercially available dental implants (Neodent® and NeoPoros®) were employed in Type I to Type IV bones (weakest to strongest bone) to determine the practical effect of surface patterns on implant stability (Silva et al., 2021). Implants having less steep and distant threads can be effectively employed in Type I bones such as maxillofacial bone and robustly patterned and V-shaped

threaded implants could be placed in Type IV bones, such as femurs that require higher shearing during implantation. In order to compare various surface patterns at sub-micron and micron levels, Wang et al. (2021) used laser guided patterning technology on Ti alloys and used bone marrow stem cells (BMSCs) to test biocompatibility (Wang et al., 2021). They concluded that proliferation and osteogenic differentiation of BMSCs occur on frequent patterns with connections and they depend on inverse relation of surface energy and roughness. Therefore, BMSCs appeared to grow and differentiate on hydrophilic yet less rough surfaces with interconnected surface patterns.

In literature, various methods have been explored over the last three decades to improve aforementioned qualities. Anodization, electrochemical etching, hydrothermal treatment, electron beam melting, microarc oxidation and ultraviolet (UV) surface treatment are among the most widely used technologies for creating surface roughness and furnishing surfaces with different patterns (Table 1.2).

1.2.1.1 Anodization

To promote quicker cell adhesion while in contact in bone, Ti implant surface could be anodized to acquire nanoscale pits (Table 1.2). A study by Xu and Jiang (2022) illustrated that enhanced hydrophilicity and closely scattered pits induced better MC3T3-E1 attachment and greater ALP activity (Xu & Jiang, 2022). In a similar study, Yang and Huang (2021) acid etched Ti alloy surface and subsequently anodized in alkali solution to form pits and nanotubular features (Yang & Huang, 2021). Anodized surfaces led to greater osteogenic differentiation *in vitro*, and allowed faster integration with rabbit femur *in vivo*. The osteogenic effect endowed by the presence of nanotubes on Ti alloy was also demonstrated by Park et al. (2021) using a similar setup (Park et al., 2021).

1.2.1.2 Electrochemical Etching and Hydrothermal Treatment

Electrochemical etching process is somewhat similar to anodization. This process involves in chemical etching under electrical voltage and heating the sample up in a solution to induce morphological and geometrical changes. As an example, Maher et al. (2021) manufactured 3D printed implants using grade V Ti-6Al-4V alloy, etched their surfaces in acidic solution and finally hydrothermally calcined in an acidic solution (Maher et al., 2021). This treatment led to formation of nanoscale roughness and drastically improved osteogenic capacity and CaP precipitation over time. Geng et al. (2021), on the other hand, electrochemically etched Ti alloy surfaces with water/glycerol environment followed by alkali:acidic etching and then hydrothermal treatment was done (Geng et al., 2021). Surface treated implant illustrated great performance both *in vitro* and *in vivo*, leading to extensive early bone-implant interaction.

1.2.1.3 Microarc Oxidation

Microarc oxidation (MAO) is another process which involves electrical voltage treatment in an acidic or alkaline solution to fashion implant surfaces with nano/micro texture, patterns and high roughness. MAO procedure could also be employed in a CaP solution to directly furnish implant surfaces with a bone-similar ceramic layer. In an interesting study by Liu et al. (2020), a pure Ti sample was treated with MAO in a acetic acid:sodium acetate solution (Liu et al., 2020). MAO led to formation of nanoscale topographical features that allowed an improved rate of osteogenesis compared to pure or acid etched samples. In addition, Luo et al. (2021) employed MAO to coat Ti-10Ta-2Nb-2Zr implants with microscale and nanoscale HA to further enhance bioactivity (Luo et al., 2021). Implants were acid etched and placed in an acetic acid/water solution added with phosphate and silicate precursors. Coated surfaces demonstrated a clear improvement in roughness and

topography. Moreover, MC3T3-E1s differentiated into osteogenic phenotype much more rapidly on these samples compared to their non-MAO counterparts.

Table 1.2 Surface treatments for Ti-based implants to improve osseointegration and/or antibacterial properties.

Implant	Treatment	Outcome	Reference
Ti-13Nb-13Zr	Anodization in NH_4F solution	<ul style="list-style-type: none"> Controllable porosity, pore size and hydrophilicity were obtained Anodized surfaces induced greater MC3T3-E1 proliferation compared to non-treated surfaces 	(Xu & Jiang, 2022)
Cp-Ti	Fluoric acid (HF)/nitric acid (HNO_3)/water (H_2O) in 50%:30%:20% v/v/v treatment followed by anodization in 5 M sodium hydroxide (NaOH)	<ul style="list-style-type: none"> Increased charge and porosity led to higher protein adhesion compared to non-treated surfaces. hBMSC adhesion and biomineralization were increased on treated surfaces. 	(Yang & Huang, 2021)
Ti-6Al-4V	Electrochemically etched in ammonium fluoride (NH_4F) solution and calcined in 0.6 M hydrochloric acid (HCl) at 300°C	<ul style="list-style-type: none"> Nanotubular formations on treated surfaces increased hydrophilicity and surface area. Treated surface induced higher CaP deposition and osteoblast proliferation compared to non-treated surfaces. 	(Maher, et al., 2021)
Cp-Ti	Primarily etched in sodium fluoride (NaF): HCl solution followed by electrochemical treatment in water/glycerol mixture and then hydrothermally calcined under 150°C	<ul style="list-style-type: none"> High roughness and formation of valleys on the surface improved MG63 osteoblast-like cell adhesion, growth and osteogenic differentiation. Treated surfaces decreased osteoclast differentiation. 	(Geng, et al., 2021)

Table 1.2 (cont'd) Surface treatments for Ti-based implants to improve osseointegration and/or antibacterial properties.

Cp-Ti	MAO in acetic acid/sodium acetate solution	<ul style="list-style-type: none"> MAO treatment increased osteoblast adhesion on the surface, which, in return, tremendously increased osteogenic differentiation. 	(Liu, et al., 2020)
Ti-10Ta-2Nb-2Zr	HCl: sulfuric acid (H ₂ SO ₄) etched implant was underwent MAO in acetic acid, sodium phosphate, sodium silicate, NaOH, glycerine and ethylenediaminetetraacetic acid (EDTA) solution	<ul style="list-style-type: none"> Dual treatment increased hydrophilicity and roughness. Treated surfaces increased osteoblast adhesion and osteogenic differentiation. Implant test in femur defect model in rabbits revealed fast osseointegration of dual treated surfaces. 	(Luo, et al., 2021)
Ti-6Al-4V	Additively manufactured implant was either anodized or anodized and grafted with bacterial adhesion inhibitor	<ul style="list-style-type: none"> Additively manufactured surfaces having pre-determined pore size, porosity and topography allowed controlled release of bactericidal and showed excellent antibacterial activity. Meanwhile it led to higher MSC adhesion and coverage of surface compared to non-treated surfaces. 	(Li et al., 2020)
Ti-24Nb-4Zr-8Sn	Alloy was sandblasted, HCl:H ₂ SO ₄ (9.5:0.5 mol ratio) etched, and then either treated with MAO under 250 V for 10 min or anodized in (1:0.15 mol ratio) ammonium sulfate (NH ₄ SO ₂) and NH ₄ F	<ul style="list-style-type: none"> Controlled pore size and roughness achieved by MAO allowed higher BMMSC adhesion. Anodized surface, on the other hand, led to significantly greater osteogenic differentiation rate compared to MAO. 	(Zhan et al., 2020)
Cp-Ti	Surface polished samples were irradiated under UV produced by AC100V at 172 cm ⁻¹ , 15-30°C, and kept under the flow of ozone briefly	<ul style="list-style-type: none"> Dual treatment improved macrophage activity towards pro-healing response, prevented bacterial adhesion and significantly increased rate of osseointegration. 	(Yang et al., 2021)

Because abovementioned methodologies had a transient biological activity to control osteogenic, angiogenic and immunological responses, additional methods to augment bioactivity are required (Davis, et al., 2022). Since spontaneously adsorbed plasma proteins and ECM molecules can affect overall biological responses, various bioactive molecules have been employed to orchestrate regenerative and immunomodulatory signaling cascades to result in favorable initial innate response, acute/chronic adaptive immune response, osteogenesis and angiogenesis (Guo et al., 2012; Silva-Bermudez & Rodil, 2013). Therefore, grafting with bioactive molecules to govern initial response has been explored as an effective way to embellish permanent implants with a multifunctional surface (Tang et al., 2008). The method to achieve this via cost-effective and straightforward fashion could be coating the surfaces by bioceramics, polymer-based networks or their combinations in composite form.

1.2.2 Bioceramic-based Coatings

Bioactive ceramic coatings or bioceramic coatings on Ti-based implants are applied to enhance bone-making ability of the otherwise bioinert surfaces. The implant surfaces treated with similar methods are given in Table 1.2. Increasing surface roughness allows osteogenic ion release. Bioceramic coatings resulting in higher surface roughness have been employed on various commercial implants and exhaustively studied in literature (Gil et al., 2021). Generally, bioactive inorganic coating prepared on Ti-based implants is in the form of CaP molecules. Due to chemical similarities with native bone inorganic part, which is HA, CaP combinations having similar Ca/P ratio to HA have been coated on Ti-based implants through predominantly through electrophoretic deposition (Stevanović et al., 2018). The most utilized HA coating is in the form of stoichiometric HA, which has calcium to phosphate ratio (Ca/P) as 1.67. This HA structure could be used as a base ceramic for doping with cationic ions such as strontium (Sr), magnesium (Mg), copper (Cu) etc. or anionic ions such as fluoride (F), boron (B), sulfur (S) (Prodana et al., 2021).

In addition to doping, biological performance of bioceramic coatings can be improved with adsorption of proteins, drugs, or antibacterial agents (Priyadarshini, et al., 2019).

1.2.2.1 Pure HA Coatings on Ti-based Implants

Pure HA and its derivatives (such as doped HA products) have been coated on Ti-based implants through various methods (Table 1.3). One of the most employed coating methods is plasma spraying (PS). Sarkar et al. (2021) reported an interesting study in which they coated the surface of Ti-6Al-4V implants with PS at 25 kW power and 110 cm distance from nozzle to implant surface under the flow of argon, which was used as the main pressure gas to coat surfaces (Sarkar et al., 2021). They demonstrated a rapid osteogenic response *in vitro* as implants revoked remodeling process when osteoblasts and osteoclasts (derived from THP-1 cells) work in harmony to integrate implant with bone after deposition of bone-similar apatite layer by colonizing osteoblasts. Distinctively to “dry” formation of HA on implant surface, Naderi et al. (2021) coated Cp-Ti meshes with sol-gel method under “wet” conditions (Naderi et al., 2021). The sol-gel state was achieved by mixture of stoichiometric HA precursors ($\text{Ca/P} = 1.67$) at pH 9 and implants were dipped in solution several times to achieve multiple layers of coating. HA-Ti surfaces were improved not only in terms of biocorrosion resistance but also higher biocompatibility as observed by extensive adhesion of adipose derived stem cells (ASCs). Although they are most commonly employed in the literature, particle release, spontaneous breaks and high-density product formed on the implant surface render these methods obsolete. Moreover, irregularly shaped or micron-scale porous implants have not been coated successfully with PS due to directionality and high viscosity of sol-gel procedure which prevents homogeneous diffusion over the surface and pores.

Another highly employed method to coat surfaces of Ti implants with bioceramics is biomimetic method (Yilmaz et al., 2020). This method allows deposition of pure HA at different Ca/P ratios depending on the feed concentration. As an example, Cp-Ti samples were acid etched and then either calcined at 600°C or alkali etched prior to be placed in SBF for 4 h (Morejón-Alonso et al., 2020). These samples were then incubated in supersaturated SBF and were observed to have significantly higher bioactivity. Moreover, Jiang et al. (2021) acid/alkali etched Cp-Ti surfaces and sequentially (20 cycles) introduced supersaturated calcium hydroxide and diammonium hydrogen phosphate ((NH₄)₂HPO₄) to form HA (Jiang et al., 2021). This surface modification encouraged MC3T3-E1 proliferation, ECM production and osteogenic differentiation. Kreller et al. (2021) acid/alkali etched Ti-6Al-4V implants and placed in a saturated SBF solution for 14 days (Kreller et al., 2021). Besides improvement of roughness and topography, surfaces induced greater rate of osteogenic and angiogenic cytokine release from primary human osteoblasts. In spite of various studies demonstrated the use of biomimetic method in order to establish a HA layer on Ti-based implants, it is also elucidated that this method is highly time consuming, there is almost no control over the final product in terms of structural and physical properties and this method cannot be scaled up.

As an improvement compared to biomimetic coating method, pure HA can also be deposited on implant surfaces with defined patterns, particle size and porosity through hydrothermal coating procedure (Kien et al., 2021) and electrochemical deposition (He et al., 2021). As reported in many studies in the literature, it is important to note that both hydrothermal coating and electrochemical deposition procedures could be employed together to further control the rate of HA deposition, lattice characteristics of deposited HA and overall roughness and topography of coated layer. Jiang et al. (2019) treated Ti-6Al-4V with alkali etching, and then incubated in calcium nitrate (Ca(NO₃).4H₂O) and (NH₄)₂HPO₄ mixture under 180°C for 24 h (Jiang et al., 2019). A slight increase in surface roughness and a drastic improvement in electrochemical corrosion resistance were achieved. In addition,

human umbilical vein endothelial cells (HUVECs) attached and demonstrated highest proliferation rate on coated samples compared to uncoated samples. In order to achieve better control over the surface topography and crystallinity of the final HA product, Bucur et al. (2020) employed both hydrothermal and electrochemical coating methods at the same time (Bucur et al., 2020). Samples were placed in electrochemical deposition setup and soaked in mixture of same Ca and P sources as aforementioned. Samples were coated under 1.5 V for 4 h at 80°C. Highly crystalline HA coating on the surface with a nanoscale topography and extensive roughness was achieved. These surfaces further enhanced bioactivity as they increased CaP deposition over time in SBF, however, cracks and delaminated layer were also observed.

Low adhesion strength of coated layer on implant, spontaneous delamination, excessive ion release, inability to replace with new bone and to induce vascularization can be given as the main disadvantages of biomimetic, hydrothermal and electrochemical deposition methods. Collectively, pure HA coatings have been shown not good enough to prompt *de novo* bone formation and establish a functional bridge with host bone. Therefore, in order to overcome aforementioned limitations without significantly altering these methodologies, ion-doped HA and/or additionally introduced biological factors have been coated on Ti-based implants recently.

1.2.2.2 Ion Doped HA Coatings on Ti-based Implants

In order to effectively endow multifunctionality to HA, various cationic or anionic ions can be utilized (Table 1.3). Using the methods presented in Section 1.2.2.1, doped HA coatings can be achieved by adding respective ions (either for single ion doping or multiple ion doping) into the reaction medium of given coating procedure. As suggested by Wei et al. (2021), surface elemental composition of an implant surface is critical in prompting desired cellular response (Wei et al., 2021). They

coated Ti-6Al-4V with Sr-doped HA through MAO and subsequent hydrothermal treatment. It was determined that highly crystalline SrHA coating on implant significantly improved corrosion resistance, and improved hydrophilicity and apatite deposition.

In order to propagate the effect of ions, multiple ion doped HA coatings can be produced. Moloodi et al. (2021) dipped Ti-6Al-4V in Sr and F precursor added HA sol-gel and hydrothermally treated at 190°C for 7 h (Moloodi et al., 2021). Sr and F doped HA (SrFHA) coated implants induced better MG63 osteoblast-like cell attachment and improved ALP activity. Ullah et al. (2022) used plasma coating process to coat Ti-6Al-4V with Zn and Sr doped HA at 140 mm distance and 90V (Ullah et al., 2022). Continuous Sr and Zn ion release and significantly higher CaP deposition rate were achieved. These coatings further enhanced MC3T3-E1 adhesion, proliferation and osteogenic differentiation while showing good antibacterial effect against *E. coli*.

It is also very vital note that bioceramic-coated implants are generally produced to induce rapid bone deposition or allow fast CaP deposition. However, many studies in the literature reported that angiogenic and immunomodulatory properties should not be overlooked because these properties play key roles to generate biofunctional interface at the implant periphery for prolonging service time of metallic implants. Therefore, one of the methods to endow multifunctionality on the bioceramic-coated implants is to graft these layers with additional biological factors or antimicrobial agents.

1.2.2.3 Composite Bioceramic-based Coatings with Biological Factors and Antimicrobial Agents

In combination with a vast number of methods presented in literature to modify implant surface, grafting with biofunctional molecules has been explored as an effective way to embellish permanent implants with a rapid and cost-effective

multifunctional surface coating (Tang, et al., 2008). To prolong implant service time, self-assembled monolayers (SAMs) and polymers can be grafted on metal surface to obtain functional end groups such as amine (-NH₂), amide (-CONH₂), carboxyl (-COOH), phosphate (PO₄H₂), allyl (-CH=CH₂) and hydroxyl (-OH) groups (Finke et al., 2011; Lan et al., 2020; Phan et al., 2015; Schröder et al., 2010; Testrich et al., 2013). These coatings could influence the biochemical response given by host tissue. In broader perspective, rapid colonization of the implant surface by stem cells involving in osteoblastogenesis and angiogenesis could bring about contact osteogenesis, which potentially improves the rate of osseointegration. Moreover, immunomodulatory effect of SAMs has been studied as an imperative parameter in designing metallic surfaces with improved osseointegration. To design immunoresponsive surfaces at material-tissue interface, Moyano et al. (2012) coated gold nanoparticles with different functional groups (nitrogen-based charged and hydrophilic functional groups with hydrophilicity value ranging from 0.53 to 5.35) and showed an increase in pro-inflammatory response with increase in SAM as determined by TNF- α upregulation (Moyano et al., 2012). In an interesting study, Zhang et al. (2015) prepared tertiary amine coatings on polyethylene surfaces and observed upregulation in iNOS genes in BMSCs with a direct correlation with upregulated ALP, OSX, RUNX2 and OCN genes involving in osteoblastogenesis (Zhang et al., 2015). Further enhancing the ability to control cell fate via surface-host tissue interactions, macromolecular coatings were also employed as promising surface modification. Macromolecules in the form of hormones (Naito et al., 2014; Posa et al., 2018)), genetic materials (Atluri et al., 2017), functional sequences belonging to ECM glycoproteins and proteins (Clauder et al., 2019; Dayan et al., 2019; Tan et al., 2013), and polymeric (synthetic or natural) grafts and brushes providing readily available biological patterns for cellular adhesion and continuous release of bioactive agents supporting tissue growth (Alas et al., 2017; Gao et al., 2017; Jia et al., 2019; Rosenthal et al., 2018) are utilized to confer osteoinductivity and angiogenic properties to prompt osseointegration.

Important studies concluded a clear advantage for the use of biological factors and antimicrobial agents along with bioceramic coatings in recent studies. As striking examples, Gu et al. (2022) coated a Ti-6Al-4V implant with HA via biomimetic coating method and introduced BMP-2 during this procedure to simultaneously graft BMP-2 along with HA (Gu et al., 2022). Slow and continuous release of BMP-2 led to significantly higher biomineralization after 4 weeks when implanted in beagle dog muscle pouch. Li et al. (2021) prepared a Cp-Ti surface treated with MAO in a CaP solution leading to formation of Fe and Si doped HA coating on the surface (Li et al., 2021). This layer was then grafted with an aminosilane, N-(3-aminopropyl) methacrylamide hydrochloride (APMA), to bridge poly(dimethylsiloxane) brush, which was further functionalized with antibacterial HHC36 polypeptide. This study demonstrated a very good bioactivity of the composite layer while good biocompatibility with human fetal osteoblasts (hFOB), very strong antibacterial activity against *S. aureus* and *E. coli*, and very low innate immune response within first 4 days post-implantation in subcutaneous model in rats.

Other important studies are given in Table 1.3 with the details of coating procedure and outcomes of *in vitro* and *in vivo* studies. It should be stressed that bioceramic coatings and their composites with biological factors and antimicrobial agents cannot provide a 3D structure and influence Ti surface biological properties as much as polymer-based coatings. In this sense, long-term functionality of the peptides, proteins and even bioceramics have been established as the major concern for their use in especially harsh conditions. In order to improve stability, it could be proposed that a composite layer of coating based on a polymeric network can be employed to boost osseointegration capacity. This composite layer could be rendered highly bioactive via homogeneous dispersion of multifunctional bioceramics in the matrix along with additional biological factors and drugs.

Despite the fact that there has been a meticulous work on metallic implant surface modifications, aseptic loosening and peri-implant infection leading to osteolysis and osteomyelitis have not been overcome yet. Overall, metal surface treatments have

been employed to achieve single or dual functionality. However, additional reinforcements on biological properties are required. Polymers, showing high positive or negative charge density when coated on implant surfaces, could easily ward off chronic inflammatory response due extensive neutrophil activation, exaggerated fibrin coating and biofilm formation (Boni et al., 2019).

Table 1.3 Various bioceramic coatings with or without additional biological factors or antimicrobial agents on Ti-based implants.

Implant	Bioceramic Coating Method	Outcome	Reference
Ti-6Al-4V	Hydrothermal coating under 100-200°C in Ca(OH)_2 and sodium triphosphate ($\text{Na}_5\text{P}_3\text{O}_{10}$, STP) solution	<ul style="list-style-type: none"> • Porous pure phase HA coating on implant and increase in implant surface wettability. • Higher U2OS adhesion and rapid colonization of surface. 	(Lo et al., 2021)
Ti-19Zr-10Nb-1Fe	Electrodeposition of HA in solution prepared by $\text{Ca(NO}_3)_2 \cdot 4\text{H}_2\text{O}$ and ammonium dihydrogen phosphate ($\text{NH}_4\text{H}_2\text{PO}_4$) on previously anodized implant	<ul style="list-style-type: none"> • Highly rough nanotubular formations coated with phase pure HA and increased wettability. • Significantly improved MC3T3-E1 adhesion, proliferation, and osteogenic activity as evidenced by higher ALP activity, and osterix (OSX), osteonectin (OCN) and osteopontin (OPN) gene expressions. 	(Wu et al., 2021)
Ti-6Al-4V	Electrophoretic deposition of HA and plasma spray of HA on separate 3D printed implants to compare methods	<ul style="list-style-type: none"> • Similar pure phase HA coating with same pore size and porosity. • Plasma sprayed implant demonstrated statistically improved osteogenic properties such as ALP activity, CaP deposition and osteogenic gene markers. • Higher bone mineral density and bone volume were achieved by plasma sprayed implants in rabbit femoral model in 12 weeks. 	(Sun et al., 2021)
Cp-Ti	MAO in calcium acetate ($(\text{CH}_3\text{CHOHCOO})_2\text{Ca}$), monosodium phosphate (NaH_2PO_4) and EDTA copper disodium ($\text{Na}_2\text{Cu-EDTA}$) solution	<ul style="list-style-type: none"> • Pure phase copper doped HA (CuHA) coating with increased surface roughness and wettability was achieved. • Corrosion resistance was tremendously improved. • Statistically higher MC3T3-E1 adhesion and ALP activity were achieved. 	(Zhang et al., 2021)

Table 1.3 (cont'd) Various bioceramic coatings with or without additional biological factors or antimicrobial agents on Ti-based implants.

Ti-6Al-4V	Sol-gel cerium (Ce) and silicon (Si) doped HA spin coated and calcined at 500°C for 2 h	<ul style="list-style-type: none"> • Pure phase, low crystalline CeSiHA coating demonstrated controlled release of Ce, Si and Ca ions over time. • High bioactivity on the surface. 	(Priyadarshini & Vijayalakshmi, 2021)
Cp-Ti	Ca(NO ₃) ₂ ·4H ₂ O, triethyl phosphate ((C ₂ H ₅) ₃ PO ₄) mixture was added with Ag(NO ₃)	<ul style="list-style-type: none"> • Pure phase AgHA on the surface of implant was formed. • A rapid early (4 h) antibacterial effect (approximately 90%) on <i>E. coli</i> and <i>S. aureus</i> was achieved. • No cytotoxicity and alteration on cell morphology were observed when tested with L929 (murine fibroblasts) and U2OS cells. 	(Švagrová et al., 2022)
Ti-6Al-4V	Two types of coatings were tested: one was plasma sprayed Sr, Zn and F doped HA and other was Sr, Zn and Ag doped HA	<ul style="list-style-type: none"> • All achieved high pure phase multi-ion doped HA with high bioactivity and great electrochemical corrosion resistance. • SrZnAg-HA led to higher rate of bone formation and bone volume in femoral bone defect model in rabbits. 	(Ratha et al., 2022)
Cp-Ti	Silicate (SiO ₃ ⁻) added SBF solution was used to coat the surface with biomimetic SiHA, followed by functionalization with GFOGER polypeptide and pDA-grafted vancomycin-bovine serum albumin nanoparticles (Van/BSA)	<ul style="list-style-type: none"> • Strong bioactivity and continuous release of antibacterial agent were achieved. • Tremendously improved BMSC adhesion, focal adhesion production (integrin β1), osteogenic differentiation and antibacterial activity against <i>Staphylococcus epidermidis</i> (<i>S. epidermidis</i>). • Ectopic bone formation in intramuscular pouch 6 months post-implantation in dog model. 	(Zhang et al., 2020)

1.2.3 Polymer-based Coatings

In order to prevent quick washing off of the peptides, proteins, bioactive agents, drugs and bioceramics, Ti has been coated with various polymer-based composite coatings lately. In the last decade, different methods and polymers have been used to improve Ti integration with bone. As reviewed above, surface treatments have been observed to induce contact osteogenesis on metallic implants. Whereas, a functional integration involves gap filling through a scaffold structure located at the interphase which allows osteoconduction leading to concomitant trigger of distance and contact osteogenesis. These coatings could be designed to include bioactive reinforcements to show osteoconductivity by providing a matrix supporting bone mineral deposition and growth (Boschetto et al., 2020).

Acquiring surface properties to manipulate sophisticated and intertwined cascade of events is imperative to govern short-term pro-healing answer and predict long term biological response. Tailored materials, such as polymers, can be used to obtain supplementary surface properties. Polymer-based coatings, in this sense, could grant distinct material properties conferred by the use of composite biomaterials in various topographies and chemistries (Dammati et al., 2018; Wang et al., 2019). Polymers employed as coating base materials can be categorized in two: Synthetic or natural polymers.

1.2.3.1 Synthetic Polymer-based Coatings

Synthetic polymers have exceptional ability to be easily processed, lower batch to batch variability and have much better ability to be tailored for mechanical and physical properties compared to natural counterparts (Alizadeh-Osgouei et al., 2019). United States Food and Drug Administration (FDA) and European Medicines Agency (EMA) approved various highly biocompatible synthetic polymers such as poly(vinyl alcohol) (PVA), poly(ϵ -caprolactone) (PCL), poly(acrylamide) (PAA),

poly(urethane) (PU), poly(lactic acid) (PLA), poly(lactic-co-glycolic acid) (PLGA), poly(glycolic acid) (PGA), poly(ethylene oxide) (PEO), poly(methyl methacrylate) (PMMA), poly(hydroxyethyl methacrylate) (PHEMA) (Mandal et al., 2020). Their application as a base matrix for multifunctional coatings have been under the spotlight since the last decade (Jiang et al., 2020). Various studies elucidated these coatings as highly functional layers for BTE implants, however, it is hard to categorize them due to quite similar biological responses. Therefore, different examples of gap filling synthetic polymer-based examples are given here without subgroups.

A study by et al. (2021) demonstrated significance of use of a polymer-based matrix so as to establish a bioactive agent reservoir at the implant periphery (Zhang et al., 2021). They coated Cp-Ti surface with PLGA/recombinant human bone morphogenic protein 2 (rhBMP-2) via dip-coating and observed continuous release of rhBMP-2 for 28 days. The release of osteogenic agent led to a drastic increase in osteogenic response of MC3T3-E1 cells *in vitro* as well as increment in the rate of bone deposition around implants in a rabbit tibial defect model *in vivo*. He et al. (2021) utilized PLGA as a coating to release an antimicrobial peptide (AMP) named as Pac-525 at the local defect site of HA coated Cp-Ti dental implant (He et al., 2021). Besides good proliferative and osteogenic differentiation rate achieved by MC3T3-E1s, Pac-525 presence significantly improved bactericidal effect of the coating on *E. coli* and *S. aureus*.

Recent studies on synthetic polymer-based coatings revealed a huge possibility on endowing multiple features on the Ti-based implants. Especially the combination of distinct yet most desired features such as osteogenic and antibacterial properties allowed scientists to develop new perspectives. In order to obtain a yield coating process and control ion release, Luo et al. (2021) employed electrochemical coating process on Cp-Ti in a medium composed of poly(pyrrole) (PPy), HA precursors and zinc nitrate ($\text{Zn}(\text{NO}_3)_2$), $\text{Ag}(\text{NO}_3)$ and copper nitrate ($\text{Cu}(\text{II})(\text{NO}_3)_2$) to further dope HA during deposition (Luo et al., 2021). Composite coating allowed Zn, Ag and Cu

release over the course of 10 days, and illustrated significant enhancement of BMSC and vascular endothelial cells (VECs) growth on the surface, bioactivity through rapid CaP deposition in SBF, and good antibacterial activity against *E. coli* and *S. aureus*. Another highly used synthetic polymer, PCL, has been employed in various Ti-based implant coatings. Jariya et al. (2022) employed PCL-based coating to allow retention of graphene oxide (GO) and vaterite which were loaded with ciprofloxacin (Iynoon Jariya et al., 2022). They reached over 80% release of loaded ciprofloxacin in a period of 120 h, and coated implants demonstrated good bioactivity. Similar studies conducted using synthetic polymer-based coatings are reported in Table 1.4.

Table 1.4 Synthetic polymer-based coatings on Ti-based implants.

Implant	Polymer	Outcome	References
Cp-Ti	PVA loaded HA/folic acid/methoxtrate	<ul style="list-style-type: none"> Electrospun layer on Ti implant was produced. High bioactivity and greater rate of BMSC growth compared to non-biological agent loaded counterparts. 	(Jing et al., 2021)
Cp-Ti	PEG and tannic acid (TA)	<ul style="list-style-type: none"> Aimed to design anti-biofouling layer to prevent microbial adhesion. Smooth and hydrophilic layer was obtained. Both bacteria (<i>S. aureus</i> and <i>E. coli</i>) and platelet adhesion was prevented . 	(Guo et al., 2021)
Cp-Ti	PCL and PU blends loaded with ciprofloxacin	<ul style="list-style-type: none"> Highly rough composite coating layer was achieved. Significantly improved drug release rate over 21 days and antibacterial activity against <i>S. aureus</i> were observed. 	(Xu et al., 2021)
Cp-Ti	PVA/PEG loaded with Zn, Mg and Si doped HA and <i>Cissus quadrangularis</i> (QC) extract	<ul style="list-style-type: none"> Electrospun layer on implant showed highly rough, nanofibrous topography and continuous release of both metallic ions and QC. Higher osteogenic activity and CaP deposition were obtained for coatings compared to non-HA and QC loaded counterparts. 	(Song et al., 2021)

Table 1.4 (cont'd) Synthetic polymer-based coatings on Ti-based implants.

Cp-Ti	Electrochemical deposition in PPy solution with HA precursors and Zn(NO ₃) ₂	<ul style="list-style-type: none"> Controlled release of Ca and Zn over 10-day period was achieved. Highly porous and rough surface allowed VECs and BMSCs to grow and colonize, and showed good antibacterial activity against <i>S. aureus</i> and <i>E. coli</i>. 	(Maimaiti et al., 2020)
Cp-Ti	Poly(di(ethylene glycol) methylether methacrylate) (PDEGMA) loaded with levofloxacin	<ul style="list-style-type: none"> PDEGMA coating in the form of brushes was designed to release cargo at physiological temperature (36.5°C). Coatings demonstrated continuous release of drug at 36.5°C <i>in vitro</i> (with almost 100% antibacterial effect against <i>S. aureus</i>) and diminished bacterial activity in rat intramuscular bacterial infection model. 	(Choi et al., 2021)

In spite of tremendous applicability and pliability, synthetic polymers lack natural peptide sequences or patterns that can be recognized by cells or induce biosimilar apatite deposition. In this context, natural polymers tend to mimic natural osseous ECM more effectively in comparison to synthetic counterparts (Pazarçeviren, et al., 2021). Additionally, degradation products of synthetic polymers could unexpectedly alter local pH which may lead to highly acidic environment, such as in the case of PLA, PGA or PLGA degradation, and may bring about cytotoxicity (Deng & Gao, 2016). Moreover, synthetic polymers are either dissolved or treated with extremely hazardous organic solvents while they are manufactured and utilized to obtain final implant coating (Pagel & Beck-Sickingler, 2017). Last but not the least, innate immune cells cannot effectively degrade or recognize external molecules that cannot be bioresorbed. Therefore, a stronger immune response may lead to chronic inflammatory response until synthetic polymer particles are cleared out (Mariani et al., 2019). Realizing these situations, novel natural polymer-based coatings for BTE

implants have been developed to tune both regenerative responses such as osteogenesis and angiogenesis and innate/adaptive immune responses.

1.2.3.2 Natural Polymer-based Coatings

Besides providing a supportive niche for pre-osteoblastic cells and bone-similar mineral deposition directly on the implant surface, cellular attachment of fibroblasts and endothelial precursors, osteoimmunomodulation as well as formation of ECM-like structure acting as an osteoconductive and osteoinductive interphase gained prominence. For these reasons, protein-based and polysaccharide-based coatings show great potential as metallic implant coatings because of simulating natural host ECM-like structure enabling robust osseointegration. Hence, it can be hypothesized that natural polymer-based coatings show a great potential to meet the following requirements and address multiple problems that may arise during implant service time:

1. Natural polymers can perform as a temporary ECM scaffold that can be replaced overtime with growing and integrating bone at the interphase. Moreover, a functional bridging can be achieved, and wear stress could be prevented (Saveleva et al., 2019).
2. To attain osseointegration, the interphase should be mechanically interlocked and vascularized to maintain healthy bone homeostasis. A 3D natural polymer-based hydrogel and a thin film coating could allow angiogenesis and therefore it may prompt osteoinduction and anti-inflammatory pathways (Jurczak et al., 2019).
3. Peri-implantitis is one of the major reasons for long-term implant failure as discussed previously in detail. Natural polymer-based coatings can act as reservoirs providing continuous release of antibacterial drugs and peptides during wound healing phase, similar to synthetic polymer-based coating (Lyndon et al., 2014).

4. Similarly, controlled release of peptides, cytokines, growth factors etc. can be accomplished by using a natural polymer-based coating. Owing to design of coatings that could improve protein adsorption kinetics, cellular colonization can be promoted. Higher colonization may bring about higher rate of integration with bone (Barik et al., 2020).
5. A greater spatiotemporal control of biological events and ability to modify or induce a specific signaling cascade for accomplishing desired response from the host can be achieved by natural polymer-based coatings.
6. Since bioceramic and synthetic polymer-based coatings lack important biological cues to endow multifunctionality, which has been shown to improve osseointegration capacity, naturally recognized polymers can be applied via straightforward and cost-effective procedures.

Similar to synthetic polymers, FDA and EMA approval plays a critical role in the use of natural polymers. However, depending on the source and usage, natural polymer-based biomedical products require specific license and recognition. Although this appears to be a limitation, applicability and tailorable structural properties increase the chance of use of natural polymer-based method in BTE. In addition, it can be noted that most of the tissue engineering and cosmetic products in the form of hydrogel are completely or partly composed of natural polymers (Mandal, et al., 2020). In spite of a myriad of natural polymer-based procedures have been developed in BTE, only a handful of natural polymers has been meticulously studied and characterized: Gelatin, collagen, silk fibroin, alginate, chitosan, hyaluronic acid and chondroitin sulfate (Table 1.5).

1.2.3.2.1 Gelatin

Gelatin (GEL) is a protein polymer derived from thermally and chemically degraded collagen (Echave et al., 2019). It is generally employed to mimic peptide part of the

ECM, and it has lower immunogenicity and highly chemically tailorable properties compared to collagen (COL) while being highly bioresorbable and low-cost to obtain (Tondera et al., 2016). One of the most useful and highly utilized property of GEL is its tremendous ability to form polyanionic complexes and intertwined network with other natural polymers. Additionally, it has a good liability to various reagents to form chemical crosslinks to stabilize 3D structure of the polymeric networks. Therefore, this single strand polypeptide is the most widely used natural polymer in BTE field owing to the ability to decorate scaffolds and surfaces with integrin-binding arginine-glycine-aspartic acid (RGD) sequence while structurally supporting the hydrogels (Echave et al., 2017; Kim et al., 2017).

Taking advantage of RGD sequence of GEL for better cell adhesion, Ti-based implant surfaces can be coated with GEL-based composite structures. One of the good examples for the use of GEL as a coating matrix is the study conducted by Su et al. (2022). The group achieved osteogenic ion release from chemically attached GEL layer on Cp-Ti (Su et al., 2022). GEL was coated on HA and pDA treated surface to induce covalent interaction to form amide bonds. This allowed HA to release Ca and P over time and induced rapid BMSC colonization osteogenic differentiation. Interestingly, the composite layer prompted similar content of pro-inflammatory cytokines with non-coated surfaces to be released and triggered greater release of pro-healing immunomodulatory interleukin 10 (IL-10) and transforming growth factor β 1 (TGF- β 1) production.

Being able to form strong hydrogel structure with unhindered diffusion, GEL-based matrices could be utilized to encapsulate cells and then used to coat Ti-based implants. Li et al. (2022) conducted a proof-of-concept study using photo-crosslinkable GEL (Li et al., 2022). This hydrogel containing MSCs, HUVECs or both cell types, were used to coat Ti-6Al-4V implants designed in the form of human patient-specific acetabular cap through dip-coating and subsequently photo-crosslinked. Immense improvement in vascularization and bone deposition on Ti-6Al-4V implant were reported *in vitro*, proving the point that additively

manufactured metallic implants of a given anatomically-relevant shape, size and complexity could be coated with natural polymer-based composite structures.

However, being a moderately degraded form of COL, GEL tends to be degraded very quickly in *in vivo* environment through hydrolysis and enzymatic degradation (Jaipan et al., 2017). In addition, GEL-based hydrogels have been reported to lack mechanical strength and thermal stability, meaning that they tend to swell at physiological temperature. Therefore, GEL has been utilized as a base matrix component with other polymers to synergistically improve overall structural and biological properties of other natural polymers.

1.2.3.2.2 Collagen

Human bone is composed of approximately 70% (w/w) inorganic phase, which is made of calcium deficient carbonated HA having trace elements such as B and mono- and divalent metallic ions such as Na, K, Mg, Ca, Sr, Fe, etc., and 30% (w/w) organic phase having 90% (w/w) collagen (COL) type I (Tzaphlidou, 2008). COL was shown to mediate osteoblast adhesion (Martocq & Douglas, 2021), increase the overall mechanical strength of the hydrogels (Ferreira et al., 2012) and allow HA deposition (Xia et al., 2012). Hence, it has been employed as an ECM mimicking interface coating on Ti-based implants.

Ciobanu and Harja (2019) demonstrated a very straightforward method to improve osteogenic potential of Ti implants (Ciobanu & Harja, 2019). Cp-Ti implants were placed in a supersaturated cerium (Ce) doped HA precursor solution containing COL and incubated for 2 h to be coated. The composite interface not only demonstrated good roughness and moderately crystalline CeHA loaded COL layer but also showed high bactericidal activity against *S. aureus* (~73%) and *E. coli* (~92%). In another study, Zhang et al. (2021) pre-coated Cp-Ti surface with calcium sodium hydrogen silicate (pectolite) and subsequently further functionalized the interface layer with HHC-36 antibacterial peptide loaded COL matrix (Zhang et al., 2021). Significant

improvement in osteogenic capacity of hFOB cells as well as 100% killing rate against both adherent and planktonic *S. aureus* were obtained. More strikingly, coated layers were kept in saline environment for 28 days, then interacted with *S. aureus* and the interface layer still demonstrated good antibacterial activity (60%). Therefore, good control over release, even better than GEL, could be concluded with COL-based coatings.

On the other hand, low degradation rate and use of acidic solutions in fabrication decreases usability of COL with delicate biological agents. As reported by Li et al. (2021), biomimetic COL-based coatings were fabricated in combination with alginate to enable controlled release of VEGF from Ti-6Al-4V implants and also to protect VEGF during coating process (Li et al., 2021). In this sense, COL is overlooked in comparison to GEL owing to immense pliability, solubility and compatibility of GEL compared to COL with other biological factors.

1.2.3.2.3 Silk Fibroin

Similar to COL, silk fibroin (SF) is another protein polymer tremendously employed biomaterial. Recently, SF has been utilized as a Ti-based implant coating base matrix owing to good mechanical properties and ability to interact rapidly with both organic and inorganic polymers (Wu et al., 2021). In addition, SF can synergistically improve cell adhesion properties and enhance structural stability (Guo et al., 2019). In this context, Yang et al. (2019) blended SF solution with $\text{Ca}(\text{NO}_3)_2$ and $\text{NH}_4\text{H}_2\text{PO}_4$ to induce mineralization after coated on Cp-Ti implants (Yang et al., 2019). SF-Ca-P coating on Ti via electrochemical deposition under voltage, allowed formation of octacalcium phosphate (OCP), a similar CaP to HA, and extensively improved bone-similar CaP deposition and osteogenic response of MC3T3-E1. In another interesting study, SF loaded with Ag was coated on Sr doped Cp-Ti surfaces to endow antibacterial and osteogenic properties to Ti implant (Wang et al., 2021). It was reported that both Sr and Ag release from SF layer was obtained in a continuous

trend over 14 days. Dual ion release improved bone formation in a unicortical rabbit femur model within 8 weeks, and further enhanced antibacterial activity against *S. aureus* and *E. coli*.

SF has also been utilized as a controlled release reservoir for biological agents from Ti-based implant surfaces. Sang et al. (2021) dip-coated Cp-Ti surface with SF and immersed in gentamicin sulfate, a large spectrum antibiotic (Sang et al., 2021). They demonstrated controlled release of antibiotic agent from SF-based coating and good bactericidal rate against both *S. aureus* and *E. coli* both *in vitro* and in subcutaneous implant model in rats. Keceli et al. (2021) illustrated effectiveness of dual release of BMP-6 and platelet derived growth factor (PDGF) from SF-based coating in terms of bioactivity and osteogenic differentiation (Keceli et al., 2020). MC3T3-E1s demonstrated a rapid osteogenic response as well as biomineralization on SF-BMP-6-PDGF coated Cp-Ti implants.

In addition, SF coating and structural modification do not require potentially toxic reagent on the contrary to COL-based coating fabrication. Thus, especially in the context of immunomodulation, either SF has been employed as anti-inflammatory agent or various immunomodulatory agents have been introduced to Ti implant surfaces with the help of SF. In a study by Ma et al. (2021), 3D printed Ti-6Al-4V implants were dip-coated with SF and employed in a diabetic sheep cylindrical unicortical iliac crest defect model (Ma et al., 2021). SF coated Ti-6Al-4V demonstrated good immunomodulatory activity as it led to lower ROS formation, nuclear factor kappa B (NFkB) stimulation and improved bone growth on Ti-6Al-4V implants. Wenhao et al. (2020) grafted Ti-6Al-4V surfaces with pDA to crosslinking SF which was loaded with Ag and gentamicin (Wenhao et al., 2020). After 8 weeks post-implantation in rabbit femoral defect model, SF-Ag-Gentamicin coated implants demonstrated bone deposition while slowly receded coated layer, gradual formation of blood vessels and loss of fibrous tissue over time in comparison to surface treated Ti-6Al-4V.

Although good mechanical properties and capacity for structural and chemical modifications make SF a good candidate for a natural polymer coating base matrix, SF is not as cost-effective as GEL and may lead to low yield during isolation (Nguyen et al., 2019). Moreover, another peptide, sericin, could contaminate SF isolate and it may compromise biocompatibility. Thus, SF is collected and purified intensively to remove both sericin and chemicals employed during isolation, prior to use. Taking these drawbacks into account, GEL appeared to be the most employed polypeptide polymer as biomaterial when compared to COL or SF.

1.2.3.2.4 Alginate

Alginate (ALG) is one of the most employed polysaccharides that can be modified by various functional groups to achieve both biochemically and structurally tailor-made properties (Witzler et al., 2019). ALG is made up of alternating chains of β -D-mannuronate and α -L-guluronate, and can be easily obtained via cost-effective methods, thus making ALG a very efficient natural polymer to modify implant surfaces in distinct morphologies, topographies, surface charge, electrochemistry and biology (Lee & Mooney, 2012). Moreover, ALG has been demonstrated to be highly pliable and have tailorable physical and chemical characteristics that make various coating methodologies easily utilized to enhance bioactivity of Ti-based implants.

Chen et al. (2018) grafted Cp-Ti rods and discs with cationic protamine bridging molecule and coated with ALG through electrophoretic deposition (Chen et al., 2018). Then, ALG layer was again bonded with protamine (PRO) and finally activated with BMP-2. PRO/ALG/P/BMP-2 sandwich provided a sustained release of BMP-2 over 11 days and enhanced MC3T3-E1 adhesion and osteogenic differentiation. After implanted in rat femur model, coatings remarkably increased BV/TV ratio as well as prompted bone ingrowth. An intriguing study by Yin et al. (2020) revealed that ALG-based composite coating could be electrophoretically

deposited on Ti-based implant (Yin et al., 2020). Lanthanum (La) and silicon (Si) co-doped HA (LaSiHA) containing ALG composite coatings had a strong adhesion to implant surface and showed dual-functionality in terms of antibacterial activity and osteogenic ion release. In a recent study, ALG was utilized as a matrix to be coated on Cp-Ti via both ionic and chemical crosslinking (Wang et al., 2021). Initially calcium carbonate (CaCO_3) coated Cp-Ti was dipped in DA and ALG mixture and further crosslinked with CaCl_2 . It was reported that ALG matrix released DA over 24-day period and suppressed osteoclastogenesis while improved BMSCs growth and differentiation towards osteocytes.

Being a natural highly anionic polysaccharide, ALG-based coatings has been shown to alleviate immune response. As an important example, Yin et al. (2021) anodized Cp-Ti, grafted with interleukin 4 (IL-4) immunomodulatory cytokine and deposited ALG/chitosan (CHI) multilayered films (Yin et al., 2021). Presence of ALG/CHI layers allowed a controlled release of IL-4 over time, and subsequently improved pro-healing markers of RAW 264.7, murine macrophage cells. Interestingly, conditioned media collected from RAW 264.7s interacted with the implants enhanced osteogenic response of murine BMSCs *in vitro* and increased osteogenesis in medullar rat femur implant model without any signs of chronic inflammatory response in 4 weeks.

Although ALG possesses immense potential as a reservoir-like matrix that can be coated on Ti-based implants via various procedures, it is disadvantageous to be employed as sole polymeric layer in coatings. Having high polyanionic nature, ALG prevents cellular adhesion if employed alone (Hurtado et al., 2022). Therefore, ALG is mostly used in combination with a polypeptide polymer such as GEL or a positively charged polysaccharide, CHI, to improve cell adhesion capacity.

1.2.3.2.5 Chitosan

Chitosan (CHI) is an outstanding multifunctional polysaccharide utilized in various biomedical applications. CHI is made up of N-acetyl D-glucosamine and D-glucosamine subunits, and can easily be obtained from N-deacetylation of chitin [199]. It is an abundantly produced, cheap, biodegradable and cationic polysaccharide that can be employed in combination with different synthetic or natural polymers, bioceramics and drugs to confer osteogenic, angiogenic, immunomodulatory and antibacterial properties on Ti-based implants [200].

In recent years, most of the coating studies involved CHI as the main matrix or as a natural polymer reinforcement. In a study by Mutuk and Gürbüz (2021), graphene nanosheets and AgHA containing CHI was electrospun on Cp-Ti (Mutuk & Gürbüz, 2021). The composite layer improved not only topographical features but also antibacterial capacity against *E. coli*. In another study by Villegas et al. (2022), a Ti-6Al-4V medical implants surface was grafted with a fluorosilane (Trichloro(1H,1H,2H,2H-perfluorooctyl) silane (TPFS)) and coated with CHI layer through chemical crosslinking on surface. CHI-fluorosilane layer allowed greater rate of cell adhesion in comparison to other CHI-silane coated layers and pure Ti-6Al-4V. Moreover, this layer significantly improved antibacterial activity against biofilm-forming *S. aureus*.

One of the important features of CHI is its ability to form stable hydrogel or film layer with other polymers, especially GEL, on Ti-based implants. In order to take advantage of positively charged nature of CHI to achieve a multifunctional and multilayered surface, Tang et al. (2021) coated Cp-Ti with alternating naringin (an osteogenic natural flavonoid) and gentamicin loaded CHI and GEL layers by layer-by-layer (LbL) method (Tang et al., 2021). LbL CHI/GEL/Naringin/Gentamicin coating both improved MC3T3-E1 osteogenic response and demonstrated very high antibacterial activity against *S. aureus* and *E. coli*. Wu et al. (2021) blended CHI, GEL and Ag nanoparticles to achieve osteogenic and antibacterial surface properties

on 3D designed Cp-Ti implants (Wu et al., 2021). CHI/GEL/Ag was used as a novel composite bioink to deposit a 3D structure on implants, and led to mechanically strong, highly adhesive, Ag releasing and easily deposited 3D layer. It demonstrated good biocompatibility and high antibacterial capacity against *S. aureus* and *E. coli*.

1.2.3.2.6 Glycosaminoglycans

Glycosaminoglycans (GAGs) are composed of repeating units of disaccharides, namely a hexuronic acid and an amine added saccharide unit (Sodhi & Panitch, 2021). Among these, hyaluronic acid (HyA) and chondroitin sulfate (ChoS) have been the most widely utilized GAGs. HyA is a non-sulfated mucopolysaccharide composed of N-acetylglucosamine and D-glucuronic acid subunits, and an important ECM GAG prompting desirable cellular responses (Gribova et al., 2020). Due to electronic nature, HyA can be employed with another natural polymer to form electrostatically interacting polymer networks and can act as perfect candidate for LbL methodologies to form polyelectrolyte matrices (PEMs). As an example, Wu et al. (2020) coated Cp-Ti with HyA and COL loaded with BMP-2 and BMP-7 as a multilayered PEM on implants (Wu et al., 2020). Coated layer allowed rapid increase (within first 7 days of incubation) in ALP activity and OCN release, and hence, demonstrated great osteogenic potential.

ChoS, which is made up of N-acetyl galactosamine and D-glucuronic acid, is another ECM GAG mostly employed in cardiovascular studies and also utilized in a limited number of chondrogenesis and osteoblastogenesis studies in literature (Hayes et al., 2018). In a study by Ye et al. (2021) Ti-6Al-4V was coated with nerve growth factor and HA loaded ChoS (Ye et al., 2021). Coated implants were directly placed in mandibular premolar region in beagle dogs as dental implants. Results demonstrated an extensive bone formation achieved by coatings at the end of 8 weeks. In addition, nerve fiber formation and absence of fibrous tissue were observed.

Owing to tremendous capacity to form supramolecular networks through electrostatic interactions, high wettability, water retention and native ECM structure, GAGs are employed mostly in soft tissue regeneration studies. Hence, mechanical weakness and production cost are noted as major drawbacks of these GAGs and therefore substantially prevent their wide use.

Table 1.5 Natural polymer-based coatings on Ti-based implants.

Implant	Coating	Outcome	Reference
Ti-6Al-4V	GEL loaded with Minodronate, CaCl ₂ and (NH ₄) ₂ HPO ₄	<ul style="list-style-type: none"> • Formation of HA on coating. • Biomimicking CaP deposition in SBF in 7 days. • Continuous Minodronate and Ca release for 14 days. 	(Yamaguchi et al., 2022)
NiTi	GEL blended with PVA	<ul style="list-style-type: none"> • Increased corrosion resistance. • High biocompatibility and colonization of Balb/3T3 fibroblasts. 	(Simsek et al., 2021)
Cp-Ti	Pitavastatin loaded GEL-based LbL coating with β -cyclodextrin grafted CHI	<ul style="list-style-type: none"> • Tremendous improvement in osteogenic response of MSCs and angiogenic response of HUVECs. • Coated layer allowed recruitment of MSCs and vascularization in rat subcutaneous implant model. • Highest bone-implant interaction area and new bone formation in intramedullar rat femur bone defect. 	(Chen et al., 2022)
Cp-Ti	Genipin crosslinked COL	<ul style="list-style-type: none"> • High porosity, hydrophilicity and roughness on the surface. • High cell adhesion, proliferation and osteogenic differentiation while allowing CaP deposition on COL fibers. 	(Liu et al., 2021)
Cp-Ti	COL coating on pDA and GO grafted implant; loaded with Ag or BSA for two separate release studies	<ul style="list-style-type: none"> • Increment in cell adhesion proteins, cell proliferation rate and migration capacity on coated implants. • Exceptional increase in ALP activity and mineralization rate. • After loaded with BSA and Ag, allowed continuous release over 10-day period. 	(Xu et al., 2021)

Table 1.5 (cont'd) Natural polymer-based coatings on Ti-based implants.

Cp-Ti	COL coating on F doped TiO ₂ and pDA grafted implant	<ul style="list-style-type: none"> • On demand release of FTiO₂ particles from COL layer. • Allowed osteosarcoma cell (Saos-2) ablation with near infrared irradiation. • Increased mineralization and ALP activity of BMSCs. 	(Wu et al., 2022)
Ti-6Al-4V	SF loaded with HA and Ag	<ul style="list-style-type: none"> • 100% antibacterial rate against <i>S. aureus</i>. • Higher MC3T3-E1 proliferation and colonization compared to pure TC4. 	(Zhang et al., 2021)
Cp-Ti	Poly(L-lysine) grafted surface coated with ALG loaded with Ag nanoparticles	<ul style="list-style-type: none"> • Continuous release of Ag over 27 days was achieved. • Almost 100% antibacterial rate against <i>S. aureus</i> and <i>Streptococcus. mutans</i> (<i>S. mutans</i>). • Good MC3T3-E1 proliferation and colonization. 	(Guo et al., 2020)
Pure Ti	Ciprofloxacin and HA loaded CHI microspheres coated on silanized implants	<ul style="list-style-type: none"> • Cumulative >90% release of drug over 20 days. • Good antibacterial activity against <i>S. aureus</i> and good bioactivity observed by deposition of CaP in SBF within 3 weeks. 	(Doymus et al., 2021)
Cp-Ti	CHI/ALG loaded with Ag and coated on pDA grafted implants	<ul style="list-style-type: none"> • Greatly improved electrochemical corrosion resistance. • High antibacterial activity against <i>S. mutans</i>. 	(Duan et al., 2021)
Ti-6Al-4V	DA grafted HyA loaded with vancomycin	<ul style="list-style-type: none"> • Rapid bone-implant contact, marrow and trabecular bone formation in rabbit intramedullary femoral implant model. • Good anti-metachillin resistant <i>S. aureus</i> activity <i>in vivo</i>. 	(Guarise et al., 2021)
Cp-Ti	HyA/Heparin PEM multilayers loaded with Tanfloc	<ul style="list-style-type: none"> • Good adipose derived stem cell (ADSCs) growth and colonization. • Induced osteogenic differentiation of ADSCs. 	(Sabino et al., 2021)

1.3 Aim of the Study

Ti-based implants were shown to integrate with host bone through sophisticated pathways leading to intertwined events such as immune response, vascularization, provisional matrix and woven bone formation at the interphase, contact/distance osteogenesis and bone remodeling to finalize osseointegration (Pazarçeviren, et al., 2021). During pre-conditioning of the implant surface prior to successful integration with bone, concurrent events of resolution of inflammation, pre-osteoblasts, fibroblasts and endothelial precursors homing and colonization occur at the interphase. Therefore, bioactive surfaces provide a more suitable substrate for a rapid and complete osseointegration with the host bone. Consequently, risk of peri-implantitis and aseptic loosening could be drastically diminished.

Protein and polysaccharide-based metallic implant coatings have been employed in different studies to confer additional functions to the implant surfaces as well as establishing an ECM-like structure for better osseointegration. However, there is no protein and polysaccharide-based metallic implant coating approved for clinical translation. Most of these studies focus on single or dual functionality on the surfaces. However, as explained previously, osseointegration is a process heavily dependent on biological properties of the implanted material. Collectively, comments and critics on the studies can be elaborated as follows:

- Previously described surface modifications showed good results *in vitro* and they have been employed in various commercial implants, however, *in vivo* stability, long term effectiveness and no loss of function over time **have not been successfully demonstrated**. Hence, polymer-based coatings have been developed and still being investigated thoroughly.
- Attaining structural stability should be the primary concern for natural polymer-based coatings. These coatings should endure drying and sterilization processes without delamination and maintain cohesion during handling, implanting and initial contact with the blood. It is strongly stressed

that pliability, reproducibility and shelf-life are important attributes of a successful coating.

- Omitting relatively low yield method of functional group grafting and establishing a 3D structure exploiting surface properties such as topography and morphology, and gap filling ability to bridge implant and host bone could be pointed out as next generation of permanent implant modification realizing natural polymer-metal covalent bonding.
- Polysaccharide-based coatings were shown to mimic the structural properties of natural ECM. Mechanical stability and easy-to-alter chemical properties promote polysaccharides as the key element of a multipurpose coating. They can be modified to precisely tune degradation rate, mechanical strength, functional bonding with drugs or other biological agents for controlled release over longer periods. In addition, throughout rapid freezing, drying and subsequent wetting, these coatings could further preserve peptides and drugs, and reduce sterilization-related structural damages. However, polysaccharides swell much more than proteins that they could bring about larger osmotic pressure. Therefore, their use in combination with protein-based polymers are highly encouraged to endow multifunctionality to a natural polymer-based coating on metallic implant.
- It was also observed in a large body of studies that polysaccharides could confer immunological-privilege owing to tailored surface charge and functional groups. In this sense, protein-based coatings could present various cell recognition sequences (such as RGD in GEL) for greater colonization of stem cells. As a consequence, polymer-polysaccharide blended coatings may have greater potential in provoking pro-healing osteoimmunomodulatory response.

In order to take advantage of structural similarities with the natural bone ECM, a protein-based and a polysaccharide-based polymer, namely gelatin and alginate, were selected to be employed as main coating matrix. It should be noted that abovementioned studies involving polysaccharides such as ALG and CHI mostly

employed GEL as protein phase in order to mimic natural ECM. In addition, it is proven that polysaccharides can be crosslinked with GEL in order GEL to impart biocompatibility and increase gelation and pliability of the coated structure. Taking these factors into account, ALG was blended with GEL in 1:3 w/w ratio in this study to achieve ECM mimicry while endowing strong mechanical strength and enhance biological performance of the coatings.

Similar to previously mentioned studies, natural polymer-based coatings are mostly loaded with HA or a derivative of HA to further enhance osteogenic potential of coatings. In this study, boron doped hydroxyapatite/ β -tricalcium phosphate (BHT) species were produced, characterized and one of the boron (B) doped samples (5BHT) was selected to impart osteogenic, angiogenic and immunomodulatory properties to ALG/GEL (A/G) coatings on medical grade Ti-6Al-4V (Grade 5, ELI) implants (Figure 1.2).

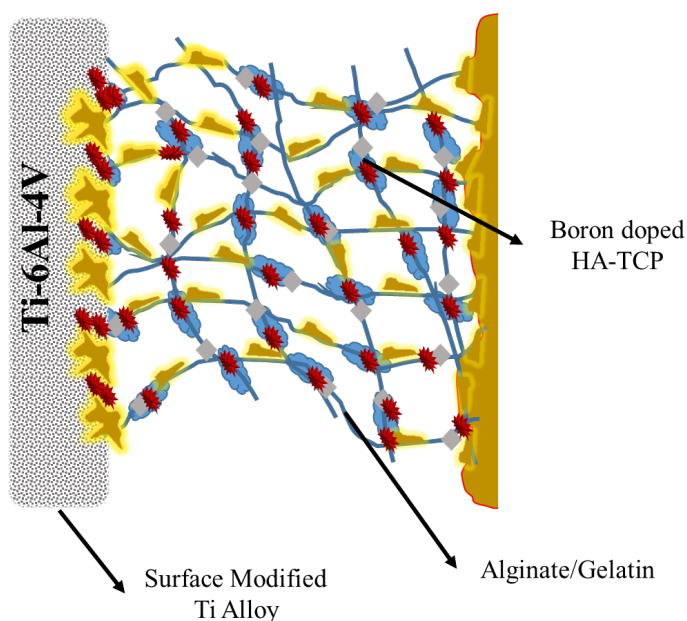


Figure 1.2 Proposed composite coating layer on Ti-6Al-4V as gap-filling interphase to support osseointegration of implant.

Owing to complex and hierarchical nature of osseous tissue, bone healing could be enhanced and regeneration may be supported via the use of highly bioactive and multifunctional bioceramics forming a suitable microenvironment. Boron is a trace element present in bone (Ying et al., 2011). Furthermore, it is a metalloid (semi-metal) having electron deficiency thus forms various covalently bonded compounds such as Borax ($\text{Na}_2[\text{B}_4\text{O}_5(\text{OH})_4] \cdot 8\text{H}_2\text{O}$), boron nitride (BN) and boric acid (H_3BO_3). Recently, boron containing compounds are intensively studied in BTE in production of permanent prosthodontic and orthopedic implants (especially BN and Neodymium-Boron-Iron (NeBFe)) (Er et al., 2018; Tozar et al., 2019; Watanabe et al., 2005). Moreover, boron can be used as an osteogenic dopant in osteoconductive bioceramics such as bioglass (BG) (Wu et al., 2011). In another study, Çalış et al. (2017) applied boron doped hydroxyapatite in dental defects and observed improved osteogenic response (Calis et al., 2017). On the other hand, utilization of boron in bioinert structures (BN coating on Ti-6Al-4V), in fast-biodegrading BG and slow-biodegrading HA bring about mistimed osteogenic response, cytotoxicity and biocompatibility issues (Chan et al., 2015; Cortez et al., 2017; Han et al., 2016). Considering the rate of biodegradation and response to the ratio of calcium (Ca) and phosphate (P), a bioceramic having Ca/P ratio as 1.6 with biphasic HT will be synthesized in this study.

CHAPTER 2

MATERIALS AND METHODS

2.1 Materials

Calcium nitrate tetrahydrate ($\text{Ca}(\text{NO}_3)_2 \cdot 4\text{H}_2\text{O}$), diammonium phosphate ($(\text{NH}_4)_2\text{HPO}_4$) and boric acid (H_3BO_3), ethanol, ammonia (NH_4OH), acetic acid (glacial), 3-(4,5-Dimethylthiazol-2-yl)-2,5-diphenyltetrazolium bromide (MTT), dimethyl sulfoxide (DMSO), dexamethasone (Dex), L-ascorbic acid (L-AA), β -glycerophosphate (β -GP), para-nitrophenyl phenol, 4-nitrophenol, sodium chloride (NaCl), sulfuric acid (H_2SO_4), hydrogen peroxide (H_2O_2), sodium hydroxide (NaOH), acetone, 2,4,6-trinitrobenzene sulfonic acid (TNBS), hydrochloric acid (HCl), glycine, ethanol (EtOH), methanol (MeOH), sodium cacodylate, paraformaldehyde (PFA), bovine serum albumin (BSA), sodium azide (NaN_3) and (LPS, from *Escherichia coli* O55:B5) were acquired from Sigma (USA). Nitric acid (HNO_3), acetone, methanol, magnesium chloride hexahydrate ($\text{MgCl}_2 \cdot 6\text{H}_2\text{O}$), sodium bicarbonate (NaHCO_3), potassium chloride (KCl), dipotassium phosphate (K_2HPO_4), magnesium chloride hexahydrate ($\text{MgCl}_2 \cdot 6\text{H}_2\text{O}$), calcium chloride (CaCl_2), sodium sulfate (Na_2SO_4), tris(hydroxymethyl)aminomethane ($((\text{CH}_2\text{OH})_3\text{CNH}_2)$) were purchased from Merck (USA). All chemicals were reagent grade.

DMEM/F12, heat inactivated fetal bovine serum (FBS), penicillin-streptomycin (P/S, 10000 U), RPMI 1640, EndoGo XF, and EndoGoXF supplements were purchased from Biological Industries (Israel). Picogreen® assay kit from Invitrogen (USA). LPS, PMA and Normocin were obtained from Invivogen, USA. Media and supplements were cell culture tested and used without further purification.

Distilled water is produced by purifying through a resin bed, reverse osmosis, and flowing through a UV electrodeionization device (Millipore ELIX-5, Sigma, USA).

2.2 Methods

2.2.1 Preparation and Characterization of BHT

2.2.1.1 Preparation of BHT

HT and BHT were synthesized by wet precipitation/microwave reflux method (Alshemary et al., 2018). Briefly, Ca source ($\text{CaNO}_3 \cdot 4\text{H}_2\text{O}$) and P source ($(\text{NH}_4)_2\text{HPO}_4$) were dissolved separately in 250 mL beakers. Boron source (H_3BO_3) was dissolved along with Ca and P source for BHT. The amounts of all components in synthesis are given in Table 2.1. Then, for Ca source pH was set above 10 using NH_4OH , P source was then introduced in Ca source dropwise over 10 min. The mixture was aged at 800 rpm for 30 min at RT. Finally, mixtures were poured into 1 L flasks, attached with condenser circulating cold water, placed in microwave and HT wet cakes were formed after exposing to at 800 W for 15 min. After microwave reflux procedure, samples were filtered through crude filter paper, dried at 150°C overnight and sintered at 1100°C for 2 h. Synthesized HT and BHT species were then undergone downsizing procedure. Prior to further analysis, samples were grounded, ball milled for 1 h at 30 Hz and ultrasonicated continuously for 1 min. at 25% amplitude in acetone using a probe type ultrasonicator (Bandelin, Germany) and dried at 75°C under a vacuum (-1 bar) overnight.

Table 2.1 Molar percent of each component in HT and BHT species.

Species	Ca(NO ₃) ₂ ·4H ₂ O (molar%)	(NH ₄) ₂ HPO ₄ (molar%)	H ₃ BO ₃ (molar%)
HT	61.538	38.462	-
BHT	61.538	37.462	1
2BHT	61.538	36.462	2
3BHT	61.538	35.462	3
5BHT	61.538	33.462	5
10BHT	61.538	28.462	10

2.2.1.2 XRD Analysis

XRD analysis was employed to determine crystallographic diffraction spectra of the materials produced. Resultant spectra were used to calculate the lattice parameters, crystalline structure, phase determination and particle crystallinity of different BHTs. BHT powders were analyzed by XRD under CuK α radiation having $\lambda=1.5456$ nm. The analysis was done at 2θ in $10-80^\circ$ and step size of $1^\circ/s$ (METU Central Laboratory, PANalytical Empyrean, Netherlands).

2.2.1.3 FTIR Analysis

The functional groups present in the BHT samples were analyzed by FTIR analysis. The analysis was employed at mid-IR range ($4000-400\text{ s}^{-1}$, using the facility of BIOMATEN, Bruker IFS66/S, USA) to detect OH⁻, PO₄³⁻, BO₃³⁻ and BO₂⁻ bands.

2.2.1.4 Particle Size, Elemental Composition, Total Surface Area and Mesoporous Volume Analyses

Dried particles (10 mg) were dispersed in 1 mL dH₂O and particle sizes of samples were determined by wet analysis (METU Central Laboratory, Malvern Mastersizer 2000, UK). Elemental composition of each samples was determined by (n=3) ICP-OES. Then, degassed HT and BHTs at 200°C for 16 h were characterized for total surface area (TSA, n=3) by BET analysis and mesoporous volume (n=3) for each sample was detected by BJH analysis (Autosorb II 6B, Anton Paar, Austria). Both analyses were done at standard temperature and pressure (STP, 77 K) under N₂ environment. BET and BJH analyses were normalized against particle weight.

2.2.1.5 SEM-EDX Analysis

HT and BHT samples were compressed uniaxially under 250 MPa by a cold press (Bench Top Press, Carver, USA). Then, the samples were rinsed with dH₂O and dried in a vacuum oven at 100°C. Finally, samples were analyzed for morphology, grain structure and grain size by SEM. EDX analysis was conducted to determine Ca/P ratio before mineral deposition analysis.

2.2.1.6 CaP Deposition Analysis

Discs were sterilized under UV irradiation for 1 h on each side and placed in 50 mL centrifuge tubes as given in ISO 23317 (**n=3**). All sample surfaces were in contact with SBF (pH 7.4). SBF was prepared according to Table 2.2 in a 250 mL sterile polypropylene beaker to mimic blood plasma ionic environment. Samples were incubated in SBF for 7 days. At the end of incubation, samples were rinsed with dH₂O and EtOH and then stored in a desiccator at RT until SEM-EDX analysis.

Table 2.2 Composition of SBF (Kokubo & Takadama, 2006).

Order	Chemical	Amount (g or mL)
1	NaCl	2
2	NaHCO ₃	0.0875
3	KCL	0.056
4	K ₂ HPO ₄	0.057
5	MgCl ₂ .6H ₂ O	0.07625
6	1 M HCl	10 mL
7	CaCl ₂	0.0695
8	Na ₂ SO ₄	0.01775
9	(CH ₂ OH) ₃ CNH ₂	1.51425
10	1 M NaOH or HCl	Until pH 7.4 is reached

2.2.1.7 *In vitro* Biocompatibility Analysis with HT and all BHTs

In vitro cytotoxicity of HT and all BHTs was tested using indirect elution test. HT and BHT powders were thermally sterilized at 200°C for 2 h. For extract preparation, 1 g of powder was placed in 15 mL polypropylene falcon tubes containing 10 mL human fetal osteoblast cell line growth medium (hFOB-GM), and incubated for 24 h. Composition of this media is given in Table 2.3. Then, hFOB cells (passage 8, 5x10³/well in 48 well plate) were incubated with the extracts for 24 h at 37°C, 95% CO₂ in the incubator (Panasonic Incusafe, Japan (n=8)). After incubation, media were discarded, and wells were rinsed with PBS (0.01 M, pH 7.4). After PBS removal, cells were incubated with MTT viability reagent prepared in hFOB-GM (0.5 mg/mL) for 2 h at 37°C. Precipitated formazan salts were then dissolved with DMSO and ODs were measured for each sample at 570 nm (OD₅₇₀) using a microplate reader (Molecular Devices, USA). HT was selected as the positive control for cellular

viability. Samples were also placed in 0.02% (w/v) NaN₃ added dH₂O in the same concentration as the MTT assay (n=3). Extracts were collected after 24 h and analyzed for Ca, P and B ion release with ICP.

2.2.1.8 *In vitro* Cell Culture Studies with HT and Selected BHT

2.2.1.8.1 Cell Proliferation Analysis

Proliferation analysis was conducted to determine the growth of hFOB cells under the influence of ions released by HT and BHT. hFOB cells (passage 8, 5x10³/well in 48 wellplate) were incubated with HT and 5BHT extracts obtained in hFOB-GM for 1, 4 and 7 days (n=12). Cell viability was measured at the end of each incubation period using the Alamar Blue viability assay using the supplier's protocol (Thermo Fisher, USA). Briefly, media were discarded, cells were rinsed with PBS and Alamar Blue viability agent prepared in hFOB-GM (10% v/v) was added into the wells. Cells were incubated for 2 h. Afterward, aliquots were collected and OD₅₇₀ and OD₆₀₀ were measured. hFOB proliferation was calculated using the formula provided by the supplier.

Please note that structural properties, bioactivity and good biocompatibility allowed 5BHT to be more effective than counterparts. Hence, 5BHT was selected as representative sample of boron doped HTs. Therefore, it is abbreviated as “BHT” from this point on.

2.2.1.8.2 Osteogenic Properties

2.2.1.8.2.1 ALP Activity and OCN Release

HT and BHT were placed in an osteogenic differentiation medium (hFOB-OMM, Table 2.3) at a concentration of 100 mg/mL to obtain extracts, and then filtered through a 0.22 µm syringe filter both to sterilize the media after mixing and to

remove any unwanted particles prior to media refresh. In 24 wellplates, hFOB cells were seeded (2×10^4 cells/well), incubated in hFOB-GM for 3 days and then interacted with HT and BHT extracts in hFOB-OM for 2 weeks ($n=18$). Every two days, the media were refreshed. At the end of 1st and 2nd weeks of incubation, media were discarded, wells were rinsed with PBS and 0.1% Triton X-100 in carbonate buffer (CB) was added. After that, single step of freeze-thaw (-80°C and 25°C) was applied to completely lyse the cells. Aliquots of lysates were combined with the following solutions: (1) pNpp working solution for 1 h and (2) Picogreen assay solution in Tris-EDTA (TE) buffer for 5 min. The contents of the mentioned solutions are given in Table 2.3. Lysates were used to determine osteogenic ALP enzyme production. Phosphate moieties of pNpp can be cleaved by ALP to form 4-nitrophenol, therefore concentration of ALP in the lysates can be estimated by the change in color of the original pNpp solution (colorless) into 4-nitrophenol yellow. Meanwhile, media were collected prior to ALP activity analysis at the end of each week ($n=6$). Then, media ELISA assay to quantify OCN in accordance with the protocol given by supplier (Human OCN ELISA kit, E4762, Biovision, USA).

Following quantification of ALP activity and OCN release, total DNA concentration of the lysates was determined by Picogreen assay. Picogreen is a soluble fluorescent protein that binds to double stranded DNA and used to quantify total unsheared DNA. Picogreen calibration curve (Appendix C1 Figure 1) was prepared using different concentrations (0-300 ng/mL) unsheared calf thymus DNA (Sigma, USA). Lysates and Picogreen solution in TE were interacted for 5 min in an opaque 96 wellplate, and total fluorescence at 485 nm of excitation and 538 nm of emission were measured with a microplate reader. ALP activity was normalized to total DNA content for each sample. ALP calibration curve was prepared using various concentrations (0-250 μM) of 4-nitrophenol (Sigma, USA) in CB ($n=6$, Appendix B1 Figure 1). Calibration curve for OCN ($n=6$, Appendix D1 Figure 1) was drawn by measuring the absorbance of the kit product at 450 nm following the supplier protocol (Human OCN ELISA kit, E4762, Biovision, USA).

Table 2.3 Media used in biocompatibility, cell proliferation and osteogenic differentiation analyses with hFOBs.

Media	Components
hFOB-GM	89% v/v Dulbecco's Modified Eagle Medium
	10% v/v Fetal bovine serum (FBS, heat treated)
	1% v/v Penicillin-Streptomycin (100U)
hFOB-OM	hFOB-GM components
	50 µg/mL L-ascorbic acid
	10 ⁻⁷ M dexamethasone
	10 mM β-glycerophosphate
CB (0.2 M)	2 vol 0.2 M sodium carbonate (Na ₂ CO ₃)
	1 vol 0.2 M sodium hydrogen carbonate (NaHCO ₃) and pH was set to 10.2
pNpp working solution	1 vol CB added with 100 mM MgCl ₂ .6H ₂ O
	3 vol pNpp solution
TE buffer	10 mM Tris base
	1 mM EDTA and pH was set to 7.5
Picogreen assay solution	1 vol Picogreen dye
	50 vol TE buffer

2.2.1.8.2.2 Osteogenic Gene Expression Analysis

To study the effect of ions released from HT and BHT hFOBs were seeded on 6 wellplates at 10⁶ cells/well concentration and treated with HT and BHT extracts for 2 weeks, as described in Section 2.2.1.8.2.1 (n=4, duplicate study). At the end of each incubation period, total RNA was isolated in accordance with the supplier's protocol (High Pure mRNA Isolation Kit, Roche, Switzerland) for qPCR study of osteogenic markers such as ALP, OSX, COL1A1, and RUNX2. Quality of isolated

RNA was determined by measuring OD at wavelengths of 260 nm and 280 nm and calculating their ratios (A260/280) which need to be close to 1.8 (Alphaspec, USA). High quality RNAs were then utilized and cDNAs were synthesized (Applied Biosystems PCR System 9700, USA) in accordance with the supplier's protocol (Transcriptor High Fidelity cDNA Kit, Roche, Switzerland). Using SYBR Green RT-PCR Kit, cDNAs were combined with the primers given in Table 2.4, and qPCR was conducted (Roche Lightcycler 480, Switzerland). Amplification reactions were done for 45 cycles, cycle number at detection threshold (C_t) for each sample was determined. β -actin was used as the housekeeping gene to determine cycle threshold (ΔC_t) values for each sample. Relative changes in gene expression of samples were calculated by $2^{-\Delta\Delta C_t}$ method.

Table 2.4 Primers used in osteogenic gene expression analyses. Primers were designed and tested using BLAST (NIH, USA) and Primer3 software.

Gene	Forward Primer (5' – 3')	Reverse Primer (5' – 3')
ALP	ATGGGATGGGTGTCTCCACA	CCACGAAGGGGAAGTTGTC
OSX	TGCTTGAGGAGGAAGTTCAC	AGGTCACTGCCCACAGAGTA
RUNX2	CCCAGTATGAGAGTAGGTGTCC	GGGTAAGACTGGTCATAGGACC
COL1A1	GATTCCTGGACCTAAAGGTGC	AGCCTCTCCATCTTTGCCAGCA
β-Actin	CACCATTGGCAATGAGCGGTTC	AGGTCTTTGCGGATGTCCACGT

2.2.1.8.3 Angiogenic Properties

2.2.1.8.3.1 Tube Formation Analysis

HT and BHT powders (100 mg/mL) were sterilized at 200°C for 2 h and extracts were prepared after 24 h incubation in human umbilical cord vein endothelial cells growth medium (HUVEC-GM). HUVEC-GM was composed of EndoGo XF medium and supplement mix (Sartorius, Germany). Before seeding HUVECs, ice cold growth factor reduced basement membrane matrix (Matrigel, Corning, USA) was pipetted in 96 well plates (50 µL/well) and incubated in a CO₂ incubator for 30 min to gel. Then, HUVECs (passage. 4, 4x10⁴ cells/well) were seeded on Matrigel and they were directly exposed to extracts for 4 h to achieve the maximum rate of tube formation. At the end of incubation period, wellplate lid was removed and microscopic images at 5 different locations were taken to quantify the number of nodes (n=5), total tube length (n=5) and total tube area (n=5) using Angiogenesis Analyzer plugin in ImageJ (NIH, USA). The plugin was written and prepared by Carpentier et al. (2020) and their protocol was employed for determining the aforementioned parameters (Carpentier et al., 2020).

2.2.1.8.3.2 Vascular Endothelial Growth Factor A Release Study

HUVECs were seeded on tissue culture treated 24 wellplates at an initial seeding density of 2.5x10⁵ cells/well and allowed to adhere for 2 h in CO₂ incubator. Afterwards, cells interacted with HT and BHT conditioned media for 4 h (n=3). Media were then collected and stored at 4°C while cells were lysed using ice cold phosphate buffered saline (0.01 M, pH 7.4) and subsequent freeze-thaw cycles. Lysates and media were combined in 1:1 v/v ratio and total VEGF-A production was quantified using a human VEGF-A ELISA kit (Human VEGF-A kit, CSB-E11718h, Cusabio, China). Concurrently, the same setup was used to determine the cellular viability using MTT assay (Sigma, USA). Supplier's protocol was followed and

HUVECs seeded in tissue culture plates served as positive control in both VEGF-A detection and MTT assays. The viability of cells incubated in medium only was assumed 100%. Total VEGF-A release was normalized to the total DNA content of each sample as described in Section 2.2.1.8.2.1. Calibration curve for VEGF-A (n=6, Appendix E1 Figure 1) was drawn by measuring the absorbance of the kit product at 450 nm following the supplier protocol (Human VEGF-A kit, CSB-E11718h, Cusabio, China).

2.2.1.8.4 Immunomodulatory Properties

Immunomodulatory properties of HT and BHT were characterized in the context of inflammatory response and formation rate of pyroptotic inflammasome protein assembly (Tweedell et al., 2020). To determine these properties a human monocyte cell type was utilized. THP-1-ASC-GFP is a variety of human monocyte cell line (THP-1) which can stably express apoptosis associated speck-like protein containing a caspase activation and recruitment domain (ASC) conjugated with a green fluorescent protein (GFP) to monitor inflammasome production (Man & Kanneganti, 2015). For all studies, THP-1s were incubated in a monocyte growth medium (THP-GM, Table 2.5). THP-1s were checked every day and allowed to proliferate until reaching desired cell number. In order to increase viability, cell density exceeding 2 million/mL was not allowed. Whenever this is the case, cell density was adjusted to 0.5 million/mL by dilution.

2.2.1.8.4.1 Inflammasome Response

THP-1s were seeded on 24 wellplates at a density of 0.45 million/mL and stimulated with 50 ng/mL PMA for 24 h. After PMA addition, cells were differentiated into monocyte derived macrophage-like cells (MGMs), and became adherent. Thereafter, they were rinsed twice with phosphate buffered saline (0.01 M, pH 7.4) to completely remove PMA and 1 μ M Nigericin was added to induce inflammasome assembly.

THP-1s that were not exposed to Nigericin were designated as negative control (PMA⁺Nig⁺). Extracts of HT and BHT (100 mg/mL) in an extraction medium (Table 2.5) containing 1 μ M Nigericin was added on cells. THP-1s were incubated with the extracts for 24 h. After incubation, aliquots from each sample (n=6) were collected, centrifuged at 8000 g for 10 min and assayed in CAS-1 ELISA kit (Human CAS-1 kit, Biovision, Sweden). Calibration curve for CAS-1 (n=8, Appendix F1 Figure 1) was drawn by measuring the absorbance of the kit product at 450 nm following the supplier protocol (Human CAS-1 kit, Biovision, Sweden).

Cell viability was determined by Alamar Blue assay. Briefly, media were discarded, cells were rinsed with PBS and Alamar Blue viability agent prepared in monocyte growth medium (10% v/v concentration) was added into the wells. Cells were incubated for 2 h at 37°C, under 5% CO₂ and 95% humidity in the incubator (Panasonic Incusafe, Japan). Afterward, aliquots were collected and optical densities at 570 nm and 600 nm were measured and the viability of THP-1s were calculated using the formula provided by the supplier. Negative control (PMA⁺Nig⁻) was set to 100% and cell viability in the sample groups was normalized accordingly. Experiments were performed in duplicates. In addition, ASC specks were observed using Fluorescent Microscopy (Axio Scope, Zeiss, Germany). Cells were visualized after the collection of aliquots for CAS-1 ELISA kit analysis. Fluorescent microscope images were obtained at 488 nm excitation/ 509 nm emission for GFP conjugated ASC specks for qualitative analysis.

Table 2.5 Media used in immunomodulatory studies (Tweedell, et al., 2020).

Media	Composition
THP-GM	89.4% v/v RPMI 1640
	10% v/v FBS
	0.5% v/v P/S
	0.1% v/v Normocin
Extraction medium	90% v/v RPMI 1640
	10% v/v FBS

2.2.1.8.4.2 Inflammatory Response

THP-1s were used in macrophage response analysis towards HT and BHT extracts to elaborate the secretion trend of pro-inflammatory and pro-healing proteins. Intracellular NOS was selected as the marker enzyme for pro-inflammatory enzyme and IL-10 was selected as the pro-healing cytokine (Yang et al., 2019). Initially, THP-1s were primed with PMA, and activated with 150 ng/mL LPS (from *Escherichia coli* O55:B5, Sigma, USA). Cells that were not activated with LPS were designated as the negative control. Similar to that of the inflammasome study, HT and BHT release products (100 mg/mL) were added in addition to 150 ng/mL LPS prior to incubation with THP-1s. At the end of incubation, aliquots were collected and assayed for IL-10 secretion (n=6) using a human IL-10 ELISA kit (Human IL-10 kit, CSB-E04593h, Cusabio, China). After that, media were removed, sterile PBS were added into the wells and placed in -80°C freezer (DF490, Nuve, Turkey). After one freeze-thaw cycle, cells were lysed, aliquots were collected and iNOS assay was conducted (n=6) using human iNOS ELISA kit (Human iNOS kit, E4648-100, Biovision, Switzerland). Cellular viability during iNOS and IL-10 assays was also determined by Alamar Blue assay as explained previously. Calibration curves for IL-10 (n=8, Appendix G1 Figure 1) and iNOS (n=8, Appendix H1 Figure 1) were drawn by measuring the absorbance of the kit product at 450 nm following the supplier protocol.

2.2.2 Grafting and Optimization of Aminosilane on Ti-6Al-4V

Medical grade V Ti-6Al-4V ELI implants having 2 cm x 2 cm x 1 cm dimensions were initially sandblasted (SB) in SiC containing drum for 1 day and after SB, rinsed in dH₂O, EtOH (99% v/v) and sonicated in acetone. Implants were then air-dried under chemical hood. Ti-6Al-4V were placed in sulfuric acid: hydrogen peroxide (3 part H₂SO₄: 7 part H₂O₂) for 15 min at room temperature. Then, they were rinsed

with dH₂O and placed in 5 M NaOH for 1 h at 60°C. At the end of etching (Ti-APA), they were rinsed with EtOH and stored in desiccator until use.

APTES, is a silanization agent that bears a primary amine group opposite to siloxane units allowing the formation of an amide bond in the presence of carboxyl groups. Triethoxysilane subunit that forms a covalent bond on metallic surfaces through silanol formation upon hydrolysis (Figure 2.1). In this study, surface modified Ti-6Al-4V was used since it is thought that surface would be made labile to covalent bonding which forms Ti-O-Si-O bonding.

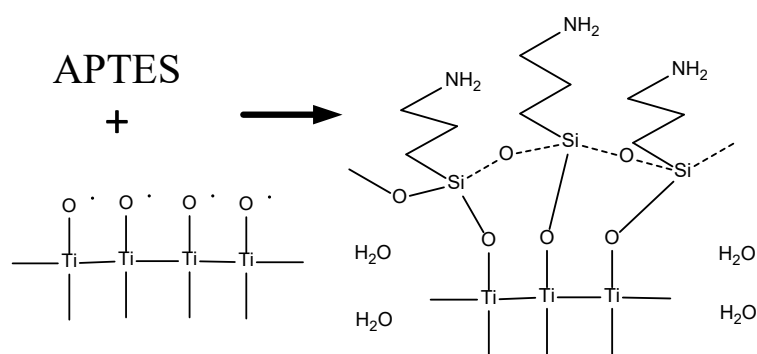


Figure 2.1 APTES activation of Ti-OH on Ti-6Al-4V implants.

APTES coating procedure was optimized according to the following criteria: miscible medium for APTES dissolution, APTES concentration, coating period and curing temperature. In order to overrule the effect of pH on APTES hydrolysis, APTES (2% v/v) was dispersed in dH₂O and pH was set to alkaline pH (12.00) by 1 M NaOH, to acidic pH (3.00) by 1 M HCL and kept at neutral pH in dH₂O in separate beakers. The solutions were observed for 15 min. It was detected that alkaline and acidic pH led to white precipitates showing fast hydrolysis (<1 min) of APTES molecule. Therefore, optimization studies were conducted at neutral pH to have more control over APTES hydrolysis.

The optimal APTES medium was determined using methanol, ethanol, toluene and dH₂O. Toluene is one of the highly used organic solvents in coating studies due to

high boiling point and expels water effectively (Godoy-Gallardo et al., 2015). However, toluene slows the reaction rate down so that APTES coating procedure generally takes place at a high temperature ($>100^{\circ}\text{C}$) for an extended period (24 h) (Goonasekera et al., 2013). Moreover, it was observed that vaporized toluene during the coating procedure allowed a thin film of APTES to form over Ti-6Al-4V implants that were not completely adhered to the surface. Consequently, toluene was opted out of optimization studies. The other solvents were combined along with water are given in Table 2.6. Because APTES hydrolysis occurs in an aqueous environment and the byproduct is ethanol, two simple alcohols in a homogeneous blend with dH_2O were selected. Namely, Methanol: dH_2O (25 MD, 1:3 v/v), Methanol: dH_2O (75MD, 3:1 v/v) (Marques et al., 2013) and Ethanol: dH_2O (95ED, 95:5 v/v) (Sridar et al., 2017) were the media used in optimization studies.

The best medium, the concentration of APTES, period of coating and curing temperature after coating were determined by evaluating the results of XPS (Phi 5000 VersaProbe, USA) and primary amine quantitation by TNBSS treatment.

2.2.2.1 XPS Analysis

APTES coated Ti-6Al-4V samples (Ti-APTES) ($n=3$) were scanned under monochromatic Al- $\text{K}\alpha$ X-Ray (METU Central Laboratory, PHI 5000 VersaProbe, USA). Survey spectra were collected over 200 μm linear line with an incident angle of 45° having 188 eV and regional spectra were obtained over 200 μm linear line with an incident angle of 45° having 54 eV. C1s peaks at 283 eV obtained on uncoated Ti-6Al-4V were assumed as adventitious carbon peaks and all spectra were normalized according to C1s.

2.2.2.2 TNBS Analysis

Ti-APTES samples ($n=3$) were placed in 3% (w/v) sodium borate buffer containing 0.2% (w/v) TNBSS and incubated for 30 min at 70°C . Yellow color of TNBSS

changes into orange color in direct correlation with the concentration of active primary amine. Then, 200 μ L aliquots were collected from each sample and OD₄₁₀ was measured using a microplate reader. Also, the samples were removed, rinsed with borate buffer, dried in oven at 70°C for 30 min and their photos were taken using a conventional camera. APTES coated samples were stained in yellow and non-stained samples appeared metallic gray. All studies were conducted in triplicates.

Table 2.6 Parameters tested and optimized for APTES coating.

Analysis	APTES Concentration (v/v%)	Media	Coating Period	Curing Temperature (°C)
Media	2	25MD	15 min	80°C
	2	75MD	15 min	80°C
	2	95ED	15 min	80°C
APTES Concentration	0.2	25MD	15 min	80°C
	0.4	25MD	15 min	80°C
	0.8	25MD	15 min	80°C
	2	25MD	15 min	80°C
	4	25MD	15 min	80°C
	8	25MD	15 min	80°C
Period of Coating	2	25MD	Dip Coating	80°C
	2	25MD	15 min	80°C
Curing Temperature	2	25MD	15 min	Air-Dry
	2	25MD	15 min	80°C
	2	25MD	15 min	120°C

2.2.3 Fabrication of Alginate/Gelatin Coating on APTES Grafted Ti-6Al-4V and Optimization Studies

In order to covalently attach A/G blend on Ti-APTES, a two-step coating procedure with a slightly modified EDC/NHS method was utilized. Briefly, ALG and GEL in various concentrations (Table 2.7) were dissolved in dH₂O at 45°C under 500 rpm stirring for 1 h and 0.2 M NaCl was also added to A/G solution to decrease the viscosity of ALG solution. Then, NHS was added at a final concentration of 20 mM in the pre-gel, vigorously stirred for 15 min prior to coating. After A/G/NaCl/NHS pre-gel was formed, Ti-APTES was dipped fast (100 mm/s) into the pre-gel to break the surface tension, kept in the pre-gel for 1 min and very slowly taken out (20 mm/s) to prevent coated layer from sloughing off at the interface. Coated samples were dried at 35°C for 30 min and placed in 20 mM EDC/NHS/CaCl₂ crosslinking solution overnight. Afterward, they were rinsed 5 times thoroughly with dH₂O before freeze-dried at -80°C for 24 h. Rheological analysis of the pre-gels, and morphological, physical, mechanical and biological analyses of the coatings were conducted to determine the most suitable A/G concentration for further studies.

Table 2.7 Concentration of A/G coating components.

Coating	Alginate (w/v%)	Gelatin (w/v%)	NaCl/NHS (mM)
Ti-APA ^a	0	0	0
A/G 1:1	1	1	200 / 20
A/G 1:2	1	2	200 / 20
A/G 1:3	1	3	200 / 20
A/G 1.5:1	1.5	1	200 / 20
A/G 1.5:2	1.5	2	200 / 20
A/G 1.5:3	1.5	3	200 / 20

^a APA stands for acid:peroxide:alkali etching process on Ti-6Al-4V. This universal procedure was employed on Ti-6Al-4V implants before APTES grafting and coating processes.

The reaction scheme proposed is presented in Figure 2.2. Preliminary findings suggested that NaCl and NHS should be present in the pre-gel before settling in order to achieve homogeneous crosslinking without loss of the material and to protect hydrogel topography.

2.2.3.2 Morphology Analysis

Samples were coated with 3 nm gold/palladium (Au/Pd) and their morphologies were observed with Scanning Electron Microscopy under high vacuum (METU Central Laboratory, SEM, FEI Quanta 400F, ABD). In addition, macroscopic images of the dried and wetted samples were taken. Representative samples were colored with 0.5% (w/v) methylene blue, scratched using a spatula to ensure strong adhesion at the interface, and photographed using a conventional camera.

2.2.3.3 Water Uptake and Hydrolytic Degradation

Water uptake (n=4) and hydrolytic degradation (n=4) analyses were performed for all A/G samples. Dry samples were weighed (w_{D1}), immersed in excessive PBS with 0.02% NaN_3 , and shaken at 100 rpm for 0.25, 1, 6, 24 and 48 h at 37°C in a water bath (ST-30 Water Bath, Nüve, Turkey). At the predetermined time periods collected samples were slowly tapped on a filter paper to remove PBS droplets and their wet weights were recorded (w_w). Then, water uptake ratios (%) were calculated according to the Equation 1:

$$\text{Water Uptake (\%)} = \frac{w_w - w_{D1}}{w_{D1}} * 100\% \quad (1)$$

In addition, samples placed in PBS with NaN_3 were also incubated for 1-4 weeks under the same conditions mentioned above. At the end of each week, samples were removed, freeze-dried weights were recorded (w_{Di}), and weight loss was calculated according to Equation 2:

$$\text{Weight Loss (\%)} = \frac{w_{D1} - w_{Di}}{w_{D1}} * 100\% \quad (2)$$

2.2.3.4 Qualitative Adhesion Test

Adhesion test was employed at the end of each week during degradation analysis to test whether coatings were still attached firmly on the implants or not. This type of cross-testing is unique to this study, and applied to affirm reproducibility of each step. Simply, randomly selected sample from each group analyzed in the degradation study was thoroughly rinsed with dH₂O, and ultrasonicated in bath for 15 min at 35 kHz at room temperature to determine the effect of physical stress. Then, samples were placed in 0.2 M NaCl for 24 h and rinsed 3 times with 70% (v/v) EtOH:dH₂O to observe ionic and chemical stress on the coatings. Macroscopic images were taken and coatings were manually tested before moving on to the next incubation period. A/G coatings on Ti-SB and Ti-APA were also analyzed along with Ti-APTES to compare the positive influence of silanized surface.

2.2.3.5 Microscratch Analysis

2.2.3.5.1 Scratch Test for As-is Coatings

In order to determine the adhesion strength and evaluate scratching feature of the coating on the surface, a conical diamond indenter with a radius of 100 μm was employed at 90° to penetrate the coating (METU Central Laboratory, CSM Instruments, Nano-Micro Indentation Tester, Austria). Progressive scratching was applied at constant rate of 4.95 N/min starting from 50 mN to final 5 N. Normal (F_N) and frictional forces (F_T) of each coating was determined ($n=3$). The thickness of coating was determined by measuring penetration depth (PD) at the final point of scratch test. Critical load (L_c) was determined by visually observing coating fail event by SEM, measuring the scratch distance and detecting concomitant F_T given by the testing device.

2.2.3.5.2 Scratch Test to Determine Shelf-Life

Abovementioned studies were conducted prior to shelf-life analysis. Similar to the case with BHT (which is actually 5BHT), A/G 1:3 coatings were determined to be superior to its counterparts. **Therefore, A/G 1:3 (denoted as A/G throughout the manuscript) samples stored at room temperature (25°C) for 4, 8 and 12 months were analyzed for the change of adhesion strength using microscratch tester.**

Same scratch test was employed as described in Section 2.2.3.5.1.

2.2.3.6 Cell Viability Assay

All samples were sterilized by applying UV irradiation for 1 h on both sides. Then, samples were wetted in hFOB-GM. hFOBs were seeded on samples in 100 μ L at a seeding density of 2×10^4 cells/sample and incubated for 1 h ($n=8$). Then, samples were thoroughly rinsed with sterile filtered PBS to discard unattached cells and placed in hFOB-GM. After that, hFOB were incubated on samples for 1, 4 and 7 days. At the end of incubation periods, media were discarded, samples were rinsed with PBS once, Alamar Blue assay was conducted for 2 h. Thereafter, aliquots were collected and OD₅₇₀ and OD₆₀₀ were measured and similar protocol given in Section 2.2.1.8.1 was followed. Cells seeded on Ti-APA were used as the control.

In addition, at the end of 1st and 7th days of incubation, implants were rinsed with 0.01 M PBS and fixed in 2.5% (v/v) glutaraldehyde. Cells were then stained with (1000 times diluted) Alexa Fluor 488 and (300 times diluted) DRAQ5 according to supplier's protocol (Thermo, USA), and cell morphology on samples was analyzed using CLSM (Leica Olympus, Germany). After that, samples were rinsed with 0.1 M cacodylate in dH₂O (pH 7.2) and freeze-dried for 6 h. Completely dried samples were coated with Au and qualitatively analyzed using SEM.

2.2.4 Fabrication of A/G/BHT Coating on Ti-APTES and Optimization Studies

In this part, implants were coated with a slightly modified method in comparison to bare A/G coatings. The steps given above for a Ti-APTES coating were followed. However, prior to dip-coating with A/G/BHT combinations, implants were initially coated with an 0.25% (w/w) alginate dissolved in pH 5.00 dH₂O (pH was controlled with 10% acetic acid in water) along with 20 mM EDC/NHS mixture. This step was adopted in order to prevent sliding of BHT particles from the surface. Because of sliding at the periphery of the implant, immature particle release could cause unexpected immunological problems such as extensive neutrophil activity around the implanted area in addition to potentially uneven coating thickness. For these reasons, a thin coating of alginate covalently bonded to the implant surface before actual composite layer was applied to provide better control over coating drainage, coating thickness, degradation, swelling which could also prevent delamination especially on the cylindrical implants.

The groups produced for composite coating studies are given in Table 2.8. It is also stressed that composite coatings with 20% (w/w) BHT were also produced. However, delamination was observed after preliminary adhesion strength tests. Briefly, freeze-dried coatings were subjected to 70% ethanol in dH₂O for 2 h, rinsed and placed in 200 mM NaCl in dH₂O and ultrasonicated for 15 min, and then finally placed in PBS for 1 day. After these steps, delaminated A/G/20BHT samples were photographed (Figure 2.3).



Figure 2.3 Image of A/G/20BHT after adhesion strength test.

Table 2.8 Concentration of the components employed in the composite coatings.

Coating	BHT (w/w%)	Theoretical Weight in the Final Coating (w/w%)
A/G	0	48
A/G/5BHT	5	65
A/G/10BHT	10	79

2.2.4.1 Rheological and Thermogravimetric Analyses

Similar to the procedure described in Section 2.2.3.1 A/G and A/G/BHT samples were tested for rheological properties. Thermogravimetric analysis (TGA) was conducted up to 900°C with heating a rate of 10°C/min (METU Central Laboratory, Setaram Labsys, France). The heating chamber was purged with nitrogen flow during the analysis. Since decomposition temperatures of BHT was drastically higher than the limit of heating, the total amount of BHT was determined for each sample (n=3).

2.2.4.2 Morphological Analysis

Ti-APA, A/G and A/G/BHT samples were coated with 3 nm Au/Pd and their surface morphologies were observed with SEM examination. Sample macroscopic images were captured with the help of a conventional camera.

2.2.4.3 Water Uptake and Hydrolytic Degradation Analysis

A/G and A/G/BHT samples were tested using same procedure given in Section 2.2.3.3 to determine water uptake and hydrolytic degradation properties.

2.2.4.4 Microscratch Analysis

A/G and A/G/BHT samples were tested using same procedure given in Section 2.2.3.3 to determine microscratch strength.

Owing to great structural performance, good physical and chemical properties, and high mechanical strength, A/G/10BHT was selected as the representative group for BHTs composited with A/G. From this point on, A/G/10BHT is abbreviated as A/G/BHT.

2.2.4.5 Shelf-Life Analysis

2.2.4.6 *In vitro* Cell Culture Studies

2.2.4.6.1 hFOB Proliferation and Morphology Analysis

In order to determine the effect of coatings on morphology and proliferation of hFOB Alamar blue analysis was conducted. Ti-APA, A/G and A/G/BHT were pre-conditioned with hFOB-GM for 1 h to allow hydrogel swelling approximately half of the maximum value (~300%). Swollen samples (Ti-APA was used as the positive control) were seeded with hFOB at a density of 2×10^4 /sample density and incubated for 1, 4 and 7 days (n=6, duplicate study). At the end of each period, samples were rinsed with PBS, Alamar Blue protocol was employed for 4 h. A similar protocol given in 2.2.1.8.1 was followed.

Morphology of the cells interacted with coatings was analyzed. Samples after 1st day and 7th day of incubation was rinsed thoroughly with sterile PBS and fixed with 4% (w/v) PFA. Then, hFOB on Ti-APA, A/G and A/G/BHT samples was permeabilized with 0.1% Triton X-100 in PBS, and stained with Alexa Fluor 488 for actin fibers and DRAQ5 for intact DNA in nucleus. Samples were be visualized in a CLSM (BIOMATEN, Leica DM2500, Germany).

In addition, at the end of 1st and 7th days, randomly selected samples were fixed with 4% PFA and rinsed with 0.2 M cacodylate buffer (CacoB). Samples were then freeze-dried for 4 h and observed under SEM.

2.2.4.6.2 Osteogenic Response

2.2.4.6.2.1 ALP Activity Assay

Coatings were seeded with hFOB cells in 2×10^5 cell density, incubated for 1 day to allow complete cell attachment (n=6, duplicate study). hFOB-OM were added to the wells. Every two days, media were refreshed. At the end of each week, sample media were discarded, rinsed with calcium and magnesium free PBS. Afterwards, 0.1% (v/v) Triton X-100 in CB was introduced and a single step freeze-thaw (-80°C and 25°C) was employed to cell to facilitate lysis. Then, same procedure given in Section 2.2.1.8.1 was followed.

2.2.4.6.2.2 Osteocalcin Release Assay

A similar protocol with ALP activity assay was followed (n=3, duplicate study). Briefly, 2×10^5 hFOB cells were seeded on samples and incubated in osteogenic differentiation medium for 2 weeks. At the end of each week, sample media were collected and enzyme linked immunosorbent assay was used to quantify the amount of OCN in accordance with the protocol given by supplier (Human OCN ELISA kit, E4762, Biovision, USA). Then, samples were rinsed with PBS and Picogreen assay was conducted to determine the amount of DNA in the aliquots. OCN release data were normalized to total DNA for each sample. A similar protocol given in Section 2.2.1.8.2.1 was followed.

2.2.4.6.2.3 Osteogenic Gene Expression Analysis

Osteogenic gene expression of hFOB cells in response to coatings was quantified by qPCR (n=3, duplicate). Primers used in the study are given in Table 2.9. Similar protocol to ALP activity assay was followed. At the end of each week, samples were collected, rinsed with PBS and total RNA isolation was conducted following a similar protocol given in Section 2.2.1.8.2.2. Amplification reactions were done for 45 cycles, cycle number at detection threshold for each sample was determined. β -actin was designated as the housekeeping gene to determine cycle threshold (ΔC_t) values for each sample. Relative change in gene expression of samples was calculated by $2^{-\Delta\Delta C_t}$ method.

Table 2.9 Primers used in osteogenic, angiogenic and immunomodulatory gene expression analyses.

Gene	Primer	Sequence (5' – 3')
ALP	Forward	ATGGGATGGGTGTCTCCACA
	Reverse	CCACGAAGGGGAAGTTCAC
OSX	Forward	TGCTTGAGGAGGAAGTTCAC
	Reverse	AGGTCAGTACCCACAGAGTA
RUNX2	Forward	CCCAGTATGAGAGTAGGTGTCC
	Reverse	GGGTAAGACTGGTCATAGGACC
OCN	Forward	CGCTACCTGTATCAATGGCTGG
	Reverse	CTCCTGAAAGCCGATGTGGTCA
BMP-2	Forward	CTAAGGAGGACGACAGCACC
	Reverse	AAGAAGTCCCCAGCCAAGTG
Smad4	Forward	CATCCTGCTCCTGAGTATTGG
	Reverse	GGGTCCACGTATCCATCAAC

Table 2.9 (cont'd) Primers used in osteogenic, angiogenic and immunomodulatory gene expression analyses.

Caspase-1	Forward	GCTGAGGTTGACATCACAGGCA
	Reverse	TGTCTGTCAGAGGTCTTGCTC
NfκB	Forward	GCAGCACTACTTCTTGACCACC
	Reverse	TCTGCTCCTGAGCATTGACGTC
IL-1β	Forward	CCACAGACCTTCCAGGAGAATG
	Reverse	GTGCAGTTCAGTGATCGTACAGG
IL-10	Forward	CATCAAGGCGCATGTGAACTC
	Reverse	AATCGATGACAGCGCCGTAG
iNOS	Forward	GCTCTACACCTCCAATGTGACC
	Reverse	CTGCCGAGATTTGAGCCTCATG
β-Actin	Forward	TGGAGCAATTACGGGGTGAC
	Reverse	GCGCTAGATGACACCCTCTC

2.2.4.6.3 Angiogenic Response

2.2.4.6.3.1 HUVEC Proliferation and Morphology Analysis

Samples were seeded with HUVEC cells at a density of 2.5×10^5 and placed in HUVEC-GM media to induce HUVEC colonization and growth. HUVECs were incubated on samples for 1, 4 and 7 days (n=4). At the end of each period, media were discarded and Alamar Blue assay was conducted to determine the rate of cell proliferation following the supplier's protocol (Thermo Fisher, USA). In addition, samples were collected at day 4 (preliminary studies indicated that 4th day of incubation is best for angiogenic potential analysis), rinsed thoroughly with PBS supplemented with Ca^{2+} and Mg^{2+} (PBS/Ca/Mg), and fixed with 4% paraformaldehyde prepared in PBS/Ca/Mg for 15 min at room temperature. Preliminary studies showed that PBS must be added with calcium and magnesium

sources to prevent transcellular attachment proteins for breaking the interaction between HUVEC and hydrogel by overflowing with mediator ions). Randomly selected samples (n=2) were further rinsed with Ca/Mg supplemented 0.2 M cacodylate buffer, dried in freeze-dryer for 4 h, and coated with Au/Pd and analyzed under SEM (FEI Quanta 650, USA). Randomly selected other samples (n=2) were stained with phalloidin-FITC to visualize actin filaments and DRAQ5 to observe nuclei, so that overall HUVEC morphology and colonization were determined with CLSM (Leica DM2500, Germany).

2.2.4.6.3.2 VEGF-A Release Assay

HUVECs were seeded on Ti-APA, A/G and A/G/BHT samples at an initial seeding density of 2.5×10^5 cells/well and allowed to adhere for 2 h in CO₂ incubator (n=5). Same protocol in Section 2.2.1.8.3.2 was followed. VEGF-A collected from lysates and from media after release were quantified together as total VEGF-A.

2.2.4.6.4 Immunomodulatory Response

Samples were seeded with THP-1s at a density of 5×10^5 cells/mL. Then, same protocol given in Section 2.2.1.8.4.2 was followed. After 24 h treatment, media were collected, and released CAS-1 and IL-10 from LPS treated samples were quantified using either human CAS-1 ELISA kit (E4588, Biovision, USA) or human IL-10 ELISA kit (CSB-E04593h, Cusabio, China). Then, a similar setup was used to determine cellular viability on samples with Alamar Blue study (n=6) and total DNA was quantified (n=3). Total CAS-1 released and total IL-10 were normalized to total DNA content. In addition, randomly selected non-treated samples and LPS treated samples (n=2) were collected, rinsed thoroughly with sterile PBS, fixed with 4% (w/v) PFA and visualized with SEM and CLSM. Following quantification of CAS-1 and IL-10 in the media, samples were tested for relative gene expression of CAS-1, IL-10, iNOS, NfκB and IL-1β.

2.2.4.7 *In vivo* Study

In vivo studies were approved by Ethics Committee of Afyon Kocatepe University Experimental Animal Application and Research Center (Date: 18.09.2018, Decision: 49533702/147). The prepared implants (cylindrical implants with 5 mm length and 2.5 mm diameter) were sterilized under UV irradiation. Rabbits were housed in normal conditions, they were allowed to freely move, eat and drink ad libitum. Prior to operation, knee and femur were shaved and antiseptic conditions were ensured. General anesthetic 35 mg/kg ketamine hydrochloride and 5 mg/kg xylazine lidocaine were applied. Medial parapatellar longitudinal articulation incision was applied and patella medial osteochondral zone was drilled (600-700 rpm) under continuous PBS irrigation to create 5 mm cylindrical defect. Ti-APA, A/G and A/G/BHT implants (n=4) were placed into the defects. Incision zone was stitched with Vicryl 4.0 and covered with a soft bandage. In order to prevent post-operational pain, rabbits were injected with Flunixin meglumine (Fynadine, Netherlands). Additionally, enrofloxacin was applied against possible operational infections (Bayer, Germany). At the end of 1st and 2nd months post-operation, high dose muscle relaxant was given to the rabbits to induce euthanasia. Then, femur segments were collected, placed in formaldehyde solution (10% v/v in dH₂O) for initial fixation. Harvested femurs placed in 4% (v/v) paraformaldehyde solution supplemented with glutaraldehyde having a final concentration of 0.1% (v/v) for 3 days. Samples were then placed under X-Ray device (TOP-X HF, Innomed, USA) and images were obtained at 45 kV and 10 mA/s to make sure implant place. Afterwards, samples were placed again in fixative solution for additional 7 days prior to embedding in a methacrylate resin.

2.2.4.7.1 Preparation of Sections with Intact Implant-Bone Interface

Fixed bone samples were placed in graded glycol methacrylate in dH₂O (GMA/W). Initially, samples were treated with GMA/W in 50% (v/v) for 3 h, 70% GMA/W (v/v) for 3 h, 96% GMA/W (v/v) for 3 h and finally in 100% GMA for 6 h. Fully

soaked in GMA, samples were treated with Technovit 7200/GMA mixture in 1:1 ratio for 4 h and embedded in 100% Technovit 7200 for 36 h (Technovit 7200, Kulzer, Germany). Resin was crosslinked under UV light for 24 h. This resin provided a strong bonding within bone tissue as well as preventing heat development and separation of implant from organic tissue. Embedded in the resin, implant-bone samples were produced with precision cutting (Exakt Cutting Mill, Germany) and grinding (Exakt Micro Grinding Machine, Germany). Sections from the samples (~30 µm) were taken in the longitudinal axis from osteochondral location.

2.2.4.7.2 Masson-Goldner Trichrome Staining

Non-decalcified implant-bone sections were stained with Masson-Goldner Trichrome stains using supplier's protocol (Sigma, 1.00485.001, USA). Sections were deparaffinized with xylene, partially hydrated with reverse ethanol series (absolute to 50% in dH₂O) and fully rehydrated with dH₂O. Samples were kept in Weigert's iron hematoxylin for 5 min to dye nuclei of cells. Following rinsing under running tap water, samples were incubated in 1% (v/v) acetic acid for 30 s, placed in azofloxin for 10 min and again placed in 1% (v/v) acetic acid solution in dH₂O for 30 s. Samples were then stained with tungstophosphoric acid-Orange G solution for 1 min, rinsed in 1% acetic acid solution, subsequently stained with light green SF solution and rinsed with 1% acetic acid for 30 s to remove unbound dyes. Afterwards, samples were dehydrated in ethanol series (50% in water to absolute grade). Ethanol was removed using xylene and embedded in Entellan mounting medium (Merck, USA). Stained samples were analyzed with a light microscope (Olympus BX50) and photographed (Olympus DP25). Histochemical staining was expected to produce following results: Cell nuclei are to be stained with dark brown, muscle fibers and myocyte cytoplasm to be red, erythrocytes to be bright orange, fibrous tissue to be red/pinkish and acidic mucosal structures to be green. In addition, obtained sections were quantified using a method previously shown elsewhere (Otsuki et al., 2006).

2.2.4.7.3 Decalcification prior to immunohistochemical staining

In order to prevent loss of cellular markers, samples were placed in 15% (w/v) ethylenediamine acetic acid (EDTA, pH 7.2) in dH₂O for 21 days (n=4). Every 3 days, EDTA solution was refreshed. After incubation, samples were checked manually to observe increased elasticity, which showed absence of Ca. Furthermore, samples were analyzed using X-Ray to verify complete removal of Ca (Figure 3.36). Decalcified sections were fully rehydrated, and 10 mM Cu(II)SO₄ in 50 mM NH₄Cl at pH 5 was applied 3 times for 5 min to mitigate autofluorescence. Afterwards, sections were incubated in 0.5% v/v Triton X-100 for 10 min at 37°C to retrieve antigens. Sections were also kept in 3% v/v ImmPress HRP large spectrum kit (MP-7500, Vector Labs, USA) for endogeneous peroxidase blocking for 10 min, rinsed with PBS and blocked in horse serum provided with the kit. These sections were dropped on a small amount of anti-OCN antibody solution (mouse monoclonal antibody OCG4, Abcam, UK) and incubated for 30 min. To develop staining, sections were rinsed and incubated with 3,3'-di-aminobenzidine (DAB) (SK-4100 DAB, Vector Labs, USA), and followed for 3 min under light microscope until characteristic brownish color formed. After that, sections were thoroughly rinsed and counterstained with Harris' hematoxylin, rinsed with ethanol and xylol, and covered with Entellan (Sigma, USA). Samples were visualized under light microscope (Zeiss Axio Observer Z.1 attached with Olympus DP25).

2.2.5 Statistical analysis

All data are given as average \pm standard deviation and were tested for normality using Shapiro-Wilk normality test. Statistical differences among groups were determined by One-Way ANOVA employing Tukey's Post Hoc test (* $p < 0.05$, ** $p < 0.01$, *** $p < 0.001$). Results of all TGA, qPCR and ELISA assays data were analyzed in pairs by independent pairwise two-tailed t-test. Semi-quantitative

scoring for *in vivo* studies was tested for statistical difference using Kruskal-Wallis test.

CHAPTER 3

RESULTS and DISCUSSION

3.1 Characterization and Optimization of BHTs

SEM electrographs of the HT and BHT samples are presented in Figure 3.1. Assuming spherical morphology for all particles, volume mean diameter ($d[4,3]$) was calculated and found to be around $30\text{ }\mu\text{m}$ which was not significantly different among groups (Table 3.1). Moreover, close-up SEM analysis on the powders revealed grain boundaries and provided a qualitative visual for effective surface area (Figure 3.1). It can be noted that particle area of B doped groups appeared to be higher than that of HT, and 10BHT had a more compact structure similar to that of HT. On the other hand, 2BHT, 3BHT and 5BHT displayed fine grains, and 5BHT appeared to have a large surface area. In addition, HT and 10BHT samples showed similar morphologies with larger grains than other B doped counterparts in the pellet form. In detail, HT and 1BHT had an average grain size of $1.92\text{ }\mu\text{m}$ and as $1.59\text{ }\mu\text{m}$, respectively while 2BHT and 3BHT displayed finer grains with a grain size of $0.74\text{ }\mu\text{m}$ and $0.53\text{ }\mu\text{m}$, respectively. Concurrently, 5BHT exhibited significantly ($p<0.05$) the smallest grain size ($0.21 \pm 0.06\text{ }\mu\text{m}$) and 10BHT appeared much coarser with a grain size of $0.84 \pm 0.26\text{ }\mu\text{m}$. Consequently, it can be said that B doping has a limiting condition by which B incorporation results in a fine and ordered grain structure with a highly uniform size distribution thus granting a control over the final product up to a certain dopant concentration (5%).

BET and BJH analyses were conducted to characterize TSA and mesoporosity of B doped HT. It was observed that 5BHT and 10BHT possessed statistically higher TSA than other groups and the highest mesoporosity was acquired for 10BHT (Table 3.1). Wang et al. (2007) conducted BET analysis for differentially sintered HA, and reported that mass transport phenomenon affected growth of the crystallite size and

TSA (Wang et al., 2008). In this study, B was shown to impact sinterability thus improving crystallization by temperature treatment and limiting crystallite growth in the meantime.

Table 3.1 SSA and mesopore volume, and grain sizes of BHT samples detected with BET analysis (n=3) and SEM analysis (n=50).

Sample	d[4,3] (μm)	TSA (m ² /g)	Mesopore Volume (μL/g)	Grain Size (μm)
HT	35.21 ± 1.82	1.36 ± 1.06	6.84 ± 1.73	1.92 ± 0.65
1BHT	28.21 ± 4.71	3.07 ± 0.71 ^a	15.70 ± 7.33	1.59 ± 0.67
2BHT	34.70 ± 0.68	3.57 ± 1.63	13.50 ± 3.69 ^a	0.74 ± 0.30
3BHT	31.68 ± 4.82	2.71 ± 0.18 ^a	13.60 ± 2.89 ^a	0.53 ± 0.11
5BHT	24.84 ± 4.54	3.04 ± 0.52 ^a	16.7 ± 7.40 ^a	0.21 ± 0.06 ^b
10BHT	30.63 ± 3.86	3.44 ± 1.2 ^a	23.90 ± 7.92 ^a	0.84 ± 0.26

^a Statistically higher than HT (p<0.05).

^b Statistically the smallest value (p<0.001).

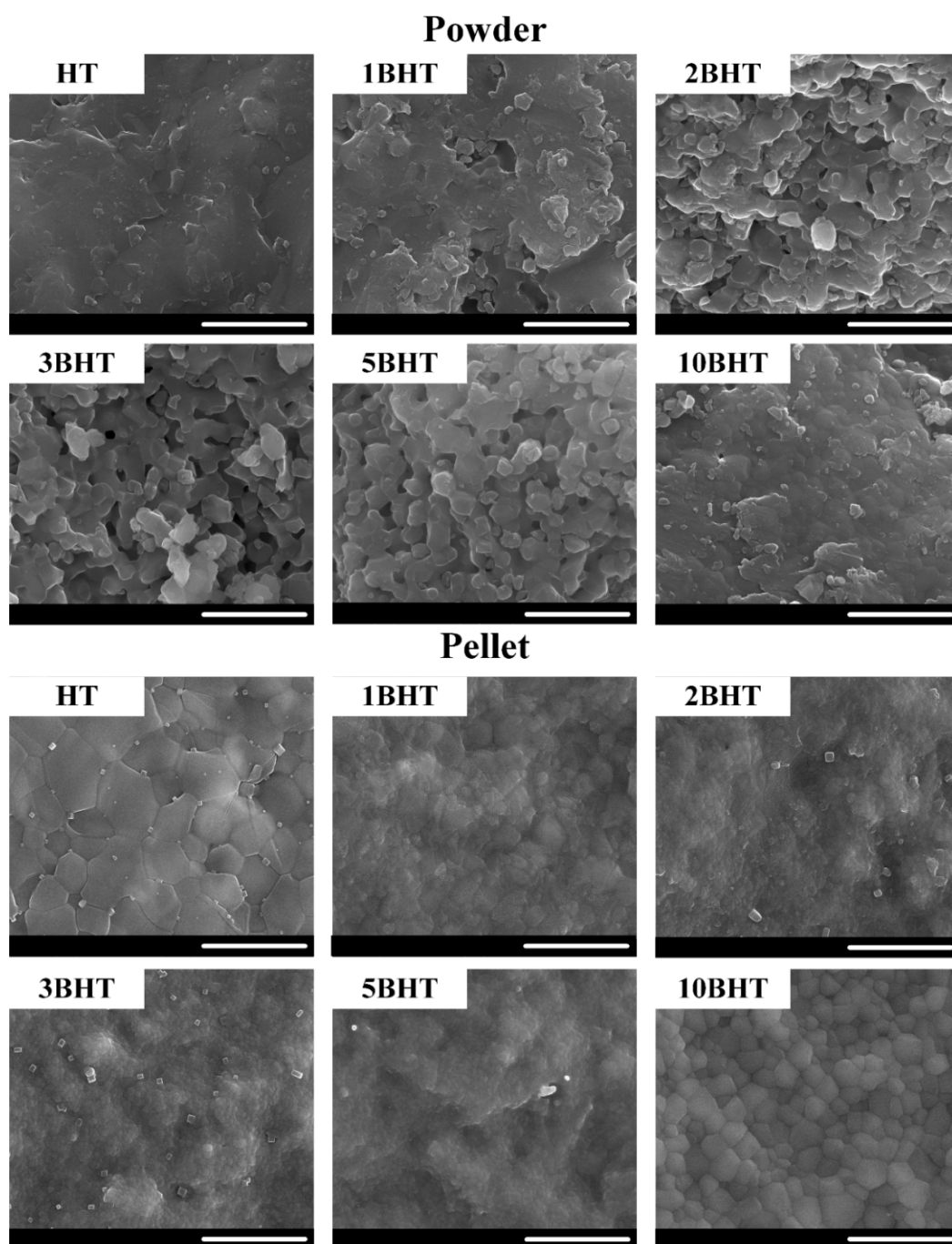


Figure 3.1 SEM electrographs of BHT samples in disc form. Scale bar is 5 μ m.

Employing the method of microwave reflux at 800 W for 15 min in a single run and utilizing only one sintering temperature and pH (1100°C for 2h, pH 10), we designated B concentration as the sole parameter that allowed us to determine the efficiency of B doping and overall effect of B on the microstructural characteristics of HT. According to XRD patterns presented in Figure 3.2A, all samples showed HA characteristic reflections (Li et al., 2014), namely (002), (211), (112) and (300) and unique β -TCP reflection (0210), except for 10BHT. Focusing on the peaks at 2θ of 30.72° for (0210) and 32.20° for (211), HT was found to have the lowest intensities for all reflections and maintained 86.3% HA and 13.7% β -TCP phases (**Table 3.2**). It was further observed that B incorporation brought about an increase in $I(211)$ while a steep decrease in $I(0210)$. β -TCP (0210) reflection was diminished in successive B additions and completely lost at 10BHT. HT and 1BHT were determined to have similar HA phase concentrations and it was found to be significantly small when compared with other BHTs. Moreover, a distinct (002) reflection was utilized to determine the crystallinity percentage (X_c) of HT and it was found as $89.03 \pm 4.65\%$. In the case of BHTs, the peaks shifted in direct correlation with B content in samples in addition to the altered intensities (Figure 3.2B). Especially HA related reflections were shifted to lower 2θ degrees, which indicated that B was incorporated in the lattice via B-type substitution (Madupalli et al., 2017). $V_{112/300}$ value showing the hollow between (112) and (300) reflections was gradually shifted to a smaller distance in BHTs (Figure 3.2B). Moreover, (211) and (002) peaks attained greatest intensities for 5BHT. When calculated, 5BHT was found to have the highest X_c ($95.77 \pm 2.08\%$). However, no significant difference was detected among groups (Table 3.2). The increase in X_c towards 5BHT could be a result of slight distortion in the structure (Mansour et al., 2017). Since the sinterability depends also on diffusion in the solid crystal, expanded lattice up to a threshold level could provide a faster maturation. Thus, an increment in the X_c was observed.

In FTIR study (Figure 3.2B), peaks at 472 cm^{-1} , 557 cm^{-1} , 601 cm^{-1} , 960 cm^{-1} , 1034 cm^{-1} and 1086 cm^{-1} showed the presence of PO_4^{3-} and they were in good correlation with literature (Reyes-Gasga et al., 2013). Furthermore, peak observed at 646 cm^{-1}

confirmed the presence of OH^- (Bollino et al., 2017). However, the intensity of the OH^- related peak as the B content increases in the structure implied that OH^- was replaced with an ion supplied by H_3BO_3 . According to a study conducted by Albayrak (2016), it was reported that B doped HA was found to contain both BO_2^- and BO_3^{3-} as dissociation products of H_3BO_3 and they substituted PO_4^{3-} and OH^- (Albayrak, 2016). In addition, peaks at 746 cm^{-1} , 787 cm^{-1} , 1233 cm^{-1} and 1374 cm^{-1} showed the presence of BO_3^{3-} (Narwal et al., 2018; Obayes et al., 2016). According to XRD and FTIR results, it is possible to state that HT structure can be doped with B successfully without the formation of additional phases.

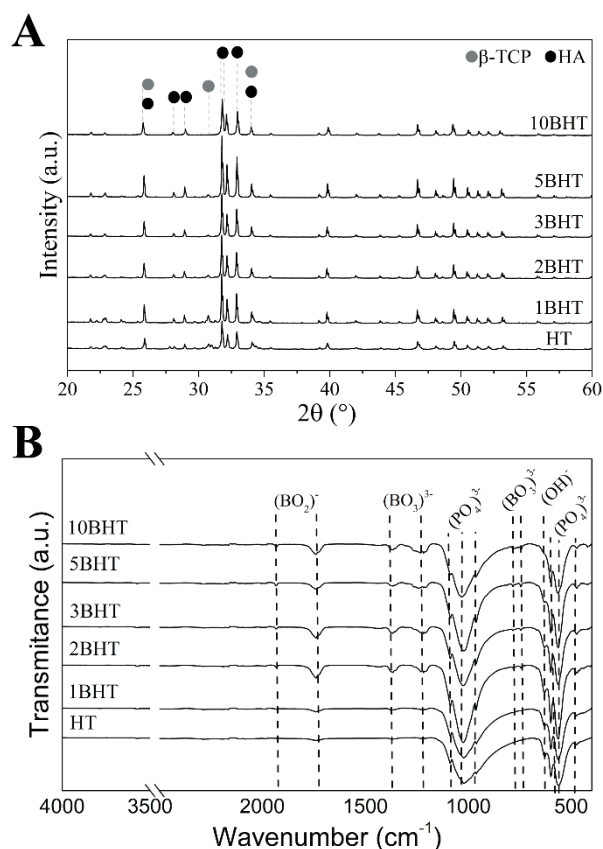


Figure 3.2 XRD (A) and FTIR (B) spectra of HT and BHTs.

B doping in HT caused distortion in the lattice of biphasic structure in a way that $a = b$ axes shrunk while c axis expanded (Table 3.2). A similar finding was presented by Barheine et al. (Barheine et al., 2011). They concluded that structural disorder was increased as more B replaces PO_4^{3-} and OH^- in HA lattice resulting in a significant change in c axis. In addition, V_{sample} initially increased as B substitution increased until a threshold of B concentration in HT was reached (Table 3.2). From HT to 5BHT a slightly increasing trend for V_{sample} was observed while the lowest value was obtained for $V_{10\text{BHT}}$ (611\AA^3). In the meantime, we did not observe any newly formed peaks in the XRD study in accordance with the change in $a = b$ and c axes upon doping with B. In a study by Kolmas et al. (2017), strontium and B co-doped HA was prepared. They reported that the absence of an extra peak could be interpreted as B units might be incorporated in the HA lattice without an undesirable crystal formation (Kolmas et al., 2017). Therefore, it can be stressed that only HA and β -TCP phases were present and B was successfully incorporated in HT lattice (Figure 3.2A). Crystallite sizes (L) were obtained to be close to each other for all samples (Table 3.2). Although not significant, 10BHT was found to have the smallest crystallite size (78.30 ± 12.51 nm). As a result, it can be stated that B encouraged the formation of HA phase, increase in X_c and improved the rate of crystal maturation.

In a study by Reger et al. (2019), multi-ion doped HA containing strontium (Sr), silver (Ag), zinc (Zn) and fluoride (F) ions were prepared by a wet precipitation method followed by a range of sintering temperatures between 800°C and 1250°C (Reger et al., 2019). They observed that negatively charged dopants, such as F^- , prohibited crystal growth and improved X_c over a concentration range (up to 2.5%). Comparably, we observed an overall increase in crystallite size (except for 10BHT) and HA phase stability increased as the B dopant was incorporated in the HT crystal. A study by Itatani et al. (2011) evaluated ball mill blended boron oxide (B_2O_3) particles (1 to 10% mol) and commercial HA that was pulse-current sintered up to 1200°C after isostatically compaction at 100 MPa (Itatani et al., 2011). They have selected 3% mol B_2O_3 doped HA for comparison. They determined the grain size after sintering at 1100°C for 5 h and tested for tensile strength of pellets under

1100°C, 50 MPa uniaxial deformation. They concluded that B₂O₃ dopant enabled grain boundaries to slide over each other to reach superplastic deformation and therefore it could be speculated that B acted as a nanoreinforcement to alter L and X_c.

Table 3.2 Structural properties of BHT samples (n=3).

Sample	a = b (Å)	c (Å)	V ³ (Å ³)	HA (%)	X _c (%)	L (nm)
HT	9.4221	6.8881	611.5	86.34 ± 3.90	89.03 ± 4.65	97.63 ± 29.00
1BHT	9.4234	6.8884	611.7	91.39 ± 3.40	93.77 ± 2.24	95.81 ± 20.52
2BHT	9.4236	6.8887	611.7	95.28 ± 1.18*	93.92 ± 4.39	107.57 ± 31.62
3BHT	9.4223	6.8899	611.7	95.96 ± 0.12*	94.37 ± 3.24	101.22 ± 25.66
5BHT	9.4195	6.8931	611.6	96.81 ± 0.84*	95.78 ± 2.08	103.39 ± 23.47
10BHT	9.4047	6.9083	611.0	98.68 ± 0.56*	92.86 ± 4.18	78.30 ± 12.51

* shows significant difference compared to HT (p<0.05).

In order to verify presence of B in the crystal structure and determine Ca/P ratio, samples were analyzed by ICP-OES (Table 3.3). Although not significantly different, increment in B content resulted in a lower Ca/P ratio. Parallel to literature, B dopants appeared to increase the disorder in lattice leading to Ca deficient CaP formation as previously discussed. Barheine et al. (2009) demonstrated that borate (BO²⁻ or BO₃³⁻) substitution in HA lattice results in the formation of two intricate phases in the crystal (Barheine et al., 2009). They further verified that the highly crystalline pure HA phase resists borate incorporation as well as Ca²⁺ uptake by the core lattice. Therefore, borate doped HA, borohydroxyapatites, were shown to

possess both lower than initially reacted B and Ca deficiency in the final product. In good agreement with the literature, an increase in B dopant concentration increase was followed by a sharp decrease of P/B ratio owing to PO_4^{3-} to BO_3^{3-} substitution (Table 3.3). P/B ratio and B content in mineral (%) displayed significant differences among samples ($p < 0.05$). Among these samples, 5BHT led to the highest B release in 1-day ion release study.

Table 3.3 ICP results of HT and BHTs (n=3).

Sample	Ca/P ^a	B (%) ^a	P/B ^a	B ($\mu\text{g/L}$) ^b
HT	1.48 ± 0.05	0	-	0
1BHT	1.47 ± 0.06	0.63 ± 0.11	65.17 ± 10.66	71.0 ± 1.4
2BHT	1.46 ± 0.05	1.16 ± 0.13	34.05 ± 3.22	92.5 ± 2.1
3BHT	1.46 ± 0.03	1.71 ± 0.12	22.78 ± 1.32	92.5 ± 0.7
5BHT	1.45 ± 0.05	2.33 ± 0.22	16.60 ± 1.23	186 ± 0.7
10BHT	1.43 ± 0.05	5.24 ± 0.52	6.92 ± 0.72	104 ± 1.4

^a ICP-OES was conducted after dissolving mineral in HNO_3 .

^b ICP-OES was conducted after collecting media at the end of MTT study.

All groups were significantly different from each other for B(%), P/B, and B, with the exception of 2BHT and 3BHT for B (last column).

The mineral deposition ability of the samples in a 1X SBF environment was also tested. B doped samples showed evidently better ability to induce CaP deposition of the samples (Figure 3.3). To elaborate, we employed EDX and determined Ca/P ratios (Figure 3.4). HT demonstrated significantly lower Ca/P ratio at the end of 1st and 7th days of SBF incubation. On the contrary, B doped samples, especially 5BHT

(1.69 ± 0.02) and 10BHT (1.69 ± 0.02), performed far better and permitted higher Ca/P precipitate formation on the surface than other samples. Hence, it was concluded that B promoted a more bioactive surface to prompt Ca and P.

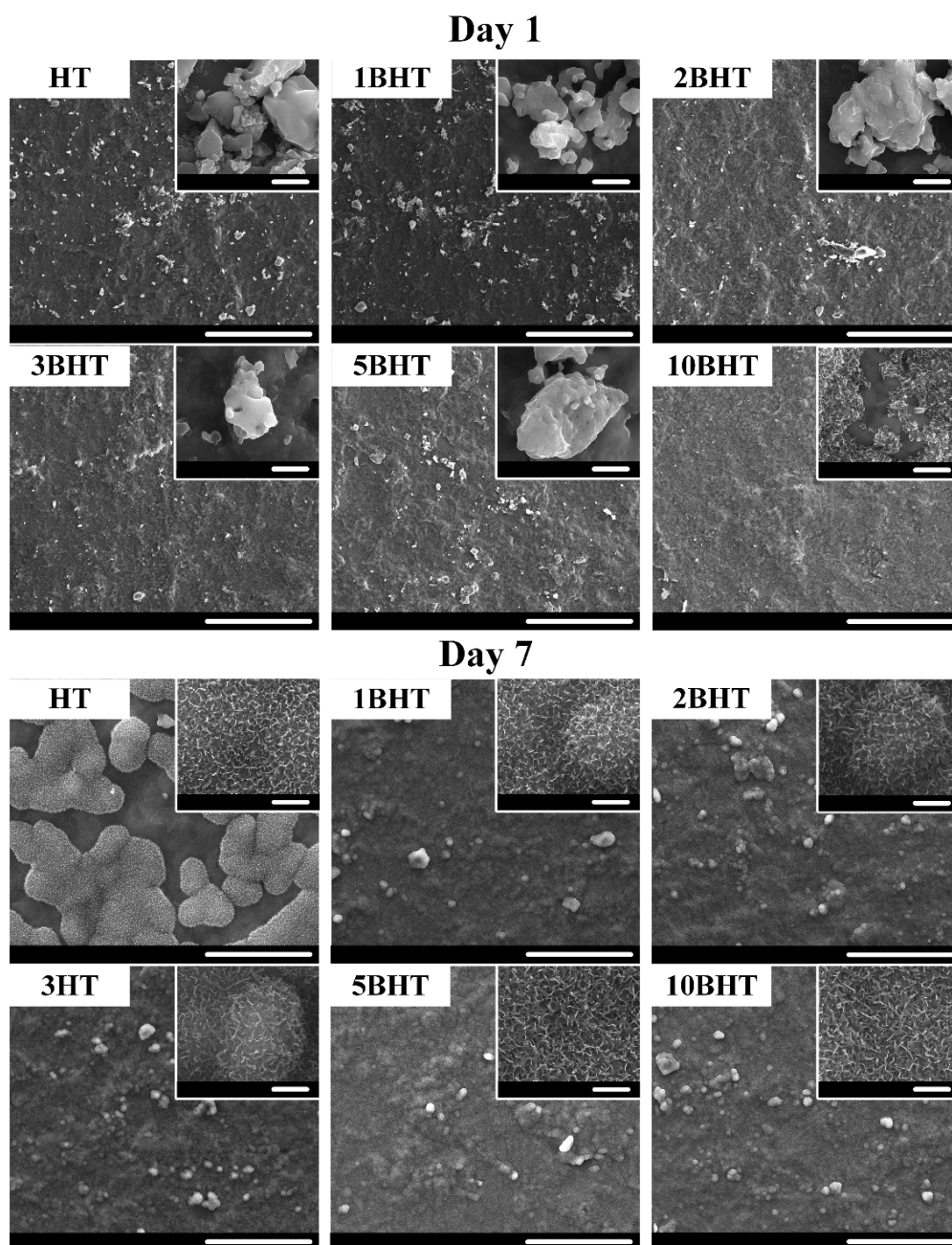


Figure 3.3 Mineral deposition on samples after 1 and 7 days of incubation in SBF (Scale bar: 100 μm , inset scale bar: 2 μm).

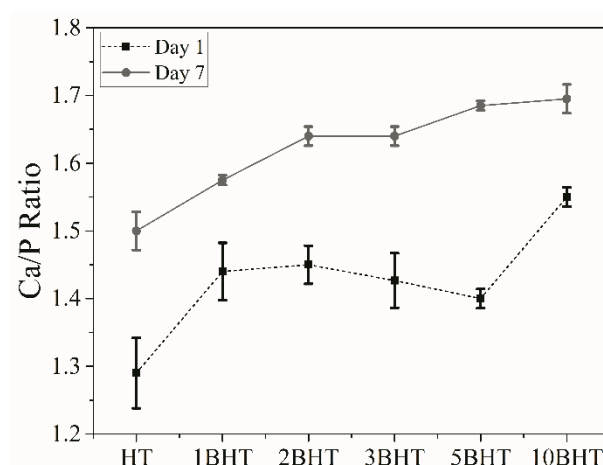


Figure 3.4 Ca/P ratio obtained after SBF analysis at the end of 1st day and 7th day of incubation. All groups showed statistically higher Ca/P ratio at the end of the analysis compared to HT.

Samples were characterized for their biocompatibility with MTT assay (Figure 3.5). Extracts were collected and no abrupt change in pH was observed (pH was around 7.8). Filter sterilized extracts were placed on hFOBs. At the end 1-day biocompatibility analysis, no cytotoxicity was observed for any of the BHTs. **Taking this information into account in addition to previous structural and chemical characterizations, 5BHT was selected as the main representative of BHTs and from this point, 5BHT will be referred as BHT to prevent any confusion.**

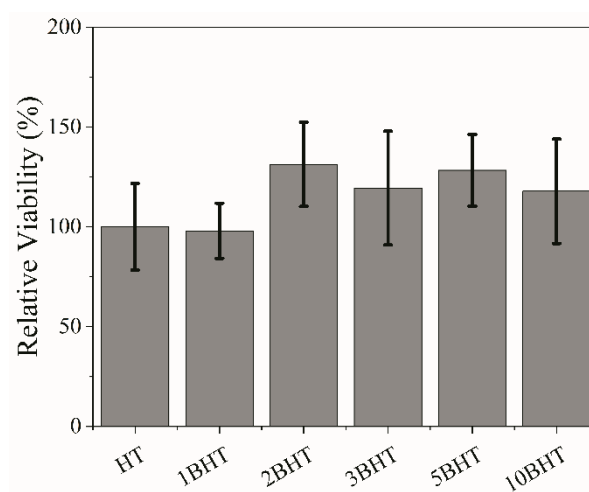


Figure 3.5 Indirect elution test results using MTT conducted with the extracts of HT and BHTs (n=8).

3.2 *In Vitro* Biological Characterization of BHT

3.2.1 Bioactive Ion Release

In order to characterize Ca and B ion release over time, a 2-week study was conducted. It was observed that BHT led to significantly lower Ca release compared to HT while maintained B release over the course of 2 weeks (Table 3.4). Nonetheless, BHT demonstrated good cumulative regenerative ion release.

Table 3.4 Release of Ca and B from HT and BHT (n=3).

Sample	Week 1		Week 2	
	Ca (mg/L)	B (mg/L)	Ca (mg/L)	B (mg/L)
HT	62 ± 4	0	128 ± 5	0
BHT	36 ± 5	39 ± 12	66 ± 5	52 ± 14

HT showed the highest Ca release while only BHT showed B release.

3.2.2 Effect of BHT on Cellular Proliferation

All samples demonstrated similar relative viability over 7-day incubation period (Figure 3.6). No sign of cytotoxicity was observed and samples increased relative viability up to 6 times of their initial 1st day viability percentage. Hence, it can be stated that both HT and BHT are highly cytocompatible and can be further characterized biologically.

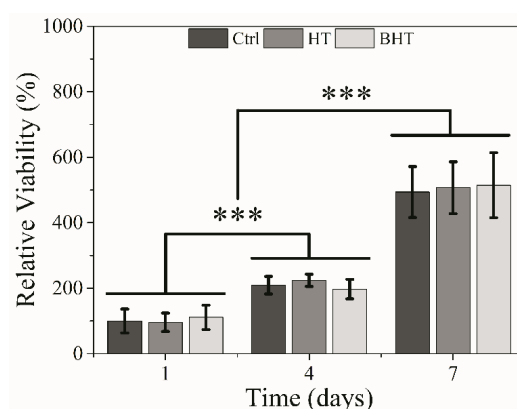


Figure 3.6 Proliferation analysis of HT and BHT (n=12). Proliferation rate of samples were given as relative viability having hFOB seeded on tissue culture plates as positive control (100%). Statistical differences were given as $*p<0.05$, $**p<0.01$ and $***p<0.001$.

3.2.3 Osteogenic Properties

In terms of osteogenic protein production, BHT demonstrated better performance compared to HT (Figure 3.7). Although a similar value obtained at the end of 1st week, BHT resulted in significant improvement in ALP activity in 2nd week (Figure 3.7A). This value was also significantly higher than that of HT ($p<0.001$). In addition to ALP tested as early osteogenic marker (Alshemary et al., 2016), OCN was selected as late osteogenic marker which involves in biomineralization (Hosseini et al., 2019). At the end analysis, almost same amount of OCN release was observed for both groups (Figure 3.7B).

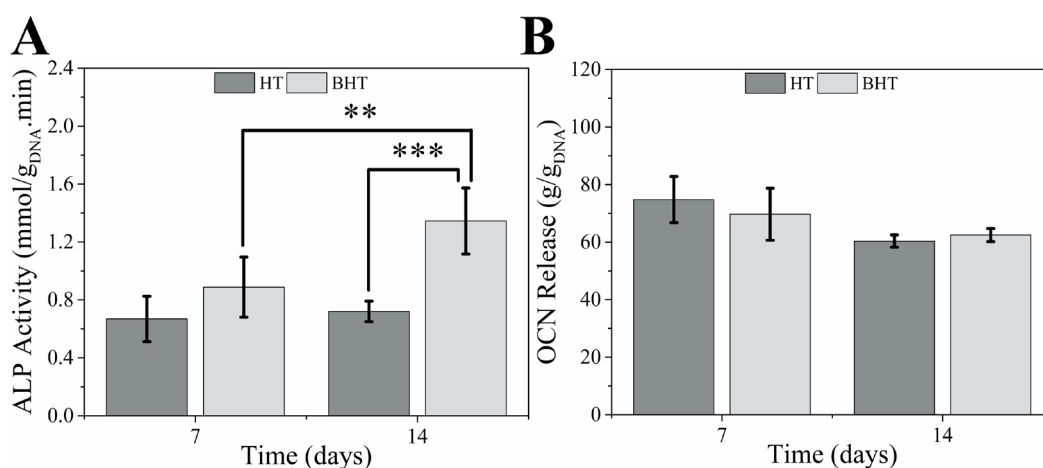


Figure 3.7 Osteogenic protein production analysis in terms of ALP activity (A, $n=18$) and OCN release (B, $n=6$). Statistical differences are denoted by $*p<0.05$, $**p<0.01$ and $***p<0.001$ as not significant.

During osteogenic differentiation, various early and late stage markers can be detected to monitor differentiation process. Among these, RUNX2 is an important early marker for osteoblast growth (Baniwal et al., 2012). It was also reported in the

literature that absence of negative feedback on RUNX2 expression can lead to suppression of osteogenic differentiation (Yahiro et al., 2020). On the other hand, ALP has been demonstrated as key enzyme in osteoblast growth, maturation and biomineralization (Chen et al., 2019). ALP is maintained from the early stages of osteoblast growth to osteocyte formation with an increasing rate. In addition, OSX expression was analyzed as a late marker for osteoblast differentiation (Shekaran et al., 2014).

Although RUNX2 expression did not changed over time for both of the groups, BHT resulted in significantly higher ALP and OSX expression ($p<0.001$, Figure 3.8). Moreover, in combination with improved ALP activity and OCN release data, it was clearly observed that BHT supported more extensive and rapid osteogenic maturation of hFOB3, therefore, BHT was shown to induce osteogenesis *in vitro*.

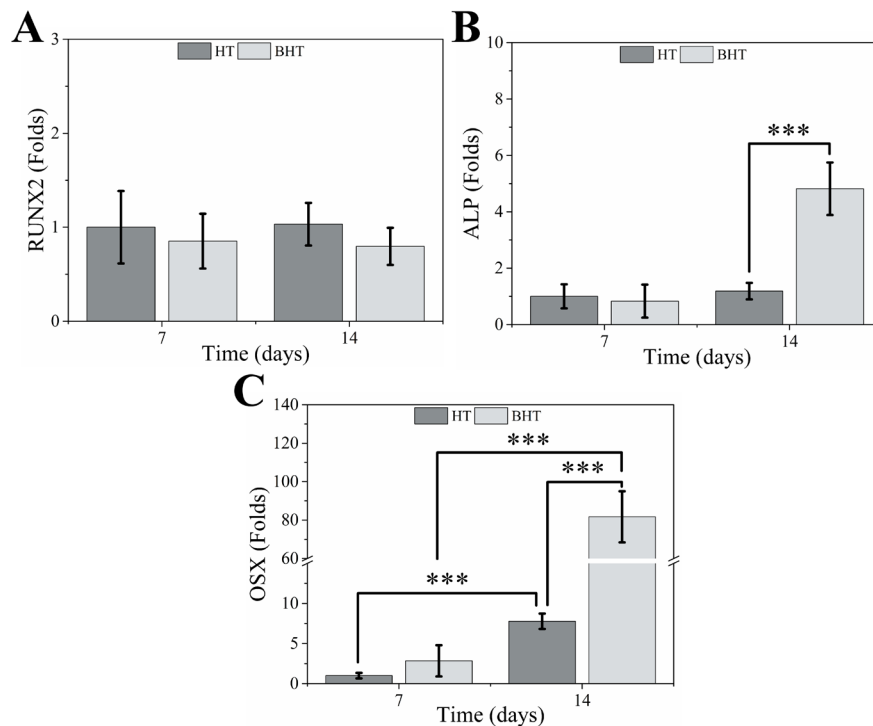


Figure 3.8 Osteogenic gene expression analysis results HT and BHT (n=6). Statistical differences were given as $*p<0.05$, $**p<0.01$ and $***p<0.001$.

3.2.4 Angiogenic Properties

Osteogenic properties of HT and BHT powders had been studied and characterized. Another aspect of regenerative properties, angiogenic response of HUVECs treated with HT and BHT extracts was also characterized. As reported in various literature, boron has been proposed to induce angiogenic response (Balasubramanian et al., 2017; Durand et al., 2015; Li et al., 2019). Therefore, VEGF-A release and angiogenic response in the form of vessel-like tube growth and evolution over time in the presence of boron ion was analyzed in our study.

Prior to further analysis, cell viability and the concentration of VEGF-A released to cell culture supernatant were quantified. As given in Figure 3.9A, BHT extracts demonstrated a significantly higher cellular viability than HT while it was in the non-cytotoxic range. Moreover, HUVECs treated with BHT extracts resulted in significantly higher VEGF-A release within 4 h (Figure 3.9B). VEGF-A is an important regulator of angiogenesis and osteogenesis (Raines et al., 2019). Especially having a role in endochondral ossification (EO), VEGF-A could support healing-repair process at bone defect site as well as allow establishing a functional bridge between bone and implant (Hu & Olsen, 2016). Therefore, it can be stated that BHT can improve angiogenesis at the bone-implant interface.

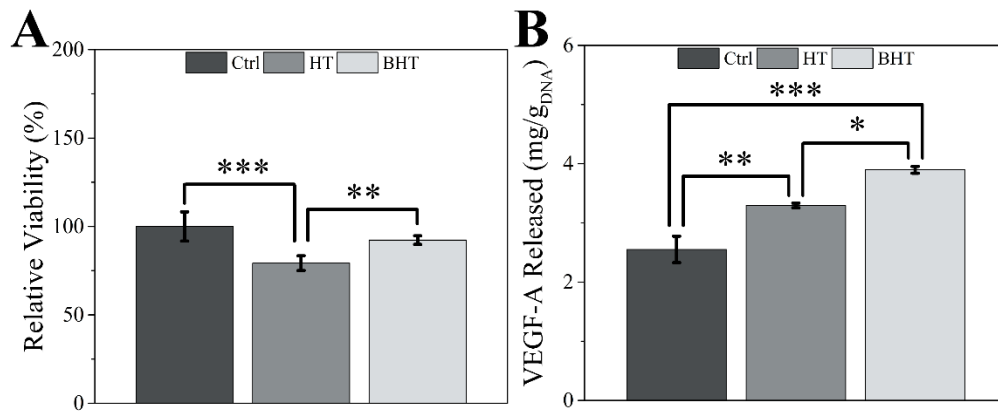


Figure 3.9 HUVEC viability after incubation in HT and BHT conditioned media for 4 h (A) and total amount VEGF-A released from these cells (B) (n=3). Statistical differences were shown as * $p < 0.05$, ** $p < 0.01$ and *** $p < 0.001$.

In addition, BHT was also shown to prompt higher vessel formation and growth (Figure 3.10A). BHT-conditioned medium was observed to trigger higher number of tube formation. When analyzed further, node and tube length quantification revealed that BHT led to statistically higher tube formation and larger tube area (Figure 3.10B). Collectively, it can be pointed out that BHT is new bioceramic that could possess regenerative effects, and could be employed as a BTE modality.

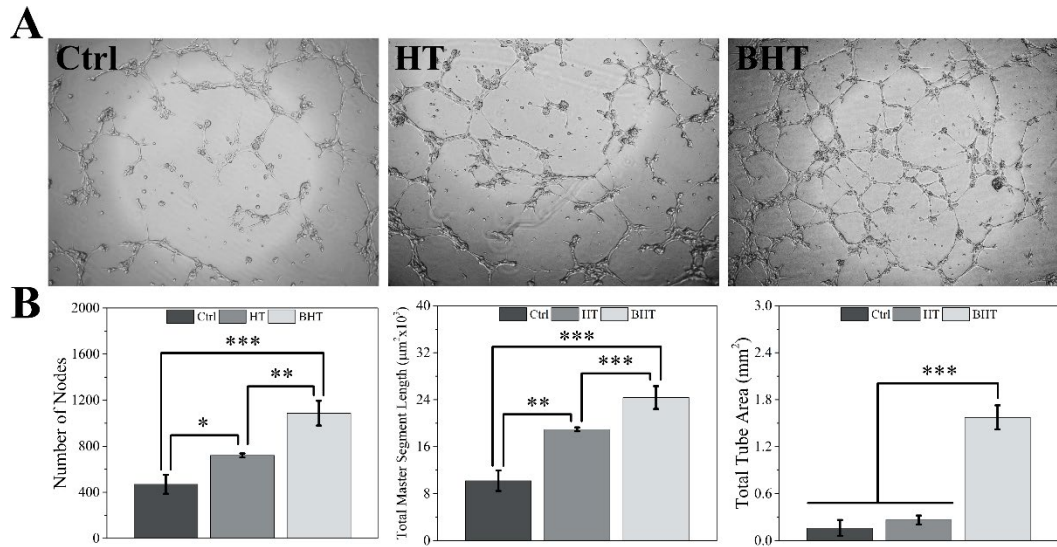


Figure 3.10 Phase contrast micrographs of HUVECs after incubation for 4 h with media only, HT and BHT extracts (A), number of nodes formed (B), tube length (C) and tube area (D) obtained at the end of tube formation study (n=5). Statistical differences are shown as $*p<0.05$, $**p<0.01$ and $***p<0.001$.

3.2.5 Immunomodulatory Properties

Host immune reactions play a critical role in resolution of inflammatory response upon implantation of a biomaterial. Although the mechanism of inflammasome production has been studied meticulously for the elucidation of immunological response to viral or bacterial infections, innate immune reaction towards biomaterials has not been fully appreciated. In this work, THP-1s were tested for inflammasome production in the presence of HT and BHT extracts (Figure 3.11). ASC is an adapter protein which forms a multiprotein assembly called speck and cleaves pro-caspase-1 into caspase-1 (CAS-1) (Fernandes-Alnemri et al., 2007). Upon uptake of danger signals in innate immune cells, nuclear factor kappa B (NF κ B), a regulator of innate immune response, is activated (Kelley et al., 2019). NF κ B triggers expression of pro-inflammatory cytokines such as pro-interleukin 1 β (IL-1 β), and NOD-like receptor

family pyrin domain containing 3 (NLRP3) sensor protein. Inflammasome multiprotein complexes are formed by NLRP3, ASC and CAS-1 assembly (Baljon et al., 2019). Inflammasome further elevates inflammatory response as a result of cleaving pro-IL-1 β into mature IL-1 β (Miao et al., 2011). In addition to coincidental IL-1 β production and CAS-1 activation, CAS-1 could induce pyroptotic cell death unless inflammatory response is resolved. Therefore, determination of CAS-1 enzymatic activity by an ELISA study using a suitable substrate, and ASC specks via visualization of GFP reporter could indicate inflammatory potential of HT and BHT.

THP-1s without Nig treatment (PMA⁺Nig⁻) showed significantly the lowest CAS-1 release ($p < 0.05$, Figure 3.11A). Nig is a strong antibiotic inducing NLRP3 inflammasome production leading to CAS-1 production (Armstrong et al., 2019). Therefore, addition of 1 μ M Nig showed a striking increase in CAS-1 release, from 100 ± 4 ng/mL to 863 ± 64 ng/mL ($p = 0.01$). In comparison with Nig treated cells (PMA⁺Nig⁺), HT (186 ± 14 ng/mL) and BHT (135 ± 10 ng/mL) treated cells demonstrated lower CAS-1 (Figure 3.11A). Among these samples, HT treated cells displayed significantly higher CAS-1 release than PMA⁺Nig⁻ ($p = 0.016$). On the other hand, BHT treated samples showed a higher release of CAS-1 than PMA⁺Nig⁻, but no significant difference was detected ($p = 0.44$). To further elucidate the effect of HT and BHT on induction of inflammasome complex, fluorescence microscopy analysis was conducted (Figure 3.12). Undifferentiated THP-1 cells demonstrate round morphology and ASC proteins appear diffused in the cytoplasm (blurred green fluorescence). After ASC specks assemble with inflammasome, specks converge in multiprotein structure and radiate bright green fluorescence under microscope (Tzeng et al., 2016). Positive cells showed highest concentration of ASC specks observed via fluorescent microscopy, despite the fact that cellular morphology did not alter significantly. Greater number of inflammasome assembly detected in PMA⁺Nig⁺ cells resulted in drastic pyroptosis (Figure 3.11B, Figure 3.12).

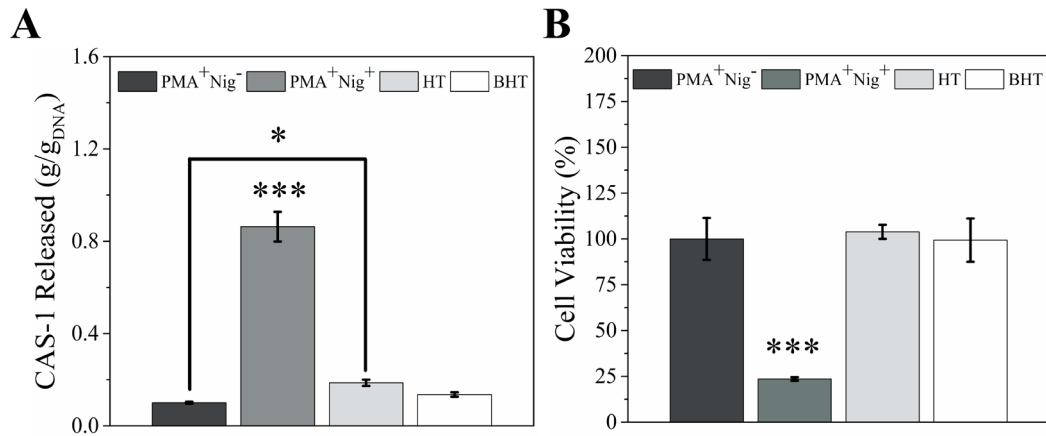


Figure 3.11 Pyroptotic immune response and cell viability of THP-1s with HT and BHT extracts (n=6). Cells were primed with 50 ng/mL PMA, and activated with 1 μ M Nig prior to CAS-1 ELISA analysis (A) and cell viability analysis during inflammasome assembly (B). Statistical differences are shown as * $p<0.05$, ** $p<0.01$ and *** $p<0.001$.

THP-1s were homogeneously distributed with round morphology without any signs of pyroptotic activity. However, cell death was evident for Nig treated cells. ASC specks were extensively pronounced in these cells while other samples demonstrated speck formation at lesser extend (Figure 3.12). ASC specks appeared in slightly lower concentration in BHT treated cells compared to HT treated cells. While analyzing the formation of ASC specks and thus production of CAS-1, it is important to determine the cell viability. Because a high response obtained during the analysis might be a result of extensive cell death or on the contrary, immense increment in cell number. Similar to previous data, Alamar Blue analysis revealed that all groups, PMA⁺Nig⁺, displayed comparable cell viability (Figure 3.11B). Higher ASC speck formation observed was thought to bring about by the increased pyroptosis in Nig treated cells. Accordingly, these results suggested that BHT treatment could lead to distinctively lower CAS-1 production, hence it may mitigate inflammasome-related pyroptosis in contrast to HT.

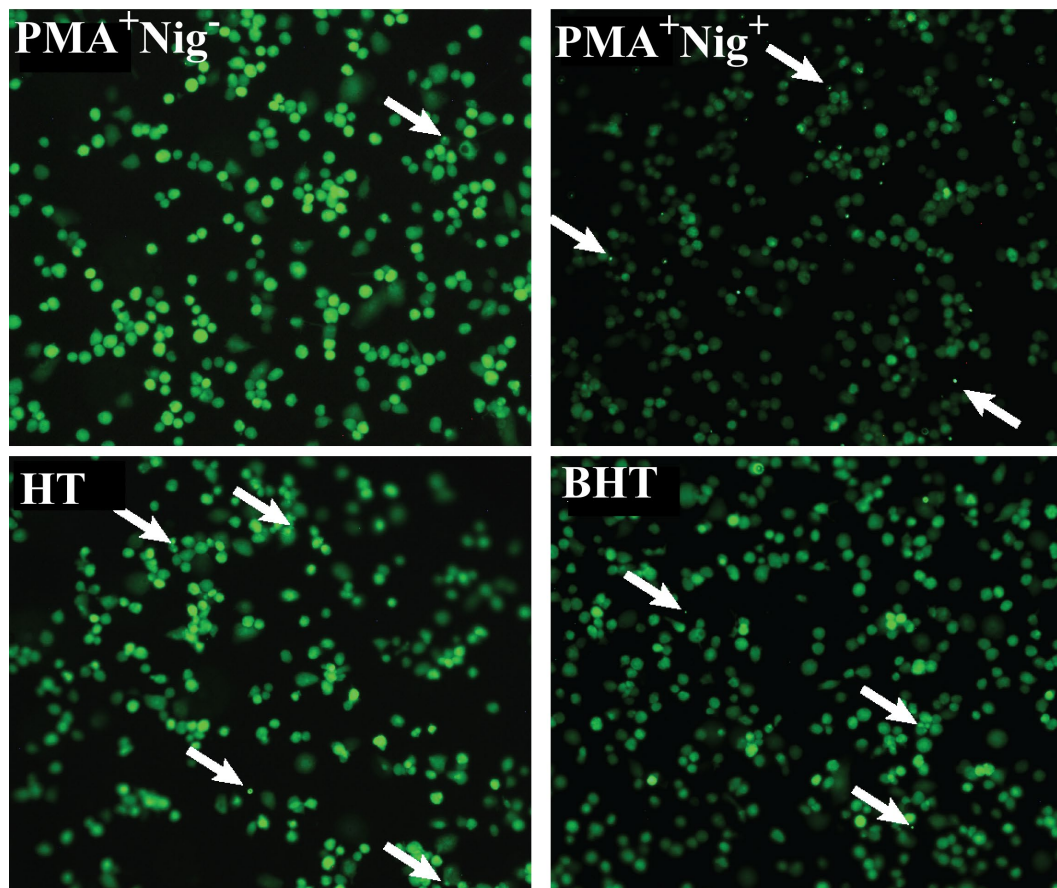


Figure 3.12 Fluorescence microscopy images of GFP conjugated ASC specks. White arrows indicate ASC specks in inflammasome assembly. General morphologies of the cells are round, characteristic “M0” state of monocyte-derived macrophage-like (MDM-like) morphology was achieved. Lesser green fluorescent reflection was acquired from PMA⁺Nig⁺ with extensive ASC-GFPs, hence, a high pyroptosis can be inferred.

Another aspect of inflammatory response is the type and release rate of cytokines from immune cells to control the fate of inflammation. Inherent activities of each of the downstream component in inflammatory response could significantly impair or aggregate inflammation. In the case of biomaterial application, persistent

inflammatory response plays a crucial role in development of chronic inflammation which could lead to foreign body giant cell formation (Vishwakarma et al., 2016). On the contrary, timed resolution of inflammation could prompt pro-healing cascade, hence improve the rate of implant integration as well as attaining functional bridging. In the light of current studies in the literature, two important factors of inflammation cycle, namely iNOS and IL-10, were used for the assessment of immunomodulatory effects brought about by HT and BHT. Although iNOS and IL-10 mark two opposite sides of immune response spectrum to a stimulus (anti- or pro-healing, respectively), they are produced by MDMs (Baseler et al., 2016; Dagvadorj et al., 2009). A change in balance of iNOS and IL-10 secretion can be detected in THP-1s, and could be interpreted as specific immunological responses of human MDM-like cells towards the bioceramics studied. Here, BHT showed a strong immunomodulatory effect compared to HT counterpart (Figure 3.13). IL-10 secretion to the extracellular environment upon incubation with BHT release product was accompanied with significantly higher increase in IL-10 protein production than observed for HT ($p < 0.05$). Untreated THP-1s (PMA^+LPS^-), however, showed significantly higher IL-10 release compared to all other samples ($p < 0.05$, Figure 3.13A). On the other hand, pro-inflammatory iNOS production was significantly higher in LPS treated cells ($p < 0.05$, (PMA^+LPS^+), Figure 3.13B). NF- κ B/iNOS pathway is inducible by LPS, leading to THP-1 phenotypic differentiation into M1 macrophage (van Putten et al., 2013). Pro-inflammatory response observed by LPS activation was exaggerated by the presence of HT release product (Figure 3.13B). Despite no significant difference was observed among HT and BHT release products, BHT showed evidently lesser iNOS concentration than both PMA^+LPS^- and PMA^+LPS^+ groups ($p = 0.001$ and $p = 0.01$, respectively). It can be interpreted that BHT could attenuate LPS-related degenerative inflammatory cascade. In addition, BHT provided an increase in THP-1 growth without an aberrant immunological response (Figure 3.13C). In this regard, our data revealed that BHT possesses potential to alleviate inflammatory response. By employing BHT as an immunomodulatory reinforcement in composite coatings would support successful osseointegration.

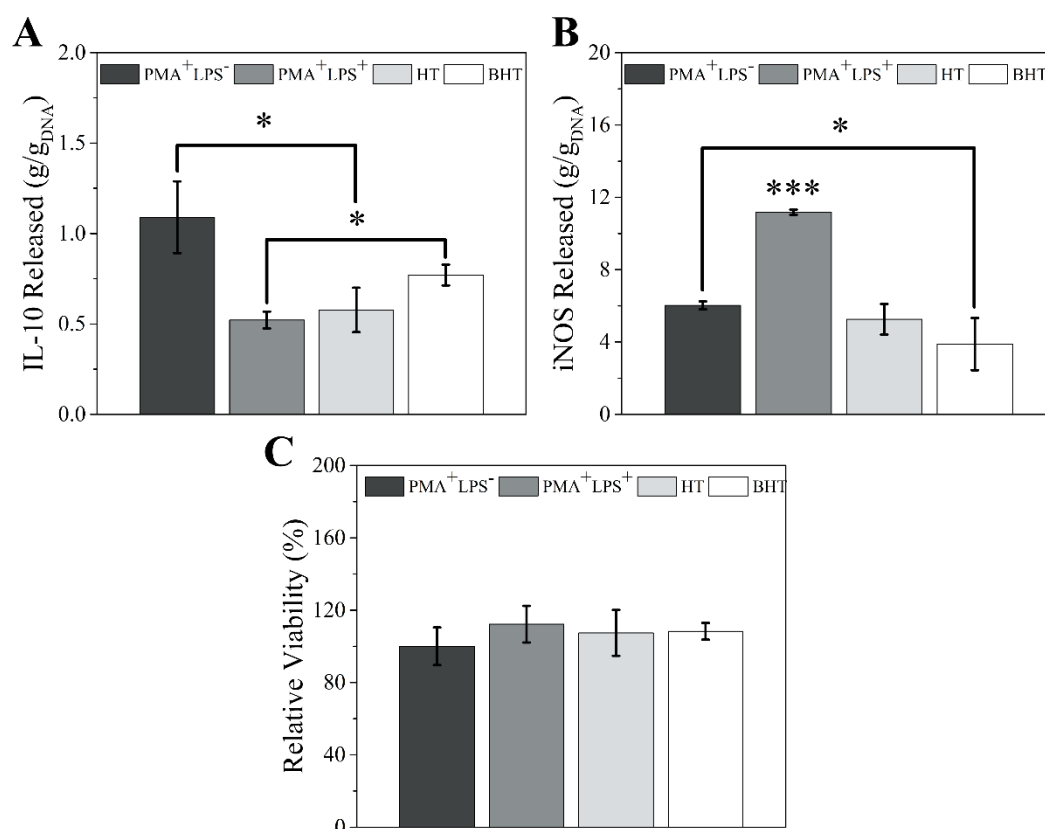


Figure 3.13 Inflammatory immune response and cell viability of THP-1s in HT and BHT extracts (n=6). PMA conditioned cells were also activated with 150 ng/mL LPS (without Nig) to allow either release IL-10 (A) or produce iNOS (B) to direct inflammatory response. During IL-10 and iNOS ELISA analyses, cell viability was also determined (C). Statistical differences are shown at * $p < 0.05$.

3.3 Characterization And Optimization of Ti-Aptes And A/G Coatings

3.3.1 APTES grafting on Ti-APA surfaces

XPS spectrum of Ti-APA demonstrated more pronounced structural Ti2s, Ti2p3, Ti3s and Al2p3 (Figure 3.14A). A sharp decrease (45%) in adventitious C1s atomic ratio at 285 eV and in Na1s peaks at 495 eV and 1070 eV occurred owing to alkaline treatment (Figure 3.14A). Moreover, the area of Ti2p3 peak at 458 eV of APTES grafted samples was observed to be less than that of Ti-APA (Figure 3.14B). These findings verified the formation of titanate (TiO_3^{2-}) structure in parallel with literature (Zhang et al., 2017). Additionally, shift in O1s from 530 eV to 529 eV was attributed to evolution of Ti-O bonds (Takadama et al., 2001). Thus, elevated intensity of O1s peak (Figure 3.14A) compared to Ti-SB after etching process was ascribed to the formation of Na_2TiO_3 .

Acid-peroxide-alkaline etched Ti alloys (Ti-APA) were used as control in determination of best APTES grafting medium with XPS analysis and TNBS assay. APTES was employed in 4% (v/v) in all media for comparison of grafting rates. Spectra of Ti-APA and Ti-APTES samples revealed no contamination related peaks (Figure 3.14B). Atomic percentages were normalized against Ti2p3 (458 eV) on each sample. Na1s (495 eV), Ti2p3 (458 eV) and O1s (530 eV) demonstrated lesser peak area for APTES grafted samples. Increase in C1s (285 eV) peak area, and N1s (400 eV) and Si2p (153 eV) peak formations were detected after APTES grafting (Figure 3.14B). Changes in atomic ratios are presented in Table 3.5. All samples showed comparable N/Ti ratios ($p > 0.05$). Among these media, samples grafted in 4% (v/v) APTES in 25MD, which is proposed for the first time in this manuscript, achieved higher Si/Ti ratio than 75MD and 95ED.

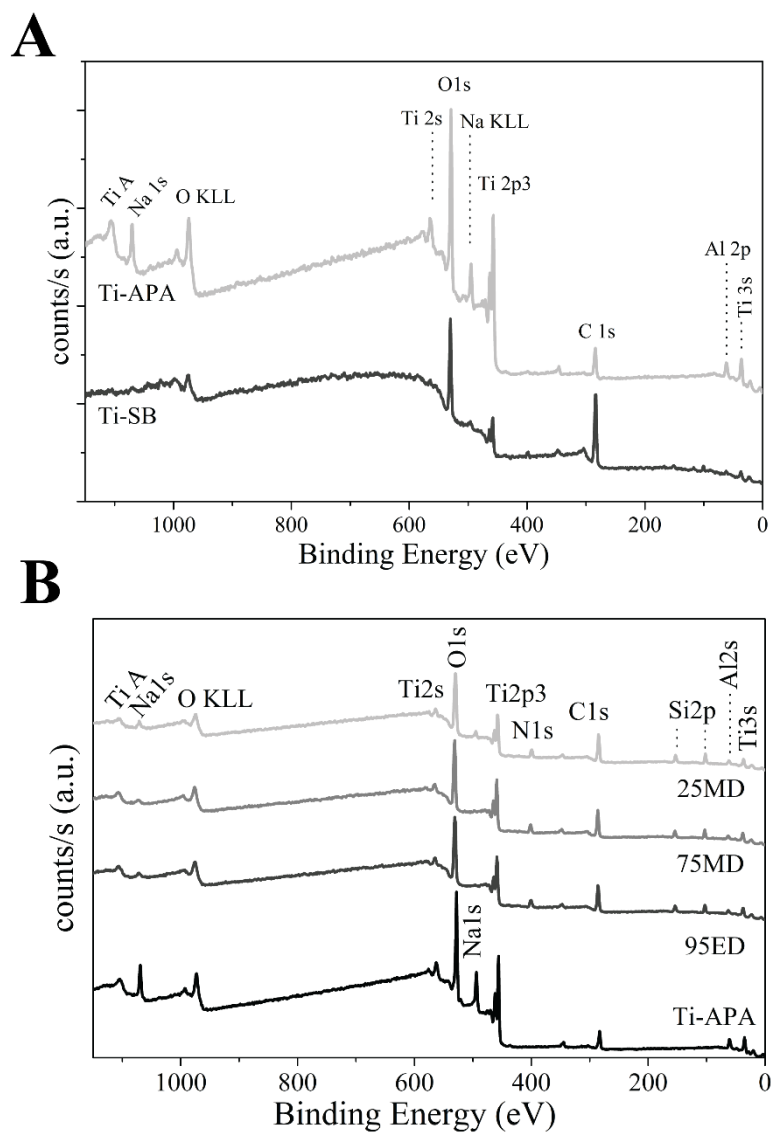


Figure 3.14 XPS spectra of Ti-SB and Ti-APA (A), and 4% (v/v) APTES grafted surfaces in different silanization media (B).

Table 3.5 Atomic ratios of N1s and Si2p against Ti2p3 on APTES grafted samples in various media (n=3).

Medium	N/Ti	Si/Ti	Active Amine Content (nmol/cm ²)
95ED	0.61 ± 0.26	0.69 ± 0.29	25.24 ± 2.22
75MD	0.72 ± 0.15	0.76 ± 0.29	42.51 ± 7.30 *
25MD	0.68 ± 0.13	1.05 ± 0.31	47.77 ± 6.56 *

* denotes the groups statistically different than 95ED ($p < 0.05$).

APTES is a well-known silanization agent which is often grafted on metallic surfaces to bridge the biological molecules (Godoy-Gallardo, et al., 2015; Öztürk-Öncel et al., 2020; Wang et al., 2019). It has aminosilane structure forming a covalent bond through its primary amine. Although highly employed in the literature, an optimized method to adhere natural polymers to metallic implant surfaces has yet to be established. Hence, in order to increase Ti tendency to be grafted with APTES, implant surface was treated with APA. Tremendous increase in O1s (530 eV), decrease in C1s (285 eV) adventitious carbon peaks, and appearance of Na1s (495 eV) clearly demonstrated successful etching process with sodium titanate (Na_2TiO_3) formation on implant surfaces (Rodriguez et al., 2017). This structure was previously shown to enable silanol (-Si-O-H) grafting and engage in covalent bonding (Marques et al., 2020; Plodinec et al., 2014). Therefore, APTES grafting resulted in a significant change in XPS spectrum of Ti-APA (Figure 3.14B).

Furthermore, N1s (400 eV), Si2p (153 eV) peaks appeared while intensity of Na1s decreased and C1s increased. Peak area ratio of N1s and Si2p to Ti2p3 prohibited a comparison in accordance with the effectiveness of APTES hydrolysis in given media. Ti-APTES surfaces grafted with 4% (v/v) APTES in 25MD, 75MD and 95ED revealed similar N/Ti and Si/Ti ratios (Table 3.5). For this specific reason, active amine content was determined via TNBS assay (Xu et al., 2020).

FTIR analysis was done to detect evolution of functional groups on the implant surface after APTES grafting in 25MD (Figure 3.15). Aminosilane related peaks were clearly identified. Si related peaks were detected in modes of Si-O-Si stretching at around 760 cm^{-1} , 1006 cm^{-1} , 1197 cm^{-1} , and at small shoulder around 1107 cm^{-1} (Gunda et al., 2014; Roghani-Mamaqani & Haddadi-Asl, 2014; Zako et al., 2008). Peaks observed at 3322 cm^{-1} and 2936 cm^{-1} were assigned to symmetric and asymmetric stretching modes of -NH_2 and stretching mode of -CH_2 , respectively (Majoul et al., 2015). Double peaks at 1482 cm^{-1} and 1572 cm^{-1} corresponded to N-H bending vibration, and C-H vibration mode corresponded to 1314 cm^{-1} (Sharan et al., 2018; Tan et al., 2011). Hydrolyzed APTES and subsequent adsorption on Ti were detected by Si-O-Ti formation at 936 cm^{-1} (Bai et al., 2017). Peaks at 443 cm^{-1} and 689 cm^{-1} were accredited to Ti-O and Ti-O-Ti bonds (Zhang et al., 2018). Although Si-O-C related shoulder was detected at 1104 cm^{-1} by FTIR, presence of -NH_2 , N-H, -CH_2 , -C-N between $1300\text{-}3300\text{ cm}^{-1}$, and large band of Si-O-Si at around $960\text{ to }1100\text{ cm}^{-1}$ demonstrated that APTES grafting was successful (Li et al., 2020). Collectively with XPS data, it can be concluded that 4% (v/v) APTES in 25MD could be grafted on Ti alloys and readily present -NH_2 groups to establish amide bonds with natural polymers.

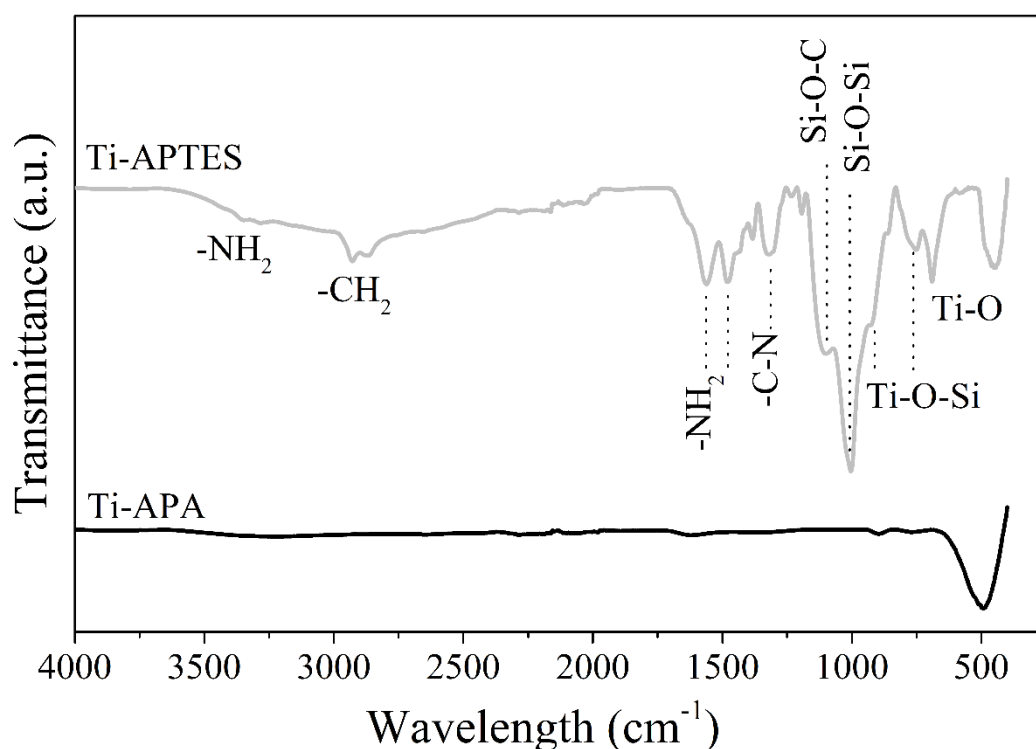


Figure 3.15 FTIR spectra of Ti-APA and Ti-APTES.

Moreover, samples coated in different grafting media were further analyzed for active amine content to finalize APTES grafting procedure. It was observed that 25MD medium allowed higher active amine units to be presented to the environment. For these reasons, optimization studies for APTES grafting conditions were conducted using 25MD as the main medium. 25MD was selected to induce APTES hydrolysis and subsequent grafting on Ti-APA. To reach the highest amine content, initial APTES concentration, curing temperature and coating methods were optimized (Table 3.6). Initial observations showed that over 8% (v/v) APTES and more than 30 min incubation could lead to premature polymerization and inactivation of silane (data not shown). Within these limits, between 2 and 8% (w/w) APTES in 25MD demonstrated significantly higher active amine groups compared to other media ($p < 0.05$). However, no statistical difference was observed in terms of

active amine content on Ti-APTES prepared in 2%, 4% or 8% (v/v) APTES in 25MD. Additionally, 15 min incubation period in APTES solution showed drastic improvement in grafting rate compared to dip coating ($p=0.011$).

In this context, despite comparable active amine content achieved on Ti-APTES, 4% (v/v) silane in 25MD allowed greater amine content on Ti-APTES (54.36 ± 1.05 nmol/cm²). This datum also displayed a significant difference ($p=0.011$) when the same protocol was applied via dip-coating, which resulted in 38.56 ± 0.80 nmol/cm² NH₂. On the other hand, curing temperatures of 80°C and 120°C did not result in a significant difference ($p=0.552$). Therefore, APTES grafting procedure with 4% (v/v) APTES in 25MD grafted on Ti-APA by curing at 120°C after 15 min incubation was selected as the best protocol.

Table 3.6 Active amine content on Ti-APTES samples prepared with different conditions (n=6).

APTES (%v/v)	Coating Method	Curing Temperature (°C)	Active Amine Content (nmol/cm ²)
0.2	15 min	80	15.20 ± 1.32
0.4	15 min	80	23.64 ± 7.63
0.8	15 min	80	23.52 ± 3.46
2	15 min	80	56.43 ± 14.19
4	15 min	-	50.34 ± 2.04 *
4	15 min	80	54.22 ± 9.72 *
4	Dip Coating	80	38.05 ± 0.85
4	15 min	120	54.36 ± 1.05 *
8	15 min	80	55.97 ± 9.24 *

Significantly higher than dip coating method at * $p<0.05$.

The morphology and surface topography of implants after various modifications were altered drastically (Figure 3.16). Sandblasting did not particularly affect the surface topography, however, caused superficial morphological change. Ti-SB displayed coarser morphology lacking microstructural features. Whereas chemically etched samples, Ti-APA, displayed fine surface structure and porosity. Ti-APTES displayed fine surface structure and porosity.

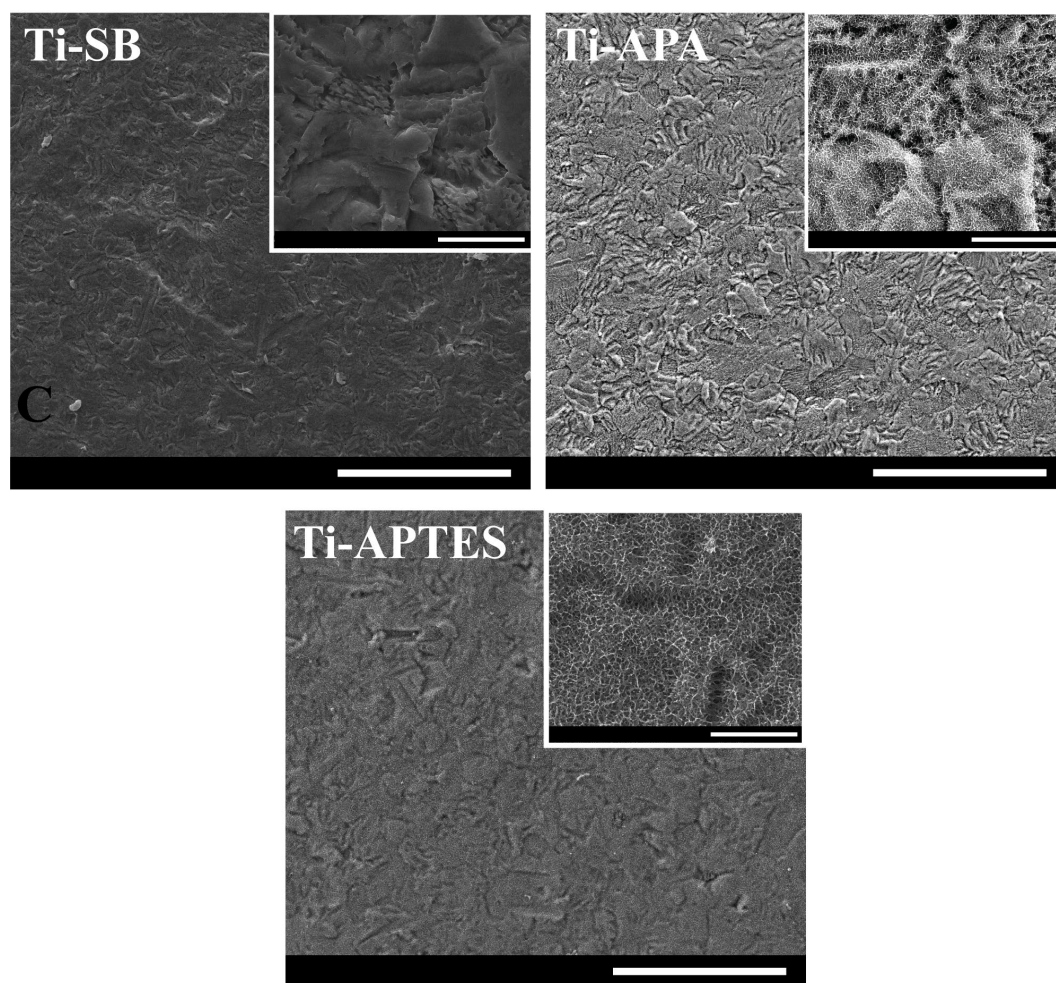


Figure 3.16 SEM electrographs of various sample surfaces. Ti-SB denotes initial Ti surface obtained after sandblasting, Ti-APA after acid:peroxide:alkali treatment and Ti-APTES after APTES grafting. Scale bar is 100 μm , inset scale bar is 10 μm .

Furthermore, Ti-APTES showed a more homogeneous surface morphology when compared to the other samples (Figure 3.17). Valleys or peaks observed in both Ti-SB and Ti-APA were not detected in Ti-APTES at the same extent. Moreover, surface porosity and nanotubular features formed by APA modifications were retained. AFM measurements affirmed a significant change in surface roughness after etching and APTES grafting processes (Table 3.7). APA treatment remarkably increased the surface roughness compared to Ti-SB ($p=0.001$). Moreover, APTES grafting did not lead to any change in surface roughness compared to APA ($p>0.05$).

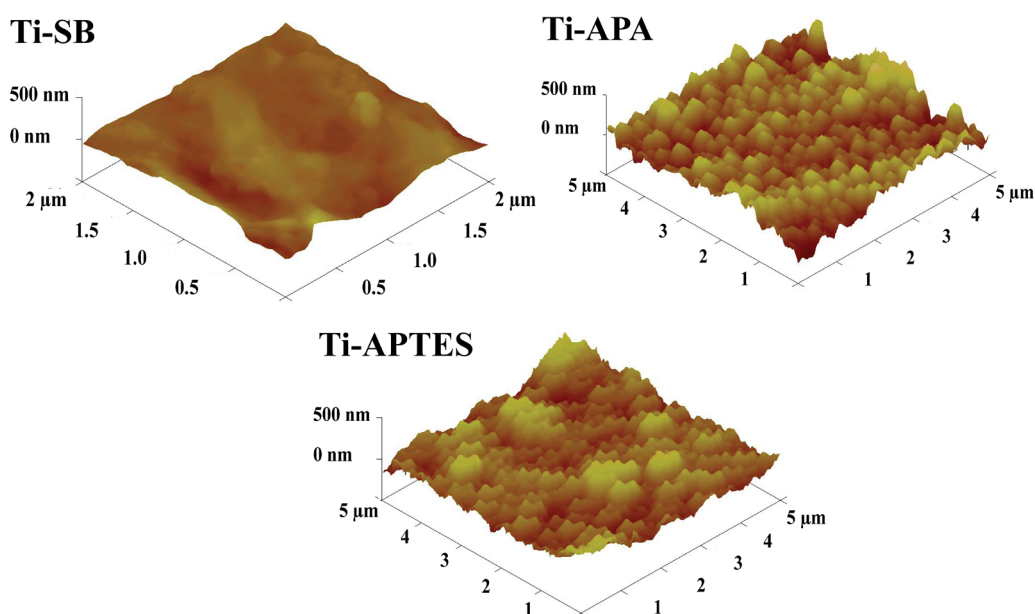


Figure 3.17 Images obtained for AFM surface topography analysis for various samples. APTES grafting slightly decreased the surface roughness.

Table 3.7 Roughness (R_q) and contact angle measurements of surface modified implants (n=3).

Sample	R_q (nm)	Contact Angle (°)
Ti-SB	37.13 ± 3.37	46.5 ± 3.1
Ti-APA	78.53 ± 3.19 *	2.6 ± 0.2
Ti-APTES	79.53 ± 7.81 *	71.2 ± 0.7 *

Statistically the highest data are marked by * ($p < 0.05$).

When morphological and topographical data for different surface treatments were interpreted together, it can be concluded that Ti-APA resulted in a drastic change in surface porosity and roughness. APA chemical etching method was shown to induce titanate gel formation that can be stabilized in the form of nanotubes (Zhao et al., 2020). This morphology of Ti-APA surface did not change after APTES grafting. Additionally, surface roughness was not significantly different for Ti-APA and Ti-APTES samples ($p > 0.05$). Similar roughness values around 79 nm for Ti-APA and Ti-APTES justified that APTES did not form a thick silane film, instead, it formed a thin multilayered graft on the implant (Meroni et al., 2017).

In order to determine the effect of APTES on the surface of Ti, water contact angle measurements were conducted (Figure 3.18A). APA treatment resulted in extensive increase in surface hydrophilicity ($p = 0.001$). On the other hand, APTES grafting dramatically increased the contact angle ($p = 0.001$). Collectively, it was observed that Ti-APA which were incubated for 15 min in 4% (v/v) APTES dispersed in 25MD and cured at 120°C showed the highest APTES content on the surface. Having hydrophobic alkyl chains in APTES backbone and grafted layer of silane brought about extensive surface hydrophobicity, thus proving robust APTES grafting (Malekzadeh & Zhang Newby, 2020). Therefore, it can be stated that APTES grafted layer showed good coverage on the implants, and possibly attached through

secondary interactions among intertwined polymeric network and intermolecular covalent bonding between the polymer chains and Ti-APTES (Elshereksi et al., 2017). Change in surface properties after each modification step could be seen by in the images taken by microscopy or macroscopically. After incubating in TNBS, Ti-APTES turned yellow and APTES grafted surface was clearly visible (Figure 3.18B).

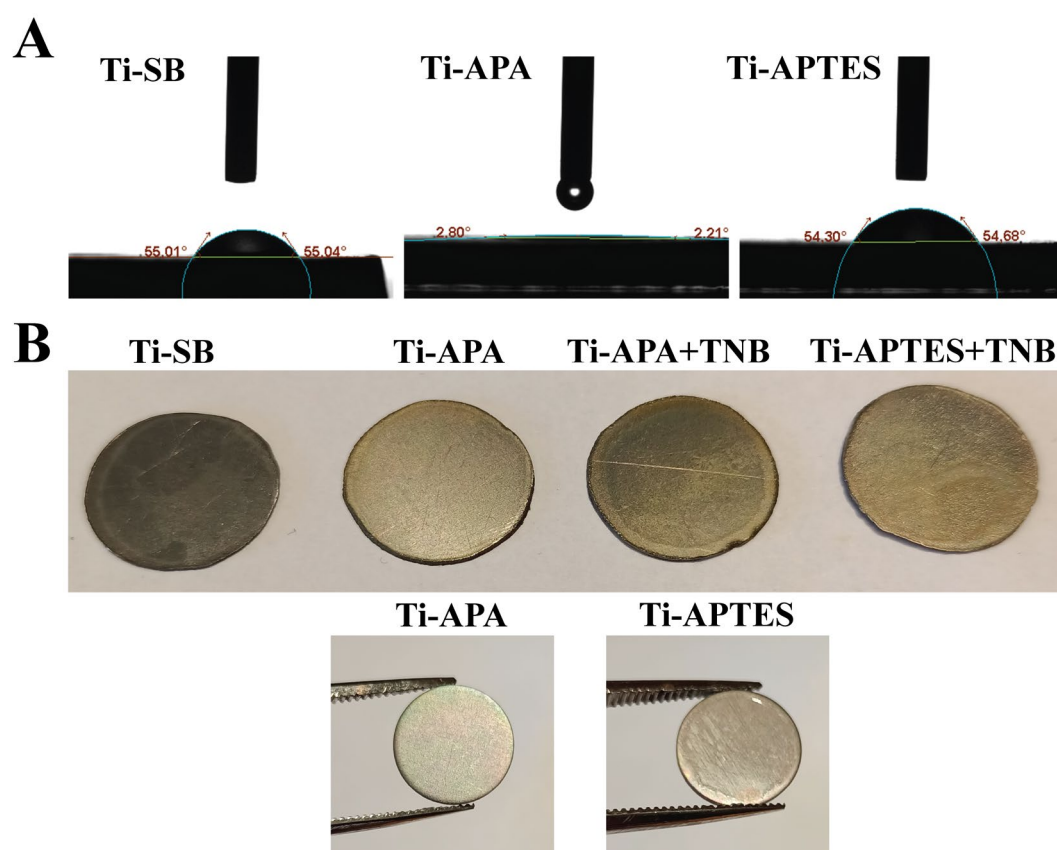


Figure 3.18 Water contact angle (A) and macroscopic images of Ti-SB, Ti-APA, Ti-APA and Ti-APTES stained with TNBS, and as prepared Ti-APA and Ti-APTES (B). APTES grafting drastically increased the hydrophobicity. APTES presence was shown by TNBS staining, and could be detected by naked eye due to high reflectance of APTES grafted samples.

3.3.2 A/G Coating on Ti-APTES

In this thesis, A/G layer was designed to serve as a gap filling natural polymer-based matrix that could assume hydrogel structure post-implantation, and support metal implant osseointegration when added with BHT. For this reason, we hypothesized that presence of 0.2 M NaCl could decrease the cohesive strength conferred by hydrogen bonding around the alginate polymer chains thus increasing the flow of polymer solution (Figure 3.19A). With lower viscosity, gelatin polymer chains and NHS were thought to diffuse easily into the alginate backbone hence favoring greater rate of intermolecular interactions between the chains and Ti-APTES (Figure 3.19A). It is also hypothesized that decreasing intramolecular interactions prior to crosslinking and having control over intermolecular covalent bonding might allow us to design hydrogel coatings with tailorable properties (Figure 3.19B). In addition, it was expected that lower viscosity may provide a more homogeneous suspension of pre-gel A/G and BHT.

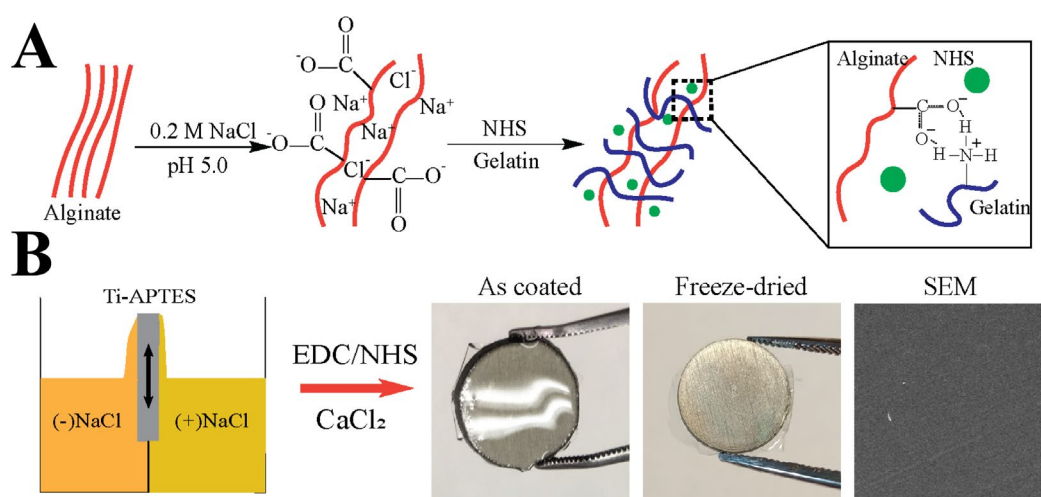


Figure 3.19 Schematic display of A/G coating steps (A), and photos and microscopic images of dip-coated A/G hydrogel on Ti-APTES as coated and after freeze-dried (B).

Rheological analysis was conducted on the pre-gels prior to coating (Figure 3.20). Samples having 1.5% (w/w) alginate showed very high initial viscosities. Although a significant decrease in apparent viscosity occurred under increasing shear rates, pre-gels having 1% (w/w) alginate (A/G 1:x) showed almost a linear decrease under shearing. Therefore, it was noted that NaCl presence showed a more pronounced effect on A/G 1:1, A/G 1:2 and A/G 1:3 pre-gels in terms of viscosity.

A/G/NHS/NaCl pre-gels revealed that A/G 1:X (groups with 1% (w/v) alginate) pre-gels had significantly lower viscosity and better shear-thinning. Having shear-thinning behavior, they may fill topographical features on the surface of implants and interlock mechanically in addition to covalent bonding via APTES coupling agent owing to more loosely packed polymeric chains, thanks to NaCl (Gao et al., 2018). Additionally, A/G 1:X groups could lower entanglement of alginate and gelatin polymer chains while presenting higher number of crosslinking points as hypothesized (Li et al., 2020). Therefore, these could grant good adhesion strength at the interface between coating and Ti-APTES.

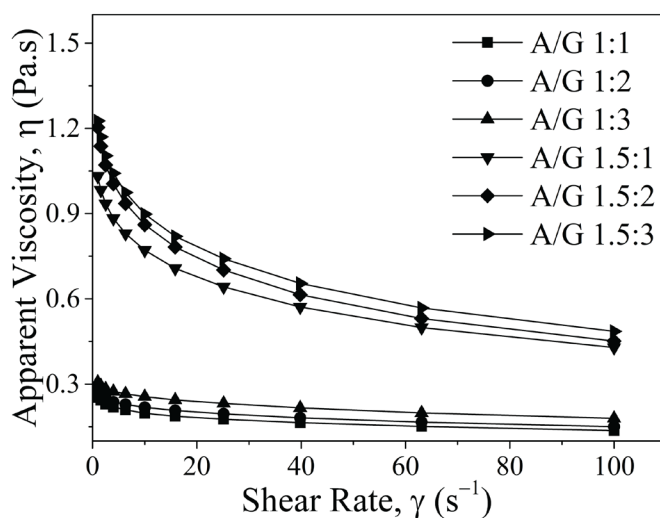


Figure 3.20 Apparent viscosity of A/G pre-gel samples (n=1).

Water uptake analysis of A/G coatings revealed that all samples showed a significant swelling as early as 15 min (Figure 3.21A). This behavior is more dominant in A/G 1.5:1. It showed the highest water uptake capacity at all periods ($p < 0.05$). A/G 1:1 demonstrated a striking increase in water uptake capacity compared to other groups. However, except for A/G 1.5:1, all samples reached similar swelling at equilibrium (3 h). Among A/G 1:X groups, A/G 1:2 exhibited the lowest water uptake. It was significantly lower than A/G 1.5:2 ($p = 0.001$), while it showed a similar swelling with A/G 1.5:3 ($p = 0.462$). The lowest water uptake was observed in A/G 1.5:3. Despite a substantial difference was obtained within A/G 1.5:x groups, water uptake of A/G 1.5:3 samples was not significantly different than any of the A/G 1:x samples ($p > 0.05$).

On the other hand, a different outcome was observed in hydrolytic degradation analysis (Figure 3.21B). A/G 1:3 samples demonstrated significantly the lowest weight loss at the end of 4 weeks ($p < 0.05$). Moreover, a clear difference was observed in between A/G 1:3 and A/G 1.5:3 ($p = 0.022$). Within A/G 1.5:x group, A/G 1.5:3 displayed the lowest weight loss ($p < 0.05$). Although A/G 1:1 and A/G 1:2 were not significantly different than A/G 1.5:1, they degraded much faster than A/G 1.5:x counterparts.

Water uptake is an essential feature of hydrogel coatings by which nutrient transport and exchange of biochemical factors can occur. However, extensive swelling could lead to detachment of the coat layer, and substantially decrease the mechanical strength (Khutoryanskaya et al., 2010). It is vital to control the rate of water uptake to attain a strong interphase that can endure mechanical stress during implantation. The coatings were also expected to function as an interphase during the initial healing period of the post-implantation. Therefore, a lower rate of degradation is favorable for a gap bridging interphase to act as a scaffold conducting bone growth around the defect zone (Li et al., 2017). A/G 1:3 coatings exhibited amiable viscosity, water uptake, low degradation rate as well as structural stability throughout the analyses. As a consequence of homogeneous and complete intermolecular

crosslinking, A/G 1:3 possessed tremendous cohesive strength and excellent adhesion on Ti-APTES (Jin et al., 2020).

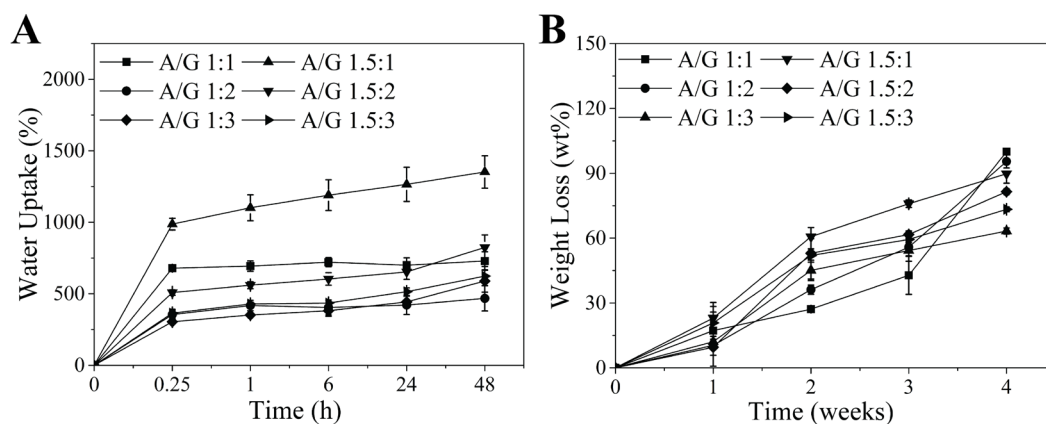


Figure 3.21 Water uptake (A) and hydrolytic degradation (B) test results of A/G coatings.

Surface morphology of the A/G coated samples can be seen in Figure 3.22A. Similar morphologies were obtained for all samples having different A/G ratios. Coated and freeze-dried surfaces showed no cracks or delamination. Meanwhile, macroscopic images were also taken (Figure 3.22B and C). These images were obtained at the complete swelling state after 3 days and stained with MB. In order to manually control the surface attachment and check the bonding at the interface, coatings were scratched with the help of a needle (Movie 1, to be presented during defence). A good bonding among all groups was observed. On the other hand, coatings on APTES-free Ti-APA (Figure 3.22B) demonstrated distinct morphologies compared to A/G coatings on Ti-APTES (Figure 3.22C). Apparent shrinkage, delamination and breaks were observed in the A/G coated layer of Ti-APA.

Freeze-drying is known to be an effective method to remove intermolecular water and allows complete drying for further shelf-life. However, it could lead to

accumulation of stress on polymeric coatings and may generate defects at areas having low adhesiveness (Francis et al., 2002). Evidently, it can be confirmed that coating with strong and resistant adhesion on implant surfaces can be attained by freeze-drying as a result of the employed coating method as seen in Figure 3.22. Without APTES grafting, an initial attachment could be achieved due to electrostatic interactions. However, inclusion of water followed by extensive swelling led to detachment of A/G layer and premature failure (Figure 3.22B and C).

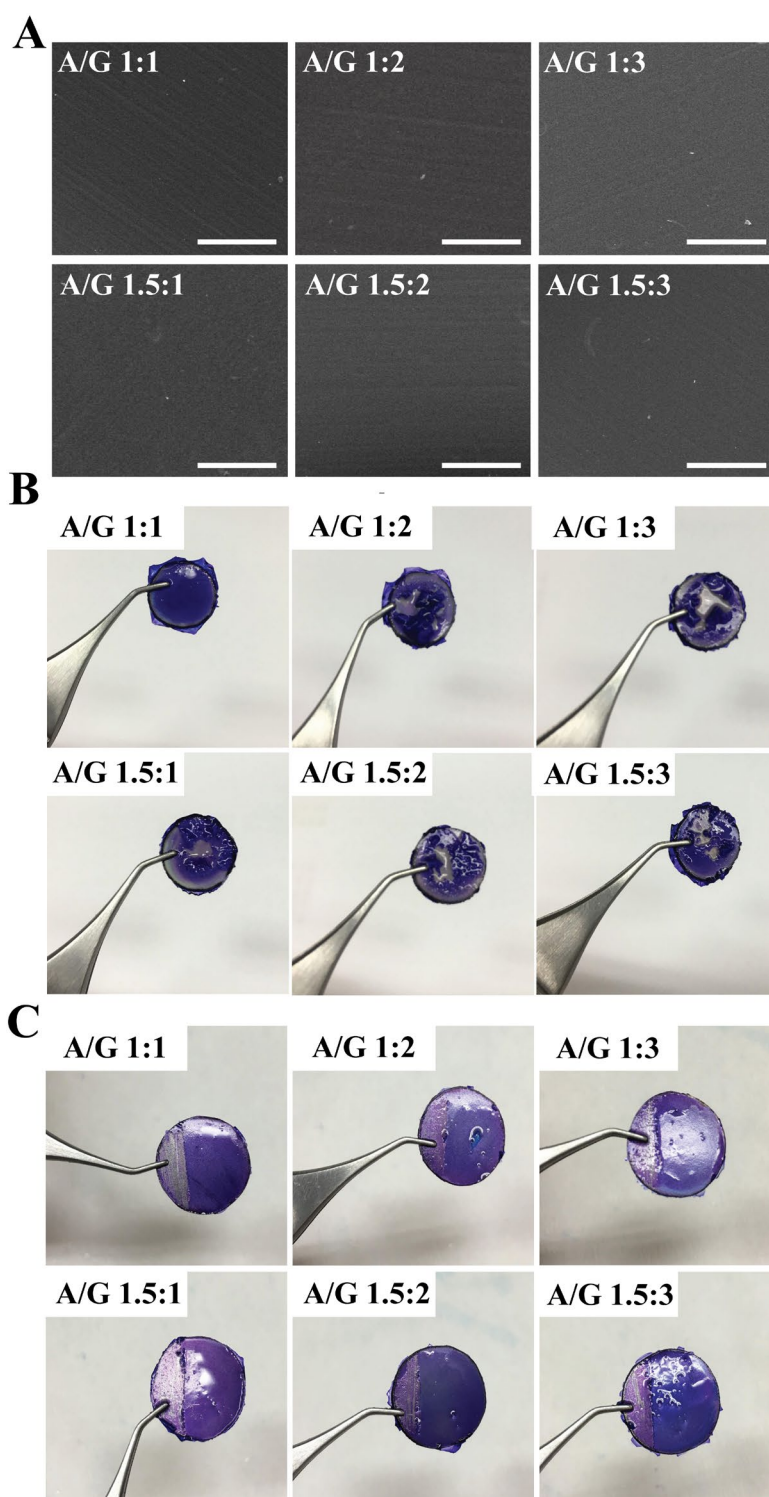


Figure 3.22 SEM electrographs of freeze-dried coatings (A) and macroscopic images of swollen coatings on Ti-APA (B) and Ti-APTES (C). SEM scale bar is 500 μm .

Scratch testing was employed using a Rockwell indenter under constant speed (4.95 N/min). Test was concluded once the indenter pin reached pre-designated 3 mm length. Thickness of the coatings were determined by measuring the penetration depth at the end of the test. Morphological observations were made using SEM to determine critical force (L_c) where coated layer failed (Figure 3.23A) (Cekas et al., 2018). All samples demonstrated quite close L_c and thickness values (Figure 3.23B and C, and Table 3.8). A/G 1:3 showed statistically higher L_c than A/G 1.5:2 ($p=0.005$) but no difference was detected between their thicknesses.

Interestingly, scratch testing revealed that both coating groups (A/G 1:x and A/G 1.5:x) displayed good adhesion strength which was inversely related with the thickness of coatings. This finding also explains the SEM images of the scratching test, which revealed a foul-free coating without pits or polymer aggregates. It can be seen that the coating failure occurred in all samples had compliant polymeric nature (Mallikarjunachari & Ghosh, 2016). At the end of scratch pathway (Figure 3.23A), piled up polymeric coating demonstrated typical cohesive failure (Paretkar et al., 2013). Owing to absence of adhesive failure, which occurs in the form of delamination, buckling of the coating under load can be interpreted as robust adhesion was achieved at the interface.

Therefore, the method employed in this thesis study evidently improved natural polymer adhesion on the metallic implant through covalent bonding. Since adhesiveness of a coated layer is defined by the balance of cohesive and adhesive strengths, it can be pointed out that polymer blends strongly favor adhesion on the surface (Rodriquez et al., 2018). Specifically, A/G 1:3 samples showed good swelling ability, the lowest weight loss and the highest adhesion strength. This clearly exhibited a strong relationship between cohesive strength and adhesive strength. Samples having extensive intramolecular crosslinking showed a lower rate of hydrolytic degradation while intermolecular covalent bonding prevented loosening at the interface, thus allowed greater number of polymeric chains to interact with Ti-APTES. Furthermore, increment in surface area upon APA treatment as a result of Na_2TiO_3 nanotube formation induced higher rate of APTES

grafting (Duong et al., 2017), which, in return, encouraged higher number of A/G chains to covalently bond with Ti-APTES surface (Wei et al., 2020). Hence, lower thickness with remarkable adhesion strength was achieved by A/G 1:3 coatings.

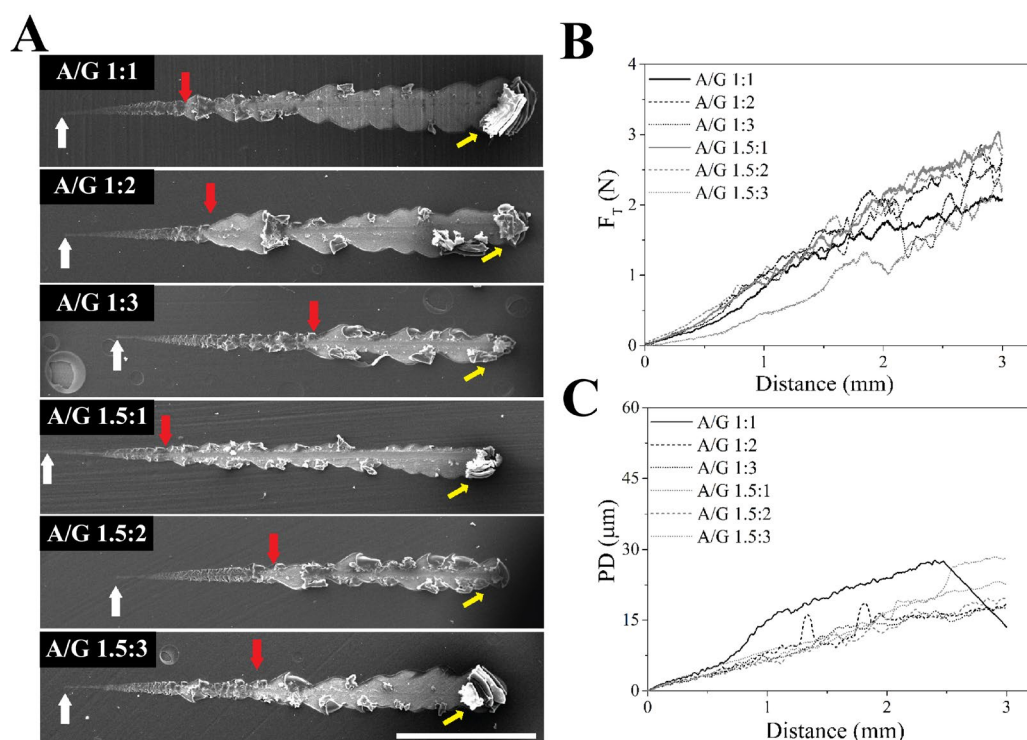


Figure 3.23 SEM images of scratched A/G coatings on Ti-APTES (A, scale bar is 1 mm), and average F_T (B) and PD (C) obtained during the scratch test of different A/G coatings. White arrows indicate the start of scratching, red arrows demonstrate the locations of L_c for each coating, yellow arrows show end of the scratch test, and green arrows show the thickness of coating.

Table 3.8 Microscratch analysis results conducted on A/G coatings (n=3).

Coating	L_c (N)	Thickness (μm)
A/G 1:1	0.74 ± 0.16	27.64 ± 4.76
A/G 1:2	1.06 ± 0.14	18.46 ± 4.39
A/G 1:3	$1.28 \pm 0.32^*$	16.41 ± 0.34
A/G 1.5:1	0.77 ± 0.14	21.22 ± 5.07
A/G 1.5:2	1.01 ± 0.12	19.62 ± 0.76
A/G 1.5:3	$0.55 \pm 0.12^*$	23.09 ± 6.58

* A/G 1:3 showed significantly higher L_c and compared to A/G 1.5:3 ($p < 0.05$)

A/G 1:3 demonstrated a significantly higher adhesion strength compared to A/G 1.5:3 ($p < 0.005$).

Taking shelf-life study into account, it was observed that A/G 1:3 maintained adhesiveness and stayed unscathed over 12-months' period during which coated interphase layer retained its strength (Table 3.9). At the end of 4th, 8th and 12th months, A/G 1:3 coating was intact and non-delaminated (Figure 3.24A and B). Moreover, a statistically insignificant decrease in strength at the end of 12 months was observed ($p < 0.062$), and A/G 1:3 coatings remained on the surface demonstrating good adhesive strength. Moreover, results showed that a freeze-dried hydrogel structure which can readily swell with bodily fluids at the defect zone, and act as a bioactive interphase could be stored long periods and could be directly applied. Therefore, it can be concluded that A/G 1:3 could be a structurally favorable base matrix for an interphase coating.

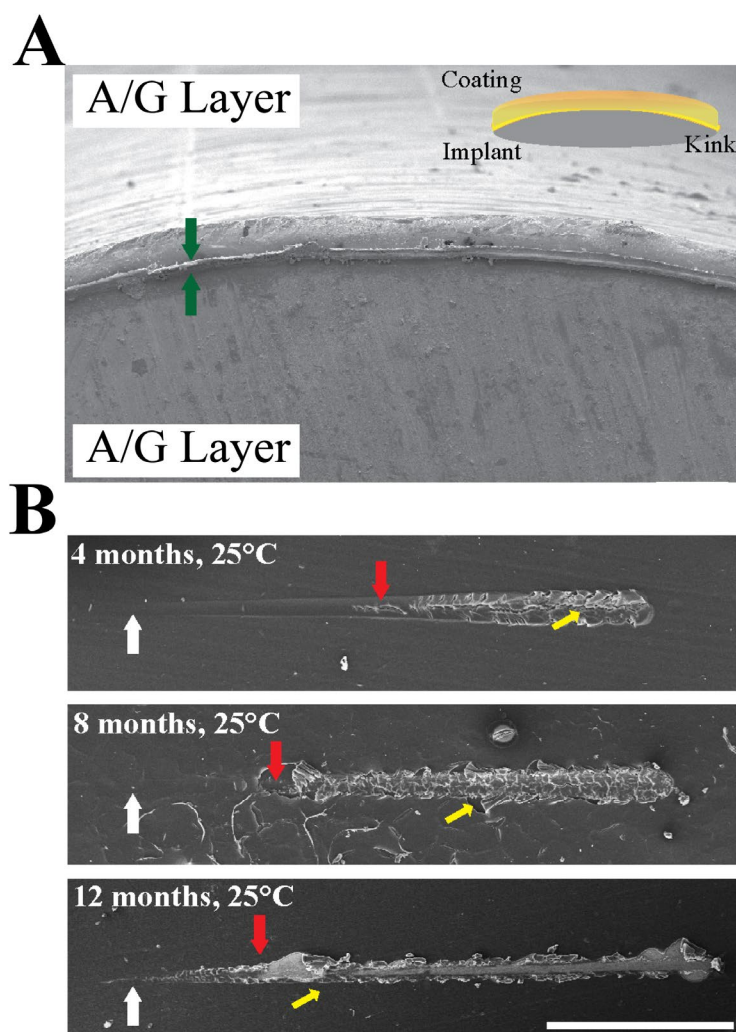


Figure 3.24 Representative SEM image of A/G 1:3 coatings demonstrating fine wrapping around a cylindrical implant with a small kink at the top (A) to determine coating thickness, and SEM images of scratched A/G 1:3 samples after shelf-life analysis (B). Scale bar for SEM images is 1 mm. White arrows indicate the start of scratching, red arrows demonstrate the locations of L_c for each coating, yellow arrows show end of the scratch test, and green arrows show the thickness of coating.

Table 3.9 Microscratch results of A/G 1:3 after incubation at room temperature for different periods (n=3).

Storage Period	L_c (N)	Thickness (μm)
As prepared	1.28 ± 0.32	16.41 ± 0.34
4 months	0.77 ± 0.20	25.13 ± 5.51
8 months	0.70 ± 0.30	24.21 ± 4.86
12 months	0.61 ± 0.32	24.83 ± 4.33

No significant difference was observed for L_c values and thicknesses.

3.3.3 Biological Characterization of A/G Coatings

Ti-APA was used as the control to study the effect of coating on cell behavior (Figure 3.25). hFOB growth on Ti-APA was significantly lower than coatings at all time points ($p < 0.05$). At the end of first day of incubation, cellular attachment on Ti-APA (9.19%) was lower than observed on A/G coatings (lowest attachment was 18.14% on A/G 1:1). This significant difference was maintained throughout the incubation periods. All A/G coatings prompted higher hFOB proliferation than Ti-APA. Additionally, A/G 1.5:3 supported higher cell growth compared to A/G 1:1 ($p < 0.001$).

Human osteoblasts were shown to adhere through integrins $\alpha v \beta 3$ and $\alpha 5 \beta 1$ on arginine-glycine-aspartate (RGD) sequences represented by gelatin (Davidenko et al., 2016). It was noted that increase in gelatin content in the coatings resulted in a positive effect on hFOB proliferation, whereas, alginate could not encourage osteoblast adhesion in spite of providing favorable physical and mechanobiological properties. In this sense, here, obtaining a 3D hydrogel layer containing gelatin at the

metallic surface was shown to improve cellular attachment and induce a remarkable increase in hFOB proliferation as early as day 1.

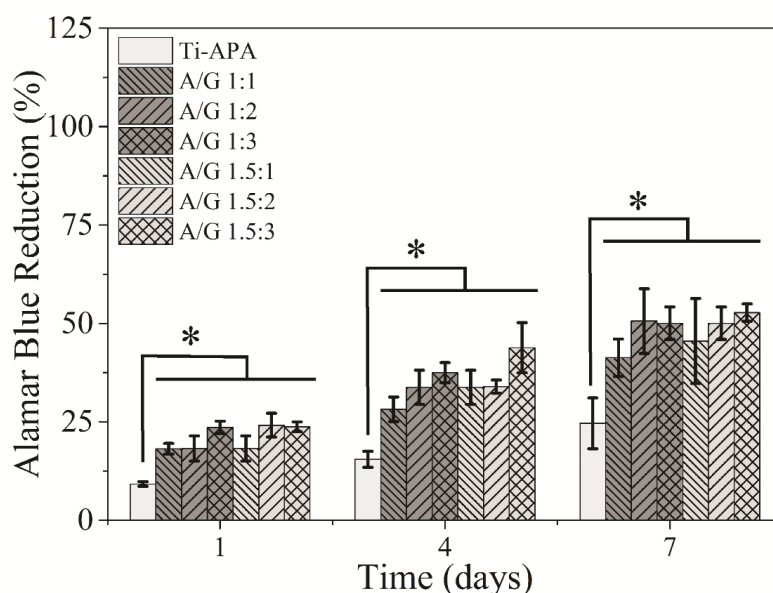


Figure 3.25 Proliferation of hFOB on Ti-APA and A/G coatings on Ti-APTES (n=8). Statistical differences among samples at given incubation period are denoted by * ($p<0.05$).

Cells seeded on Ti-APA samples were mostly present at the center of the implants where initial seeding (Day 1) was done (Figure 3.26). hFOB cells were not in spread morphology as can be seen in the images taken by CLSM. SEM images of hFOB on Ti-APA revealed that cells tend to establish low number of interactions initially on day 1. After 7 days of incubation, a cell monolayer was observed by CLSM. SEM images also showed spread morphology. On the contrary, A/G coatings showed cell sheets and higher number of hFOBs established cell-to-cell contacts. Moreover, cells colonized in the A/G coatings approximately 50 μm towards the Ti substrate at the end of 7th day. These observations by CLSM supported the SEM findings. A/G

coatings demonstrated large cell patches which were homogeneously distributed over the samples.

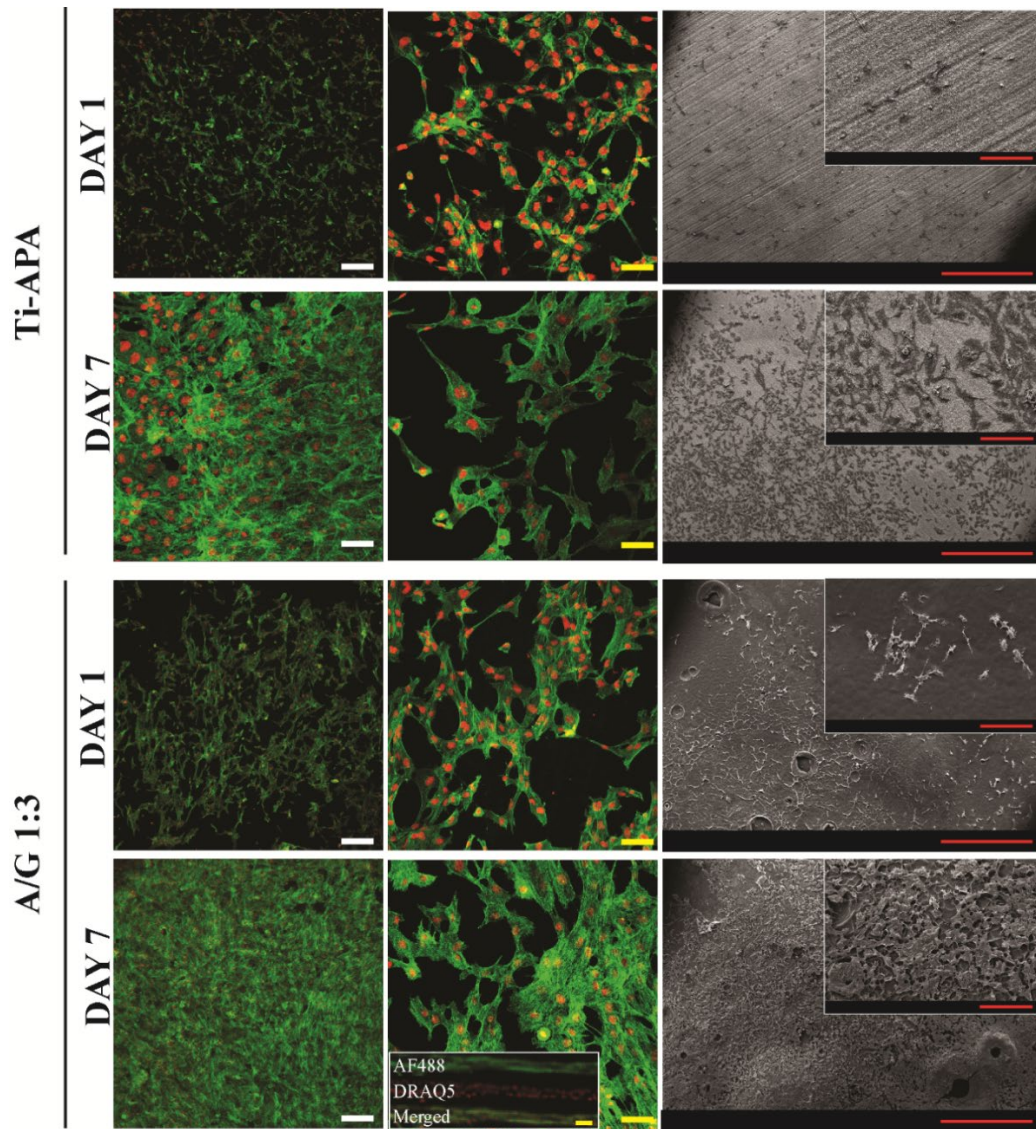


Figure 3.26 CLSM and SEM images of hFOB seeded on Ti-APA and A/G coatings after 1 and 7 days of incubation. hFOB on A/G coatings showed cell proliferation and migration into the coating layer as much as 50 μm . Highest cell density was observed on A/G coatings after 7 days. CLSM scale bars: White bar is 250 μm and yellow bar is 50 μm . SEM scale bars: Long red bar is 1 mm, short red bar is 200 μm .

3.4 Design Considerations and *In Vitro* Properties of A/G/BHT

Employing the similar coating procedure as given in part 3.32 “A/G Coating on Ti-APTES”, BHT was also introduced to the mixture and Ti-APTES implants were coated with A/G and A/G/BHT via dip-coating.

3.4.1 Rheological and Thermogravimetric Properties

Addition of NaCl in the pre-gels was shown to improve adhesion strength and allowed homogeneous coating on Ti-APTES. It was hypothesized that achieving lower viscosity in the composite pre-gels may grant an increment in the ability to flow and it could maintain a homogeneous dispersion of BHT reinforcement in the coatings. NaCl dissolution in the pre-gel was expected to trigger an expansion in terms of distance in between alginate chains (main contributor to viscosity) thus providing lesser chain entanglement (Doderio et al., 2020). In return, BHTs were anticipated to integrate in both intramolecular and intermolecular space occurring in alginate and gelatin dissolution. Rheological study revealed that a similar performance was observed in the case of composite coatings (Figure 3.27A). NaCl presence induced a dramatic decrease in the viscosity of the A/G/5BHT and A/G/10BHT pre-gels. All pre-gels exhibited shear-thinning property (Chen et al., 2020). Therefore, the results can be interpreted that BHTs may freely and evenly disperse in the pre-gels without bubbling and no local aggregations are expected to form during mixing. Furthermore, they could take part in crosslinking process and increase the cohesive strength of the coatings.

TGA analysis resulted in a close relationship between the theoretical content of BHTs (wt%) and the experimental result (Figure 3.27B). A/G/5BHT showed the same amount of BHTs as that of the expected value. However, A/G/10BHT demonstrated a significantly higher ratio of BHT (wt%) in the structure ($p=0.038$). Higher weight obtained than theoretical value after TGA analysis suggested that greater concentration of BHT was added in the pre-gels. In return, lower amount of

decomposition (lower weight loss) was detected. Nonetheless, inclusion of BHT at the final product in both A/G/5BHT and A/G/10BHT close to theoretical values validates the effectiveness of the coating method.

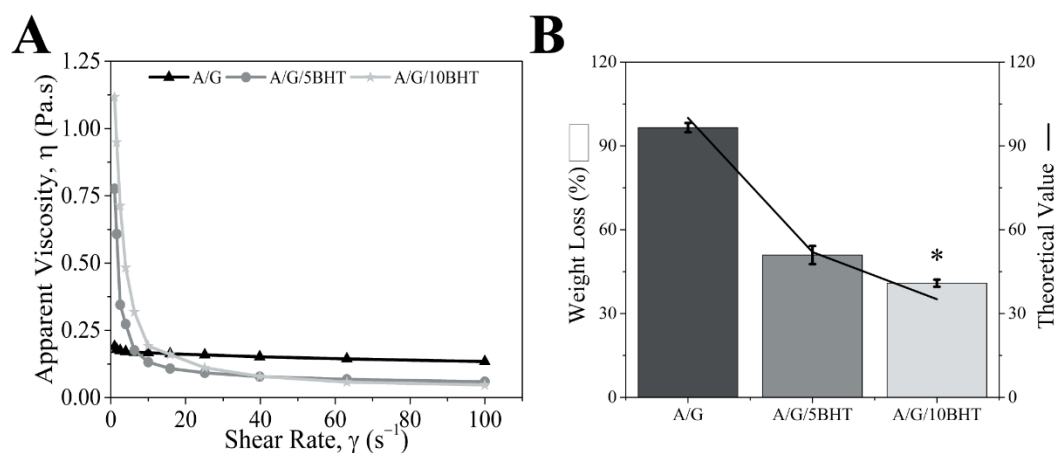


Figure 3.27 Apparent viscosity measurement of pre-gels (A) and TGA analysis of the coatings (B). Statistical differences were given as $*p<0.05$, $**p<0.01$ and $***p<0.001$.

3.4.2 Morphological Properties

In addition, morphological analysis of the coating revealed a crack-free and non-delaminated composite coating on Ti implant (Figure 3.28A and B). It was also observed well-spread BHT particles were present in A/G matrix. Within the coated layer, particles were clearly seen in the macroscopic images. However, SEM electrographs of both A/G/5BHT and A/G/10BHT showed a slight shrinkage and change in topography due to presence of bioceramic particles. It is thought that polymer chains were entangled around BHT particles and ionically crosslinked at a greater rate due to Ca^{2+} release from BHTs (Su et al., 2018). Therefore, accumulation

around BHTs revealed a dramatic change in topography. Nonetheless, these composite coatings were not cracked or delaminated after freeze-drying. They showed strong adherence to Ti-APTES surface similar to A/G coatings.

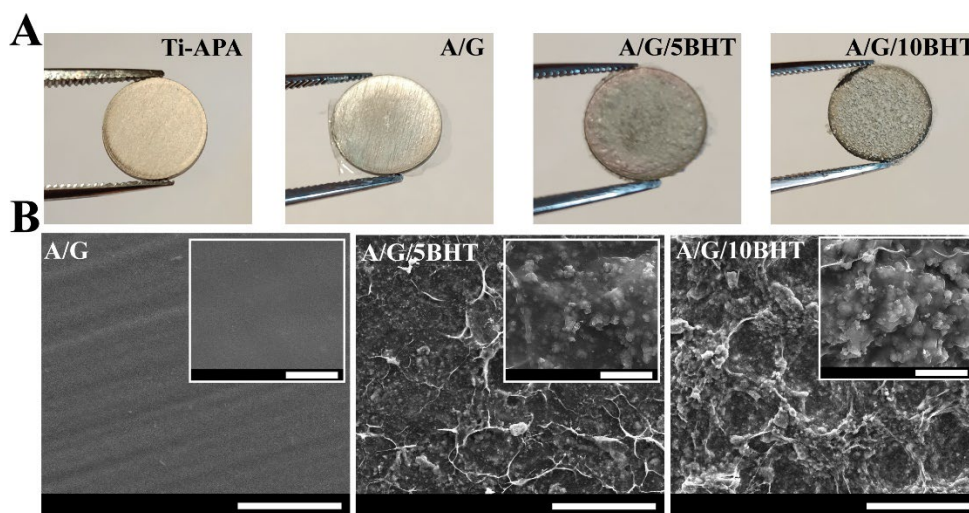


Figure 3.28 Macroscopic (A) and SEM images (B) of samples. Scale bar is 100 μm and inset scale bar is 20 μm .

3.4.3 Water Uptake and Hydrolytic Degradation Properties

When water uptake capacities of the coatings were analyzed, it was observed that they reached maximum swelling value as early as 24 h (Figure 3.29A). A/G samples showed highest water uptake while A/G/10BHT demonstrated lowest water uptake ($p < 0.05$). In terms of hydrolytic degradation over 4 weeks (Figure 3.29B), A/G/10BHT showed a significantly low rate of weight loss compared to A/G ($p = 0.01$), but no difference between A/G/5BHT and A/G/10BHT, and A/G/5BHT and A/G was observed. Another important point was that although an increasing rate of hydrolysis was observed for A/G/10BHT samples over 4 weeks, weight loss obtained at the end of 1st and 4th weeks did not exhibit any statistical difference ($p < 0.05$). Therefore, it can be concluded that slightly altered coating method

employed in the composite coatings brought about better stability and resistance to hydrolysis when A/G weight loss data for initial and pre-coating methods were compared. Because the proposed method led to ~60% weight loss over 4 weeks and pre-coating method resulted in only ~20% weight loss. However, higher swelling was observed in samples prepared with the altered method. This could be explained by the fact that the first layer of alginate and the main composite layer had swollen concurrently and increased the water uptake synergistically. Moreover, the presence of BHT was determined to further strengthen ionic interactions, and enhanced the rate of crosslinking due to probable higher compaction of polymeric chains in the vicinity of BHT particles.

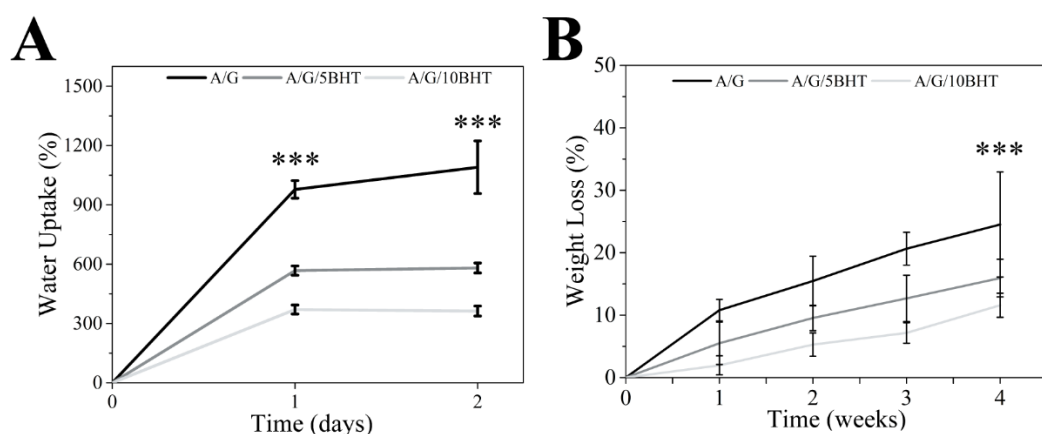


Figure 3.29 Water uptake (A) and hydrolytic degradation (B) results of the coatings (n=4).

3.4.4 Mechanical, Shelf-Life and Ion Release Properties

In addition to rheological and physical analyses, microscratch study revealed an improvement in mechanical properties (Table 3.10, Figure 3.30). Despite the fact that no significant increase was present, the pre-coating method improved L_c ($p=0.05$). On the other hand, A/G coatings produced with the pre-coating procedure exhibited the substantial increase in thickness. An alginate layer coated prior to the main composite coating of A/G might have caused a thicker layer absorbed on the implants and also potentially induced a higher crosslinking rate. Furthermore, utilization of BHTs in the composite coating strikingly enhanced the coating adhesion to the implant surface ($p=0.004$ for A/G/10BHT). The increment in L_c was stacking with the increase in BHT concentration. In parallel, coating thickness was significantly lower for A/G/10BHT coatings. This could be as a result of exceptional cohesive strength observed in these coatings (Maji et al., 2020). Since chains of the alginate tend to electrostatically and sterically reach in close proximity around BHT particles, coating might have shrunk in volume as well as showing lower rate of degradation and swelling. Therefore, thickness of A/G/10BHT was the lowest while their L_c was the highest ($p<0.05$).

Table 3.10 Results of microscratch analysis conducted on A/G coatings (n=3).

Coating	L_c (N)	Thickness (μm)
A/G	1.93 ± 0.32	16.41 ± 0.34
A/G – Pre-coating Method	2.17 ± 0.11	$70.90 \pm 0.19^{a,b}$
A/G/5BHT	2.64 ± 0.11^a	$90.83 \pm 6.34^{a,b}$
A/G/10BHT	$3.33 \pm 0.17^{a,b}$	33.41 ± 17.92

^a Statistically higher value observed compared to A/G.

^b Statistically highest value in the particular analysis.

Scratch paths were inspected to determine the type of failures observed on various composite coatings. Similar to the findings acquired during microscratch analysis of A/G coatings, cohesive failure was observed (Figure 3.30). From the start point (white arrows) up until to the end point (yellow arrows), all samples showed no delamination or cracking beyond the scratch path. Moreover, presence of BHT affirmed that coating strength was exceptionally improved, thus break in the coatings was observed at a later point on the A/G/5BHT and A/G/10BHT samples (red arrows). Similar to that of A/G coatings, A/G/BHT samples also revealed non-adhesive failure. It can be concluded that A/G/BHTs can be produced successfully without sacrificing mechanical properties or homogeneity.

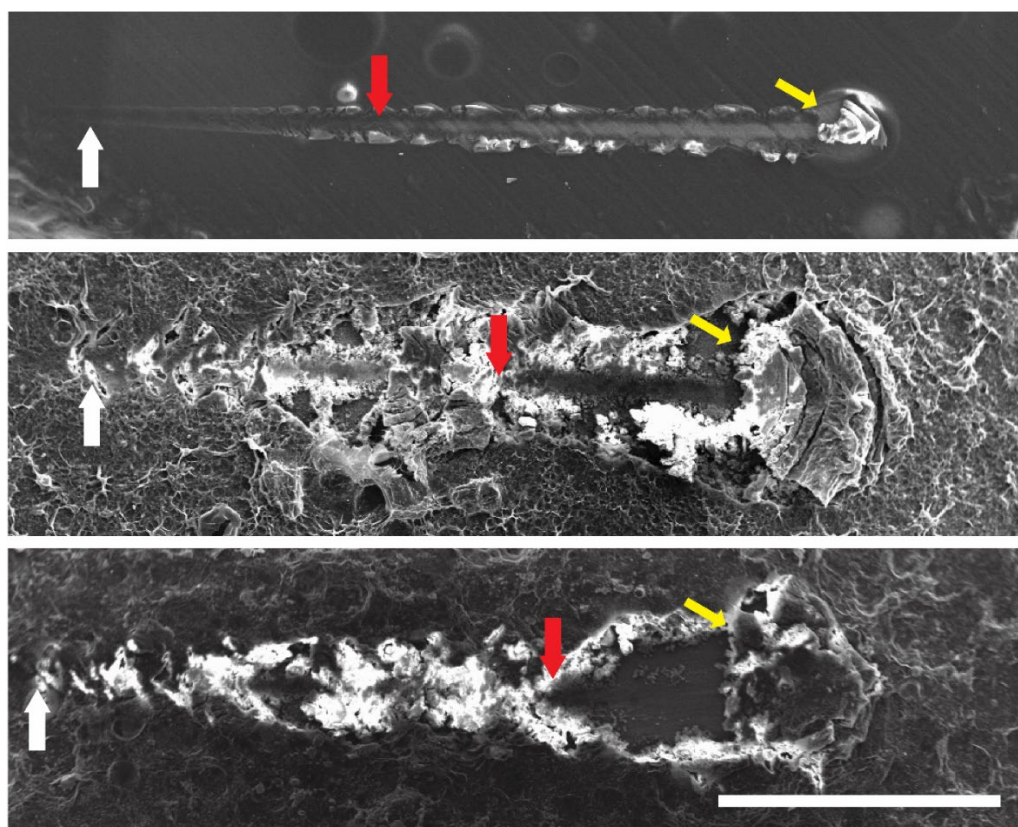


Figure 3.30 SEM images of scratched A/G coatings on Ti-APTES. White arrows indicate the start of scratching, red arrows demonstrate the locations of L_c for each coating, and yellow arrows show the end of the scratch test. Scale bar is 1 mm.

As stated in the Materials and Methods section, A/G/10BHT demonstrated good performance overall and it was selected as the representative group for A/G/BHT. A/G/BHT coatings were stored at 25°C for 8 months to determine shelf-life of the coatings (Table 3.11, Figure 3.31). Similar to the data obtained in Table 3.10, as-is A/G/BHT coating resulted in significantly higher mechanical strength compared to A/G ($p < 0.001$). This trend was followed until the end of 8th month period. Interestingly, all of the samples exhibited similar thickness values with a slight increase over time probably as a result of moisture leading to expansion in the polymer chains. Moreover, failure modes were similar to as-is coating and none of the samples led to delamination, thus proving that the coatings strongly adhere to implant surface and show exceptional cohesion.

Table 3.11 Microscratch testing of A/G and A/G/BHT for determination of coating strength and shelf-life (n=3).

Samples		L _c (N)	Thickness (μm)
As is	A/G	1.72 ± 0.11	57.74 ± 13.39
	A/G/BHT	2.66 ± 0.10 ***	68.85 ± 13.84
4 months stored	A/G	1.32 ± 0.19	63.73 ± 2.68
	A/G/BHT	2.48 ± 0.07 ***	69.27 ± 4.47
8 months stored	A/G	0.63 ± 0.04	65.25 ± 17.48
	A/G/BHT	1.78 ± 0.25 ***	89.80 ± 1.65

*** A/G/BHT demonstrated significantly higher adhesive strength.

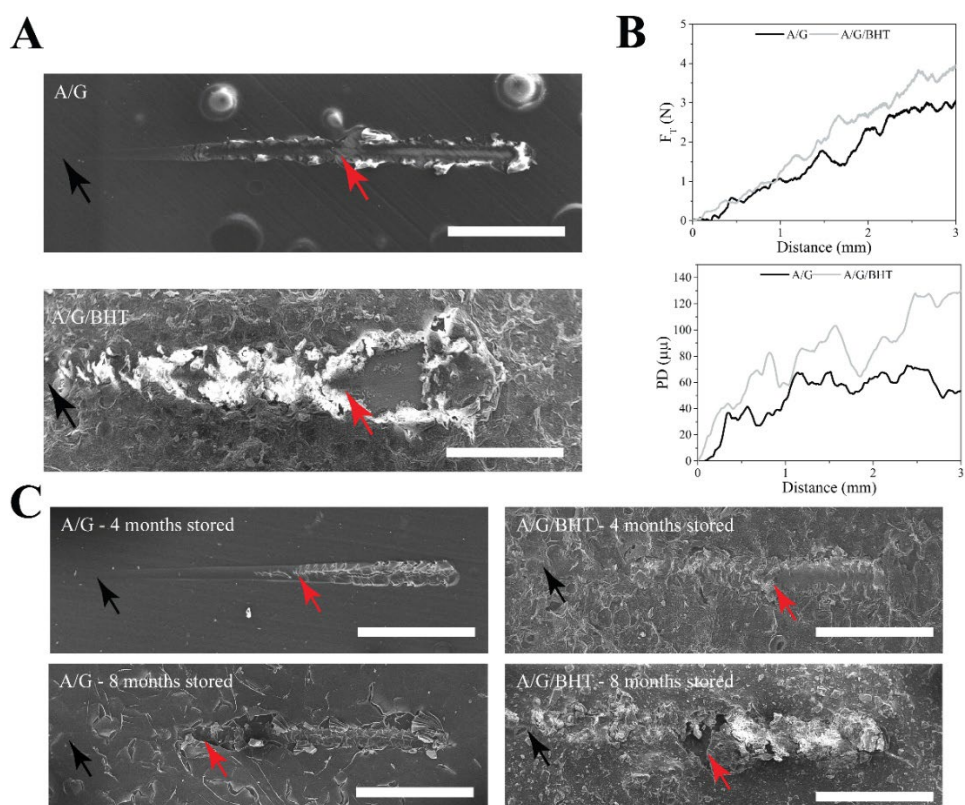


Figure 3.31 SEM images taken during microscratch testing. As-is images (A), accompanying F_T and PD data measurements to determine L_c and thickness (B), and images of resultant surfaces at the end of each period of shelf-life analysis (C). Black arrows indicate the starting point of scratching and red arrows show the point where tip reached the bottom surface. Scale bars are 1 mm.

Besides structural, mechanical and physical properties, ion release characteristics of the coating revealed that A/G/BHT could provide a continuous release of Ca and B for two weeks (Table 3.12). Ca release from A/G/BHT was highest for all periods ($p < 0.001$). It should also be noted that there is a small increase in B release overtime. This could be as a result of B taking part in the physical crosslinking of ALG chains in addition to Ca. Nevertheless, A/G/BHT acted as a reservoir allowing bioactive Ca and B release throughout the study.

Table 3.12 Cumulative release of Ca and B from A/G and A/G/BHT (n=3).

Sample	Day 1		Day 7		Day 14	
	Ca (mg/L)	B (mg/L)	Ca (mg/L)	B (mg/L)	Ca (mg/L)	B (mg/L)
A/G	7.4 ± 0.1	0	45.3 ± 1.04	0	84.4 ± 3.2	0
A/G/BHT	96 ± 2	0.41 ± 0.1	251 ± 3	1.1 ± 0.2	286 ± 3.6	1.53 ± 0.2

HT showed highest Ca release while only BHT showed B release.

Prior to analyzing the effect of samples on osteogenic differentiation of hFOB, cells were seeded on the samples and cell proliferation was analyzed (Figure 3.32A). A/G/BHT resulted in strikingly higher cell attachment as early as Day 1 compared to Ti-APA ($p<0.001$) and A/G ($p<0.01$). This trend continued on the 7th day of incubation as A/G/BHT demonstrated highest cellular proliferation compared to other samples ($p<0.001$). Furthermore, owing to surface roughness and release of osteogenic ions such as Ca, P and B, A/G/BHT might have resulted in significantly the highest cellular growth compared to Ti-APA and A/G ($p<0.001$). Osteoblasts appeared separate, they did not assume spindle-like morphology and proliferated on all surfaces effeciently (Figure 3.32B and C). Despite this, Ti-APA failed to bring about multilayered colonization as effectively as A/G or A/G/BHT (Figure 3.32C). hFOBs on A/G/BHT surfaces additionally produced larger lamellopodia and completely spread on the coated layer. Collectively, the results exhibited the ability of coatings to induce osteoblast attachment and growth.

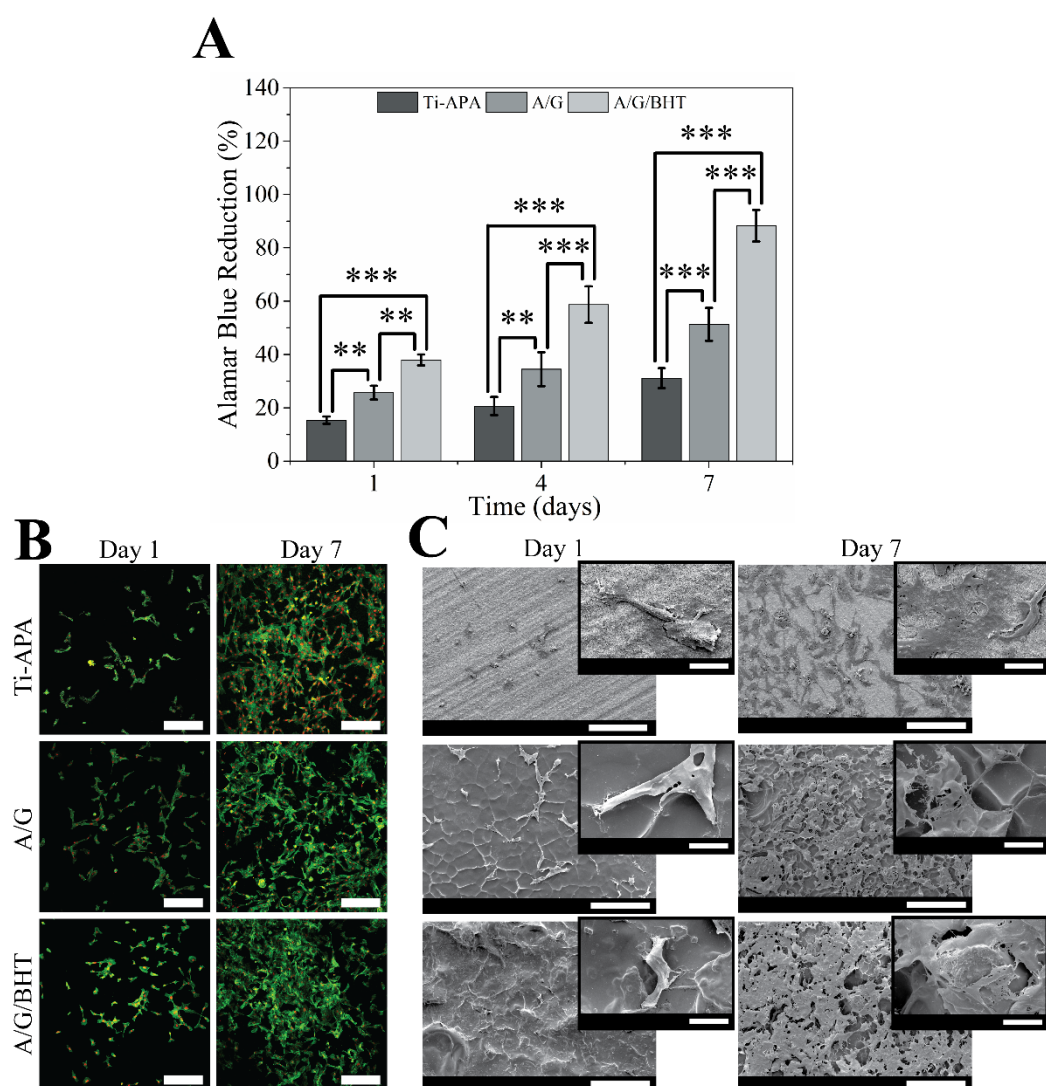


Figure 3.32 Results of Alamar Blue study (n=12, A), CLSM (B) and SEM (C) analyses for characterization of hFOB attachment and proliferation on various surfaces. Scale bar in part B is 450 μm , scale bar in part C is 200 μm and inset bar is 20 μm . Statistical differences are given as $*p<0.05$, $**p<0.01$ and $***p<0.001$.

3.4.5 Osteogenic Properties

Osteogenic differentiation analysis was conducted at protein and gene expression levels. ALP activity analysis revealed similar results for A/G and A/G/BHT samples while A/G/BHT resulted in significantly higher activity compared to Ti-APA ($p=0.046$) in the 1st week (Figure 3.33A). At the end of 2nd week, A/G/BHT demonstrated the highest ALP activity in comparison to that of A/G and Ti-APA ($p<0.001$). Comparing A/G and Ti-APA, A/G displayed higher ALP activity ($p=0.008$). With early marker ALP, OCN was also determined as a late marker of osteogenesis. As ECM is deposited with CaP, OCN is actively upregulated and released to ECM (Duman et al., 2019). Interestingly, OCN presence in ECM during osteoblast maturation also leads to competition with ALP to bind CaP deposits to prevent phosphatase activity and reinforce rapid biomineralization. In this context, ALP and OCN content in the ECM could change inversely, however, this may not be the case intracellularly. A/G/BHT induced greater OCN release to ECM, but this did not result in any statistical difference between the groups at the end of 1st and 2nd weeks (Figure 3.33B). Specifically, A/G/BHT resulted in a higher value in comparison to A/G ($p=0.133$) and Ti-APA ($p=0.052$).

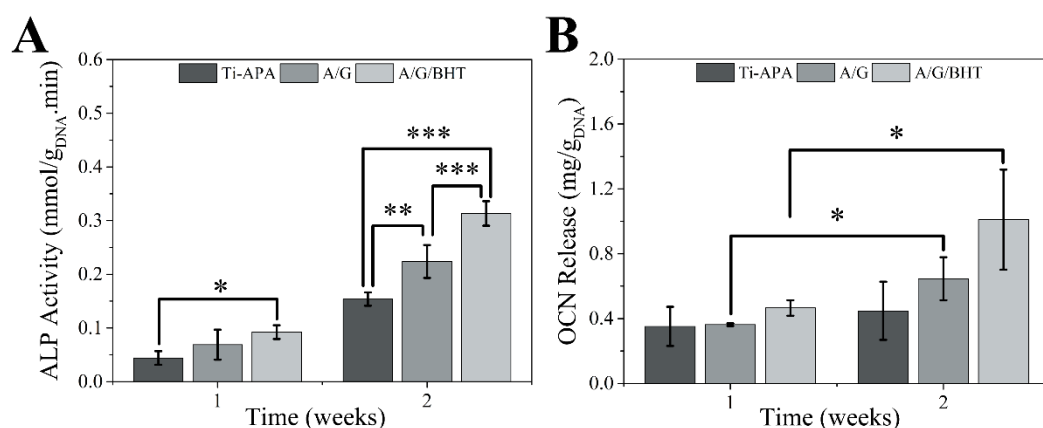


Figure 3.33 Osteogenic differentiation of hFOB seeded on Ti-APA, A/G and A/G/BHT analyzed in terms of ALP activity (n=12, A) and OCN release (n=6, B). Statistical differences are denoted by * $p<0.05$, ** $p<0.01$ and *** $p<0.001$.

Following the quantification of osteogenic proteins produced during differentiation analysis, qPCR study was conducted (Figure 3.34). ALP gene expression analysis demonstrated statistically insignificant difference among samples at the end of both 1st and 2nd weeks (Figure 3.34A). It should be noted that A/G/BHT provided greater ALP expression at the end of the 1st week, but all samples demonstrated a significant increase at the end of 2nd week ($p<0.001$). Another important early marker, RUNX2, was also studied in qPCR study (Figure 3.34B). It was observed that, like ALP expression, RUNX2 was the highest in cells incubated on A/G/BHT while there was no statistical difference. At the end of 2nd week, A/G/BHT triggered lower RUNX2 expression in comparison to other samples.

Smad4, and late osteogenic markers such as BMP-2, OSX and OCN were also analyzed by qPCR studies to establish overall osteogenic effect of BHT presence in A/G coatings (Figure 3.34). Cells on A/G/BHT induced a significant increase in Smad4 expression in 1st week, however, this trend discontinued in 2nd week ($p<0.001$, Figure 3.34C). Although not significant, both Ti-APA and A/G increased

the rate of Smad4 expression towards the 2nd week while A/G/BHT showed a clear decrease. Since Smad4 was found to reinforce biomineralization acting as signal transducer in BMP-2 pathway, taking part in TGF- β signaling cascade and maintaining bone mass (Morita et al., 2016).

In contrast, all late osteogenic markers analyzed in this study collectively resulted in the highest values for the hFOBs on A/G/BHT (Figure 3.34D-F). Although Ti-APA appeared to trigger a higher rate of BMP-2 expression at the end of 1st week, A/G/BHT surpassed both Ti-APA and A/G at the end of 2nd week and resulted in statistically higher BMP-2 expression ($p < 0.05$ vs Ti-APA and $p < 0.01$ vs A/G, Figure 3.34D). A similar trend was observed for both OSX and OCN expressions. A/G/BHT enhanced OSX expression more significantly than the counterparts ($p < 0.05$, Figure 3.34E) and also induced tremendously higher OCN expression compared to A/G ($p < 0.001$, Figure 3.34F). This improvement observed for all late osteogenic markers could be explained by the fact that A/G/BHT has been shown to have higher roughness and mechanical strength compared to A/G. Similarly, Ti-APA demonstrated submicron roughness, however, it had tremendously high surface stiffness compared to the composite hydrogel-based coatings. Interestingly, it should be stressed that Ti-APA was prepared through highly standardized implant surface treatment methodology which is applied universally, and as a result, APA might have brought about an increment in the expression of genes which are involved in osteogenic maturation through mechanotransduction (Liu et al., 2015; Moon et al., 2018). However, taking into account the release of ions such as Ca, P and B playing role in osteogenic phenotype shift (Gizer et al., 2020) in addition to surface characteristics, A/G/BHT led to a greater rate of osteogenic gene expression. Presence of these ions might have led to higher gene expression of ALP and OCN, as well as their production by the cells. In this context, because BMP-2 involves in osteogenic differentiation through collagen mineralization and suppressing osteoclastogenesis (Tenkumo et al., 2018) and OSX is an important gene taking part in osteoblast maturation and ECM development (Shekaran, et al., 2014), it was observed that these markers were high in A/G/BHT coatings.

In another aspect, early stage of osteogenic commitment could be signaled by a rapid surge in Smad4 expression followed by significant decrease upon osteoblastogenesis and this is paralleled by a decrease in RUNX2 expression as osteoblast commitment is completed (Yan et al., 2018). Therefore, it can be concluded that hFOBs on A/G/BHT upregulated osteogenic genes more compared to the other samples and it could corroborate the favorable results obtained in osteogenic protein production for A/G/BHT samples.

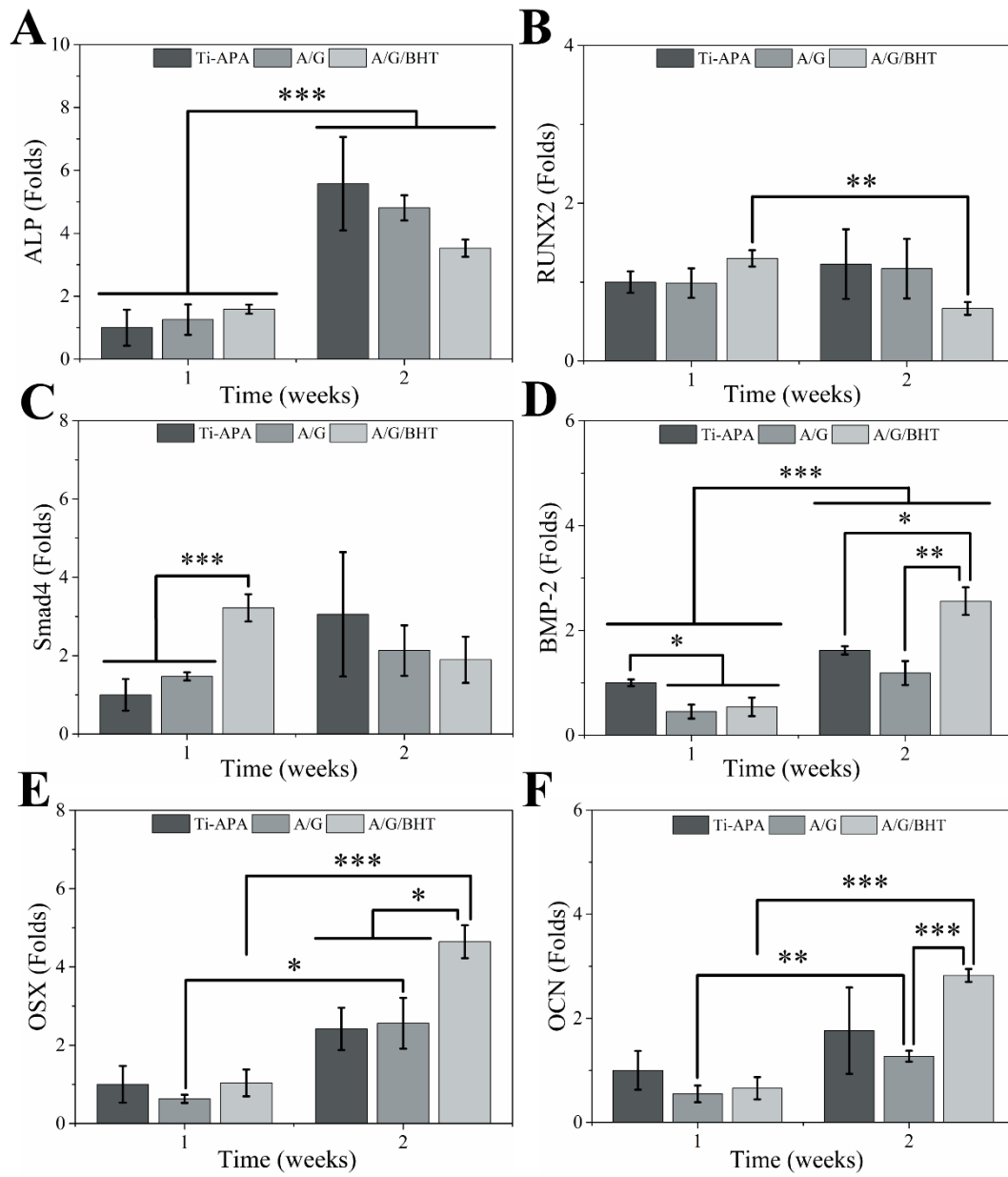


Figure 3.34 Osteogenic ALP (A), RUNX2 (B), Smad4 (C), BMP-2 (D), OSX (E) and OCN (F) gene expression analysis of Ti-APA, A/G and A/G/BHT using qPCR (n=6). Statistical differences are denoted by * $p<0.05$, ** $p<0.01$ and *** $p<0.001$.

3.4.6 Angiogenic Properties

The ability of a surface to accommodate endothelial cell and support its growth play a vital role in implant osseointegration. Establishment of vascularized tissue around the newly developed bone tissue at the implant-bone interface could provide a continuous highway for nutrient and gas exchange while balancing pH and removing wastes (Farzin et al., 2021). In this study, HUVECs were utilized to determine the ability of A/G/BHT to induce angiogenic response (Kocherova et al., 2019). It was determined that HUVECs could proliferate and grow on all samples (Figure 3.35). However, a significant decrease in HUVEC viability on A/G and A/G/BHT was observed at the end of 7th day of incubation. Thus, VEGF-A detection was conducted at the end of 4th day of incubation due to having highest cell number on all samples (Dashnyam et al., 2019).

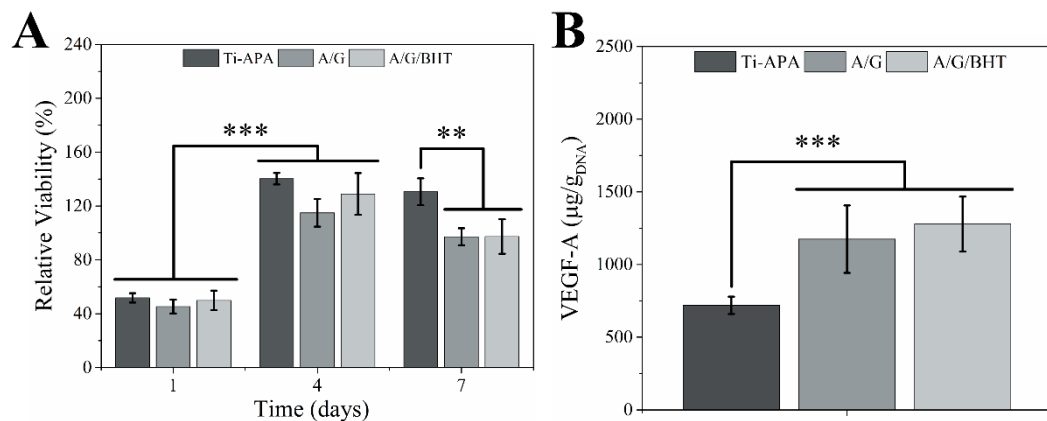


Figure 3.35 HUVEC proliferation over time on Ti-APA, A/G and A/G/BHT surfaces (n=4, A) and total VEGF-A at 4th day of incubation (n=5, B).

When compared, A/G/BHT and A/G revealed similar total VEGF-A, which is significantly higher compared to Ti-APA despite similar the rate of HUVEC

proliferation on all samples (Figure 3.36). Morphologically, all samples resulted in healthy HUVECs growing on their surfaces at the end of 4th day, however, CLSM images revealed that both A/G and A/G/BHT demonstrated colony-like formations on surfaces, which were strikingly different than Ti-APA. SEM images demonstrated HUVECs on both samples forming small multi-layered agglomerates and slightly forming into tubular structures (Trujillo et al., 2020).

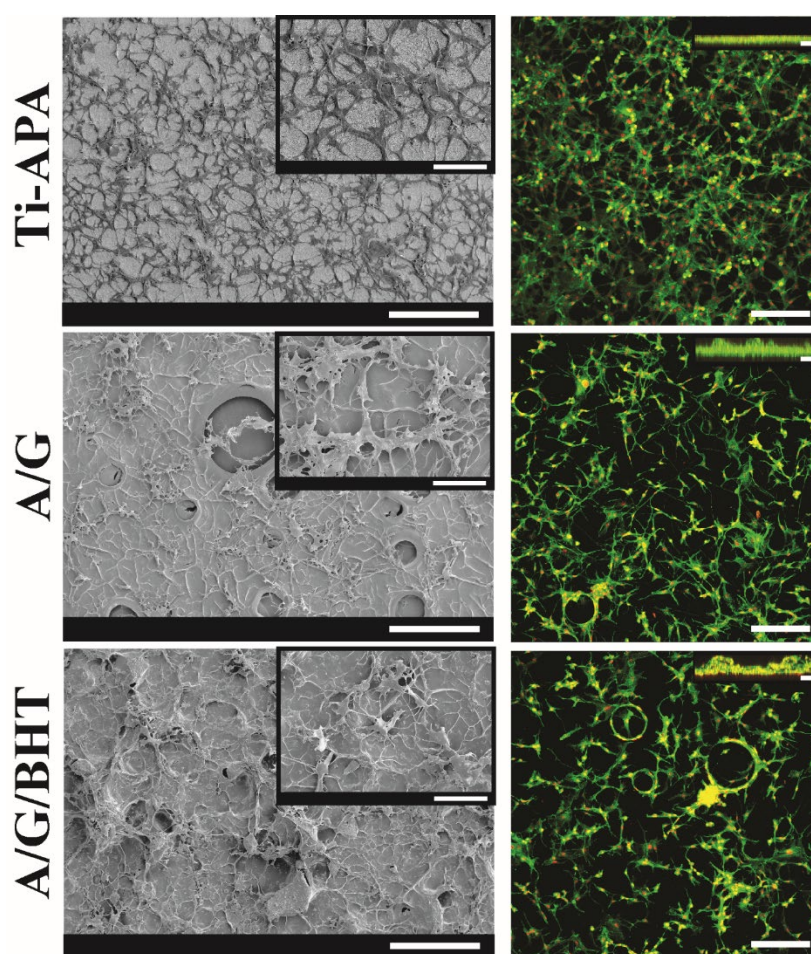


Figure 3.36 SEM and CLSM images obtained during angiogenesis study. Images were obtained at the 4th day of incubation. CLSM scale bar is 450 µm, SEM scale bar is 200 µm and inset bar is 20 µm.

In a recent study by da Silva Sasso et al. (2021) successfully determined spatiotemporal colocalization of VEGF-A with important osteogenic markers such as RUNX2 and OSX during bone development (da Silva Sasso et al., 2021). They further reported that osteoblastogenesis is accompanied with VEGF-A secretion, however, osteoclasts could dampen angiogenesis. In this context, implant coatings that are designed to induce ossification at the defect site could be designated as the next generation multifunctional coatings. Thus, induction of angiogenic processes concurrently with osteoblastogenesis may demonstrate the immense potential of a given implant surface. Similar to the aforementioned study, Geng et al. (2021) showed that BMP-2 and VEGF-A are colocalized in osteoblasts during biomineralization, and it also enhances OCN expression, but did not significantly reinforce RUNX2 expression (Geng et al., 2021). In the proposed coating, namely A/G/BHT, highest VEGF-A release was achieved in spite of no statistical difference compared to A/G ($p>0.05$). Morphologically, multilayered HUVEC growth accompanied by tubular formation on A/G/BHT samples could further corroborate high angiogenic potential, in addition to osteogenic properties. Therefore, osseointegration, which could be realized as an outcome of multiple concurrent events, may be achieved after A/G/BHT coating on Ti-based implants.

3.4.7 Immunomodulatory Properties

Similar to the immunomodulatory studies conducted using HT and BHT, here THP-1s were seeded on Ti-APA, A/G and A/G/BHT to determine the viability of macrophages on coatings and immunomodulatory potential of the coatings. It was first detected that both A/G and A/G/BHT resulted in a decrease in macrophage viability (Figure 3.37). In addition, it was further detected that Ti-APA drastically hampered macrophage viability by more than 20% within 24 h.

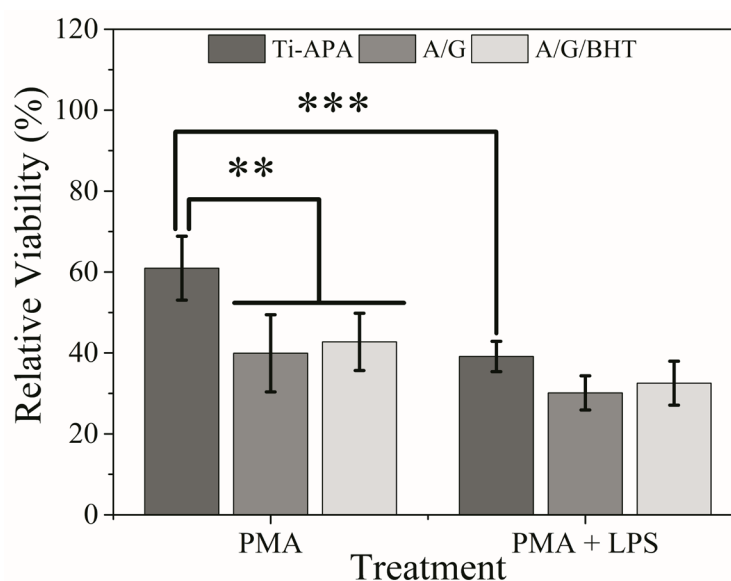


Figure 3.37 Relative viability of THP-1s incubated on samples under various conditions (n=6). Statistical differences are denoted by $*p<0.05$, $**p<0.01$ and $***p<0.001$.

Interestingly, Ti-APA allowed the highest THP-1 colonization without LPS priming ($p<0.01$) while coatings prevented THP-1 adhesion unlike Ti-APA (Figure 3.38). SEM images demonstrated that THP-1s formed into clusters and maintained round morphology. It is also apparent that Ti-APA surfaces were much more provocative towards THP-1s in comparison to A/G and A/G/BHT counterparts. On the other hand, THP-1s tended to alter their morphology under various conditions such as bare samples and treatment with LPS. Among these samples, A/G/BHT was revealed to protect the round morphology of THP-1s compared to A/G. Moreover, THP-1s on A/G/BHT coatings appeared in rounder morphology and more stable that there was no extensive cell damage observed in opposed to THP-1s incubated with A/G coatings.

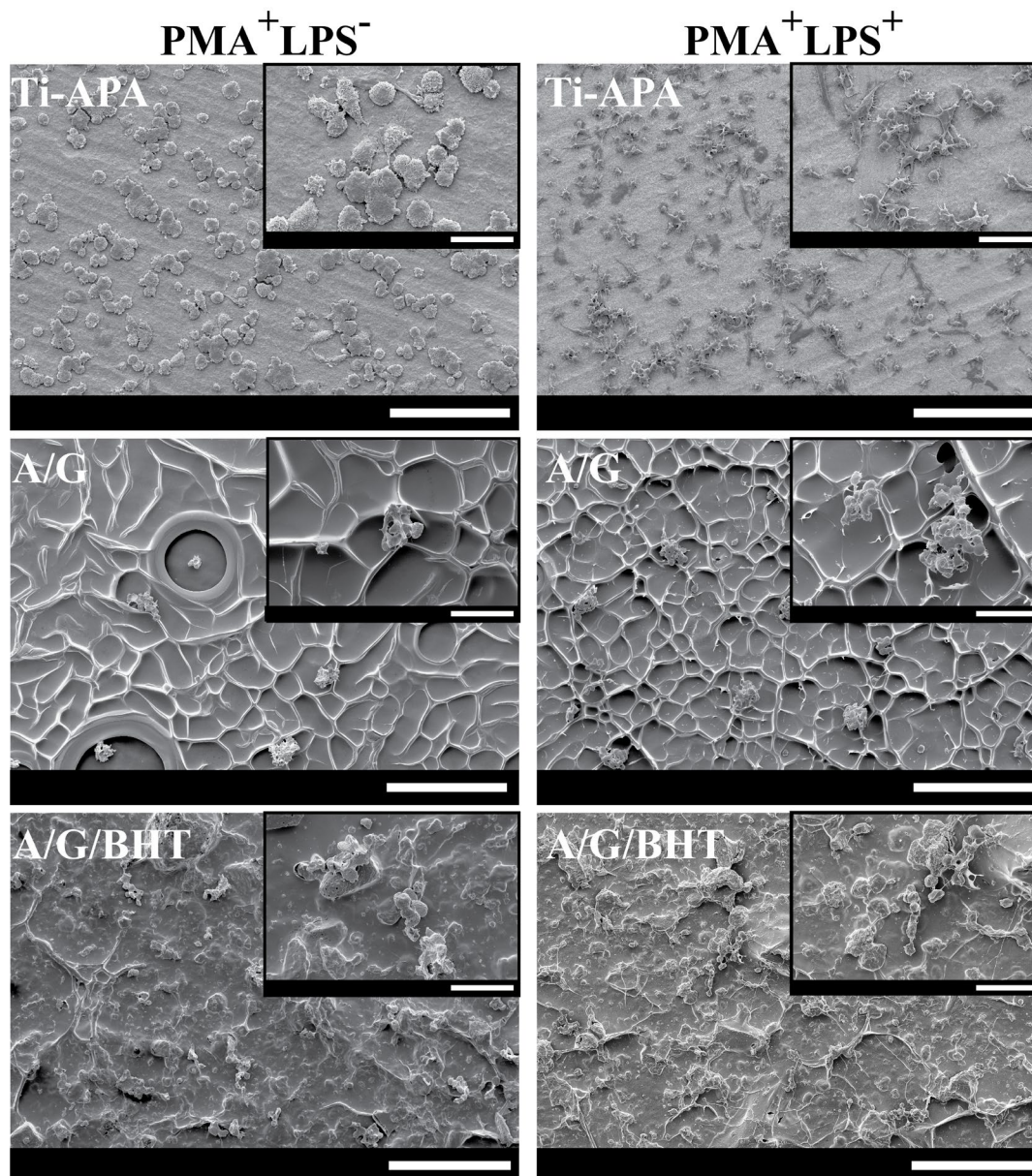


Figure 3.38 SEM electrographs of THP-1s incubated on samples under two different conditions. Cells on Ti-APA showed colonization in a larger area than other samples and cells appeared separate. A/G and A/G/BHT led to clustered appearance of THP-1s which colonized their surface. Ruffled appearance of THP-1s on Ti-APA after $\text{PMA}^+ \text{LPS}^+$ shows extensive inflammatory action. Scale bars in large electrographs are 200 μm , and scale bar in insets are 50 μm .

Pyroptotic CAS-1 (Vande Walle & Lamkanfi, 2011) release by A/G and A/G/BHT was significantly higher compared to Ti-APA ($p<0.001$, Figure 3.39A). After introducing LPS to simulate aggravated inflammatory response (Coullin et al., 2013), Ti-APA brought about 134% increase in CAS-1 production, and A/G and A/GBHT triggered 78% and 53% increase, respectively (Figure 3.39A). Furthermore, primed samples with LPS exhibited a significant increase in IL-10 release, a pro-healing cytokine (Tan & Al-Rubeai, 2021), compared to non-primed samples. Although no significant difference among groups was observed, A/G/BHT revealed the highest increase in IL-10 production (Figure 3.39B). In terms of inflammation-related protein productions, A/G/BHT demonstrated an increase in early response, however, also improved anti-inflammatory protein production. This could infer that A/G/BHT could maintain an immunomodulatory environment without suppressing initial inflammatory response which is much needed to employ antibacterial measures and induce pro-healing cascades.

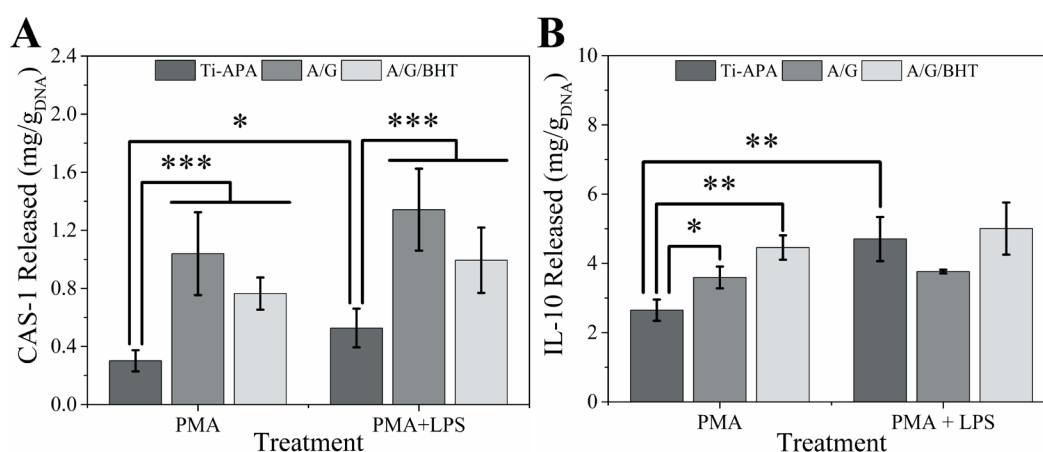


Figure 3.39 Immunomodulatory properties of Ti-APA, A/G and A/G/BHT samples. CAS-1 and IL-10 releases were determined via ELISA (n=4). Statistical differences are denoted by * $p<0.05$, ** $p<0.01$ and *** $p<0.001$.

In addition to the protein production, inflammatory gene expression analysis was conducted (Figure 3.40). Expression analysis showed that both coatings induced higher NfκB expression (Figure 3.40A). NfκB is a modulator in inflammatory response and also it is an important player in osteoblast and osteoclast activities (Lin et al., 2017). It is inducible by excess Ca^{2+} , pathogen associated molecular patterns (PAMPs) and damage associated molecular patterns (DAMPs) such as membrane residues, RNAs, DNA of the surrounding native cells (Yu et al., 2021). NfκB upregulation causes pyrin domain-containing protein 3 (NLRP3) and subsequent recruitment of inflammasome production that involves in CAS-1 maturation and IL-1 β production to mount pyroptotic activity. Overexpression of IL-1 β was reported to decrease RUNX2 and OCN expression while increasing RANKL production in a study by Li et al. (2019) (Li et al., 2019).

Interestingly, it was also discussed in the literature that a mild pyroptotic and inflammatory response may be required for tissue regeneration and mounting pro-healing response (Liu et al., 2018; Sun, et al., 2021; Wang, et al., 2021). In addition, the osteoimmunomodulatory surfaces were also demonstrated to favor the upregulation of osteogenic/angiogenic markers such as BMP-2, ALP and VEGF-A (He et al., 2021). It was also observed that angiogenic response could be generated as iNOS and IL-1 β were downregulated while IL-10 and VEGF-A were upregulated, however, both pro- and anti-inflammatory genes as well as pyroptotic genes were shown to be maintained (Chen et al., 2021; Ding et al., 2021; Peng et al., 2021). In summary, reinforcing a key gene acting as a switch to mount rapid inflammatory response could be interpreted as the fact that A/G and A/G/BHT may demonstrate high innate immune answer towards early invasion and damage around the implants. Further analyzing genes such as CAS-1 and IL-1 β , Ti-APA showed higher CAS-1 expression without any statistical differences (Figure 3.40B and C).

On the other hand, Ti-APA demonstrated a lower expression of IL-1 β in comparison to A/G ($p < 0.01$) while a similar value was obtained with A/G/BHT. In the sense of acute answer to damage or bacterial invasion at peri-implant area, despite all samples

showing good answer, A/G appeared to incite slightly more prominent response. When IL-10 and iNOS expressions were taken into account after LPS trigger, A/G/BHT demonstrated clearly higher IL-10 expression while having comparable iNOS expression with other samples (Figure 3.40D and E). Despite the fact that no statistical difference was observed between samples, A/G led to higher iNOS expression compared to Ti-APA and A/G/BHT. Comparing these results with IL-10 production as aforementioned, there was no clear indication of direct effect of coatings in terms of protein production. Nevertheless, coatings, especially A/G/BHT, exhibited good tendency to support pro-healing response and ability to mount a limited and an acute response at peri-implant area. Presented results are found to be in parallel with literature and A/G/BHT could exhibit immunomodulatory activity to support rapid bone healing around implants.

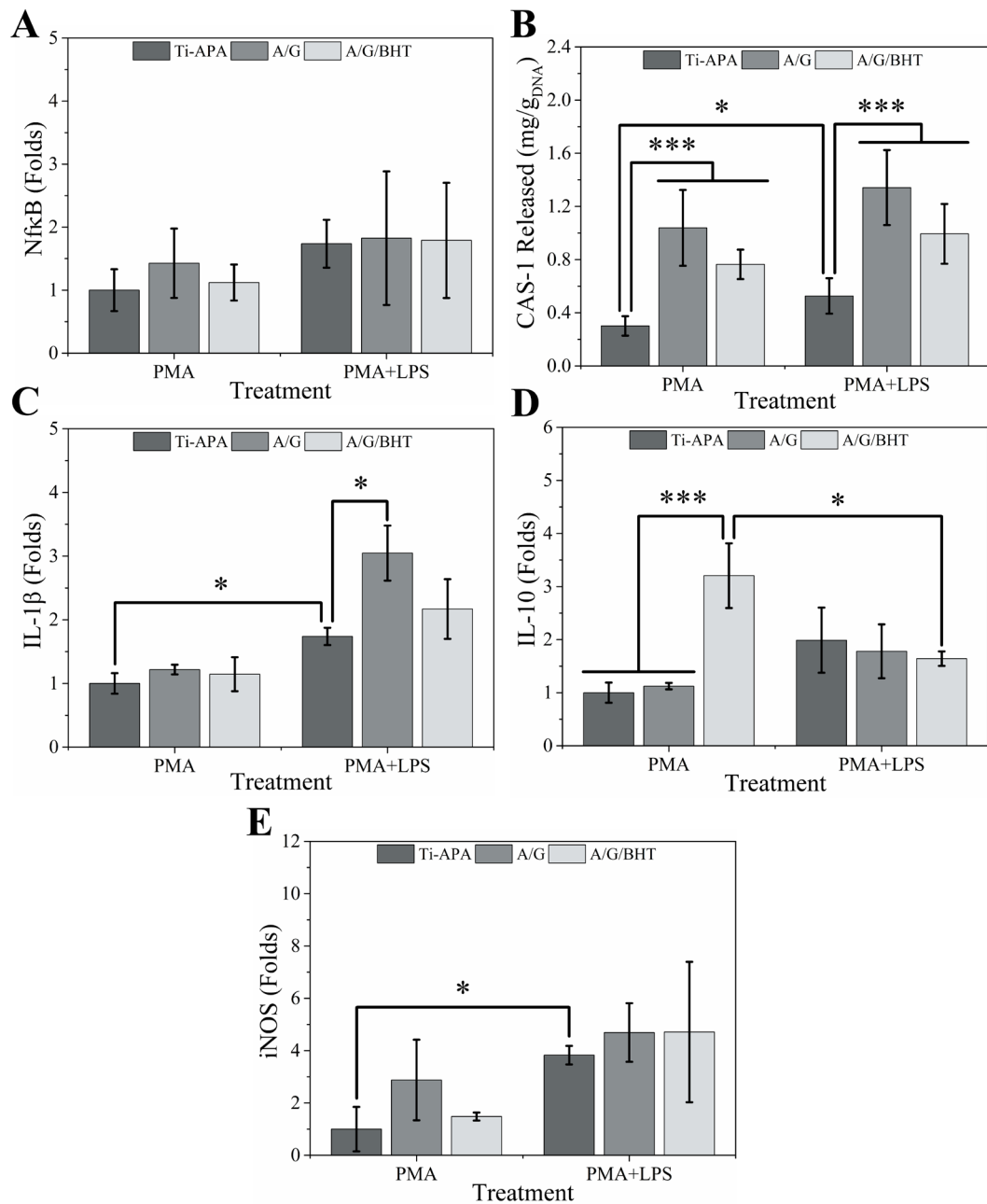


Figure 3.40 Immunomodulatory properties of Ti-APA, A/G and /A/G/BHT in terms of gene expression. Changes in gene expression of THP-1s on different surfaces and under inflammatory condition were detected by qPCR study (n=4). Statistical differences are denoted by * $p<0.05$, ** $p<0.01$ and *** $p<0.001$.

In a recent and very interesting study, Tan et al. (2020) coated alkali-heat treated Ti implant surface with *Lactobacillus casei* and UV irradiated to establish an inactivated biofilm layer (Tan et al., 2020). They aimed to induce rapid macrophage colonization, prevention of film formation while deterring methicillin-resistant *Staphylococcus aureus* adhesion (MRSA), and then release of potent osteogenic cytokines from macrophages to drive osseointegration. In a similar context, our A/G/BHT coated layer demonstrated a good potential in terms of provoking a strong innate immune response which could be rapidly resolved into pro-healing/regenerative phenotype, in addition to osteogenic and angiogenic properties. Hence, the versatility of the proposed gap-filling composite coating had been proven. As a promising interphase structure, the structural, morphological, mechanical and chemical properties of the coatings were presented and discussed previously. Among these, A/G/BHT samples exhibited high mechanical strength, cohesiveness, and surface roughness. These samples also demonstrated high capacity to support cell adhesion and growth. Furthermore, these coatings could be used as reservoir for multifunctional custom-made peptides, antibacterial agents, regenerative factors or disease-specific drugs such as anti-osteoporotic agents so that they may be released with greater control in terms of rate and concentration directly at the defect zone.

3.5 Osseointegration of A/G/BHT In Rabbit Femur Osteochondral Defect Model

Implants were tested in a rabbit femur osteochondral unicortical defect model to determine *in vivo* performance (Figure 3.41A). At the end of pre-determined test periods, samples were collected and sectioned in longitudinal axis as given in Figure 3.41B.

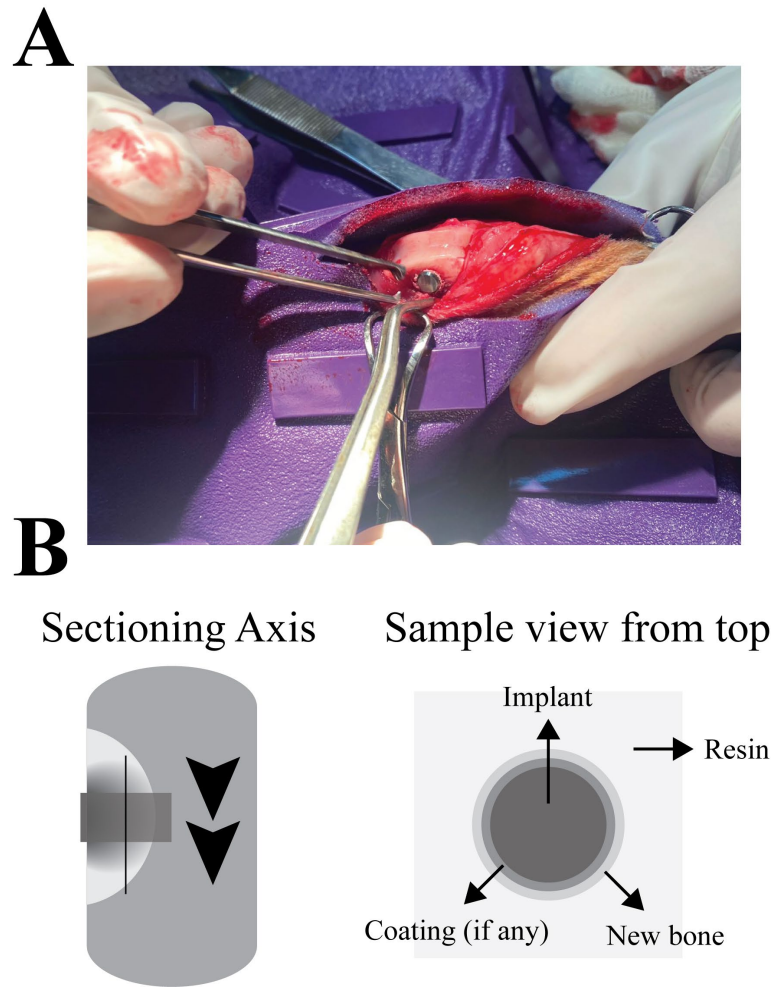


Figure 3.41 Photo taken during implantation at the osteochondral defect of rabbit femur osteochondral zone (A) and implant sectioning scheme for Ti-APA, A/G and A/BHT groups after harvest at the end of 4 and 8 weeks (B).

Reported by many studies in the literature, it is shown that an acute inflammatory response is also important in addition to good osteogenic and angiogenic properties. In a similar study, Zhao et al. (2021) fabricated a scaffold from decellularized periosteal tissue and demonstrated that natural tissue triggered an increase in innate immune response but resolved in time into pro-healing state (Zhao et al., 2021). In another study, Tan et al. (2020) coated pre-treated Ti with *Lactobacillus casei* and

sterilized by UV irradiation to establish a bioactive coat (Tan, et al., 2020). This layer allowed prominent osteogenic cytokines to be released by colonizing osteoblasts as well prevented pathogenic methicillin-resistant *S. aureus* adhesion. Thus, the results were interpreted as osteoimmunomodulatory surface properties being a key player in implant osseointegration.

In this thesis study, A/G/BHT exhibited a similar osteoimmunomodulatory property as aforementioned studies. This coating improved the rate of BMP-2, ALP, OSX, OCN and VEGF-A expression, and the release of ALP, OCN and VEGF-A (Figure 3.33, 3.34 and 3.35). Moreover, A/G/BHT induced immunological marker release higher than Ti-APA but lower than A/G coating. In addition, it supported pro-healing markers to be released faster than other groups. Therefore, it was concluded that A/G/BHT could actually allow rapid osseointegration of Ti implant (Chen, et al., 2021; Ding, et al., 2021; Peng, et al., 2021).

In this sense, A/G/BHT as well as Ti-APA and A/G were tested in a rabbit osteochondral defect model (Figure 3.41) to observe the effect of coated layers in terms of osseointegration. As given in Figure 3.42, A/G/BHT samples induced new bone formation as early as 4 weeks, comparable with Ti-APA. Although there was intact host bone (HB) around the Ti-APA, presence of a thick fibrous tissue (FT) without formation of a prominent new bone (NB) can be seen. On the other hand, A/G/BHT resulted in rapid new bone formation (NBF) at the periphery of coated zone (COAT) and induced new marrow formation (NBM). This coating also protected the host bone marrow (BM). On the contrary, despite the fact that A/G group demonstrated NBF, a thick FT layer was also observed. None of the groups led to aberrant immune reaction or destruction of surrounding bone.

When groups were analyzed at the end of 8 weeks post-implantation, complete integration with the HB was observed for the A/G/BHT group (Figure 3.42). Especially at the implant periphery, almost no FT was observable around A/G/BHT and the implant was determined to be coincide with NBF as well as NBM. A/G, on the contrary, was not able to integrate with HB and lacked NBF. It persisted FT with

formation of NBM. Similarly, Ti-APA deteriorated over time and FT thickened. Although NBF and NBM were observed for Ti-APA, it can be stated that A/G/BHT demonstrated good integration rate with surrounding HB.

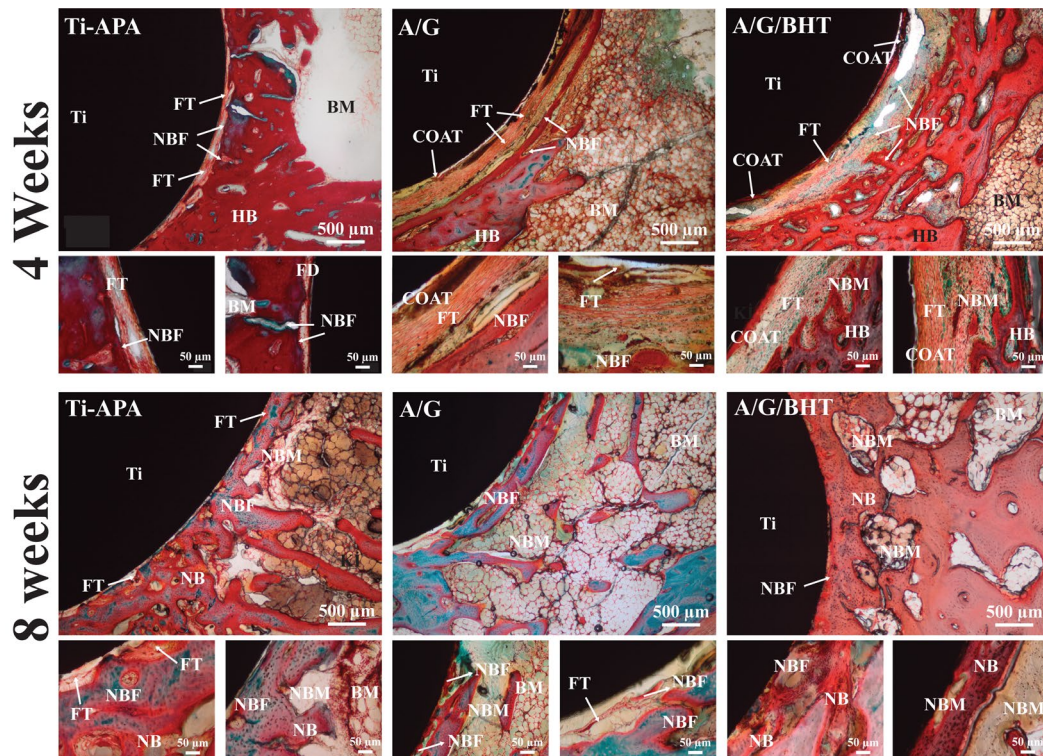


Figure 3.42 Microscopic images of Ti-APA, A/G and A/G/BHT groups after histochemical staining for qualitatively and quantitatively scoring bone-implant integration. The abbreviations used in B and C are as follows: Ti shows implant, FT fibrous tissue, COAT coating, NB new bone, NBF new bone formation, HB host bone, BM bone marrow and NBM new bone marrow formation.

In parallel, OCN marker was selected and immunohistochemically stained for determination of stable integration of implants with HB (Figure 3.43). Osteoblasts (OB) could be located at the FT periphery and they were observed to form typical

lacunae formation for all of the samples (Shi et al., 2016). It was also detected that the color changed to darker as more and more OCN-positive staining occurred (Li et al., 2020). Especially for A/G/BHT, OCN intensity was higher than Ti-APA or A/G groups. In addition, Ti-APA and A/G exhibited strong FT staining, which is quite weak in A/G/BHT implanted groups.

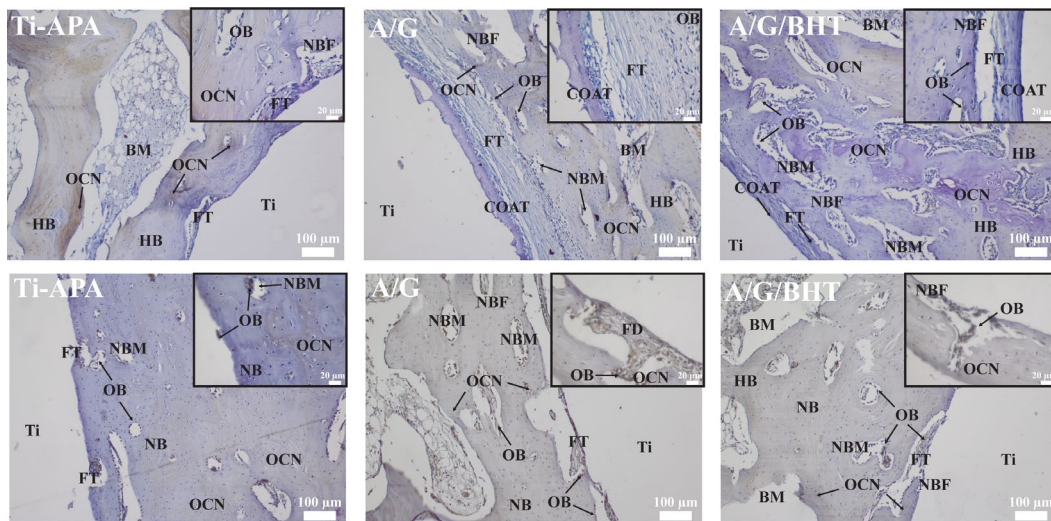


Figure 3.43 Microscopic images of Ti-APA, A/G and A/G/BHT groups after immunohistochemical staining for qualitatively and quantitatively scoring bone-implant integration. The abbreviations used in B and C are as follows: Ti shows implant, FT fibrotic tissue, COAT coating, NB new bone, NBF new bone formation, HB host bone, BM bone marrow, NBM new bone marrow formation, OB osteoblast and OCN osteocalcin.

When analyzed quantitatively, A/G/BHT resulted in a higher score compared to other groups (Table 3.13). Overall scores further demonstrated that A/G was not sufficient enough to induce osseointegration, thus it might require additional reinforcement. In this sense, BHT acted as a bioactive supplement and successfully

induced bone formation around Ti implants. Therefore, both histochemical and immunohistochemical studies showed that A/G/BHT was superior to Ti-APA and A/G in terms of achieving rapid and stable osseointegration.

Table 3.13 Osseointegration scores of samples 1st month and 2nd month of post-implantation (n=4). Scoring was done in accordance with Masson Trichrome staining.

Sample	Score	
	Month 1	Month 2
Ti-APA	4.25 ± 1.50	4.00 ± 1.15 ^a
A/G	2.25 ± 0.95	2.75 ± 0.50
A/G/BHT	2.50 ± 0.58	4.50 ± 0.58 ^b

^a Ti-APA demonstrated a deterioration that only APA modification appeared not to be good enough for establishing a functional bridge between host bone and Ti.

^b A/G/BHT could immensely reinforce the osseointegration capacity of a Ti implant. It showed a significant increase of score from 1st to 2nd month after the implant was placed.

Reported by Sheen et al. (2020), osteoimmunomodulatory events require a sequential response inducible by immunological and regenerative properties of the implants (Steen et al., 2020). For this reason, we employed BHT as an osteogenic and angiogenic CaP species which also displayed osteoimmunomodulatory activity. In a study by Li et al. (2021), plasma sprayed coatings brought about immunomodulatory and regenerative properties (Li et al., 2021). But, nonhomogeneous particle coating at the implant surface and immensely dense CaP zone interacting with relatively less dense and elastic host bone tissue may create erosion at the implant periphery and physically damage the tissue rather provide a

regenerative effect in the long run. Furthermore, direct implantation of ionic species could create a potentially chemical toxicity for the colonizing cells and they are not useful in terms of allowing controlled release of additional biological factors as stated in various studies (Palkowitz et al., 2021; Wang et al., 2021).

In this thesis study, mechanical strength, stability, osteoblast and endothelial cell adhesion as well as macrophage adhesion on a composite structure coated on a Ti implant were shown. Composite coating, namely A/G/BHT, was composed of an interpenetrating network of two most commonly used natural polymers and a boron doped CaP species. A/G/BHT coating was designed to mimic and acts as a replacement for natural osseous ECM. This structure was also shown to assume hydrogel conformation that may allow uptake of additional factors/drugs/agents to be released at the implant periphery to support osseointegration. Taking *in vitro* and *in vivo* results into account, it can be said that A/G/BHT demonstrated a great potential to be employed as a coating on Ti implant to reinforce its osseimmunomodulatory and regenerative capability.

CHAPTER 4

CONCLUSION

This study covers production of a multifunctional composite coating on a Ti-based implant. First, production and characterization studies of BHT revealed that doping with B allowed formation and crystallization of HA phase, and increased X_c and L_c when doped up to 5% molar B. BHT species increased CaP deposition, strikingly improved osteogenic and angiogenic potential of HT. Moreover, B presence introduced immunomodulatory potential to HT and thus, BHT could be utilized to soothe and direct innate immune response. osteogenic differentiation and strikingly improved angiogenic potential. Second, a novel natural polymer-based hydrogel coating as a gap filling modality was designed and optimized. Ti-APA modifications were used as underlying base for APTES grafting and subsequent composite coating. Prior to blend BHT in A/G, optimization studies revealed that A/G 1:3 coatings can resist high scratching force, demonstrate tailorable degradation and swelling rates. Furthermore, A/G 1:3 demonstrated good structural stability and strong adhesion with low thickness. Furthermore, this coating showed high proliferative capacity over 7 days, allowed osteoblast colonization throughout coated layer and high cell spread on the surface. Therefore, A/G 1:3 coatings were designated as main matrix to homogeneously mix BHT and form composite coating. As a promising interphase structure, BHT loaded in A/G to improve biological properties and A/G/BHT was designed to mimic ECM ultrastructure due to similarities with bone ECM. This layer resulted in good stiffness, microscopic roughness and release of bioactive ions such as Ca and B. Then, composite A/G/BHT exhibited intrinsic hydrogel-related properties such as good cohesion, high water uptake, very low pre-gel viscosity and tailorable degradation rate to coincide with development of new bone. Hence, it is thought that it might endow unmatched regenerative and immunomodulatory properties to Ti implant. A/G/BHT also demonstrated high capacity to support

osteoblast and endothelial cell adhesion and growth. The results presented in this work suggest that A/G/BHT can be used as reservoir for custom-made peptides, antibacterial agents, regenerative factors or disease-specific drugs such as anti-osteoporotic agents so that they may be released with greater control in terms of rate and concentration directly at the defect zone. Proposed A/G/BHT layer on Ti demonstrated immense potential in terms of provoking an early innate immune response which could rapidly be resolved into pro-healing/regenerative phenotype, in addition to osteogenic and angiogenic properties. Therefore, it could be stated that the versatility of the proposed gap-filling composite coating was proven and it could be employed in regular/irregularly shaped implants in BTE.

REFERENCES

- Acumen Research and Consulting. 2019. Dental implants market (by product: Tapered implants, parallel walled implants; by type: Endosteal implants, subperiosteal implants, transosteal implants; by material: Titanium, zirconium; by end-use: Hospitals, dental clinics, others) – global industry analysis, market size, opportunities and forecast, 2019 - 2026 Retrieved 20 April, 2020, from <https://www.acumenresearchandconsulting.com/dental-implants-market>
- Ahmadi, R., & Afshar, A. 2021. In vitro study: Bond strength, electrochemical and biocompatibility evaluations of tio₂/al₂o₃ reinforced hydroxyapatite sol–gel coatings on 316l ss, *Surface and Coatings Technology*, 405. 126594. doi: <https://doi.org/10.1016/j.surfcoat.2020.126594>
- Alas, G. R., Agarwal, R., Collard, D. M., & García, A. J. 2017. Peptide-functionalized poly [oligo (ethylene glycol) methacrylate] brushes on dopamine-coated stainless steel for controlled cell adhesion, *Acta Biomaterialia*, 59. 108-116. doi: 10.1016/j.actbio.2017.06.033
- Albayrak, O. 2016. Structural and mechanical characterization of boron doped biphasic calcium phosphate produced by wet chemical method and subsequent thermal treatment, *Materials Characterization*, 113. 82-89. doi: 10.1016/j.matchar.2016.01.006
- Alizadeh-Osgouei, M., Li, Y., & Wen, C. 2019. A comprehensive review of biodegradable synthetic polymer-ceramic composites and their manufacture for biomedical applications, *Bioactive Materials*, 4. 22-36. doi: 10.1016/j.bioactmat.2018.11.003
- Allied Market Research. 2019. Orthopedic implants market by product type (reconstructive joint replacements, spinal implants, dental implants, trauma, orthobiologics, and others), biomaterial (metallic, ceramic, polymeric, and others), and type (knee, hip, wrist & shoulder, dental, spine, ankle, and others): Global opportunity analysis and industry forecast, 2018 - 2025 Retrieved 20 April, 2020, from <https://www.alliedmarketresearch.com/orthopedic-implants-market>
- Alshemary, A. Z., Engin Pazarceviren, A., Tezcaner, A., & Evis, Z. 2018. Fe³⁺/– dual doped nano hydroxyapatite: A novel material for biomedical applications, *Journal of Biomedical Materials Research Part B: Applied Biomaterials*, 106(1). 340-352. doi: 10.1002/jbm.b.33838

- Alshemary, A. Z., Pazarceviren, A. E., Tezcaner, A., & Evis, Z. 2016. Mesoporous strontium doped nano sized sulphate hydroxyapatite as a novel biomaterial for bone tissue applications, *RSC Advances*, 6(72). 68058-68071. doi: 10.1039/C6RA16809D
- Armstrong, H., Bording-Jorgensen, M., Chan, R., & Wine, E. 2019. Nigericin promotes nlrp3-independent bacterial killing in macrophages, *Frontiers in Immunology*, 10(2296). doi: 10.3389/fimmu.2019.02296
- Atluri, K., Lee, J., Seabold, D., Elangovan, S., & Salem, A. K. 2017. Gene activated titanium surfaces promote in vitro osteogenesis, *The International Journal Of Oral & Maxillofacial Implants*, 32(2). e83–e96. doi: 10.11607/jomi.5026
- Bahraminasab, M., Sahari, B., Edwards, K., Farahmand, F., & Arumugam, M. 2013. Aseptic loosening of femoral components—materials engineering and design considerations, *Materials & Design*, 44. 155-163. doi: 10.1016/j.matdes.2012.07.066
- Bai, Y., Li, Z., Cheng, B., Zhang, M., & Su, K. 2017. Higher uv-shielding ability and lower photocatalytic activity of tio2@sio2/aptes and its excellent performance in enhancing the photostability of poly(p-phenylene sulfide), *RSC Advances*, 7(35). 21758-21767. doi: 10.1039/C6RA28098F
- Bai, Y., Zhou, R., Cao, J., Wei, D., Du, Q., Li, B., Wang, Y., Jia, D., & Zhou, Y. 2017. Microarc oxidation coating covered ti implants with micro-scale gouges formed by a multi-step treatment for improving osseointegration, *Materials Science and Engineering: C*, 76. 908-917. doi: 10.1016/j.msec.2017.03.071
- Balasubramanian, P., Hupa, L., Jokic, B., Detsch, R., Grünwald, A., & Boccaccini, A. R. 2017. Angiogenic potential of boron-containing bioactive glasses: In vitro study, *Journal of Materials Science*, 52(15). 8785-8792. doi: 10.1007/s10853-016-0563-7
- Baljon, J. J., Dandy, A., Wang-Bishop, L., Wehbe, M., Jacobson, M. E., & Wilson, J. T. 2019. The efficiency of cytosolic drug delivery using ph-responsive endosomolytic polymers does not correlate with activation of the nlrp3 inflammasome, *Biomaterials Science*, 7(5). 1888-1897. doi: 10.1039/C8BM01643G

- Baniwal, S. K., Shah, P. K., Shi, Y., Haduong, J. H., DeClerck, Y. A., Gabet, Y., & Frenkel, B. 2012. Runx2 promotes both osteoblastogenesis and novel osteoclastogenic signals in st2 mesenchymal progenitor cells, *Osteoporosis International*, 23(4). 1399-1413. doi: 10.1007/s00198-011-1728-5
- Barheine, S., Hayakawa, S., Jäger, C., Shirosaki, Y., & Osaka, A. 2011. Effect of disordered structure of boron-containing calcium phosphates on their in vitro biodegradability, *Journal of the American Ceramic Society*, 94(8). 2656-2662. doi: <https://doi.org/10.1111/j.1551-2916.2011.04400.x>
- Barheine, S., Hayakawa, S., Osaka, A., & Jaeger, C. 2009. Surface, interface, and bulk structure of borate containing apatitic biomaterials, *Chemistry of Materials*, 21(14). 3102-3109. doi: 10.1021/cm900204q
- Barik, A., Ray, S. K., Byram, P. K., Sinha, R., & Chakravorty, N. 2020. Extensive early mineralization of pre-osteoblasts, inhibition of osteoclastogenesis and faster peri-implant bone healing in osteoporotic rat model: Principle effectiveness of bone-specific delivery of tibolone as evaluated in vitro and in vivo, *Biomedical Materials*, 15(6). 064102. doi: 10.1088/1748-605x/abb12b
- Baseler, W. A., Davies, L. C., Quigley, L., Ridnour, L. A., Weiss, J. M., Hussain, S. P., Wink, D. A., & McVicar, D. W. 2016. Autocrine il-10 functions as a rheostat for m1 macrophage glycolytic commitment by tuning nitric oxide production, *Redox Biology*, 10. 12-23. doi: <https://doi.org/10.1016/j.redox.2016.09.005>
- Bollino, F., Armenia, E., & Tranquillo, E. 2017. Zirconia/hydroxyapatite composites synthesized via sol-gel: Influence of hydroxyapatite content and heating on their biological properties, *Materials*, 10(7). 757. doi: 10.3390/ma10070757
- Boni, B. O. O., Lamboni, L., Souho, T., Gauthier, M., & Yang, G. 2019. Immunomodulation and cellular response to biomaterials: The overriding role of neutrophils in healing, *Materials Horizons*, 6(6). 1122-1137. doi: <https://doi.org/10.1039/C9MH00291J>
- Boschetto, F., Ngoc Doan, H., Phong Vo, P., Zanicco, M., Zhu, W., Sakai, W., Adachi, T., Ohgitani, E., Tsutsumi, N., Mazda, O., Kinashi, K., Marin, E., & Pezzotti, G. 2020. Antibacterial and osteoconductive effects of chitosan/polyethylene oxide (peo)/bioactive glass nanofibers for orthopedic applications, *Applied Sciences*, 10(7). 2360.

- Bucur, A. I., Linul, E., & Taranu, B.-O. 2020. Hydroxyapatite coatings on ti substrates by simultaneous precipitation and electrodeposition, *Applied Surface Science*, 527. 146820. doi: <https://doi.org/10.1016/j.apsusc.2020.146820>
- Calis, M., Demirtas, T. T., Vatansever, A., Irmak, G., Sakarya, A. H., Atilla, P., Ozgur, F., & Gumusderelioglu, M. 2017. A biomimetic alternative to synthetic hydroxyapatite: "Boron-containing bone-like hydroxyapatite" precipitated from simulated body fluid, *Annals of Plastic Surgery*, 79(3). 304-311. doi: 10.1097/SAP.0000000000001072.
- Carpentier, G., Berndt, S., Ferratge, S., Rasband, W., Cuendet, M., Uzan, G., & Albanese, P. 2020. Angiogenesis analyzer for imagej — a comparative morphometric analysis of "endothelial tube formation assay" and "fibrin bead assay", *Scientific Reports*, 10(1). 11568. doi: 10.1038/s41598-020-67289-8
- Cekas, E., Janusas, G., Guobiene, A., Palevicius, A., Vilkauskas, A., & Ponelyte Urbaite, S. 2018. Design of controllable novel piezoelectric components for microfluidic applications, *Sensors*, 18(11). 4049. doi: 10.3390/s18114049
- Chan, K. W., Wong, H. M., Yeung, K. W. K., & Tjong, S. C. 2015. Polypropylene biocomposites with boron nitride and nanohydroxyapatite reinforcements, *Materials*, 8(3). 992-1008. 10.3390/ma8030992
- Chen, D., Gong, Y., Xu, L., Zhou, M., Li, J., & Song, J. 2019. Bidirectional regulation of osteogenic differentiation by the foxo subfamily of forkhead transcription factors in mammalian mscs, *Cell Proliferation*, 52(2). e12540. doi: <https://doi.org/10.1111/cpr.12540>
- Chen, M., Hu, J., Zhang, E., Hu, J., Wang, X., & Qin, G. 2021. The osteoimmunomodulatory effect of nanostructured tif x /tio x coating on osteogenesis induction, *Biomedical Materials*, 16(4). 045041. doi: 10.1088/1748-605x/ac0863
- Chen, M., Huang, L., Shen, X., Li, M., Luo, Z., Cai, K., & Hu, Y. 2020. Construction of multilayered molecular reservoirs on a titanium alloy implant for combinational drug delivery to promote osseointegration in osteoporotic conditions, *Acta Biomaterialia*, 15(105). 304-318. doi: 10.1016/j.actbio.2020.01.029

- Chen, T., Wang, S., He, F., Guo, Z., Hu, P., Zhao, R., Huang, Y., Chen, Q., Ji, P., & Chu, L. 2018. Promotion of osseointegration using protamine/alginate/bone morphogenic protein 2 biofunctionalized composite coating on nanopolymorphic titanium surfaces, *Journal of Biomedical Nanotechnology*, 14(5). 933-945. doi: 10.1166/jbn.2018.2506
- Chen, W., Xie, G., Lu, Y., Wang, J., Feng, B., Wang, Q., Xu, K., & Bao, J. 2022. An improved osseointegration of metal implants by pitavastatin loaded multilayer films with osteogenic and angiogenic properties, *Biomaterials*, 280. 121260. doi: <https://doi.org/10.1016/j.biomaterials.2021.121260>
- Chen, Z., Yan, X., Yin, S., Liu, L., Liu, X., Zhao, G., Ma, W., Qi, W., Ren, Z., Liao, H., Liu, M., Cai, D., & Fang, H. 2020. Influence of the pore size and porosity of selective laser melted ti6al4v eli porous scaffold on cell proliferation, osteogenesis and bone ingrowth, *Materials Science and Engineering: C*, 106. 110289. doi: <https://doi.org/10.1016/j.msec.2019.110289>
- Choi, H., Schulte, A., Müller, M., Park, M., Jo, S., & Schönherr, H. 2021. Drug release from thermo-responsive polymer brush coatings to control bacterial colonization and biofilm growth on titanium implants, *Advanced Healthcare Materials*, 10(11). 2100069. doi: <https://doi.org/10.1002/adhm.202100069>
- Chou, W.-C., Wang, R. C.-C., Huang, C.-L., & Lee, T.-M. 2018. The effect of plasma treatment on the osseointegration of rough titanium implant: A histomorphometric study in rabbits, *Journal of Dental Sciences*, 13(3). 267-273.
- Chrcanovic, B., Kisch, J., Albrektsson, T., & Wennerberg, A. 2016. Factors influencing early dental implant failures, *Journal of dental research*, 95(9). 995-1002. doi: 10.1177/0022034516646098
- Ciobanu, G., & Harja, M. 2019. Cerium-doped hydroxyapatite/collagen coatings on titanium for bone implants, *Ceramics International*, 45(2, Part B). 2852-2857. doi: <https://doi.org/10.1016/j.ceramint.2018.07.290>
- Clauder, F., Czerniak, A. S., Friebe, S., Mayr, S. G., Scheinert, D., & Beck-Sickinger, A. G. 2019. Endothelialization of titanium surfaces by bioinspired cell adhesion peptide coatings, *Bioconjugate Chemistry*, 30(10). 2664-2674.
- Cortez, P. P., Brito, A. F., Kapoor, S., Correia, A. F., Atayde, L. M., Dias-Pereira, P., Maurício, A. C., Afonso, A., Goel, A., & Ferreira, J. M. 2017. The in vivo performance of an alkali-free bioactive glass for bone grafting, *fastos® bg*,

- assessed with an ovine model, *Journal of Biomedical Materials Research Part B: Applied Biomaterials*, 105(1). 30-38. doi: 10.1002/jbm.b.33529
- Coullin, I., Gombault, A., & Baron, L. 2013. Atp release and purinergic signaling in nlrp3 inflammasome activation, [Mini Review], *Frontiers in Immunology*, 3. doi: 10.3389/fimmu.2012.00414
- da Silva Sasso, G. R., Florencio-Silva, R., Sasso-Cerri, E., Gil, C. D., de Jesus Simões, M., & Cerri, P. S. 2021. Spatio-temporal immunolocalization of vegf-a, runx2, and osterix during the early steps of intramembranous ossification of the alveolar process in rat embryos, *Developmental Biology*, 478. 133-143. doi: <https://doi.org/10.1016/j.ydbio.2021.07.001>
- Dagvadorj, J., Naiki, Y., Tumurkhuu, G., Noman, A. S. M., Iftekar-E-Khuda, I., Koide, N., Komatsu, T., Yoshida, T., & Yokochi, T. 2009. Interleukin (il)-10 attenuates lipopolysaccharide-induced il-6 production via inhibition of ikb- ζ activity by bcl-3, *Innate Immunity*, 15(4). 217-224. doi: 10.1177/1753425909103738
- Damiati, L., Eales, M. G., Nobbs, A. H., Su, B., Tsimbouri, P. M., Salmeron-Sanchez, M., & Dalby, M. J. 2018. Impact of surface topography and coating on osteogenesis and bacterial attachment on titanium implants, *Journal of Tissue Engineering*, 9. 2041731418790694.
- Dashnyam, K., Buitrago, J. O., Bold, T., Mandakhbayar, N., Perez, R. A., Knowles, J. C., Lee, J.-H., & Kim, H.-W. 2019. Angiogenesis-promoted bone repair with silicate-shelled hydrogel fiber scaffolds, [10.1039/C9BM01103J], *Biomaterials Science*, 7(12). 5221-5231. doi: 10.1039/C9BM01103J
- Davidenko, N., Schuster, C. F., Bax, D. V., Farndale, R. W., Hamaia, S., Best, S. M., & Cameron, R. E. 2016. Evaluation of cell binding to collagen and gelatin: A study of the effect of 2d and 3d architecture and surface chemistry, *Journal of Materials Science: Materials in Medicine*, 27(10). 148. doi: 10.1007/s10856-016-5763-9
- Davis, R., Singh, A., Jackson, M. J., Coelho, R. T., Prakash, D., Charalambous, C. P., Ahmed, W., da Silva, L. R. R., & Lawrence, A. A. 2022. A comprehensive review on metallic implant biomaterials and their subtractive manufacturing, *The International Journal of Advanced Manufacturing Technology*, 120(3). 1473-1530. doi: 10.1007/s00170-022-08770-8

- Dayan, A., Lamed, R., Benayahu, D., & Fleminger, G. 2019. Rgd-modified dihydrolipoamide dehydrogenase as a molecular bridge for enhancing the adhesion of bone forming cells to titanium dioxide implant surfaces, *Journal of Biomedical Materials Research Part A*, 107(3). 545-551.
- Dehghanghadikolaie, A., & Fotovvati, B. 2019. Coating techniques for functional enhancement of metal implants for bone replacement: A review, *Materials*, 12(11). 1795.
- Deng, J., & Gao, C. 2016. Recent advances in interactions of designed nanoparticles and cells with respect to cellular uptake, intracellular fate, degradation and cytotoxicity, *Nanotechnology*, 27(41). 412002. doi: 10.1088/0957-4484/27/41/412002
- Diebold, U. 2003. The surface science of titanium dioxide, *Surface Science Reports*, 48(5–8). 53-229. doi: [http://dx.doi.org/10.1016/S0167-5729\(02\)00100-0](http://dx.doi.org/10.1016/S0167-5729(02)00100-0)
- Ding, T., Kang, W., Li, J., Yu, L., & Ge, S. 2021. An in situ tissue engineering scaffold with growth factors combining angiogenesis and osteoimmunomodulatory functions for advanced periodontal bone regeneration, *Journal of Nanobiotechnology*, 19(1). 247. doi: 10.1186/s12951-021-00992-4
- Dodero, A., Vicini, S., Alloisio, M., & Castellano, M. 2020. Rheological properties of sodium alginate solutions in the presence of added salt: An application of kulicke equation, *Rheologica Acta*, 59(6). 365-374. doi: 10.1007/s00397-020-01206-8
- Doymus, B., Kerem, G., Yazgan Karatas, A., Kok, F. N., & Önder, S. 2021. A functional coating to enhance antibacterial and bioactivity properties of titanium implants and its performance in vitro, *Journal of Biomaterials Applications*, 35(6). 655-669. doi: 10.1177/0885328220977765
- Duan, Y., Wu, Y., Yan, R., Lin, M., Sun, S., & Ma, H. 2021. Chitosan-sodium alginate-based coatings for self-strengthening anticorrosion and antibacterial protection of titanium substrate in artificial saliva, *International Journal of Biological Macromolecules*, 184. 109-117. doi: <https://doi.org/10.1016/j.ijbiomac.2021.06.042>
- Duman, E., Şahin Kehribar, E., Ahan, R. E., Yuca, E., & Şeker, U. Ö. Ş. 2019. Biom mineralization of calcium phosphate crystals controlled by protein–

- protein interactions, *ACS Biomaterials Science & Engineering*, 5(9). 4750-4763. doi: 10.1021/acsbiomaterials.9b00649
- Duong, H. P., Le, M. D., Dao, H. C., & Chen, C.-Y. 2017. Surface modification of tio2 nanotubes by grafting with apts coupling agents, *Materials Research Express*, 4(10). 105043. doi: 10.1088/2053-1591/aa92b3
- Duraccio, D., Mussano, F., & Faga, M. G. 2015. Biomaterials for dental implants: Current and future trends, *Journal of Materials Science*, 50(14). 4779-4812. doi: 10.1007/s10853-015-9056-3
- Durand, L. A. H., Vargas, G. E., Romero, N. M., Vera-Mesones, R., Porto-López, J. M., Boccaccini, A. R., Zago, M. P., Baldi, A., & Gorustovich, A. 2015. Angiogenic effects of ionic dissolution products released from a boron-doped 45s5 bioactive glass, *Journal of Materials Chemistry B*, 3(6). 1142-1148.
- Echave, M., Sánchez, P., Pedraz, J., & Orive, G. 2017. Progress of gelatin-based 3d approaches for bone regeneration, *Journal of Drug Delivery Science and Technology*, 42. 63-74.
- Echave, M. C., Hernáez-Moya, R., Iturriaga, L., Pedraz, J. L., Lakshminarayanan, R., Dolatshahi-Pirouz, A., Taebnia, N., & Orive, G. 2019. Recent advances in gelatin-based therapeutics, *Expert Opinion on Biological Therapy*, 19(8). 773-779. doi: 10.1080/14712598.2019.1610383
- Elshereksi, N. W., Ghazali, M. J., Muchtar, A., & Azhari, C. H. 2017. Studies on the effects of titanate and silane coupling agents on the performance of poly (methyl methacrylate)/barium titanate denture base nanocomposites, *Journal of Dentistry*, 56. 121-132. doi: <https://doi.org/10.1016/j.jdent.2016.11.012>
- Engin Pazarçeviren, A., Akbaba, S., Tezcaner, A., Keskin, D., & Evis, Z. 2022. Seamless and robust alginate/gelatin coating on ti-6al-4v as a gap filling interphase, *Applied Surface Science*, 581. 152393. doi: <https://doi.org/10.1016/j.apsusc.2021.152393>
- Er, N., Alkan, A., Ilday, S., & Bengu, E. 2018. Improved dental implant drill durability and performance using heat and wear resistant protective coatings, *Journal of Oral Implantology*, 44(3). 168-175. doi: 10.1563/aaid-joi-D-16-00114

- Esposito, M., Thomsen, P., Ericson, L. E., Sennerby, L., & Lekholm, U. 2000. Histopathologic observations on late oral implant failures, *Clinical Implant Dentistry and Related Research*, 2(1). 18-32. doi: 10.1111/j.1708-8208.2000.tb00103.x
- Farzin, A., Hassan, S., Moreira Teixeira, L. S., Gurian, M., Crispim, J. F., Manhas, V., Carlier, A., Bae, H., Geris, L., Noshadi, I., Shin, S. R., & Leijten, J. 2021. Self-oxygenation of tissues orchestrates full-thickness vascularization of living implants, *Advanced Functional Materials*, 31(42). 2100850. doi: <https://doi.org/10.1002/adfm.202100850>
- Fernandes-Alnemri, T., Wu, J., Yu, J. W., Datta, P., Miller, B., Jankowski, W., Rosenberg, S., Zhang, J., & Alnemri, E. S. 2007. The pyroptosome: A supramolecular assembly of asc dimers mediating inflammatory cell death via caspase-1 activation, *Cell Death & Differentiation*, 14(9). 1590-1604. doi: 10.1038/sj.cdd.4402194
- Ferreira, A. M., Gentile, P., Chiono, V., & Ciardelli, G. 2012. Collagen for bone tissue regeneration, *Acta Biomaterialia*, 8(9). 3191-3200. doi: 10.1016/j.matdes.2021.110049
- Finke, B., Hempel, F., Testrich, H., Artemenko, A., Rebl, H., Kylián, O., Meichsner, J., Biederman, H., Nebe, B., & Weltmann, K.-D. 2011. Plasma processes for cell-adhesive titanium surfaces based on nitrogen-containing coatings, *Surface and Coatings Technology*, 205. S520-S524.
- Francis, L. F., McCormick, A. V., Vaessen, D. M., & Payne, J. A. 2002. Development and measurement of stress in polymer coatings, *Journal of Materials Science*, 37(22). 4717-4731. doi: 10.1023/A:1020886802632
- Ganjali, M., Mousavi, S., Nikzamir, S., Milan, P. B., & Mozafari, M. 2021. Effect of laser cladded co-doped strontium fluorapatite nanopowder coating on the antibacterial and cell attachment of ti-6al-4v implants for bone applications, *Materials Technology*. 37(8). doi: 10.1080/10667857.2021.1898716
- Gao, Q., Yu, M., Su, Y., Xie, M., Zhao, X., Li, P., & Ma, P. X. 2017. Rationally designed dual functional block copolymers for bottlebrush-like coatings: In vitro and in vivo antimicrobial, antibiofilm, and antifouling properties, *Acta Biomaterialia*, 51. 112-124.

- Gao, T., Gillispie, G. J., Copus, J. S., Pr, A. K., Seol, Y.-J., Atala, A., Yoo, J. J., & Lee, S. J. 2018. Optimization of gelatin-alginate composite bioink printability using rheological parameters: A systematic approach, *Biofabrication*, 10(3). 034106-034106. doi: 10.1088/1758-5090/aacdc7
- Gautam, S., Bhatnagar, D., Bansal, D., Batra, H., & Goyal, N. 2022. Recent advancements in nanomaterials for biomedical implants, *Biomedical Engineering Advances*, 3. 100029. doi: <https://doi.org/10.1016/j.bea.2022.100029>
- Geng, Y., Duan, H., Xu, L., Witman, N., Yan, B., Yu, Z., Wang, H., Tan, Y., Lin, L., Li, D., Bai, S., Fritsche-Danielson, R., Yuan, J., Chien, K., Wei, M., & Fu, W. 2021. Bmp-2 and vegf-a modrnas in collagen scaffold synergistically drive bone repair through osteogenic and angiogenic pathways, *Communications Biology*, 4(1). 82. doi: 10.1038/s42003-020-01606-9
- Geng, Z., Li, X., Ji, L., Li, Z., Zhu, S., Cui, Z., Wang, J., Cui, J., Yang, X., & Liu, C. 2021. A novel snail-inspired bionic design of titanium with strontium-substituted hydroxyapatite coating for promoting osseointegration, *Journal of Materials Science & Technology*, 79. 35-45. doi: <https://doi.org/10.1016/j.jmst.2020.11.041>
- Gil, J., Manero, J. M., Ruperez, E., Velasco-Ortega, E., Jiménez-Guerra, A., Ortiz-García, I., & Monsalve-Guil, L. 2021. Mineralization of titanium surfaces: Biomimetic implants, *Materials*, 14(11). 2879.
- Gizer, M., Köse, S., Karaosmanoglu, B., Taskiran, E. Z., Berkkan, A., Timuçin, M., Korkusuz, F., & Korkusuz, P. 2020. The effect of boron-containing nano-hydroxyapatite on bone cells, *Biological Trace Element Research*, 193(2). 364-376. doi: 10.1007/s12011-019-01710-w
- Godoy-Gallardo, M., Mas-Moruno, C., Yu, K., Manero, J. M., Gil, F. J., Kizhakkedathu, J. N., & Rodriguez, D. 2015. Antibacterial properties of hlf1–11 peptide onto titanium surfaces: A comparison study between silanization and surface initiated polymerization, *Biomacromolecules*, 16(2). 483-496.
- Goonasekera, C. S., Jack, K. S., Cooper-White, J. J., & Grøndahl, L. 2013. Attachment of poly (acrylic acid) to 3-aminopropyltriethoxysilane surface-modified hydroxyapatite, *Journal of Materials Chemistry B*, 1(42). 5842-5852.

- Grand View Research. 2019. Dental implants market size, share & trends analysis report by type (titanium, zirconium), by region (north america, europe, asia pacific, latin america, mea), and segment forecasts, 2020 - 2027 Retrieved 20 April, 2020, from <https://www.grandviewresearch.com/industry-analysis/dental-implants-market>
- Gribova, V., Boulmedais, F., Dupret-Bories, A. s., Calligaro, C., Senger, B., Vrana, N. E., & Lavalle, P. 2020. Polyanionic hydrogels as reservoirs for polycationic antibiotic substitutes providing prolonged antibacterial activity, 12(17). 19258–19267. *ACS Applied Materials & Interfaces*. doi: 10.1021/acsami.9b23140
- Gu, Y., Wei, L., Zhang, Z., Van Dessel, J., Driesen, R. B., Lambrechts, I., Jacobs, R., Tian, L., Sun, Y., Liu, Y., & Politis, C. 2022. Bmp-2 incorporated biomimetic cap coating functionalized 3d printed ti6al4v scaffold induces ectopic bone formation in a dog model, *Materials & Design*, 215. 110443. doi: <https://doi.org/10.1016/j.matdes.2022.110443>
- Guarise, C., Maglio, M., Sartori, M., Galesso, D., Barbera, C., Pavan, M., Martini, L., Giavaresi, G., Sambri, V., & Fini, M. 2021. Titanium implant coating based on dopamine-functionalized sulphated hyaluronic acid: In vivo assessment of biocompatibility and antibacterial efficacy, *Materials Science and Engineering: C*, 128. 112286. doi: <https://doi.org/10.1016/j.msec.2021.112286>
- Gunda, N. S. K., Singh, M., Norman, L., Kaur, K., & Mitra, S. K. 2014. Optimization and characterization of biomolecule immobilization on silicon substrates using (3-aminopropyl)triethoxysilane (aPTES) and glutaraldehyde linker, *Applied Surface Science*, 305. 522-530. doi: <https://doi.org/10.1016/j.apsusc.2014.03.130>
- Guo, C., Cui, W., Wang, X., Lu, X., Zhang, L., Li, X., Li, W., Zhang, W., & Chen, J. 2020. Poly-l-lysine/sodium alginate coating loading nanosilver for improving the antibacterial effect and inducing mineralization of dental implants, 5(18). 10562–10571. *ACS Omega*. doi: 10.1021/acsomega.0c00986
- Guo, C. Y., Matinlinna, J. P., & Tang, A. T. H. 2012. Effects of surface charges on dental implants: Past, present, and future, *International Journal of Biomaterials*, 381535. doi: 10.1155/2012/381535

- Guo, L. L., Cheng, Y. F., Ren, X., Gopinath, K., Lu, Z. S., Li, C. M., & Xu, L. Q. 2021. Simultaneous deposition of tannic acid and poly(ethylene glycol) to construct the antifouling polymeric coating on titanium surface, *Colloids and Surfaces B: Biointerfaces*, 200. 111592. doi: <https://doi.org/10.1016/j.colsurfb.2021.111592>
- Guo, Y., Guan, J., Peng, H., Shu, X., Chen, L., & Guo, H. 2019. Tightly adhered silk fibroin coatings on ti6al4v biomaterials for improved wettability and compatible mechanical properties, *Materials & Design*, 175. 107825. doi: <https://doi.org/10.1016/j.matdes.2019.107825>
- Haftbaradaran-Esfahani, M., Ahmadian, M., & Nassajpour-Esfahani, A. H. 2020. Fabrication and characterization of porous biomedical vitallium alloy with 58s bioglass coating prepared by sol-gel method, *Applied Surface Science*, 506. 144959. doi: <https://doi.org/10.1016/j.apsusc.2019.144959>
- Han, J., Wan, P., Ge, Y., Fan, X., Tan, L., Li, J., & Yang, K. 2016. Tailoring the degradation and biological response of a magnesium–strontium alloy for potential bone substitute application, *Materials Science and Engineering: C*, 58. 799-811. doi: [10.1016/j.msec.2015.09.057](https://doi.org/10.1016/j.msec.2015.09.057)
- Hartjen, P., Hoffmann, A., Henningsen, A., Barbeck, M., Kopp, A., Kluwe, L., Precht, C., Quatela, O., Gaudin, R., & Heiland, M. 2018. Plasma electrolytic oxidation of titanium implant surfaces: Microgroove-structures improve cellular adhesion and viability, *In Vivo*, 32(2). 241-247. doi: [10.21873/invivo.11230](https://doi.org/10.21873/invivo.11230)
- Hayes, A. J., Smith, S. M., Caterson, B., & Melrose, J. 2018. Concise review: Stem/progenitor cell proteoglycans decorated with 7-d-4, 4-c-3, and 3-b-3 (-) chondroitin sulfate motifs are morphogenetic markers of tissue development, *Stem Cells*, 36(10). 1475-1486.
- He, D., Zhang, X., Liu, P., Liu, X., Chen, X., Ma, F., Li, W., Zhang, K., & Zhou, H. 2021. Effect of hydrothermal treatment temperature on the hydroxyapatite coatings deposited by electrochemical method, *Surface and Coatings Technology*, 406. 126656. doi: <https://doi.org/10.1016/j.surfcoat.2020.126656>

- He, G., & Hagiwara, M. 2006. Ti alloy design strategy for biomedical applications, *Materials Science and Engineering: C*, 26(1). 14-19. doi: <http://dx.doi.org/10.1016/j.msec.2005.03.007>
- He, M., Gao, X., Fan, Y., Xie, L., Yang, M., & Tian, W. 2021. Tannic acid/mg2+-based versatile coating to manipulate the osteoimmunomodulation of implants, *Journal of Materials Chemistry B*, 9(4). 1096-1106. doi: 10.1039/D0TB01577F
- He, Y., Li, Y., Zuo, E., Chai, S., Ren, X., Fei, T., Ma, G., Wang, X., & Liu, H. 2021. A novel antibacterial titanium modification with a sustained release of pac-525, *Nanomaterials*, 11(12). 3306.
- Hosseini, S., Naderi-Manesh, H., Vali, H., Baghaban Eslaminejad, M., Azam Sayahpour, F., Sheibani, S., & Faghihi, S. 2019. Contribution of osteocalcin-mimetic peptide enhances osteogenic activity and extracellular matrix mineralization of human osteoblast-like cells, *Colloids and Surfaces B: Biointerfaces*, 173. 662-671. doi: <https://doi.org/10.1016/j.colsurfb.2018.10.035>
- Hu, K., & Olsen, B. R. 2016. The roles of vascular endothelial growth factor in bone repair and regeneration, *Bone*, 91. 30-38. doi: <https://doi.org/10.1016/j.bone.2016.06.013>
- Huang, Q., Xu, S., Ouyang, Z., Yang, Y., & Liu, Y. 2021. Multi-scale nacre-inspired lamella-structured ti-ta composites with high strength and low modulus for load-bearing orthopedic and dental applications, *Materials Science and Engineering: C*, 118. 111458. doi: <https://doi.org/10.1016/j.msec.2020.111458>
- Hurtado, A., Aljabali, A. A. A., Mishra, V., Tambuwala, M. M., & Serrano-Aroca, A. 2022. Alginate: Enhancement strategies for advanced applications, *International Journal of Molecular Sciences*, 23(9). 4486.
- Intrado GlobeNewsWire. 2019. Orthopedic implants market size to reach us \$64 billion by 2026; rising number of orthopedic sports injuries to favor growth Retrieved 20 April, 2020, from <https://www.globenewswire.com/news-release/2019/11/15/1948039/0/en/Orthopedic-Implants-Market-Size-to-Reach-US-64-Billion-by-2026-Rising-Number-of-Orthopedic-Sports-Injuries-to-Favor-Growth.html>

- Itatani, K., Tsuchiya, K., Sakka, Y., Davies, I. J., & Koda, S. 2011. Superplastic deformation of hydroxyapatite ceramics with b_2o_3 or na_2o addition fabricated by pulse current pressure sintering, *Journal of the European Ceramic Society*, 31(14). 2641-2648. doi: <https://doi.org/10.1016/j.jeurceramsoc.2011.01.014>
- Ilyoon Jariya, S. A., Babu, A. A., Sankara Narayanan, T. S. N., Vellaichamy, E., & Ravichandran, K. 2022. Development of a novel smart carrier for drug delivery: Ciprofloxacin loaded vaterite/reduced graphene oxide/pcl composite coating on tio_2 nanotube coated titanium, *Ceramics International*, 48(7). 9579-9594. doi: <https://doi.org/10.1016/j.ceramint.2021.12.156>
- Jaipan, P., Nguyen, A., & Narayan, R. J. 2017. Gelatin-based hydrogels for biomedical applications, *MRS Communications*, 7(3). 416-426. doi: [10.1557/mrc.2017.92](https://doi.org/10.1557/mrc.2017.92)
- Javed, F., Ahmed, H. B., Crespi, R., & Romanos, G. E. 2013. Role of primary stability for successful osseointegration of dental implants: Factors of influence and evaluation, *Interventional Medicine and Applied Science*, 5(4). 162-167. doi: [10.1556/IMAS.5.2013.4.3](https://doi.org/10.1556/IMAS.5.2013.4.3)
- Jemat, A., Ghazali, M. J., Razali, M., & Otsuka, Y. 2015. Surface modifications and their effects on titanium dental implants, *BioMed Research International*, 791725. doi: [10.1155/2015/791725](https://doi.org/10.1155/2015/791725)
- Jia, L., Han, F., Wang, H., Zhu, C., Guo, Q., Li, J., Zhao, Z., Zhang, Q., Zhu, X., & Li, B. 2019. Polydopamine-assisted surface modification for orthopaedic implants, *Journal of Orthopaedic Translation*.
- Jiang, J., Han, G., Zheng, X., Chen, G., & Zhu, P. 2019. Characterization and biocompatibility study of hydroxyapatite coating on the surface of titanium alloy, *Surface and Coatings Technology*, 375. 645-651. doi: <https://doi.org/10.1016/j.surfcoat.2019.07.067>
- Jiang, P., Zhang, Y., Hu, R., Wang, X., Lai, Y., Rui, G., & Lin, C. 2021. Hydroxyapatite-modified micro/nanostructured titania surfaces with different crystalline phases for osteoblast regulation, *Bioactive Materials*, 6(4). 1118-1129. doi: <https://doi.org/10.1016/j.bioactmat.2020.10.006>
- Jiang, X., Yao, Y., Tang, W., Han, D., Zhang, L., Zhao, K., Wang, S., & Meng, Y. 2020. Design of dental implants at materials level: An overview, *Journal of*

Biomedical Materials Research Part A, 108(8). 1634-1661. doi: <https://doi.org/10.1002/jbm.a.36931>

Jin, S., Li, K., Gao, Q., Zhang, W., Chen, H., Li, J., & Shi, S. Q. 2020. Multiple crosslinking strategy to achieve high bonding strength and antibacterial properties of double-network soy adhesive, *Journal of Cleaner Production*. 120143.

Jing, W., Feng, L., Wang, B., Zhang, W., Xu, K., Al Aboody, M. S., Mickymaray, S., & Peng, K. 2021. Polymer-ceramic fiber nanocomposite coatings on titanium metal implant devices for diseased bone tissue regeneration, *Journal of Science: Advanced Materials and Devices*, 6(3). 399-406. doi: <https://doi.org/10.1016/j.jsamd.2021.04.001>

Jurczak, P., Witkowska, J., Rodziewicz-Motowidlo, S., & Lach, S. 2019. Proteins, peptides and peptidomimetics as active agents in implant surface functionalization, *Advances in Colloid and Interface Science*. 276. 102083. doi: 10.1016/j.cis.2019.102083

Karazisis, D., Ballo, A. M., Petronis, S., Agheli, H., Emanuelsson, L., Thomsen, P., & Omar, O. 2016. The role of well-defined nanotopography of titanium implants on osseointegration: Cellular and molecular events in vivo, *International Journal of Nanomedicine*, 11. 1367.

Keceli, H. G., Bayram, C., Celik, E., Ercan, N., Demirbilek, M., & Nohutcu, R. M. 2020. Dual delivery of platelet-derived growth factor and bone morphogenetic factor-6 on titanium surface to enhance the early period of implant osseointegration, *Journal of Periodontal Research*, 55(5). 694-704. doi: <https://doi.org/10.1111/jre.12756>

Kedia, S., Bonagani, S. K., Majumdar, A. G., Kain, V., Subramanian, M., Maiti, N., & Nilaya, J. P. 2021. Nanosecond laser surface texturing of type 316L stainless steel for contact guidance of bone cells and superior corrosion resistance, *Colloid and Interface Science Communications*, 42. 100419. doi: <https://doi.org/10.1016/j.colcom.2021.100419>

Kelley, N., Jeltema, D., Duan, Y., & He, Y. 2019. The nlrp3 inflammasome: An overview of mechanisms of activation and regulation, *International Journal of Molecular Sciences*, 20(13). 3328. doi: 10.3390/ijms20133328

- Keselowsky, B. G., Bridges, A. W., Burns, K. L., Tate, C. C., Babensee, J. E., LaPlaca, M. C., & Garcia, A. J. 2007. Role of plasma fibronectin in the foreign body response to biomaterials, *Biomaterials*, 28(25). 3626-3631. doi: 10.1016/j.biomaterials.2007.04.035
- Khan, M., Osman, K., Green, G., & Haddad, F. 2016. The epidemiology of failure in total knee arthroplasty: Avoiding your next revision, *The Bone & Joint Journal*, 98. 105-112. doi: 10.1302/0301-620X.98B1.36293
- Khutoryanskaya, O. V., Potgieter, M., & Khutoryanskiy, V. V. 2010. Multilayered hydrogel coatings covalently-linked to glass surfaces showing a potential to mimic mucosal tissues, *Soft Matter*, 6(3). 551-557. doi: 10.1039/B918007A
- Kien, P. T., Quan, T. N., & Tuyet Anh, L. H. 2021. Coating characteristic of hydroxyapatite on titanium substrates via hydrothermal treatment, *Coatings*, 11(10). 1226.
- Kim, A. Y., Kim, Y., Lee, S. H., Yoon, Y., Kim, W.-H., & Kweon, O.-K. 2017. Effect of gelatin on osteogenic cell sheet formation using canine adipose-derived mesenchymal stem cells, *Cell Transplantation*, 26(1). 115-123. doi: 10.3727/096368916X693338
- Kocherova, I., Bryja, A., Mozdziak, P., Angelova Volponi, A., Dyszkiewicz-Konwińska, M., Piotrowska-Kempisty, H., Antosik, P., Bukowska, D., Bruska, M., Iżycki, D., Zabel, M., Nowicki, M., & Kempisty, B. 2019. Human umbilical vein endothelial cells (huvecs) co-culture with osteogenic cells: From molecular communication to engineering prevascularised bone grafts, *Journal of Clinical Medicine*, 8(10). 1602.
- Kokubo, T., & Takadama, H. 2006. How useful is sbf in predicting in vivo bone bioactivity?, *Biomaterials*, 27(15). 2907-2915.
- Kolmas, J., Velard, F., Jaguszevska, A., Lemaire, F., Kerdjoudj, H., Gangloff, S. C., & Kaflak, A. 2017. Substitution of strontium and boron into hydroxyapatite crystals: Effect on physicochemical properties and biocompatibility with human wharton-jelly stem cells, *Materials Science & Engineering C-Materials for Biological Applications*, 79. 638-646. doi: 10.1016/j.msec.2017.05.066
- Komasa, S., Nishizaki, M., Zhang, H., Takao, S., Yin, D., Terada, C., Kobayashi, Y., Kusumoto, T., Yoshimine, S., & Nishizaki, H. 2019. Osseointegration of

alkali-modified nanozr implants: An in vivo study, *International Journal of Molecular Sciences*, 20(4). 842. doi: 10.3390/ijms20040842

Kordbacheh Changi, K., Finkelstein, J., & Papapanou, P. N. 2019. Peri-implantitis prevalence, incidence rate, and risk factors: A study of electronic health records at a us dental school, *Clinical Oral Implants Research*, 30(4). 306-314. doi: 10.1111/clr.13416

Kreller, T., Sahm, F., Bader, R., Boccaccini, A. R., Jonitz-Heincke, A., & Detsch, R. 2021. Biomimetic calcium phosphate coatings for bioactivation of titanium implant surfaces: Methodological approach and in vitro evaluation of biocompatibility, *Materials*, 14(13). 3516.

Kuo, Y.-J., Chen, C.-H., Dash, P., Lin, Y.-C., Hsu, C.-W., Shih, S.-J., & Chung, R.-J. 2022. Angiogenesis, osseointegration, and antibacterial applications of polyelectrolyte multilayer coatings incorporated with silver/strontium containing mesoporous bioactive glass on 316l stainless steel, *Frontiers in Bioengineering and Biotechnology*, 10. 818137. doi: 10.3389/fbioe.2022.818137

Lan, W.-C., Huang, T.-S., Cho, Y.-C., Huang, Y.-T., Walinski, C. J., Chiang, P.-C., Rusilin, M., Pai, F.-T., Huang, C.-C., & Huang, M.-S. 2020. The potential of a nanostructured titanium oxide layer with self-assembled monolayers for biomedical applications: Surface properties and biomechanical behaviors, *Applied Sciences*, 10(2). 590. doi: 10.3390/app10020590

Lee, H.-J., Yang, I.-H., Kim, S.-K., Yeo, I.-S., & Kwon, T.-K. 2015. In vivo comparison between the effects of chemically modified hydrophilic and anodically oxidized titanium surfaces on initial bone healing, *Journal of Periodontal & Implant Science*, 45(3). 94-100. doi: 10.5051/jpis.2015.45.3.94

Lee, J.-H., Jeong, W.-S., Seo, S.-J., Kim, H.-W., Kim, K.-N., Choi, E.-H., & Kim, K.-M. 2017. Non-thermal atmospheric pressure plasma functionalized dental implant for enhancement of bacterial resistance and osseointegration, *Dental Materials*, 33(3). 257-270. doi: 10.1016/j.dental.2016.11.011

Lee, K. Y., & Mooney, D. J. 2012. Alginate: Properties and biomedical applications, *Progress in Polymer Science*, 37(1). 106-126. doi: 10.1016/j.progpolymsci.2011.06.003

- Li, D., Lv, P., Fan, L., Huang, Y., Yang, F., Mei, X., & Wu, D. 2017. The immobilization of antibiotic-loaded polymeric coatings on osteoarticular ti implants for the prevention of bone infections, *Biomaterials Science*, 5(11). 2337-2346. doi: 10.1039/C7BM00693D
- Li, H., Zhong, X., Chen, Z., & Li, W. 2019. Suppression of nlrp3 inflammasome improves alveolar bone defect healing in diabetic rats, *Journal of Orthopaedic Surgery and Research*, 14(1). 167. doi: 10.1186/s13018-019-1215-9
- Li, J., Cui, X., Lindberg, G. C. J., Alcala-Orozco, C. R., Hooper, G. J., Lim, K. S., & Woodfield, T. B. F. 2022. Hybrid fabrication of photo-clickable vascular hydrogels with additive manufactured titanium implants for enhanced osseointegration and vascularized bone formation, *Biofabrication*, 14(3). 034103. doi: 10.1088/1758-5090/ac6051
- Li, J., Liu, X., Crook, J. M., & Wallace, G. G. 2020. 3d printing of cytocompatible graphene/alginate scaffolds for mimetic tissue constructs, *Frontiers in Bioengineering and Biotechnology*, 8. 824. doi: 10.3389/fbioe.2020.00824
- Li, J., Mutreja, I., Hooper, G. J., Clinch, K., Lim, K., Evans, G., & Woodfield, T. F. 2020. Combined infection control and enhanced osteogenic differentiation capacity on additive manufactured ti-6al-4v are mediated via titania nanotube delivery of novel biofilm inhibitors, *Advanced Materials Interfaces*, 7(7). 1901963. doi: <https://doi.org/10.1002/admi.201901963>
- Li, K., Chen, J., Xue, Y., Ding, T., Zhu, S., Mao, M., Zhang, L., & Han, Y. 2021. Polymer brush grafted antimicrobial peptide on hydroxyapatite nanorods for highly effective antibacterial performance, *Chemical Engineering Journal*, 423. 130133. doi: <https://doi.org/10.1016/j.cej.2021.130133>
- Li, K., Lu, X., Liu, S., Wu, X., Xie, Y., & Zheng, X. 2021. Boron-incorporated micro/nano-topographical calcium silicate coating dictates osteo/angiogenesis and inflammatory response toward enhanced osseointegration, *Biological Trace Element Research*, 199(10). 3801-3816. doi: 10.1007/s12011-020-02517-w
- Li, K., Lu, X., Razanau, I., Wu, X., Hu, T., Liu, S., Xie, Y., Huang, L., & Zheng, X. 2019. The enhanced angiogenic responses to ionic dissolution products from a boron-incorporated calcium silicate coating, *Materials Science and Engineering: C*, 101. 513-520. doi: <https://doi.org/10.1016/j.msec.2019.04.009>

- Li, L., Yang, S., Xu, L., Li, Y., Fu, Y., Zhang, H., & Song, J. 2019. Nanotopography on titanium promotes osteogenesis via autophagy-mediated signaling between yap and β -catenin, *Acta Biomaterialia*, 96. 674-685. doi: 10.1016/j.actbio.2019.07.007
- Li, Y., Liu, C., Zhai, H., Zhu, G., Pan, H., Xu, X., & Tang, R. 2014. Biomimetic graphene oxide–hydroxyapatite composites via in situ mineralization and hierarchical assembly, *RSC Advances*, 4(48). 25398-25403. doi: 10.1039/C4RA02821J
- Li, Y., Liu, Y., Bai, H., Li, R., Shang, J., Zhu, Z., Zhu, L., Zhu, C., Che, Z., Wang, J., Liu, H., & Huang, L. 2021. Sustained release of vegf to promote angiogenesis and osteointegration of three-dimensional printed biomimetic titanium alloy implants, *Frontiers in Bioengineering and Biotechnology*, 9. 1102. doi: 10.3389/fbioe.2021.757767
- Li, Y., Xie, J., Guo, C., Wang, J., Liu, H., & Hu, W. 2020. Controllable synthesis of in situ grown titanate hierarchical microspheres and subsequent chemical modifications for superhydrophobic and oil–water separation properties, *RSC Advances*, 10(19). 11182-11187. doi: 10.1039/D0RA00381F
- Li, Y., Zhou, T., Yu, Z., Wang, F., Shi, D., Ni, Z., & Chen, M. 2020. Effects of surfactant and ionic concentration on properties of dual physical crosslinking self-healing hydrogels by hydrophobic association and ionic interactions, *New Journal of Chemistry*, 44(10). 4061-4070. doi: 10.1039/C9NJ05302F
- Lin, T.-H., Hu, H.-T., Wang, H.-C., Wu, M.-C., Wu, S.-W., & Yeh, M.-L. 2017. Evaluation of osseous integration of titanium orthopedic screws with novel sla treatment in porcine model, *PloS One*, 12(11). e0188364. doi: 10.1371/journal.pone.0188364
- Lin, T. h., Pajarinen, J., Lu, L., Nabeshima, A., Cordova, L. A., Yao, Z., & Goodman, S. B. (2017). Chapter four - nf- κ b as a therapeutic target in inflammatory-associated bone diseases. In R. Donev (Ed.), *Advances In Protein Chemistry and Structural Biology* (Vol. 107, pp. 117-154): Academic Press.
- Liu, C.-F., Chang, K.-C., Sun, Y.-S., Nguyen, D. T., & Huang, H.-H. 2021. Immobilizing type i collagen via natural cross-linker genipin to enhance the osteogenic responses to titanium implant surface, *Journal of Materials*

Research and Technology, 15. 885-900. doi:
<https://doi.org/10.1016/j.jmrt.2021.08.058>

Liu, L., Zeng, D., Chen, Y., Zhou, J., Liao, Y., & Shi, B. 2020. Microarc oxidation surface of titanium implants promote osteogenic differentiation by activating erk1/2-mir-1827-osterix, *In Vitro Cellular & Developmental Biology - Animal*, 56(4). 296-306. doi: 10.1007/s11626-020-00444-7

Liu, W., Li, J., Cheng, M., Wang, Q., Yeung, K. W. K., Chu, P. K., & Zhang, X. 2018. Zinc-modified sulfonated polyetheretherketone surface with immunomodulatory function for guiding cell fate and bone regeneration, *Advanced Science*, 5(10). 1800749. doi: <https://doi.org/10.1002/advs.201800749>

Liu, Y.-S., Liu, Y.-A., Huang, C.-J., Yen, M.-H., Tseng, C.-T., Chien, S., & Lee, O. K. 2015. Mechanosensitive trpm7 mediates shear stress and modulates osteogenic differentiation of mesenchymal stromal cells through osterix pathway, *Scientific Reports*, 5(1). 16522. doi: 10.1038/srep16522

Lo, Y.-S., Chang, C.-C., Lin, P.-C., Lin, S.-P., & Wang, C.-L. 2021. Direct growth of structurally controllable hydroxyapatite coating on ti-6al-4v through a rapid hydrothermal synthesis, *Applied Surface Science*, 556. 149672. doi: <https://doi.org/10.1016/j.apsusc.2021.149672>

Lohberger, B., Eck, N., Glaenger, D., Lichtenegger, H., Ploszczanski, L., & Leithner, A. 2020. Cobalt chromium molybdenum surface modifications alter the osteogenic differentiation potential of human mesenchymal stem cells, *Materials*, 13(19). 4292.

Luo, J., Mamat, B., Yue, Z., Zhang, N., Xu, X., Li, Y., Su, Z., Ma, C., Zang, F., & Wang, Y. 2021. Multi-metal ions doped hydroxyapatite coatings via electrochemical methods for antibacterial and osteogenesis, *Colloid and Interface Science Communications*, 43. 100435. doi: <https://doi.org/10.1016/j.colcom.2021.100435>

Luo, J., Wu, Z., Dai, Y., Wang, X., Ye, R., Huang, H., & Xie, X. 2021. Biofunctional micro/nanostructured “volcano-like” layer-coated 3d porous ti-10ta-2nb-2zr scaffolds improve osteogenesis and osseointegration for dental implants in vitro and in vivo, *Surface and Coatings Technology*, 427. 127852. doi: <https://doi.org/10.1016/j.surfcoat.2021.127852>

- Lv, Y., Wang, B., Liu, G., Tang, Y., Lu, E., Xie, K., Lan, C., Liu, J., Qin, Z., & Wang, L. 2021. Metal material, properties and design methods of porous biomedical scaffolds for additive manufacturing: A review, *Frontiers in Bioengineering and Biotechnology*, 9. 641130. doi: 10.3389/fbioe.2021.641130
- Lyndon, J. A., Boyd, B. J., & Birbilis, N. 2014. Metallic implant drug/device combinations for controlled drug release in orthopaedic applications, *Journal of Controlled Release*, 179. 63-75.
- Ma, X.-Y., Ma, T.-C., Feng, Y.-F., Xiang, G., Lei, W., Zhou, D.-P., Yu, H.-L., Xiang, L.-B., & Wang, L. 2021. Promotion of osteointegration under diabetic conditions by a silk fibroin coating on 3d-printed porous titanium implants via a ros-mediated nf-kb pathway, *Biomedical Materials*, 16(3). 035015. doi: 10.1088/1748-605x/abaa1
- Madupalli, H., Pavan, B., & Tecklenburg, M. M. J. 2017. Carbonate substitution in the mineral component of bone: Discriminating the structural changes, simultaneously imposed by carbonate in a and b sites of apatite, *Journal of Solid State Chemistry*, 255. 27-35. doi: 10.1016/j.jssc.2017.07.025
- Maher, S., Wijenayaka, A. R., Lima-Marques, L., Yang, D., Atkins, G. J., & Losic, D. 2021. Advancing of additive-manufactured titanium implants with bioinspired micro- to nanotopographies, *ACS Biomaterials Science & Engineering*, 7(2). 441-450. doi: 10.1021/acsbiomaterials.0c01210
- Maimaiti, B., Zhang, N., Yan, L., Luo, J., Xie, C., Wang, Y., Ma, C., & Ye, T. 2020. Stable zno-doped hydroxyapatite nanocoating for anti-infection and osteogenic on titanium, *Colloids and Surfaces B: Biointerfaces*, 186. 110731. doi: <https://doi.org/10.1016/j.colsurfb.2019.110731>
- Maji, K., Dasgupta, S., Bhaskar, R., & Gupta, M. K. 2020. Photo-crosslinked alginate nano-hydroxyapatite paste for bone tissue engineering, *Biomedical Materials*, 15(5). 055019. doi: 10.1088/1748-605x/ab9551
- Majoul, N., Aouida, S., & Bessaïs, B. 2015. Progress of porous silicon aptes-functionalization by ftir investigations, *Applied Surface Science*, 331. 388-391. doi: <https://doi.org/10.1016/j.apsusc.2015.01.107>
- Malekzadeh, E., & Zhang Newby, B.-m. 2020. Thermoresponsive poly(vinyl methyl ether) (pvme) retained by 3-aminopropyltriethoxysilane (apt) network,

- ACS Biomaterials Science & Engineering, 6(12). 7051-7060. doi: 10.1021/acsbiomaterials.0c01376
- Mallikarjunachari, G., & Ghosh, P. 2016. Analysis of strength and response of polymer nano thin film interfaces applying nanoindentation and nanoscratch techniques, Polymer, 90. 53-66. doi: <https://doi.org/10.1016/j.polymer.2016.02.042>
- Man, S. M., & Kanneganti, T.-D. 2015. Regulation of inflammasome activation, Immunological Reviews, 265(1). 6-21. doi: <https://doi.org/10.1111/imr.12296>
- Mandal, A., Clegg, J. R., Anselmo, A. C., & Mitragotri, S. 2020. Hydrogels in the clinic, Bioengineering & Translational Medicine, 5(2). e10158. doi: <https://doi.org/10.1002/btm2.10158>
- Manivasagam, V. K., & Popat, K. C. 2021. Hydrothermally treated titanium surfaces for enhanced osteogenic differentiation of adipose derived stem cells, Materials Science and Engineering: C, 128. 112315. doi: <https://doi.org/10.1016/j.msec.2021.112315>
- Mansour, S. F., El-Dek, S. I., & Ahmed, M. K. 2017. Physico-mechanical and morphological features of zirconia substituted hydroxyapatite nano crystals, Scientific Reports, 7. 43202-43202. doi: 10.1038/srep43202
- Marenzi, G., Impero, F., Scherillo, F., Sammartino, J. C., Squillace, A., & Spagnuolo, G. 2019. Effect of different surface treatments on titanium dental implant micro-morphology, Materials, 12(5). 733.
- Mariani, E., Lisignoli, G., Borzi, R. M., & Pulsatelli, L. 2019. Biomaterials: Foreign bodies or tuners for the immune response?, International journal of Molecular Sciences, 20(3). 636.
- Marques, M. E., Mansur, A. A., & Mansur, H. S. 2013. Chemical functionalization of surfaces for building three-dimensional engineered biosensors, Applied Surface Science, 275. 347-360.
- Marques, T. M. F., Sales, D. A., Silva, L. S., Bezerra, R. D. S., Silva, M. S., Osajima, J. A., Ferreira, O. P., Ghosh, A., Silva Filho, E. C., Viana, B. C., & Matos, J. M. E. 2020. Amino-functionalized titanate nanotubes for highly efficient

removal of anionic dye from aqueous solution, *Applied Surface Science*, 512. 145659. doi: <https://doi.org/10.1016/j.apsusc.2020.145659>

Martocq, L., & Douglas, T. E. L. 2021. Amine-rich coatings to potentially promote cell adhesion, proliferation and differentiation, and reduce microbial colonization: Strategies for generation and characterization, *Coatings*, 11(8). 983.

Masamoto, K., Fujibayashi, S., Yamaguchi, S., Otsuki, B., Okuzu, Y., Kawata, T., Goto, K., Shimizu, T., Shimizu, Y., Kawai, T., Hayashi, M., Morizane, K., Imamura, M., Ikeda, N., Takaoka, Y., & Matsuda, S. 2021. Bioactivity and antibacterial activity of strontium and silver ion releasing titanium, *Journal of Biomedical Materials Research Part B: Applied Biomaterials*, 109(2). 238-245. doi: <https://doi.org/10.1002/jbm.b.34695>

Matsuno, H., Yokoyama, A., Watari, F., Uo, M., & Kawasaki, T. 2001. Biocompatibility and osteogenesis of refractory metal implants, titanium, hafnium, niobium, tantalum and rhenium, *Biomaterials*, 22(11). 1253-1262. doi: [10.1016/S0142-9612\(00\)00275-1](https://doi.org/10.1016/S0142-9612(00)00275-1)

Mehrvarz, A., Khalil-Allafi, J., Etminanfar, M., & Mahdavi, S. 2021. The study of morphological evolution, biocorrosion resistance, and bioactivity of pulse electrochemically deposited hydroxyapatite/zno composite on niti superelastic alloy, *Surface and Coatings Technology*, 423. 127628. doi: <https://doi.org/10.1016/j.surfcoat.2021.127628>

Meroni, D., Lo Presti, L., Di Liberto, G., Ceotto, M., Acres, R. G., Prince, K. C., Bellani, R., Soliveri, G., & Ardizzone, S. 2017. A close look at the structure of the tio₂-aptes interface in hybrid nanomaterials and its degradation pathway: An experimental and theoretical study, *The Journal of Physical Chemistry C*, 121(1). 430-440. doi: [10.1021/acs.jpcc.6b10720](https://doi.org/10.1021/acs.jpcc.6b10720)

Miao, E. A., Rajan, J. V., & Aderem, A. 2011. Caspase-1-induced pyroptotic cell death, *Immunological Reviews*, 243(1). 206-214. doi: <https://doi.org/10.1111/j.1600-065X.2011.01044.x>

Moloodi, A., Toraby, H., Kahrobaee, S., Razavi, M. K., & Salehi, A. 2021. Evaluation of fluorohydroxyapatite/strontium coating on titanium implants fabricated by hydrothermal treatment, *Progress in Biomaterials*, 10(3). 185-194. doi: [10.1007/s40204-021-00162-7](https://doi.org/10.1007/s40204-021-00162-7)

- Moon, Y. J., Yun, C.-Y., Choi, H., Kim, J. R., Park, B.-H., & Cho, E.-S. 2018. Osterix regulates corticalization for longitudinal bone growth via integrin $\beta 3$ expression, *Experimental & Molecular Medicine*, 50(7). 1-11. doi: 10.1038/s12276-018-0119-9
- Morejón-Alonso, L., Bussulo, M. A., Debone, R., González-Martínez, E., & González, J. E. 2020. Apatite coatings on chemically modified titanium using a new accelerated biomimetic route, *Materials Letters*, 280. 128576. doi: <https://doi.org/10.1016/j.matlet.2020.128576>
- Morita, M., Yoshida, S., Iwasaki, R., Yasui, T., Sato, Y., Kobayashi, T., Watanabe, R., Oike, T., Miyamoto, K., Takami, M., Ozato, K., Deng, C.-X., Aburatani, H., Tanaka, S., Yoshimura, A., Toyama, Y., Matsumoto, M., Nakamura, M., Kawana, H., Nakagawa, T., & Miyamoto, T. 2016. Smad4 is required to inhibit osteoclastogenesis and maintain bone mass, *Scientific Reports*, 6(1). 35221. doi: 10.1038/srep35221
- Moyano, D. F., Goldsmith, M., Solfiell, D. J., Landesman-Milo, D., Miranda, O. R., Peer, D., & Rotello, V. M. 2012. Nanoparticle hydrophobicity dictates immune response, *Journal of the American Chemical Society*, 134(9). 3965-3967.
- Muley, S. V., Vidvans, A. N., Chaudhari, G. P., & Udainiya, S. 2016. An assessment of ultra fine grained 316l stainless steel for implant applications, *Acta Biomaterialia*, 30. 408-419. doi: <https://doi.org/10.1016/j.actbio.2015.10.043>
- Mutuk, T., & Gürbüz, M. 2021. Graphene/chitosan/ag+- doped hydroxyapatite triple composite fiber coatings on new generation hybrid titanium composite by electrospinning, *Journal of Composite Materials*, 55(22). 3087-3097. doi: 10.1177/00219983211007544
- Naderi, A., Zhang, B., Belgodere, J. A., Sunder, K., & Palardy, G. 2021. Improved biocompatible, flexible mesh composites for implant applications via hydroxyapatite coating with potential for 3-dimensional extracellular matrix network and bone regeneration, *ACS Applied Materials & Interfaces*, 13(23). 26824-26840. doi: 10.1021/acsami.1c09034
- Naito, Y., Jimbo, R., Bryington, M. S., Vandeweghe, S., Chrcanovic, B. R., Tovar, N., Ichikawa, T., Coelho, P. G., & Wennerberg, A. 2014. The influence of 1 α . 25-dihydroxyvitamin d3 coating on implant osseointegration in the rabbit

tibia, *Journal of Oral & Maxillofacial Research*, 5(3). e3. doi: 10.5037/jomr.2014.5303

Narwal, P., Dahiya, M. S., Yadav, A., Hooda, A., Agarwal, A., & Khasa, S. 2018. Improved white light emission in dy^{3+} doped $\text{lif-cao-bi}_2\text{o}_3\text{-b}_2\text{o}_3$ glasses, *Journal of Non-Crystalline Solids*, 498. 470-479. doi: 10.1016/j.jnoncrysol.2018.01.042

Naujokat, H., Gökkaya, A. I., Açı, Y., Loger, K., Klüter, T., Fuchs, S., & Wiltfang, J. 2022. In vivo biocompatibility evaluation of 3d-printed nickel–titanium fabricated by selective laser melting, *Journal of Materials Science: Materials in Medicine*, 33(2). 13. doi: 10.1007/s10856-022-06641-y

Nguyen, T. P., Nguyen, Q. V., Nguyen, V.-H., Le, T.-H., Huynh, V. Q. N., Vo, D.-V. N., Trinh, Q. T., Kim, S. Y., & Le, Q. V. 2019. Silk fibroin-based biomaterials for biomedical applications: A review, *Polymers*, 11(12). 1933.

Obayes, H. K., Wagiran, H., Hussin, R., & Saeed, M. A. 2016. Strontium ions concentration dependent modifications on structural and optical features of $\text{li}_4\text{sr}(\text{bo}_3)(3)$ glass, *Journal of Molecular Structure*, 1111. 132-141. doi: 10.1016/j.molstruc.2016.01.088

Olivares-Navarrete, R., Rodil, S. E., Hyzy, S. L., Dunn, G. R., Almaguer-Flores, A., Schwartz, Z., & Boyan, B. D. 2015. Role of integrin subunits in mesenchymal stem cell differentiation and osteoblast maturation on graphitic carbon-coated microstructured surfaces, *Biomaterials*, 51. 69-79.

Otsuki, B., Takemoto, M., Fujibayashi, S., Neo, M., Kokubo, T., & Nakamura, T. 2006. Pore throat size and connectivity determine bone and tissue ingrowth into porous implants: Three-dimensional micro-ct based structural analyses of porous bioactive titanium implants, *Biomaterials*, 27(35). 5892-5900. doi: <https://doi.org/10.1016/j.biomaterials.2006.08.013>

Öztürk-Öncel, M. Ö., Odabaş, S., Uzun, L., Hür, D., & Garipcan, B. 2020. A facile surface modification of poly(dimethylsiloxane) with amino acid conjugated self-assembled monolayers for enhanced osteoblast cell behavior, *Colloids and Surfaces B: Biointerfaces*, 196. 111343. doi: <https://doi.org/10.1016/j.colsurfb.2020.111343>

- Pagel, M., & Beck-Sickinger, A. G. 2017. Multifunctional biomaterial coatings: Synthetic challenges and biological activity, *Biological Chemistry*, 398(1). 3-22. doi: doi:10.1515/hsz-2016-0204
- Palkowitz, A. L., Tuna, T., Bishti, S., Böke, F., Steinke, N., Müller-Newen, G., Wolfart, S., & Fischer, H. 2021. Biofunctionalization of dental abutment surfaces by crosslinked ecm proteins strongly enhances adhesion and proliferation of gingival fibroblasts, *Advanced Healthcare Materials*, 10(10). 2100132. doi: <https://doi.org/10.1002/adhm.202100132>
- Paretkar, D. R., Bartlett, M. D., McMeeking, R., Crosby, A. J., & Arzt, E. 2013. Buckling of an adhesive polymeric micropillar, *The Journal of Adhesion*, 89(2). 140-158. doi: 10.1080/00218464.2013.731941
- Park, J., Cimpean, A., Tesler, A. B., & Mazare, A. 2021. Anodic tio2 nanotubes: Tailoring osteoinduction via drug delivery, *Nanomaterials*, 11(9). 2359.
- Pazarçeviren, A. E., Tezcaner, A., & Evis, Z. 2021. Multifunctional natural polymer-based metallic implant surface modifications, *Biointerphases*, 16(2). 020803. doi: 10.1116/6.0000876
- Pazarçeviren, A. E., Tezcaner, A., Keskin, D., Kolukısa, S. T., Sürdem, S., & Evis, Z. 2021. Boron-doped biphasic hydroxyapatite/ β -tricalcium phosphate for bone tissue engineering, *Biological Trace Element Research*, 199(3). 968-980. doi: 10.1007/s12011-020-02230-8
- Peng, F., Qiu, L., Yao, M., Liu, L., Zheng, Y., Wu, S., Ruan, Q., Liu, X., Zhang, Y., Li, M., & Chu, P. K. 2021. A lithium-doped surface inspires immunomodulatory functions for enhanced osteointegration through pi3k/akt signaling axis regulation, *Biomaterials Science*, 9(24). 8202-8220. doi: 10.1039/D1BM01075A
- Phan, H. T., Bartelt-Hunt, S., Rodenhausen, K. B., Schubert, M., & Bartz, J. C. 2015. Investigation of bovine serum albumin (bsa) attachment onto self-assembled monolayers (sams) using combinatorial quartz crystal microbalance with dissipation (qcm-d) and spectroscopic ellipsometry (se), *PloS One*, 10(10). e0141282. doi: 10.1371/journal.pone.0141282
- Plodinec, M., Gajović, A., Iveković, D., Tomašić, N., Zimmermann, B., Macan, J., Haramina, T., Su, D. S., & Willinger, M. 2014. Study of thermal stability of (3-aminopropyl)trimethoxy silane-grafted titanate nanotubes for application

as nanofillers in polymers, *Nanotechnology*, 25(43). 435601. doi: 10.1088/0957-4484/25/43/435601

Posa, F., Di Benedetto, A., Cavalcanti-Adam, E. A., Colaianni, G., Porro, C., Trotta, T., Brunetti, G., Lo Muzio, L., Grano, M., & Mori, G. 2018. Vitamin d promotes msc osteogenic differentiation stimulating cell adhesion and $\alpha\text{v}\beta 3$ expression, *Stem cells international*. 6958713. doi: 10.1155/2018/6958713

Poser, L., Matthys, R., Schawalder, P., Pearce, S., Alini, M., & Zeiter, S. 2014. A standardized critical size defect model in normal and osteoporotic rats to evaluate bone tissue engineered constructs, *BioMed Research International*. 348635. doi: 10.1155/2014/348635

Prasad, K., Bazaka, O., Chua, M., Rochford, M., Fedrick, L., Spoor, J., Symes, R., Tieppo, M., Collins, C., & Cao, A. 2017. Metallic biomaterials: Current challenges and opportunities, *Materials*, 10(8). 884. doi: 10.3390/ma10080884

Priyadarshini, B., Rama, M., Chetan, & Vijayalakshmi, U. 2019. Bioactive coating as a surface modification technique for biocompatible metallic implants: A review, *Journal of Asian Ceramic Societies*, 7(4). 397-406.

Priyadarshini, B., & Vijayalakshmi, U. 2021. In vitro bioactivity, biocompatibility and corrosion resistance of multi-ionic (ce/si) co-doped hydroxyapatite porous coating on ti-6al-4 v for bone regeneration applications, *Materials Science and Engineering: C*, 119. 111620. doi: <https://doi.org/10.1016/j.msec.2020.111620>

Prodana, M., Stoian, A. B., Burnei, C., & Ionita, D. 2021. Innovative coatings of metallic alloys used as bioactive surfaces in implantology: A review, *Coatings*, 11(6). 649.

Raines, A. L., Berger, M. B., Patel, N., Hyzy, S. L., Boyan, B. D., & Schwartz, Z. 2019. Vegf-a regulates angiogenesis during osseointegration of ti implants via paracrine/autocrine regulation of osteoblast response to hierarchical microstructure of the surface, *Journal of Biomedical Materials Research Part A*, 107(2). 423-433. doi: <https://doi.org/10.1002/jbm.a.36559>

Raines, A. L., Olivares-Navarrete, R., Wieland, M., Cochran, D. L., Schwartz, Z., & Boyan, B. D. 2010. Regulation of angiogenesis during osseointegration by

titanium surface microstructure and energy, *Biomaterials*, 31(18). 4909-4917.

Rameshbabu, N., Ravisankar, B., Saikiran, A., Parfenov, E., & Valiev, R. (2019). *Surface modification of cp-ti metallic implant material by plasma electrolytic oxidation*. Paper presented at the IOP Conference Series: Materials Science and Engineering.

Ratha, I., Datta, P., Chand Reger, N., Das, H., Balla, V. K., Devi, K. B., Roy, M., Nandi, S. K., & Kundu, B. 2022. In vivo osteogenesis of plasma sprayed ternary-ion doped hydroxyapatite coatings on ti6al4v for orthopaedic applications, *Ceramics International*, 48(8). 11475-11488. doi: <https://doi.org/10.1016/j.ceramint.2022.01.004>

Reger, N. C., Bhargava, A. K., Ratha, I., Kundu, B., & Balla, V. K. 2019. Structural and phase analysis of multi-ion doped hydroxyapatite for biomedical applications, *Ceramics International*, 45(1). 252-263. doi: <https://doi.org/10.1016/j.ceramint.2018.09.160>

Reyes-Gasga, J., Martínez-Piñeiro, E. L., Rodríguez-Álvarez, G., Tiznado-Orozco, G. E., García-García, R., & Brès, E. F. 2013. Xrd and flir crystallinity indices in sound human tooth enamel and synthetic hydroxyapatite, *Materials Science and Engineering: C*, 33(8). 4568-4574. doi: <https://doi.org/10.1016/j.msec.2013.07.014>

Rodriguez, G. M., Bowen, J., Grossin, D., Ben-Nissan, B., & Stamboulis, A. 2017. Functionalisation of ti6al4v and hydroxyapatite surfaces with combined peptides based on kklpda and eeeeeeee peptides, *Colloids and Surfaces B: Biointerfaces*, 160. 154-160. doi: <https://doi.org/10.1016/j.colsurfb.2017.09.022>

Rodriquez, D., Kohl, J. G., Morel, P., Burrows, K., Favaro, G., Root, S. E., Ramírez, J., Alkhadra, M. A., Carpenter, C. W., Fei, Z., Boufflet, P., Heeney, M., & Lipomi, D. J. 2018. Measurement of cohesion and adhesion of semiconducting polymers by scratch testing: Effect of side-chain length and degree of polymerization, *ACS Macro Letters*, 7(8). 1003-1009. doi: [10.1021/acsmacrolett.8b00412](https://doi.org/10.1021/acsmacrolett.8b00412)

Roghani-Mamaqani, H., & Haddadi-Asl, V. 2014. In-plane functionalizing graphene nanolayers with polystyrene by atom transfer radical polymerization:

Grafting from hydroxyl groups, *Polymer Composites*, 35(2). 386-395. doi: <https://doi.org/10.1002/pc.22672>

Rosenthal, A., Mantz, A., Nguyen, A., Bittrich, E., Schubert, E., Schubert, M., Stamm, M., Pannier, A. K., & Uhlmann, P. 2018. Biofunctionalization of titanium substrates using nanoscale polymer brushes with cell adhesion peptides, *The Journal of Physical Chemistry B*, 122(25). 6543-6550.

Sabino, R. M., Mondini, G., Kipper, M. J., Martins, A. F., & Popat, K. C. 2021. Tanfloc/heparin polyelectrolyte multilayers improve osteogenic differentiation of adipose-derived stem cells on titania nanotube surfaces, *Carbohydrate Polymers*, 251. 117079. doi: <https://doi.org/10.1016/j.carbpol.2020.117079>

Sadoghi, P., Liebensteiner, M., Agreiter, M., Leithner, A., Boehler, N., & Labek, G. 2013. Revision surgery after total joint arthroplasty: A complication-based analysis using worldwide arthroplasty registers, *The Journal of Arthroplasty*, 28(8). 1329-1332.

Saini, M., Singh, Y., Arora, P., Arora, V., & Jain, K. 2015. Implant biomaterials: A comprehensive review, *World Journal of Clinical Cases*, 3(1). 52. doi: [10.12998/wjcc.v3.i1.52](https://doi.org/10.12998/wjcc.v3.i1.52)

Sang, S., Guo, G., Yu, J., & Zhang, X. 2021. Antibacterial application of gentamicin–silk protein coating with smart release function on titanium, polyethylene, and al₂o₃ materials, *Materials Science and Engineering: C*, 124. 112069. doi: <https://doi.org/10.1016/j.msec.2021.112069>

Sarkar, N., Banerjee, D., Bandyopadhyay, A., & Bose, S. 2021. Osteoclast-mediated resorption on additively manufactured porous metal and plasma-sprayed ha-coated ti implants, *Journal of Materials Research*, 36(19). 3894-3904. doi: [10.1557/s43578-021-00278-3](https://doi.org/10.1557/s43578-021-00278-3)

Saveleva, M., Vladescu, A., Cotrut, C., Van der Meeren, L., Surmeneva, M., Surmenev, R., Parakhonskiy, B., & Skirtach, A. G. 2019. The effect of hybrid coatings based on hydrogel, biopolymer and inorganic components on the corrosion behavior of titanium bone implants, *Journal of Materials Chemistry B*, 7(43). 6778-6788.

Schröder, K., Finke, B., Ohl, A., Lüthen, F., Bergemann, C., Nebe, B., Rychly, J., Walschus, U., Schlosser, M., & Liefeth, K. 2010. Capability of differently

charged plasma polymer coatings for control of tissue interactions with titanium surfaces, *Journal of Adhesion Science And Technology*, 24(7). 1191-1205.

Sharan, J., Koul, V., Dinda, A. K., Kharbanda, O. P., Lale, S. V., Duggal, R., Mishra, M., Gupta, G., & Singh, M. P. 2018. Bio-functionalization of grade v titanium alloy with type i human collagen for enhancing and promoting human periodontal fibroblast cell adhesion – an in-vitro study, *Colloids and Surfaces B: Biointerfaces*, 161. 1-9. doi: <https://doi.org/10.1016/j.colsurfb.2017.10.024>

Shekaran, A., Shoemaker, J. T., Kavanaugh, T. E., Lin, A. S., LaPlaca, M. C., Fan, Y., Guldborg, R. E., & García, A. J. 2014. The effect of conditional inactivation of beta 1 integrins using twist 2 cre, osterix cre and osteocalcin cre lines on skeletal phenotype, *Bone*, 68. 131-141. doi: <https://doi.org/10.1016/j.bone.2014.08.008>

Shi, J., Sun, J., Zhang, W., Liang, H., Shi, Q., Li, X., Chen, Y., Zhuang, Y., & Dai, J. 2016. Demineralized bone matrix scaffolds modified by cbd-sdf-1 α promote bone regeneration via recruiting endogenous stem cells, *ACS Applied Materials & Interfaces*, 8(41). 27511-27522. doi: [10.1021/acsami.6b08685](https://doi.org/10.1021/acsami.6b08685)

Silva-Bermudez, P., & Rodil, S. 2013. An overview of protein adsorption on metal oxide coatings for biomedical implants, *Surface and Coatings Technology*, 233. 147-158.

Silva, G. A. F., Faot, F., Possebon, A. P. d. R., da Silva, W. J., & Del Bel Cury, A. A. 2021. Effect of macrogeometry and bone type on insertion torque, primary stability, surface topography damage and titanium release of dental implants during surgical insertion into artificial bone, *Journal of the Mechanical Behavior of Biomedical Materials*, 119. 104515. doi: <https://doi.org/10.1016/j.jmbbm.2021.104515>

Simsek, G. M., Barthes, J., Muller, C., McGuinness, G. B., Vrana, N. E., & Yapici, G. G. 2021. Pva/gelatin-based hydrogel coating of nickel-titanium alloy for improved tissue-implant interface, *Applied Physics A*, 127(5). 387. doi: [10.1007/s00339-021-04542-5](https://doi.org/10.1007/s00339-021-04542-5)

Sodhi, H., & Panitch, A. 2021. Glycosaminoglycans in tissue engineering: A review, *Biomolecules*, 11(1). 29.

- Song, Q., Prabakaran, S., Duan, J., Jeyaraj, M., Mickymaray, S., Paramasivam, A., & Rajan, M. 2021. Enhanced bone tissue regeneration via bioactive electrospun fibrous composite coated titanium orthopedic implant, *International Journal of Pharmaceutics*, 607. 120961. doi: <https://doi.org/10.1016/j.ijpharm.2021.120961>
- Sridar, S., Churchward, M. A., Mushahwar, V. K., Todd, K. G., & Elias, A. L. 2017. Peptide modification of polyimide-insulated microwires: Towards improved biocompatibility through reduced glial scarring, *Acta Biomaterialia*, 60. 154-166.
- Steen, E. H., Wang, X., Balaji, S., Butte, M. J., Bollyky, P. L., & Keswani, S. G. 2020. The role of the anti-inflammatory cytokine interleukin-10 in tissue fibrosis, *Adv Wound Care (New Rochelle)*, 9(4). 184-198. doi: [10.1089/wound.2019.1032](https://doi.org/10.1089/wound.2019.1032)
- Stevanović, M., Došić, M., Janković, A., Kojić, V., Vukašinović-Sekulić, M., Stojanović, J., Odović, J., Crevar Sakač, M., Rhee, K. Y., & Mišković-Stanković, V. 2018. Gentamicin-loaded bioactive hydroxyapatite/chitosan composite coating electrodeposited on titanium, *ACS Biomaterials Science & Engineering*, 4(12). 3994-4007. doi: [10.1021/acsbiomaterials.8b00859](https://doi.org/10.1021/acsbiomaterials.8b00859)
- Su, T., Zheng, A., Cao, L., Peng, L., Wang, X., Wang, J., Xin, X., & Jiang, X. 2022. Adhesion-enhancing coating embedded with osteogenesis-promoting pda/ha nanoparticles for peri-implant soft tissue sealing and osseointegration, *Bio-Design and Manufacturing*, 5(2). 233-248. doi: [10.1007/s42242-022-00184-5](https://doi.org/10.1007/s42242-022-00184-5)
- Su, Y., Huang, C., Lu, F., Tong, X., Niu, J., & Mao, L. 2018. Alginate affects agglomeration state and uptake of 14c-labeled few-layer graphene by freshwater snails: Implications for the environmental fate of graphene in aquatic systems, *Environmental Pollution*, 234. 513-522. doi: <https://doi.org/10.1016/j.envpol.2017.11.087>
- Sun, Y., Sun, J., Wu, X., Li, Y., Li, X., Li, R., Wang, T., Bi, W., Cui, W., & Yu, Y. 2021. Mechanism of zirconia microgroove surface structure for osseointegration, *Materials Today Advances*, 12. 100159. doi: <https://doi.org/10.1016/j.mtadv.2021.100159>

- Sun, Y., Zhang, X., Luo, M., Hu, W., Zheng, L., Huang, R., Greven, J., Hildebrand, F., & Yuan, F. 2021. Plasma spray vs. Electrochemical deposition: Toward a better osteogenic effect of hydroxyapatite coatings on 3d-printed titanium scaffolds, *Frontiers in Bioengineering and Biotechnology*, 9. doi: 10.3389/fbioe.2021.705774
- Sun, Y., Zhao, Y., Zhang, H., Rong, Y., Yao, R., Zhang, Y., Yao, X., & Hang, R. 2022. Corrosion behavior, antibacterial ability, and osteogenic activity of zn-incorporated ni-ti-o nanopore layers on niti alloy, *Journal of Materials Science & Technology*, 97. 69-78. doi: <https://doi.org/10.1016/j.jmst.2021.04.029>
- Suresh, S., Sun, C.-N., Tekumalla, S., Rosa, V., Ling Nai, S. M., & Wong, R. C. W. 2021. Mechanical properties and in vitro cytocompatibility of dense and porous ti-6al-4v eli manufactured by selective laser melting technology for biomedical applications, *Journal of the Mechanical Behavior of Biomedical Materials*, 123. 104712. doi: <https://doi.org/10.1016/j.jmbbm.2021.104712>
- Švagrová, K., Horkavcová, D., Jablonská, E., & Helebrant, A. 2022. Titania-based sol-gel coatings with ag, ca-p applied on titanium substrate developed for implantation, *Journal of Biomedical Materials Research Part B: Applied Biomaterials*, 110(1). 115-124. doi: <https://doi.org/10.1002/jbm.b.34895>
- Takadama, H., Kim, H.-M., Kokubo, T., & Nakamura, T. 2001. Xps study of the process of apatite formation on bioactive ti-6al-4v alloy in simulated body fluid, *Science and Technology of Advanced Materials*, 2(2). 389-396. doi: 10.1016/S1468-6996(01)00007-9
- Tan, F., & Al-Rubeai, M. 2021. A multifunctional dexamethasone-delivery implant fabricated using atmospheric plasma and its effects on apoptosis, osteogenesis and inflammation, *Drug Delivery and Translational Research*, 11(1). 86-102. doi: 10.1007/s13346-019-00700-8
- Tan, G., Zhang, L., Ning, C., Liu, X., & Liao, J. 2011. Preparation and characterization of aptes films on modification titanium by sams, *Thin Solid Films*, 519(15). 4997-5001. doi: <https://doi.org/10.1016/j.tsf.2011.01.068>
- Tan, H. C., Poh, C. K., Cai, Y., & Wang, W. 2013. Anti-fibrosis effect of bmp-7 peptide functionalization on cobalt chromium alloy, *Journal of Orthopaedic Research*, 31(6). 983-990.

- Tan, L., Fu, J., Feng, F., Liu, X., Cui, Z., Li, B., Han, Y., Zheng, Y., Yeung, K. W. K., Li, Z., Zhu, S., Liang, Y., Feng, X., Wang, X., & Wu, S. 2020. Engineered probiotics biofilm enhances osseointegration via immunoregulation and anti-infection, *Science Advances*, 6(46). eaba5723. doi: doi:10.1126/sciadv.aba5723
- Tang, L., Thevenot, P., & Hu, W. 2008. Surface chemistry influences implant biocompatibility, *Current Topics in Medicinal Chemistry*, 8(4). 270-280. doi: 10.2174/156802608783790901
- Tang, Q., Zhang, X., Shen, K., Zhu, Z., Hou, Y., & Lai, M. 2021. Dual-functionalized titanium for enhancing osteogenic and antibacterial properties, *Colloid and Interface Science Communications*, 44. 100481. doi: <https://doi.org/10.1016/j.colcom.2021.100481>
- Tenkumo, T., Vanegas Sáenz, J. R., Nakamura, K., Shimizu, Y., Sokolova, V., Epple, M., Kamano, Y., Egusa, H., Sugaya, T., & Sasaki, K. 2018. Prolonged release of bone morphogenetic protein-2 in vivo by gene transfection with DNA-functionalized calcium phosphate nanoparticle-loaded collagen scaffolds, *Materials Science and Engineering: C*, 92. 172-183. doi: <https://doi.org/10.1016/j.msec.2018.06.047>
- Testrich, H., Rebl, H., Finke, B., Hempel, F., Nebe, B., & Meichsner, J. 2013. Aging effects of plasma polymerized ethylenediamine (ppeda) thin films on cell-adhesive implant coatings, *Materials Science and Engineering: C*, 33(7). 3875-3880.
- Tondera, C., Hauser, S., Krüger-Genge, A., Jung, F., Neffe, A. T., Lendlein, A., Klopffleisch, R., Steinbach, J., Neuber, C., & Pietzsch, J. 2016. Gelatin-based hydrogel degradation and tissue interaction in vivo: Insights from multimodal preclinical imaging in immunocompetent nude mice, *Theranostics*, 6(12). 2114-2128. doi: 10.7150/thno.16614
- Tozar, A., Karahan, I. H., & Yücel, Y. 2019. Optimization of the electrophoretic deposition parameters for biocomposite hydroxyapatite/chitosan/collagen/h-bn coatings on ti6al4v biomedical implants, *Metallurgical and Materials Transactions A*, 50(2). 1009-1020.
- Trujillo, S., Gonzalez-Garcia, C., Rico, P., Reid, A., Windmill, J., Dalby, M. J., & Salmeron-Sanchez, M. 2020. Engineered 3d hydrogels with full-length

- fibronectin that sequester and present growth factors, *Biomaterials*, 252. 120104. doi: <https://doi.org/10.1016/j.biomaterials.2020.120104>
- Tweedell, R. E., Malireddi, R. K. S., & Kanneganti, T.-D. 2020. A comprehensive guide to studying inflammasome activation and cell death, *Nature Protocols*, 15(10). 3284-3333. doi: 10.1038/s41596-020-0374-9
- Tzaphlidou, M. 2008. Bone architecture: Collagen structure and calcium/phosphorus maps, *Journal of Biological Physics*, 34(1). 39-49. doi: 10.1007/s10867-008-9115-y
- Tzeng, T.-C., Schattgen, S., Monks, B., Wang, D., Cerny, A., Latz, E., Fitzgerald, K., & Golenbock, D. T. 2016. A fluorescent reporter mouse for inflammasome assembly demonstrates an important role for cell-bound and free asc specks during in vivo infection, *Cell Reports*, 16(2). 571-582. doi: <https://doi.org/10.1016/j.celrep.2016.06.011>
- Ullah, I., Xu, Q., Jan, H. U., Ren, L., & Yang, K. 2022. Effects of strontium and zinc substituted plasma sprayed hydroxyapatite coating on bone-like apatite layer formation and cell-material interaction, *Materials Chemistry and Physics*, 275. 125219. doi: <https://doi.org/10.1016/j.matchemphys.2021.125219>
- van Putten, S. M., Ploeger, D. T. A., Popa, E. R., & Bank, R. A. 2013. Macrophage phenotypes in the collagen-induced foreign body reaction in rats, *Acta Biomaterialia*, 9(5). 6502-6510. doi: <https://doi.org/10.1016/j.actbio.2013.01.022>
- Vande Walle, L., & Lamkanfi, M. 2011. Inflammasomes: Caspase-1-activating platforms with critical roles in host defense, *Frontiers in Microbiology*, 2. 3. doi: 10.3389/fmicb.2011.00003
- Vishwakarma, A., Bhise, N. S., Evangelista, M. B., Rouwkema, J., Dokmeci, M. R., Ghaemmaghami, A. M., Vrana, N. E., & Khademhosseini, A. 2016. Engineering immunomodulatory biomaterials to tune the inflammatory response, *Trends in Biotechnology*, 34(6). 470-482.
- Wang, A.-J., Lu, Y.-P., Zhu, R.-F., Li, S.-T., Xiao, G.-Y., Zhao, G.-F., & Xu, W.-H. 2008. Effect of sintering on porosity, phase, and surface morphology of spray dried hydroxyapatite microspheres, *Journal of Biomedical Materials Research Part A*, 87A(2). 557-562. doi: 10.1002/jbm.a.31895

- Wang, B., Wu, Z., Lan, J., Li, Y., Xie, L., Huang, X., Zhang, A., Qiao, H., Chang, X., Lin, H., Zhang, H., Li, T., & Huang, Y. 2021. Surface modification of titanium implants by silk fibroin/ag co-functionalized strontium titanate nanotubes for inhibition of bacterial-associated infection and enhancement of in vivo osseointegration, *Surface and Coatings Technology*, 405. 126700. doi: <https://doi.org/10.1016/j.surfcoat.2020.126700>
- Wang, C., Brown, G. O., Burris, D. L., Korley, L. T., & Epps III, T. H. 2019. Coating architects: Manipulating multiscale structures to optimize interfacial properties for coating applications, *ACS Applied Polymer Materials*, 1(9). 2249-2266.
- Wang, C., Fang, H., Qi, X., Hang, C., Sun, Y., Peng, Z., Wei, W., & Wang, Y. 2019. Silk fibroin film-coated mgznca alloy with enhanced in vitro and in vivo performance prepared using surface activation, *Acta biomaterialia*, 91. 99-111.
- Wang, L., Luo, Q., Zhang, X., Qiu, J., Qian, S., & Liu, X. 2021. Co-implantation of magnesium and zinc ions into titanium regulates the behaviors of human gingival fibroblasts, *Bioactive Materials*, 6(1). 64-74. doi: <https://doi.org/10.1016/j.bioactmat.2020.07.012>
- Wang, M., Wang, C., Zhang, Y., & Lin, Y. 2021. Controlled release of dopamine coatings on titanium bidirectionally regulate osteoclastic and osteogenic response behaviors, *Materials Science and Engineering: C*, 129. 112376. doi: <https://doi.org/10.1016/j.msec.2021.112376>
- Wang, X., Dong, H., Liu, J., Qin, G., Chen, D., & Zhang, E. 2019. In vivo antibacterial property of ti-cu sintered alloy implant, *Materials Science and Engineering: C*, 100. 38-47. doi: <https://doi.org/10.1016/j.msec.2019.02.084>
- Wang, Y., Yu, Z., Li, K., & Hu, J. 2021. Study on the effect of surface characteristics of short-pulse laser patterned titanium alloy on cell proliferation and osteogenic differentiation, *Materials Science and Engineering: C*, 128. 112349. doi: <https://doi.org/10.1016/j.msec.2021.112349>
- Wang, Z., Mei, L., Liu, X., & Zhou, Q. 2021. Hierarchically hybrid biocoatings on ti implants for enhanced antibacterial activity and osteogenesis, *Colloids and Surfaces B: Biointerfaces*, 204. 111802. doi: <https://doi.org/10.1016/j.colsurfb.2021.111802>

- Watanabe, Y., Ikoma, T., Monkawa, A., Suetsugu, Y., Yamada, H., Tanaka, J., & Moriyoshi, Y. 2005. Fabrication of transparent hydroxyapatite sintered body with high crystal orientation by pulse electric current sintering, *Journal of the American Ceramic Society*, 88(1). 243-245.
- Wei, H., Xia, J., Zhou, W., Zhou, L., Hussain, G., Li, Q., & Ostrikov, K. 2020. Adhesion and cohesion of epoxy-based industrial composite coatings, *Composites Part B: Engineering*, 193. 108035. doi: <https://doi.org/10.1016/j.compositesb.2020.108035>
- Wei, Y., Hu, Y., Li, M., & Li, D. 2021. Fabrication of sr-functionalized micro/nano-hierarchical structure ceramic coatings on 3d printing titanium, *Surface Engineering*, 37(3). 373-380. doi: 10.1080/02670844.2020.1748349
- Wenhao, Z., Zhang, T., Yan, J., Li, Q., Xiong, P., Li, Y., Cheng, Y., & Zheng, Y. 2020. In vitro and in vivo evaluation of structurally-controlled silk fibroin coatings for orthopedic infection and in-situ osteogenesis, *Acta Biomaterialia*, 116. 223-245. doi: <https://doi.org/10.1016/j.actbio.2020.08.040>
- Wennerberg, A., & Albrektsson, T. 2009. Effects of titanium surface topography on bone integration: A systematic review, *Clinical Oral Implants Research*, 20(s4). 172-184. doi: 10.1111/j.1600-0501.2009.01775.x
- Witzler, M., Büchner, D., Shoushrah, S. H., Babczyk, P., Baranova, J., Witzleben, S., Tobiasch, E., & Schulze, M. 2019. Polysaccharide-based systems for targeted stem cell differentiation and bone regeneration, *Biomolecules*, 9(12). 840.
- Wu, C., Miron, R., Sculean, A., Kaskel, S., Doert, T., Schulze, R., & Zhang, Y. 2011. Proliferation, differentiation and gene expression of osteoblasts in boron-containing associated with dexamethasone deliver from mesoporous bioactive glass scaffolds, *Biomaterials*, 32(29). 7068-7078.
- Wu, C., Shao, X., Lin, X., Gao, W., Fang, Y., & Wang, J. 2020. Surface modification of titanium with collagen/hyaluronic acid and bone morphogenetic protein 2/7 heterodimer promotes osteoblastic differentiation, *Dental Materials Journal*, 39(6). 1072-1079. doi: 10.4012/dmj.2019-249

- Wu, R., Li, H., Yang, Y., Zheng, Q., Li, S., & Chen, Y. 2021. Bioactive silk fibroin-based hybrid biomaterials for musculoskeletal engineering: Recent progress and perspectives, *ACS Applied Bio Materials*, 4(9). 6630-6646. doi: 10.1021/acsabm.1c00654
- Wu, X., Liu, S., Chen, K., Wang, F., Feng, C., Xu, L., & Zhang, D. 2021. 3d printed chitosan-gelatine hydrogel coating on titanium alloy surface as biological fixation interface of artificial joint prosthesis, *International Journal of Biological Macromolecules*, 182. 669-679. doi: <https://doi.org/10.1016/j.ijbiomac.2021.04.046>
- Wu, Y., Feng, F., Xin, H., Li, K., Tang, Z., Guo, Y., Qin, D., An, B., Diao, X., & Dou, C. 2019. Fracture strength and osseointegration of an ultrafine-grained titanium mini dental implant after macromorphology optimization, *ACS Biomaterials Science & Engineering*, 5(8). 4122-4130. doi: 10.1021/acsbiomaterials.9b00406
- Wu, Y., Li, Q., Xu, B., Fu, H., & Li, Y. 2021. Nano-hydroxyapatite coated tio2 nanotubes on ti-19zr-10nb-1fe alloy promotes osteogenesis in vitro, *Colloids and Surfaces B: Biointerfaces*, 207. 112019. doi: <https://doi.org/10.1016/j.colsurfb.2021.112019>
- Wu, Y., Wang, Y., Zhao, D., Zhang, N., Li, H., Li, J., Wang, Y., Zhao, Y., Yan, J., & Zhou, Y. 2019. In vivo study of microarc oxidation coated mg alloy as a substitute for bone defect repairing: Degradation behavior, mechanical properties, and bone response, *Colloids and Surfaces B: Biointerfaces*, 181. 349-359.
- Wu, Z., Tian, Q., Wang, J., Feng, Y., Li, L., Xu, C., Lv, J., & Lv, Z. 2022. A bone implant with nir-responsiveness for eliminating osteosarcoma cells and promoting osteogenic differentiation of bmscs, *Colloids and Surfaces B: Biointerfaces*, 211. 112296. doi: <https://doi.org/10.1016/j.colsurfb.2021.112296>
- Xia, Z., Yu, X., & Wei*, M. 2012. Biomimetic collagen/apatite coating formation on ti6al4v substrates, *Journal of Biomedical Materials Research Part B: Applied Biomaterials*, 100B(3). 871-881. doi: <https://doi.org/10.1002/jbm.b.31970>
- Xu, K., Zhou, M., Chen, W., Zhu, Y., Wang, X., Zhang, Y., & Zhang, Q. 2021. Bioinspired polydopamine/graphene oxide/collagen nanofilms as a

- controlled release carrier of bioactive substances, *Chemical Engineering Journal*, 405. 126930. doi: <https://doi.org/10.1016/j.cej.2020.126930>
- Xu, L., Varkey, M., Jorgensen, A., Ju, J., Jin, Q., Park, J. H., Fu, Y., Zhang, G., Ke, D., Zhao, W., Hou, R., & Atala, A. 2020. Bioprinting small diameter blood vessel constructs with an endothelial and smooth muscle cell bilayer in a single step, *Biofabrication*, 12(4). 045012. doi: 10.1088/1758-5090/aba2b6
- Xu, Q., Xu, Z., Jiang, X., Yarmolenko, M. A., Rogachev, A. A., & Rogachev, A. V. 2021. Antibacterial coatings based on polycaprolactone and polyurethane with prolonged release of ciprofloxacin, *Surface and Coatings Technology*, 405. 126584. doi: <https://doi.org/10.1016/j.surfcoat.2020.126584>
- Xu, Z., & Jiang, X. 2022. Osteogenic tio2 composite nano-porous arrays: A favorable platform based on titanium alloys applied in artificial implants, *Colloids and Surfaces A: Physicochemical and Engineering Aspects*, 640. 128301. doi: 10.1016/j.colsurfa.2022.128301
- Yadroitsev, I., Krakhmalev, P., & Yadroitsava, I. 2014. Selective laser melting of ti6al4v alloy for biomedical applications: Temperature monitoring and microstructural evolution, *Journal of Alloys and Compounds*, 583. 404-409. doi: <http://dx.doi.org/10.1016/j.jallcom.2013.08.183>
- Yahiro, Y., Maeda, S., Morikawa, M., Koinuma, D., Jokoji, G., Ijuin, T., Komiya, S., Kageyama, R., Miyazono, K., & Taniguchi, N. 2020. Bmp-induced atoh8 attenuates osteoclastogenesis by suppressing runx2 transcriptional activity and reducing the rankl/opg expression ratio in osteoblasts, *Bone Research*, 8(1). 32. doi: 10.1038/s41413-020-00106-0
- Yamada, M., & Egusa, H. 2018. Current bone substitutes for implant dentistry, *Journal of Prosthodontic Research*, 62(2). 152-161. doi: 10.1016/j.jpor.2017.08.010
- Yamaguchi, S., Akeda, K., Shintani, S. A., Sudo, A., & Matsushita, T. 2022. Drug-releasing gelatin coating reinforced with calcium titanate formed on ti-6al-4v alloy designed for osteoporosis bone repair, *Coatings*, 12(2). 139. doi: 10.3390/coatings12020139
- Yan, J., Li, J., Hu, J., Zhang, L., Wei, C., Sultana, N., Cai, X., Zhang, W., & Cai, C.-L. 2018. Smad4 deficiency impairs chondrocyte hypertrophy via the runx2 transcription factor in mouse skeletal development, *Journal of Biological*

Chemistry, 293(24). 9162-9175. doi:
<https://doi.org/10.1074/jbc.RA118.001825>

- Yang, C., Zhao, C., Wang, X., Shi, M., Zhu, Y., Jing, L., Wu, C., & Chang, J. 2019. Stimulation of osteogenesis and angiogenesis by micro/nano hierarchical hydroxyapatite via macrophage immunomodulation, *Nanoscale*, 11(38). 17699-17708. doi: 10.1039/C9NR05730G
- Yang, W. E., & Huang, H. H. 2021. Tio2 nanonetwork on rough ti enhanced osteogenesis in vitro and in vivo, *Journal of Dental Research*, 100(10). 1186-1193. doi: 10.1177/00220345211001017
- Yang, Y., Wang, H., Zhu, J.-C., Shao, Y.-F., Bai, F.-J., Chen, X.-M., Li, X., Guo, M., Shao, Z., & Zhang, K.-Q. 2019. Silk-fibroin-assisted cathodic electrolytic deposition of calcium phosphate for biomedical applications, *ACS Biomaterials Science & Engineering*, 5(9). 4302-4310. doi: 10.1021/acsbiomaterials.9b00207
- Yang, Y., Zhang, H., Komasa, S., Morimoto, Y., Sekino, T., Kawazoe, T., & Okazaki, J. 2021. Uv/ozone irradiation manipulates immune response for antibacterial activity and bone regeneration on titanium, *Materials Science and Engineering: C*, 129. 112377. doi: <https://doi.org/10.1016/j.msec.2021.112377>
- Yavari, S. A., Croes, M., Akhavan, B., Jahanmard, F., Eigenhuis, C., Dadbakhsh, S., Vogely, H., Bilek, M., Fluit, A., & Boel, C. 2020. Layer by layer coating for bio-functionalization of additively manufactured meta-biomaterials, *Additive Manufacturing*, 32. 100991.
- Ye, J., Huang, B., & Gong, P. 2021. Nerve growth factor-chondroitin sulfate/hydroxyapatite-coating composite implant induces early osseointegration and nerve regeneration of peri-implant tissues in beagle dogs, *Journal of Orthopaedic Surgery and Research*, 16(1). 51. doi: 10.1186/s13018-020-02177-5
- Yeo, I.-S. L. 2020. Modifications of dental implant surfaces at the micro-and nano-level for enhanced osseointegration, *Materials*, 13(1). 89.
- Yilmaz, B., Pazarceviren, A. E., Tezcaner, A., & Evis, Z. 2020. Historical development of simulated body fluids used in biomedical applications: A

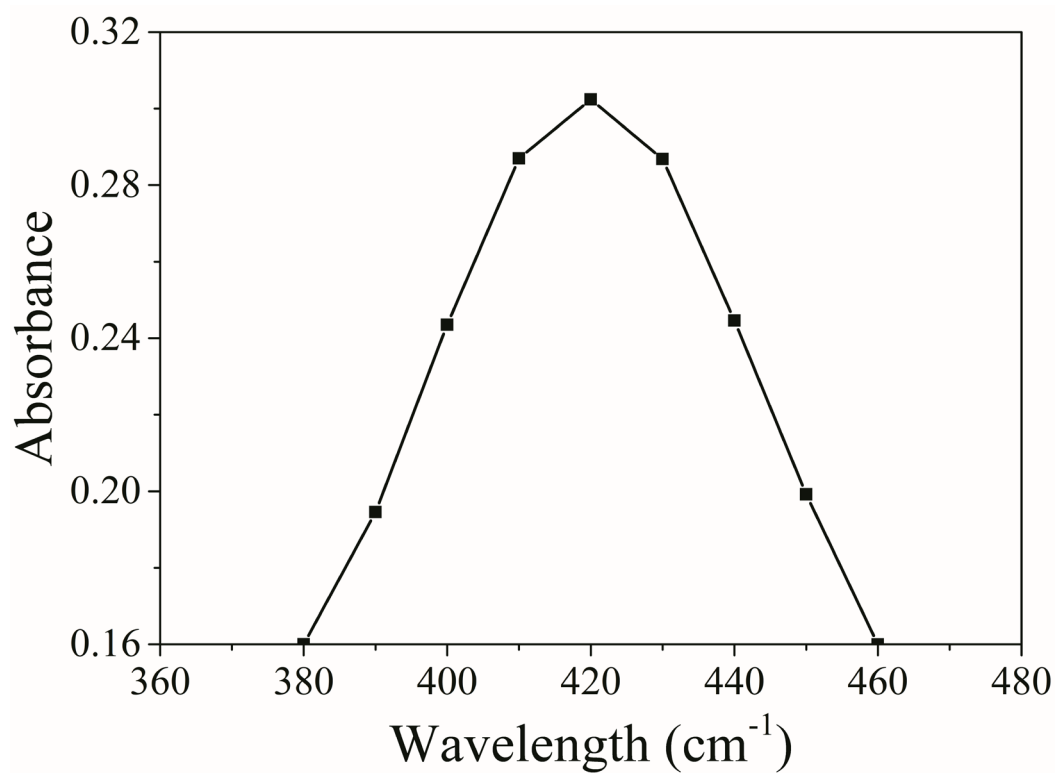
- review, *Microchemical Journal*, 155. 104713. doi: <https://doi.org/10.1016/j.microc.2020.104713>
- Yin, X., Yan, L., Hao, D. J., Liu, S., Yang, M., He, B., Prabakaran, S., & Liu, Z. 2020. Calcium alginate template-mineral substituted hydroxyapatite hydrogel coated titanium implant for tibia bone regeneration, *International Journal of Pharmaceutics*. 583. 119303. doi: 10.1016/j.ijpharm.2020.119303
- Yin, X., Yang, C., Wang, Z., Zhang, Y., Li, Y., Weng, J., & Feng, B. 2021. Alginate/chitosan modified immunomodulatory titanium implants for promoting osteogenesis in vitro and in vivo, *Materials Science and Engineering: C*, 124. 112087. doi: <https://doi.org/10.1016/j.msec.2021.112087>
- Ying, X., Cheng, S., Wang, W., Lin, Z., Chen, Q., Zhang, W., Kou, D., Shen, Y., Cheng, X., & Rompis, F. A. 2011. Effect of boron on osteogenic differentiation of human bone marrow stromal cells, *Biological Trace Element Research*, 144(1-3). 306-315. doi: 10.1007/s12011-011-9094-x
- Yu, C., Zhang, C., Kuang, Z., & Zheng, Q. 2021. The role of nlrp3 inflammasome activities in bone diseases and vascular calcification, *Inflammation*, 44(2). 434-449. doi: 10.1007/s10753-020-01357-z
- Zako, T., Nagata, H., Terada, N., Sakono, M., Soga, K., & Maeda, M. 2008. Improvement of dispersion stability and characterization of upconversion nanophosphors covalently modified with peg as a fluorescence bioimaging probe, *Journal of Materials Science*, 43(15). 5325-5330. doi: 10.1007/s10853-008-2776-x
- Zhan, X., Li, S., Cui, Y., Tao, A., Wang, C., Li, H., Zhang, L., Yu, H., Jiang, J., & Li, C. 2020. Comparison of the osteoblastic activity of low elastic modulus ti-24nb-4zr-8sn alloy and pure titanium modified by physical and chemical methods, *Materials Science and Engineering: C*, 113. 111018. doi: <https://doi.org/10.1016/j.msec.2020.111018>
- Zhang, B., Li, J., He, L., Huang, H., & Weng, J. 2020. Bio-surface coated titanium scaffolds with cancellous bone-like biomimetic structure for enhanced bone tissue regeneration, *Acta Biomaterialia*, 114. 431-448. doi: <https://doi.org/10.1016/j.actbio.2020.07.024>

- Zhang, H., Komasa, S., Mashimo, C., Sekino, T., & Okazaki, J. 2017. Effect of ultraviolet treatment on bacterial attachment and osteogenic activity to alkali-treated titanium with nanonetwork structures, *International Journal of Nanomedicine*, 12. 4633-4646.
- Zhang, H., Wang, X., Li, N., Xia, J., Meng, Q., Ding, J., & Lu, J. 2018. Synthesis and characterization of tio₂/graphene oxide nanocomposites for photoreduction of heavy metal ions in reverse osmosis concentrate, *RSC Advances*, 8(60). 34241-34251. doi: 10.1039/C8RA06681G
- Zhang, L., Xue, Y., Gopalakrishnan, S., Li, K., Han, Y., & Rotello, V. M. 2021. Antimicrobial peptide-loaded pectolite nanorods for enhancing wound-healing and biocidal activity of titanium, *ACS Applied Materials & Interfaces*, 13(24). 28764-28773. doi: 10.1021/acsami.1c04895
- Zhang, W., Liu, N., Shi, H., Liu, J., Shi, L., Zhang, B., Wang, H., Ji, J., & Chu, P. K. 2015. Upregulation of bmscs osteogenesis by positively-charged tertiary amines on polymeric implants via charge/inos signaling pathway, *Scientific Reports*, 5. 9369.
- Zhang, X., Lu, X., Lv, Y., Yang, L., Zhang, E., & Dong, Z. 2021. Enhancement of corrosion resistance and biological performances of cu-incorporated hydroxyapatite/tio₂ coating by adjusting cu chemical configuration and hydroxyapatite contents, *ACS Applied Bio Materials*, 4(1). 903-917. doi: 10.1021/acsabm.0c01390
- Zhang, X., Wang, K., Hu, J., Zhang, Y., Dai, Y., & Xia, F. 2020. Role of a high calcium ion content in extending the properties of alginate dual-crosslinked hydrogels, *Journal of Materials Chemistry A*, 8(47). 25390-25401. doi: 10.1039/D0TA09315G
- Zhang, Y., Chen, X., Li, Y., Bai, T., Li, C., Jiang, L., Liu, Y., Sun, C., & Zhou, W. 2021. Biomimetic inorganic nanoparticle-loaded silk fibroin-based coating with enhanced antibacterial and osteogenic abilities, *ACS Omega*, 6(44). 30027-30039. doi: 10.1021/acsomega.1c04734
- Zhang, Y., Fu, S., Yang, L., Qin, G., & Zhang, E. 2022. A nano-structured tio₂/cuo/cu₂o coating on ti-cu alloy with dual function of antibacterial ability and osteogenic activity, *Journal of Materials Science & Technology*, 97. 201-212. doi: <https://doi.org/10.1016/j.jmst.2021.04.056>

- Zhang, Y., Hu, L., Lin, M., Cao, S., Feng, Y., & Sun, S. 2021. Rbmbp-2-loaded plga/titanium nanotube delivery system synergistically enhances osseointegration, *ACS Omega*, 6(25). 16364-16372. doi: 10.1021/acsomega.1c00851
- Zhao, C., Qiu, P., Li, M., Liang, K., Tang, Z., Chen, P., Zhang, J., Fan, S., & Lin, X. 2021. The spatial form periosteal-bone complex promotes bone regeneration by coordinating macrophage polarization and osteogenic-angiogenic events, *Materials Today Bio*, 12. 100142. doi: <https://doi.org/10.1016/j.mtbio.2021.100142>
- Zhao, D., Liang, H., Han, C., Li, J., Liu, J., Zhou, K., Yang, C., & Wei, Q. 2021. 3d printing of a titanium-tantalum gyroid scaffold with superb elastic admissible strain, bioactivity and in-situ bone regeneration capability, *Additive Manufacturing*, 47. 102223. doi: <https://doi.org/10.1016/j.addma.2021.102223>
- Zhao, X., Ren, X., Wang, C., Huang, B., Ma, J., Ge, B., Jia, Z., & Li, Y. 2020. Enhancement of hydroxyapatite formation on titanium surface by alkali heat treatment combined with induction heating and acid etching, *Surface and Coatings Technology*, 399. 126173. doi: <https://doi.org/10.1016/j.surfcoat.2020.126173>
- Zuchuat, J., Maldonado, Y., Botteri, J., & Decco, O. 2021. In vivo effect of uv-photofunctionalization of cocrmo in processes of guided bone regeneration and tissue engineering, *Journal of Biomedical Materials Research Part A*, 109(1). 31-41. doi: <https://doi.org/10.1002/jbm.a.37004>
- Zwahr, C., Welle, A., Weingärtner, T., Heinemann, C., Kruppke, B., Gulow, N., Holthaus, M. g., & Fabián Lasagni, A. 2019. Ultrashort pulsed laser surface patterning of titanium to improve osseointegration of dental implants, *Advanced Engineering Materials*, 21(12). 1900639.

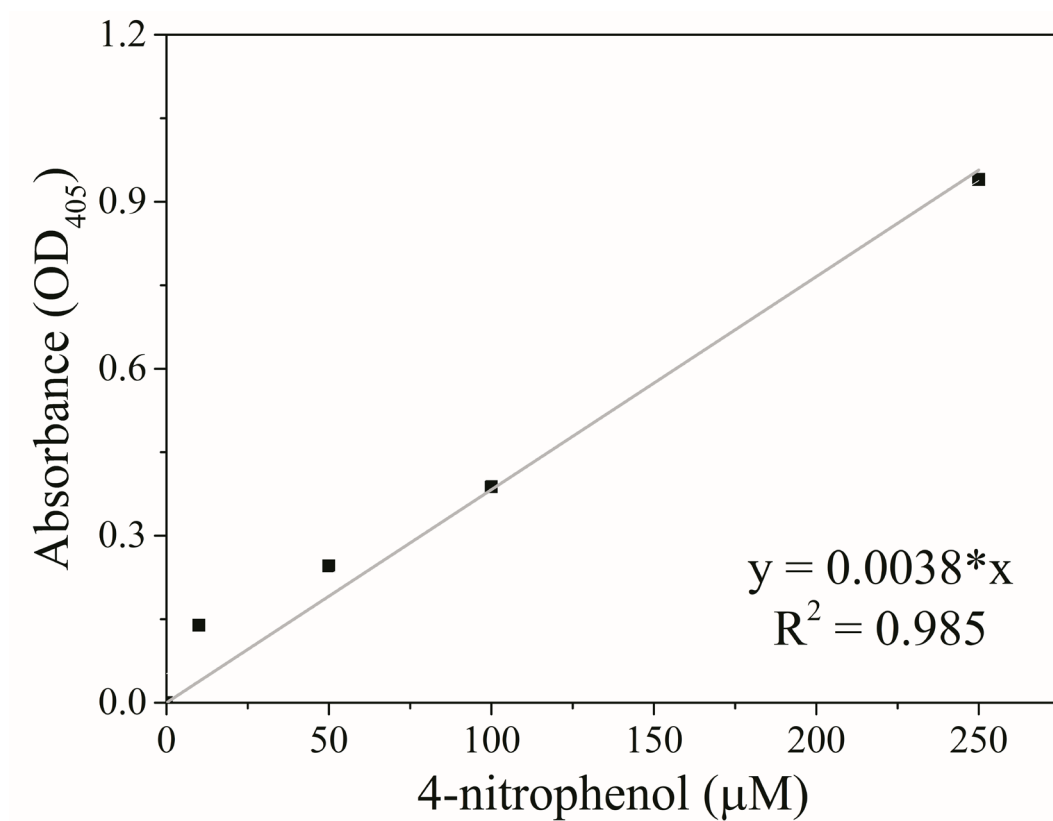
APPENDICES

A. Wavelength scan of TNBS for finding λ_{\max} .



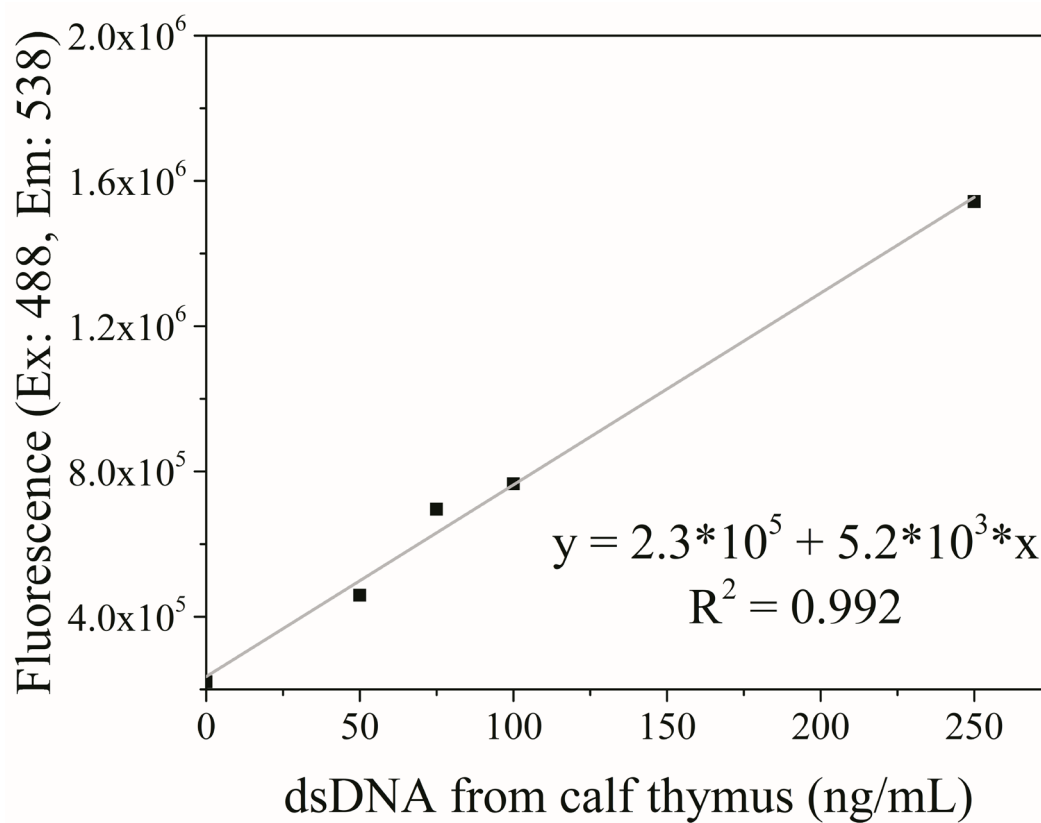
Appendix A1 Figure 1. Wavelength scan of TNBS treated APTES solution to determine λ_{\max} (n=3).

B. ALP Calibration Curve Using 4-nitrophenol



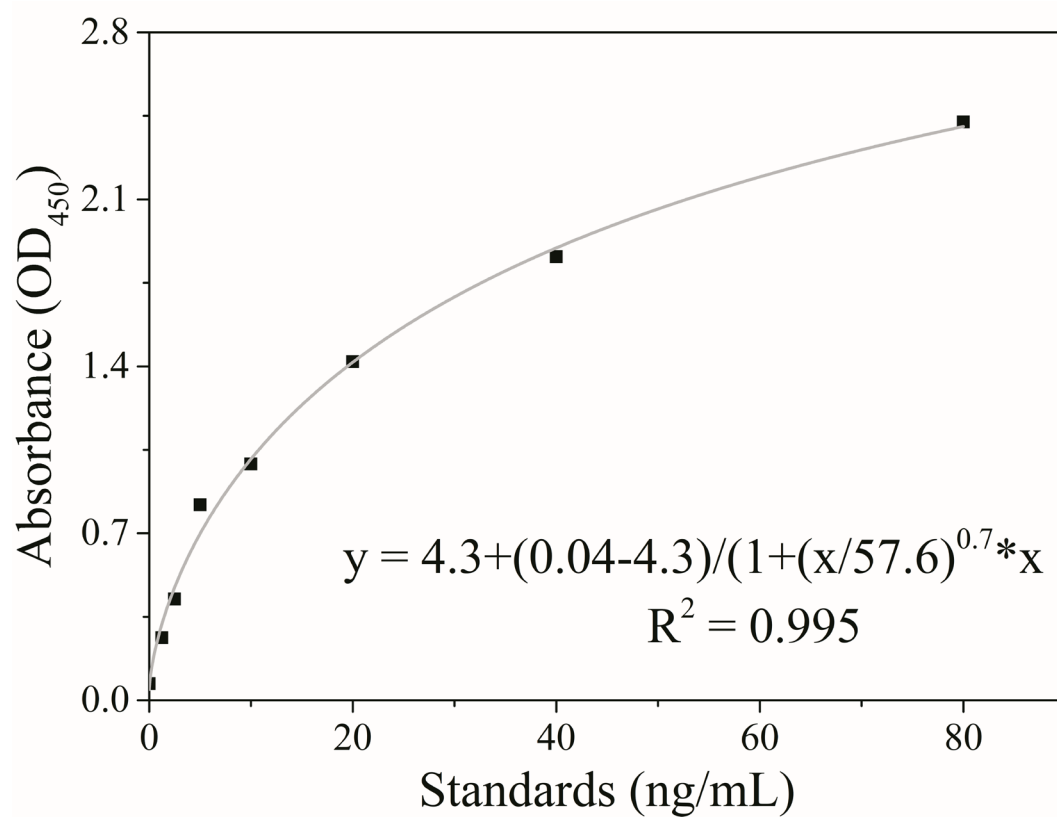
Appendix B1 Figure 1. Calibration curve of 4-nitrophenol prepared in various concentrations (0-250 μM) determined by change in absorbance at 405 nm (n=3).

C. Calibration curve of DNA using Picogreen Dye Calibration



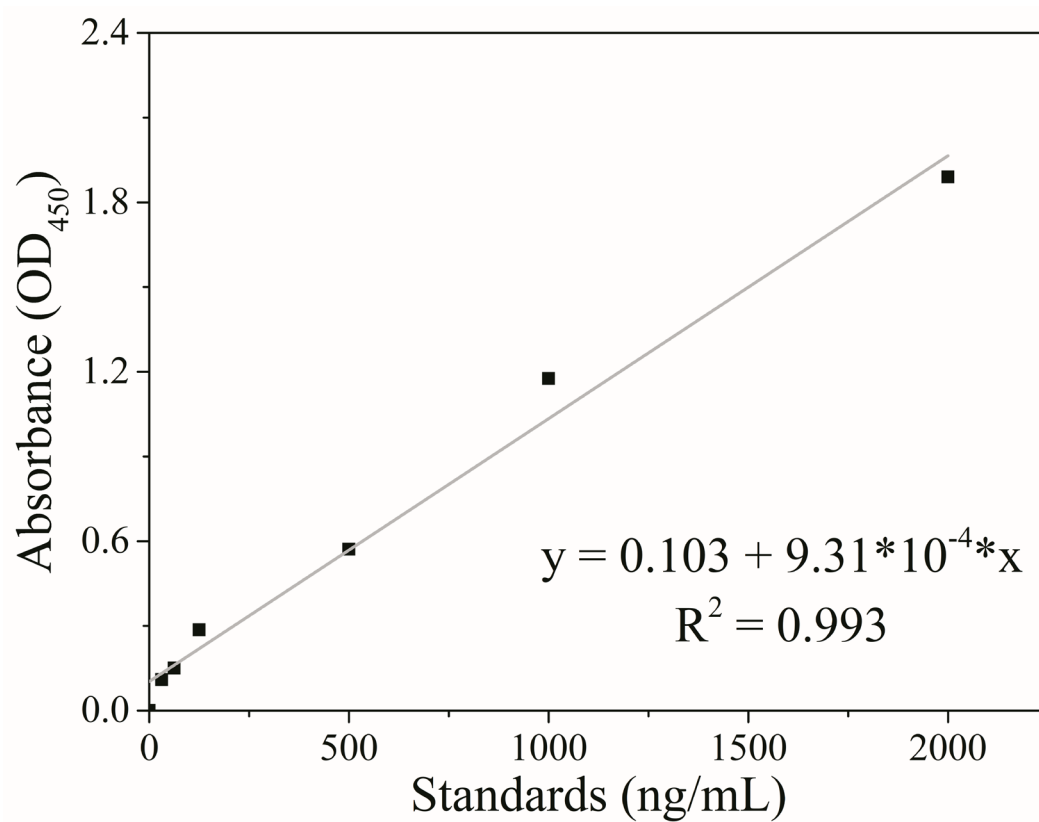
Appendix C1 Figure 1. Calibration curve of dsDNA from calf thymus in various concentrations (0-250 ng/mL) determined by fluorescence intensity measurement (n=6).

D. Calibration Curve of OCN



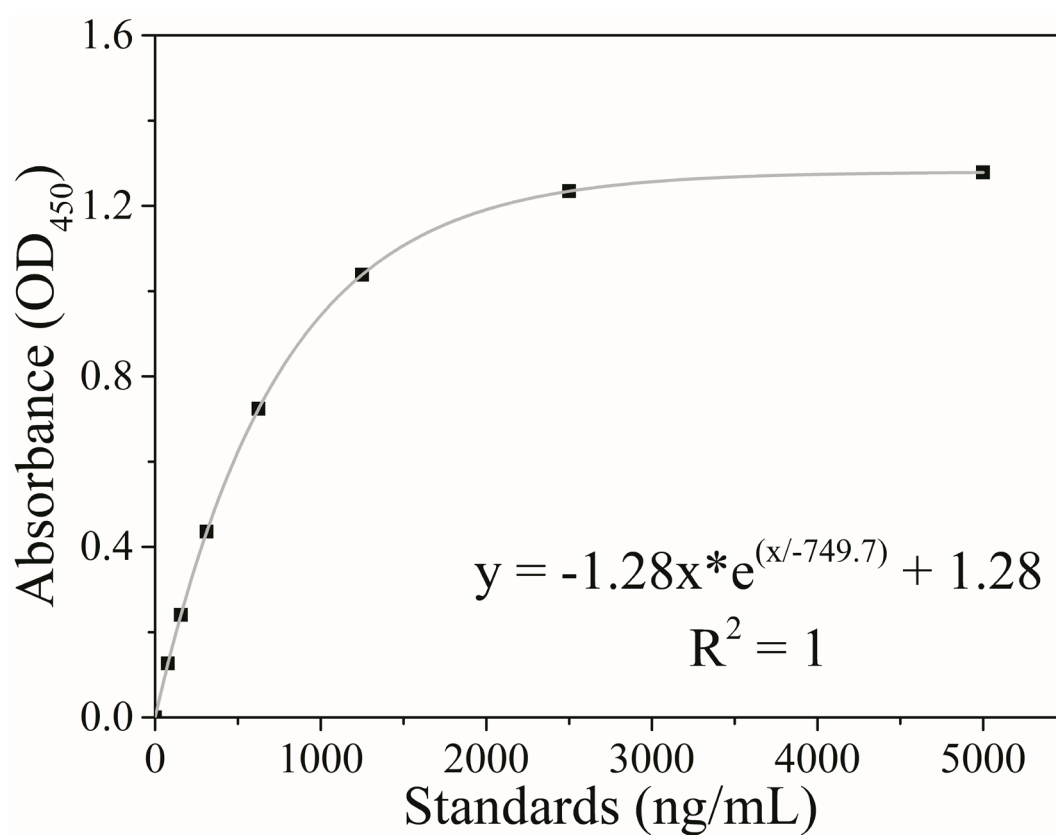
Appendix D1 Figure 1. Calibration curve of OCN in various concentrations (0-80 ng/mL) determined by absorbance at 450 nm (n=6).

E. Calibration Curve of VEGF-A



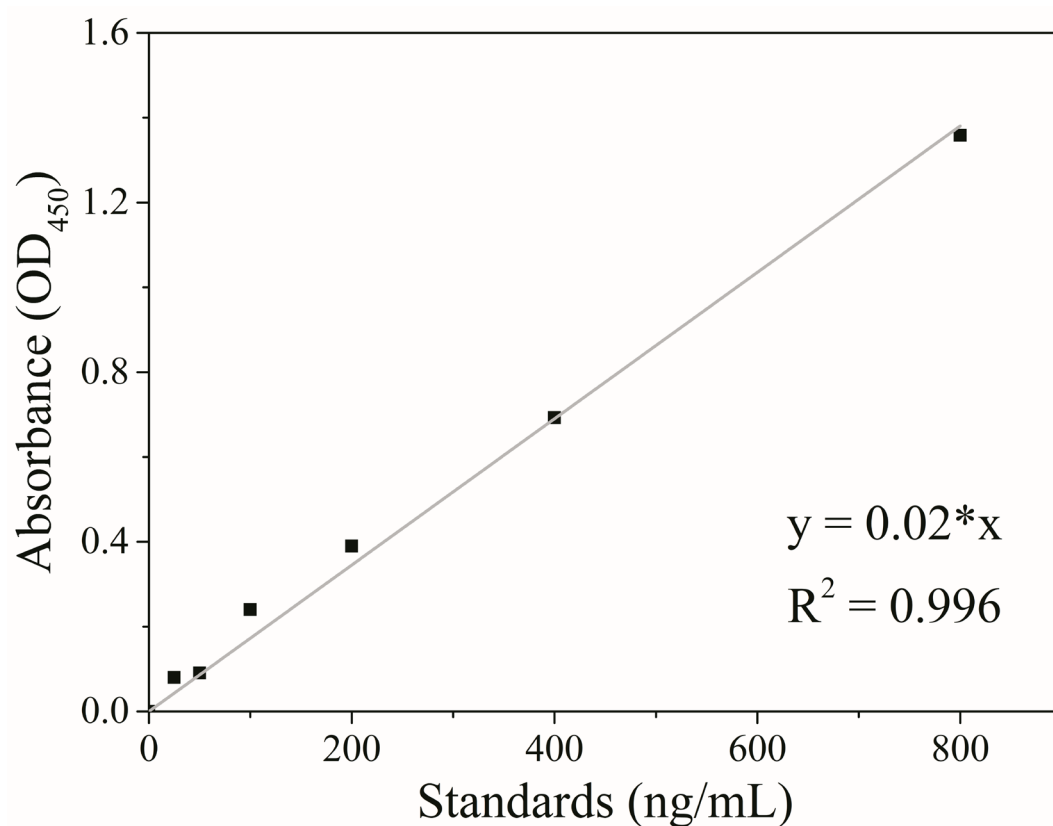
Appendix E1 Figure 1. Calibration curve of VEGF-A in various concentrations (0-2000 ng/mL) determined by absorbance at 450 nm after following the protocol provided by supplier (n=6).

F. Calibration Curve of CAS-1



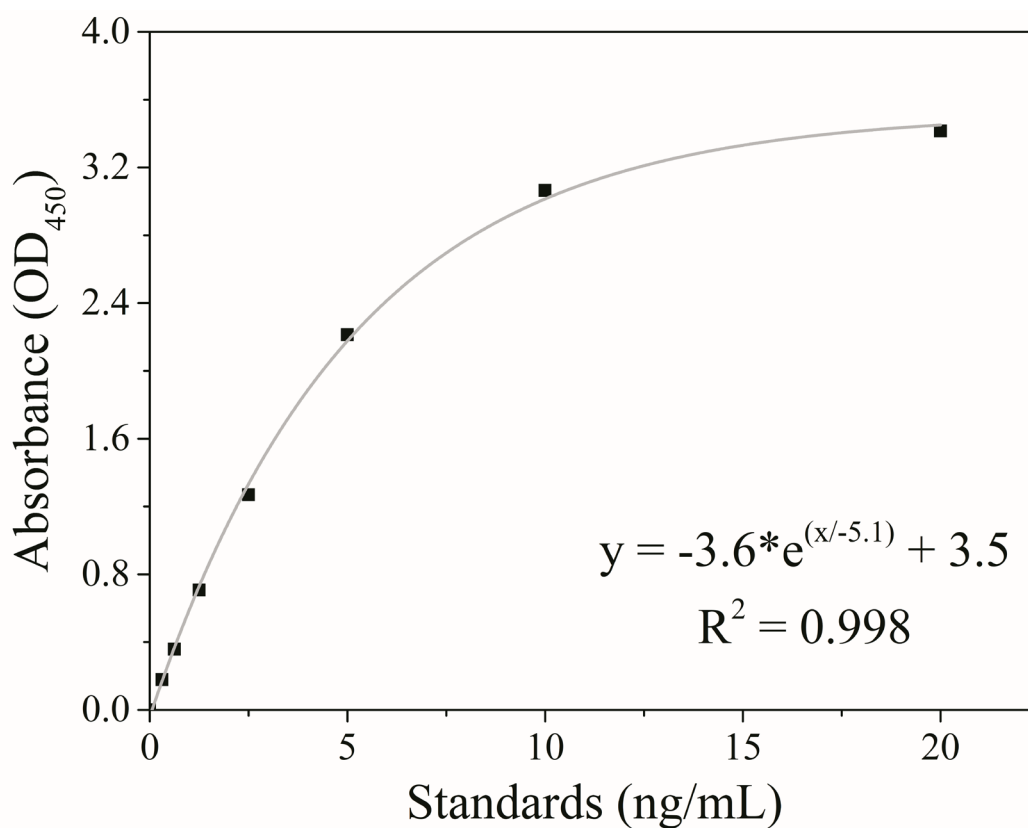
Appendix F1 Figure 1. Calibration curve of CAS-1 in various concentrations (0-5000 ng/mL) determined by absorbance at 450 nm after following the protocol provided by supplier (n=8).

G. Calibration Curve of IL-10



Appendix G1 Figure 1. Calibration curve of IL-10 in various concentrations (0-800 ng/mL) determined by absorbance at 450 nm after following the protocol provided by supplier (n=8).

H. Calibration Curve of iNOS



Appendix H1 Figure 1. Calibration curve of iNOS in various concentrations (0-20 ng/mL) determined by absorbance at 450 nm after following the protocol provided by supplier (n=8).

CURRICULUM VITAE

Surname, Name: Pazarçeviren, Ahmet Engin

EDUCATION

Degree	Institution	Year of Graduation
MS	METU Engineering Sciences	2016
BS	METU Biological Sciences	2013
High School	Burak Bora Anadolu Lisesi	2008

FOREIGN LANGUAGES

Native Turkish, Fluent English, Basic German, Basic French

PUBLICATIONS

- 1.Pazarçeviren, A. E., Akbaba, S., Evis, Z., Tezcaner, A. (2022). Versatile-in-all-trades: Multifunctional boron doped calcium deficient hydroxyapatite directs immunomodulation and regeneration. ACS Biomaterials and Tissue Engineering, doi: 10.1021/acsbiomaterials.2c00242.
- 2.Pazarçeviren, A. E., Akbaba, S., Tezcaner, A., Keskin, D., Evis, Z. (2022). Seamless and robust alginate/gelatin coating on Ti-6Al-4V as a gap filling interphase. Applied Surface Science, 581, 152393. doi: 10.1016/j.apsusc.2021.152393.
- 3.Pazarçeviren, A. E., Tezcaner, A., & Evis, Z. (2021). Multifunctional natural polymer-based metallic implant surface modifications. Biointerphases, 16(2), 020803. doi: 10.1116/6.0000876.
- 4.Pazarçeviren, A. E., Tezcaner, A., Keskin, D., Kolukısa, S. T., Sürdem, S., & Evis, Z. (2021). Boron-doped Biphasic Hydroxyapatite/ β -Tricalcium Phosphate for Bone

Tissue Engineering. Biological trace element research, 199(3), 968-980. doi: 10.1007/s12011-020-02230-8.

5.Yilmaz, B., Pazarceviren, A. E., Tezcaner, A., & Evis, Z. (2020). Historical development of simulated body fluids used in biomedical applications: A review. *Microchemical Journal*, 155, 104713. doi: <https://doi.org/10.1016/j.microc.2020.104713>.

6.Pazarçeviren, A. E., Dikmen, T., Altunbaş, K., Yaprakçı, V., Erdemli, Ö., Keskin, D., & Tezcaner, A. (2020). Composite clinoptilolite/PCL-PEG-PCL scaffolds for bone regeneration: In vitro and in vivo evaluation. *Journal of Tissue Engineering and Regenerative Medicine*, 14(1), 3-15. doi: <https://doi.org/10.1002/term.2938>.

7.Alshemary, A. Z., Pazarçeviren, A. E., Keskin, D., Tezcaner, A., Hussain, R., & Evis, Z. (2019). Porous clinoptilolite—nano biphasic calcium phosphate scaffolds loaded with human dental pulp stem cells for load bearing orthopedic applications. *Biomedical Materials*, 14(5), 055010. doi: 10.1088/1748-605x/ab3714.

8.Alshemary, A. Z., Pazarçeviren, A.E., Dalgic, A. D., Tezcaner, A., Keskin, D., & Evis, Z. (2019). Nanocrystalline Zn^{2+} and SO_4^{2-} binary doped fluorohydroxyapatite: A novel biomaterial with enhanced osteoconductive and osteoinconductive properties. *Materials Science and Engineering: C*, 104, 109884. doi: <https://doi.org/10.1016/j.msec.2019.109884>.

9.Moonesi Rad, R., Pazarçeviren, E., Ece Akgün, E., Evis, Z., Keskin, D., Şahin, S., & Tezcaner, A. (2019). In vitro performance of a nanobiocomposite scaffold containing boron-modified bioactive glass nanoparticles for dentin regeneration. *Journal of Biomaterials Applications*, 33(6), 834-853. doi: 10.1177/0885328218812487.

10.Alshemary, A. Z., Pazarceviren, A.E., Tezcaner, A., & Evis, Z. (2018). $Fe^{3+/-}$ dual doped nano hydroxyapatite: A novel material for biomedical applications. *Journal of Biomedical Materials Research Part B: Applied Biomaterials*, 106(1), 340-352. doi: <https://doi.org/10.1002/jbm.b.33838>.

11.Pazarçeviren, A. E., Evis, Z., Keskin, D., & Tezcaner, A. (2019). Resorbable PCEC/gelatin-bismuth doped bioglass-graphene oxide bilayer membranes for

guided bone regeneration. *Biomedical Materials*, 14(3), 035018. doi: 10.1088/1748-605x/ab007b.

12. Pazarçeviren, A. E., Tahmasebifar, A., Tezcaner, A., Keskin, D., & Evis, Z. (2018). Investigation of bismuth doped bioglass/graphene oxide nanocomposites for bone tissue engineering. *Ceramics International*, 44(4), 3791-3799. doi: <https://doi.org/10.1016/j.ceramint.2017.11.164>.

13. Pazarçeviren, E., Erdemli, Ö., Keskin, D., & Tezcaner, A. (2017). Clinoptilolite/PCL-PEG-PCL composite scaffolds for bone tissue engineering applications. *Journal of Biomaterials Applications*, 31(8), 1148-1168. doi: 10.1177/0885328216680152.

14. Türkkan, S., Pazarçeviren, A. E., Keskin, D., Machin, N. E., Duygulu, Ö., & Tezcaner, A. (2017). Nanosized CaP-silk fibroin-PCL-PEG-PCL/PCL based bilayer membranes for guided bone regeneration. *Materials Science and Engineering: C*, 80, 484-493. doi: <https://doi.org/10.1016/j.msec.2017.06.016>.

15. Alshemary, A. Z., Pazarceviren, A. E., Tezcaner, A., & Evis, Z. (2016). Mesoporous strontium doped nano sized sulphate hydroxyapatite as a novel biomaterial for bone tissue applications. *RSC Advances*, 6(72), 68058-68071. doi: 10.1039/C6RA16809D.